NYU WIRELESS TR 2022-001

Technical Report

Sub-THz Channel Sounding and Channel Modeling Based on Indoor and Outdoor Field Measurements at 142 GHz

Yunchou Xing and Theodore S. Rappaport

{ychou, tsr}@nyu.edu

NYU WIRELESS

NYU Tandon School of Engineering

370 Jay

Brooklyn, NY 11201

January 6th, 2022

© 2022 NYU

Acknowledgements

This work was supported by the National Science Foundation (NSF) Grants 1702967, 1731290, 1909206, 2037845, and the NYU WIRELESS Industrial Affiliates Program.

ABSTRACT

Advisor: Prof. Theodore S. Rappaport

The recent introduction of fifth-generation (5G) cellular technology is the first wireless solution to exploit millimeter wave (mmWave) frequencies for global mobility, ushering in a new era of multi-Gbps data rates and rapid streaming with extremely low latency. This new era, which exploits extremely wide bandwidths and adaptive antenna arrays in small form factors, will enable the proliferation of exciting new applications, such as wireless cognition (providing human intelligence over wireless communications), centimeter-level position location, high-resolution virtual/augmented reality (VR/AR), driver-less cars, factory automation, remote medicine, radars for transportation and motion sensing, spectroscopy, and imaging will require data rates on the order of hundreds of Gbps or even Tbps with near-zero latency. To accommodate such massive data rates, 6G and beyond will likely flourish at frequencies above 100 GHz (e.g., sub-THz bands of 100-300 GHz or THz bands of 300 GHz-3 THz) as electronics become available to exploit the abundant spectrum.

This report introduces the current propagation issues and global regulations above 100 GHz, atmosphere absorption and rain attenuation versus frequencies, and various mmWave and THz applications. This report also presents different channel sounding techniques for frequencies above 100 GHz and the state-of-the-art channel sounding measurements, channel modeling works in the literature, as well as the current sub-THz channel sounder system at NYU WIRELESS. Propagation characteristics such as antenna cross polarization discrimination (XPD), partition loss (penetration loss), reflection, and scattering at sub-THz frequencies are explored. Channel propagation measurements, channel statistics, and channel models at sub-THz frequencies in both indoor hotspot office (InH) and outdoor urban microcell (UMi) environments are presented and compared to the statistics at 28 and 73 GHz based on the measurements conducted in the same environment (most locations are the same at different frequencies). Finally, we present works on non-Terrestrial Networks (NTN) including high altitude platform stations (HAPS), unmanned aerial vehicle (UAV), and satellites, and state-of-the-art research on intelligent reflecting surfaces (IRS). In general, this report provides the fundamental knowledge and a comprehensive understanding of the wireless channels at sub-THz frequencies, and it also demonstrates how the engineering efforts to create mmWave 5G networks will carry forward to frequencies as high as 800-900 GHz, meaning that the engineering developments of adaptive beamforming, wideband channel allocation, and site-specific installation used to create today's 5G networks will hold for the coming several decades as mobile communications move up into the THz range.

Contents

List of Figures

List of Tables

Chapter 1

Introduction

1.1 Spectrum for 6G Communications

As the wireless world moves towards future generations of communications (6G and beyond), new applications such as wireless cognition (providing human intelligence over wireless communications to enable massive computations from the edge or cloud to be sent to the device or machine performing the real-time action [1, 2, 3]), will require data rates on the order of hundreds of Gbps or even Tbps with near-zero latency. To accommodate such massive data rates, 6G and beyond will likely flourish at frequencies above 100 GHz (e.g., sub-THz bands of 100-300 GHz or THz bands of 300 GHz-3 THz) as electronics become available to exploit the abundant spectrum [1, 3, 4, 5, 6]. This new era, which will exploit wide-bandwidth channels (e.g., 1 GHz or more) and adaptive antenna arrays in small form factors, will enable the proliferation of new applications such as centimeter-level position location, high-resolution virtual/augmented reality (VR/AR), unmanned aircraft system (UAS) and high altitude platform stations (HAPS), driver-less cars, factory automation, remote medicine, radars for transportation and motion sensing, spectroscopy, sensing, imaging, and fixed and mobile broadband wireless [1, 2, 4, 6].

Global regulatory bodies and standard agencies govern the use of radio frequencies (mainly below 275 GHz) to promote efficient spectrum use. Specific provisions on frequencies above 100 GHz [5, 7] were instituted by the Japanese regulator, Ministry of Internal Affairs and Communications, in 2015 at 116-134 GHz [8], and the group of European spectrum regulators, Conference of European Postal and Telecommunications, in 2018 at 122.0-122.25 GHz and 244-246 GHz [9].

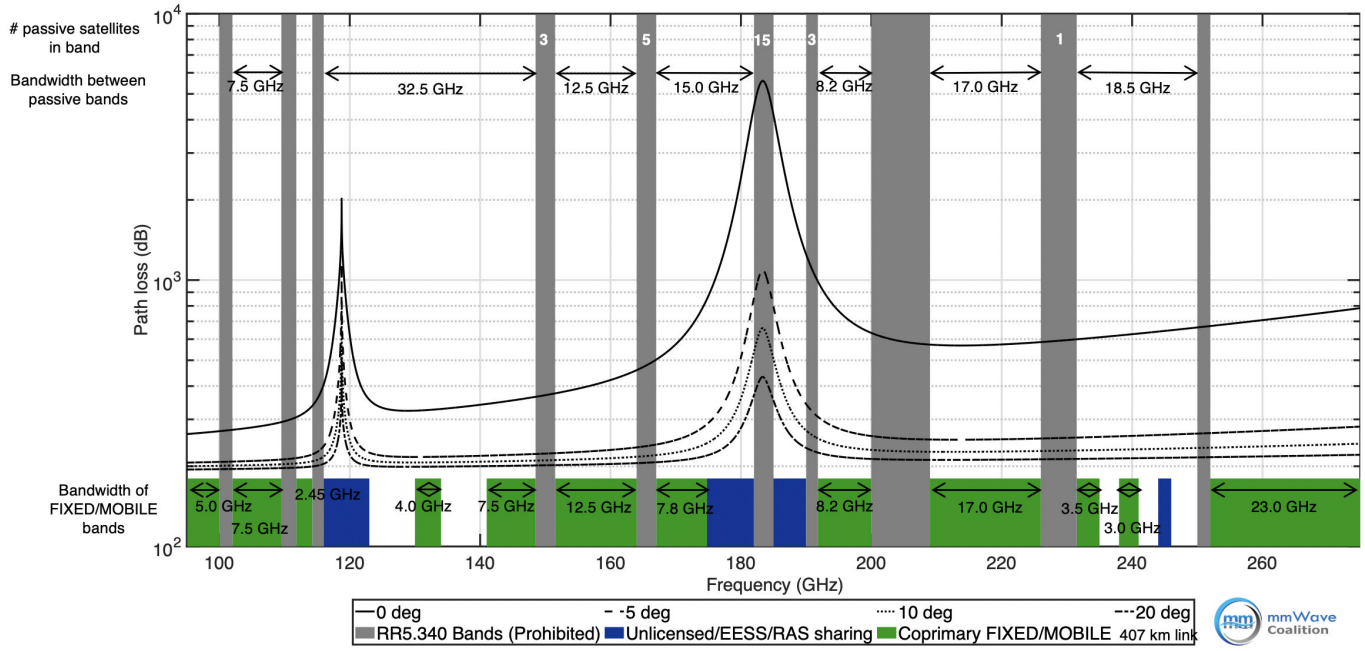

Figure 1.1: Key ITU spectrum allocation above 100 GHz with RR5.340 prohibited bands, unlicensed/EESS/RAS sharing bands, and coprimary fixed/mobile bands, from Millimeter Wave Coalition.

Table 1.1: Unlicensed spectrum proposed by FCC [10].

Frequency Band (GHz)	**Contiguous Bandwidth (GHz)**
116-123	7
174.8-182	7.2
185-190	5
244-246	2
Total	21.2

In March 2019, the Federal Communications Commission (FCC) adopted the Notice of Proposed Rulemaking ET Docket 18-21 [11] and four new unlicensed bands were authorized (116-122, 174.8-182, 185-190, and 244-246 GHz), shown as the blue segments along the bottom of Figure 1.1. The Office of Communications, the communication regulator of the UK, published a statement document in October 2020 on supporting innovation in the 100-200 GHz bands [12], and opened over 18 GHz of radio spectrum across three bands similar to the FCC (116-122, 174.8-182, and 185-190 GHz).

As seen in Figure 1.1, the International Telecommunications Union (ITU) Radio regulation 5.340 (RR5.340 which was adopted at the ITU World Radio Conference in 2000, WRC-2000) prohibits any emission in ten passive bands (the gray bars, 100-102 GHz, 109.5-111.8 GHz, 114.25-116 GHz, 148.5-151.5 GHz, 164-167 GHz, 182-185 GHz, 190-191.8 GHz, 200-209 GHz, 226-231.5 GHz, and

250-252 GHz) to protect satellite sensors and deep space observatories from 100 GHz up to 252 GHz [5]. The black double arrows show the bandwidth between RR5.340 bands, where the largest chunk of contiguous spectrum blocks available is 32.5 GHz (between 116-148.5 GHz) out of the total available 180 GHz (between 95-275 GHz) [1, 11]. Other shared bands have less severe restrictions, such as the green segments in the bottom of Figure 1.1 where Fixed and Mobile services have coprimary allocations. The ITU agreed in Resolution 731 to study if and under what conditions sharing the ten forbidden bands with terrestrial networks is possible.

The mmWave coalition [13], which is a group of innovative companies and universities united in the objective of removing regulatory barriers to technologies using frequencies ranging from 95 GHz to 275 GHz in the USA, submitted comments to the FCC and to the National Telecommunications and Information Administration (NTIA) on developing a sustainable spectrum strategy for America's future and urged NTIA to facilitate greater access to spectrum above 95 GHz for non-Federal use in January 2019 [13].

The Institute of Electrical and Electronics Engineers (IEEE) formed the IEEE 802.15.3d [14] task force in 2017 for global Wi-Fi use at frequencies across 252 GHz to 325 GHz, creating the first worldwide wireless communications standard for the 250-350 GHz frequency range, with a nominal PHY data rate of 100 Gbps and channel bandwidths from 2 GHz to 70 GHz [14]. The use cases for IEEE 802.15.3d include kiosk downloading [15], intra-device radio communication [16], connectivity in data centers, and wireless fiber for fronthaul and backhaul [13, 14, 17]. Meanwhile, FCC will launch its largest 5G spectrum auction on December 10, 2019 with 3400 MHz of spectrum in three different bands–37 GHz, 39 GHz, and 47 GHz [18].

As 5G and IEEE 802.11ay, and 802.15.3d [14, 19] are built out for the mmWave spectrum and promise data rates up to 100 Gbps, future 6G networks and wireless applications, that are probably a decade or more away from implementation, are likely to benefit from operation in the 100 GHz to 1 THz frequency bands [20, 21, 22]. The short wavelength at mmWave and THz will allow massive spatial multiplexing in hub and backhaul communications, as well as incredibly accurate sensing, imaging, spectroscopy, and other applications [23, 24, 25, 26]. The THz band, which we shall describe as being from 300 GHz through 3 THz, can also enable secure communications over highly sensitive links, such as in the military due to the fact that extremely small wavelengths (orders of microns) enable extremely high gain antennas to be made in extremely small physical dimensions [27].

Energy efficiency is always important for communication systems, and a theoretical framework to quantify energy consumption in the presence of vital device, system, and network trade-offs was presented in [28, 29]. The theory, called the *consumption factor theory* (CF, with a metric measured in bps/W), provides a means for enabling quantitative analysis and design approach for understanding power trade-offs in any communication system. It was shown in [28, 29] that the efficiency of components of a transmitter closest to the output, such as the antenna, have the largest impact on CF [28]. The power efficiency increases with the bandwidth when most of the power used by com-

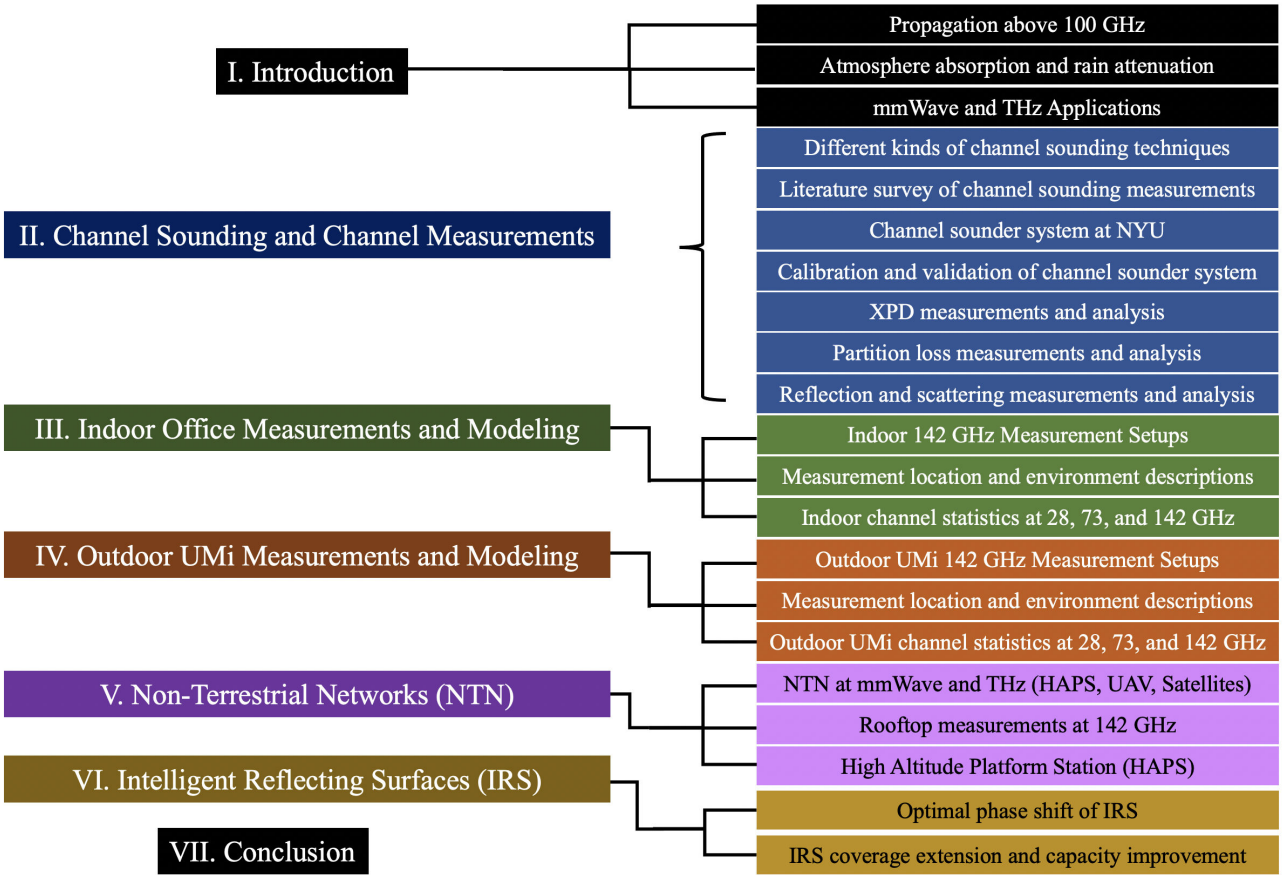

Figure 1.2: The structure of the report .

ponents that is "off", e.g., ancillary to the signal path (e.g., the baseband processor, oscillator, or a display) is predominant as compared to the power consumed by the components that are in line with the transmission signal path (e.g., power amplifier, mixer, antenna) [28, 29]. For a very simple radio transmitter, such as one that might be used in low cost IoT or "smart dust" applications, where the power required by the baseband processor and oscillator is small compared to the delivered radiated power, the power efficiency is independent of the bandwidth [28]. Thus, contrary to conventional wisdom, the CF theory proves that it is *more energy efficient* to move up to mmWave and THz frequencies which provide much wider bandwidth on a bits per seconds per watt (bps/W) basis, as compared to the current, sub-6 GHz communication networks.

The outline of the report is shown in Figure 1.2 with seven chapters. Chapter I introduces the current global regulations and propagation issues above 100 GHz, including atmosphere absorption and rain attenuation versus frequencies, and mmWave and THz applications. Chapter II presents different channel sounding techniques for frequencies above 100 GHz and the state-of-the-art channel sounding measurements, channel modeling research in the literature, and also the sub-THz channel sounder system at NYU WIRELESS. Chapter II will also introduce antenna cross polarization discrimination (XPD), partition loss (penetration loss), reflection, and scattering at sub-THz frequencies. Chapters III and IV present channel propagation measurements at 142 GHz in both indoor

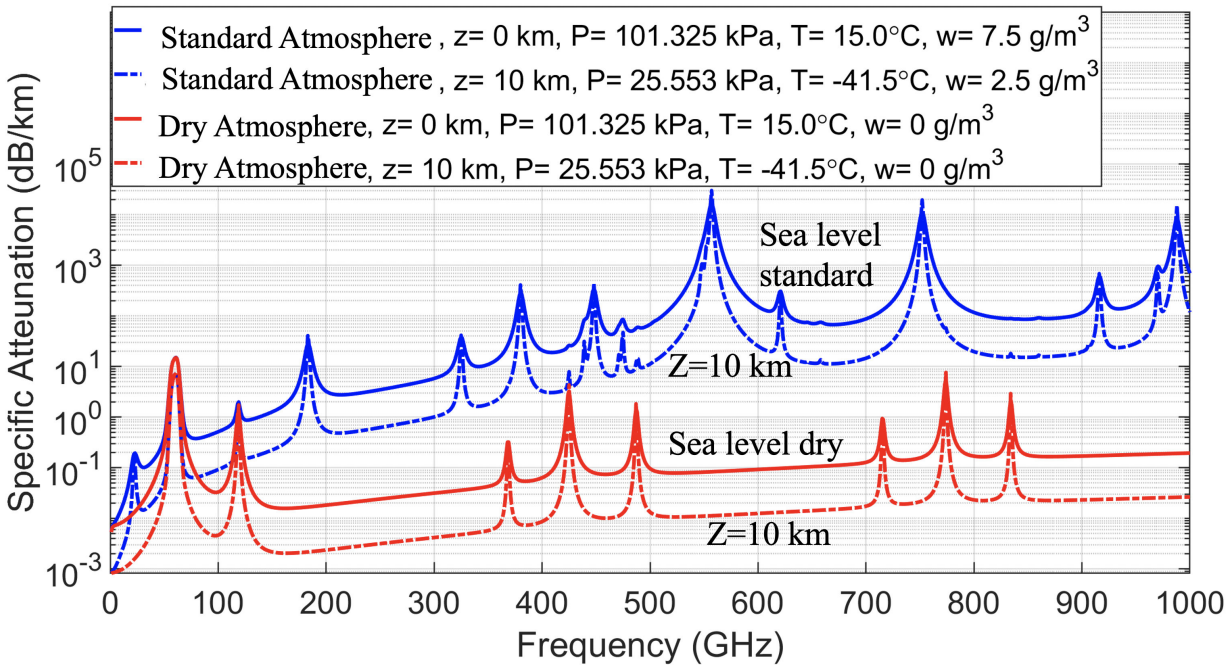

Figure 1.3: Atmospheric absorption beyond the natural Friis free space loss [30] at z = 0 km height (sea level) and z = 10 km height (10 km above the sea level) of electromagnetic waves versus frequency under different humidity conditions, computed from models in [31, 32].

hotspot office (InH) and outdoor urban microcell (UMi) environments. The channel statistics at 142 GHz for both indoor and outdoor environments are analyzed and compared to the statistics at 28 and 73 GHz based on measurements conducted in the same environment (most locations are the same at different frequencies). Monte Carlo simulations for both single-cell and multi-cell cases are conducted in an outdoor UMi environment to analyze the base station coverage of sub-THz communication systems and the system performance in terms of spectral efficiency. Chapter V shows the work on Non-Terrestrial Networks (NTN) including high altitude platform stations (HAPS), unmanned aerial vehicles (UAV), and satellites. Rooftop measurements to emulate the air-to-ground communications and the corresponding results are also presented in Chapter V. Chapter VI introduces the state-of-the-art research on intelligent reflecting surfaces (IRS). Concluding remarks are drawn in Chapter VII. In general, this work provides the fundamental knowledge and a comprehensive understanding of the wireless channels at sub-THz frequencies, and it also demonstrates how the engineering efforts to create mmWave 5G networks will carry forward to frequencies as high as 800-900 GHz, meaning that the engineering developments of adaptive beamforming, wideband channel allocation, and site-specific installation used to create today's 5G networks will hold for the coming several decades as mobile communications move up into the THz range.

1.2 Atmospheric Absorption

The importance of atmospheric absorption effects on the transmission of high frequency signals has long been recognized [33, 34]. At lower frequencies (below 6 GHz), the attenuation is mainly caused by molecular absorption [35], but at higher frequencies, as the wavelength approaches the size of dust, rain, snow, or hail, the effects of Mie scattering are expected to become more severe [36, 37, 38]. The various resonances of oxygen and other gases in the atmosphere, however, cause certain frequency bands to suffer from significant signal absorption. Figure 1.3 illustrates how the frequency bands of 183 GHz, 325 GHz, 380 GHz, 450 GHz, 550 GHz, and 760 GHz suffer much greater attenuation over distance in typical air due to the atmospheric absorption, beyond the natural Friis' free space loss, making these particular bands well suited for very short range and secure communications such as "whisper radio" applications, where massive bandwidth channels will attenuate very rapidly out to a few tens of meters, meters or fractions of a meter [37, 38, 39, 40]. Figure 1.3 also shows many mmWave and THz bands suffer surprising little loss as compared to sub 6-GHz bands, that is, only suffer less than 10 dB/km of additional loss than caused by free space propagation in air. These frequency bands could easily be used for high speed mobile wireless networks with km size coverage range, and perhaps even up to 10 km or beyond [31, 40, 41, 42].

The atmospheric attenuation is highly related to the altitude above earth, air pressure, temperature, and water vapor density. Figure 1.3 shows the atmospheric absorption beyond the natural Friis free space path loss (FSPL) from [30] at sea level (z = 0 km) and for the channel operating at 10 km above the sea level (z= 10 km) in both dry conditions (e.g., desert where water vapor density w is close to 0 g/m^3) and standard conditions (e.g., $w = 7.5$ g/m^3). The air pressure, temperature, and water vapor density decrease when the altitude increases (the relationship can be found in [31]), which results in larger atmospheric absorption at sea level than higher up in the troposphere compared to today's 4G networks below 6 GHz (e.g., but only about 6 dB/km at 300 GHz, z=0 km) and even less attenuation at higher altitudes (e.g., only about 1 dB/km at 300 GHz, z=10 km). This dispels myths, and shows air attenuation is inconsequential up to THz.

Notably, the atmospheric absorption at sea level in standard condition (the blue curve in Figure 1.3) at 200-300 GHz is remarkably less than 10 dB/km, and even at 800-900 GHz the additional atmospheric absorption beyond the natural Friis free space loss is 100 dB/km at sea level, meaning only 10 dB per 100 m over today's 4G cellular, which will be compensated for by the antenna gains at higher frequencies [1]. Work in [43] shows that within office buildings, there is a remarkable similarity in terms of large-scale path loss exponents when going from 28 GHz to 140 GHz, when referenced to the first meter of free-space propagation [44, 45], implying that the THz channels are very similar to today's mmWave wireless propagation channels except for the path loss in the first meter of propagation when energy spreads into the far field [1, 43, 44, 45]. Figure 1.6 shows that there is a vast amount of spectrum up to 1 THz with relatively little attenuation that can be utilized for future mobile and fixed terrestrial communication.

Figure 1.4 shows how the earth's troposphere offers a natural impenetrable wall to interference in space at low elevation angles (large slant paths). Atmospheric attenuation rapidly increases to

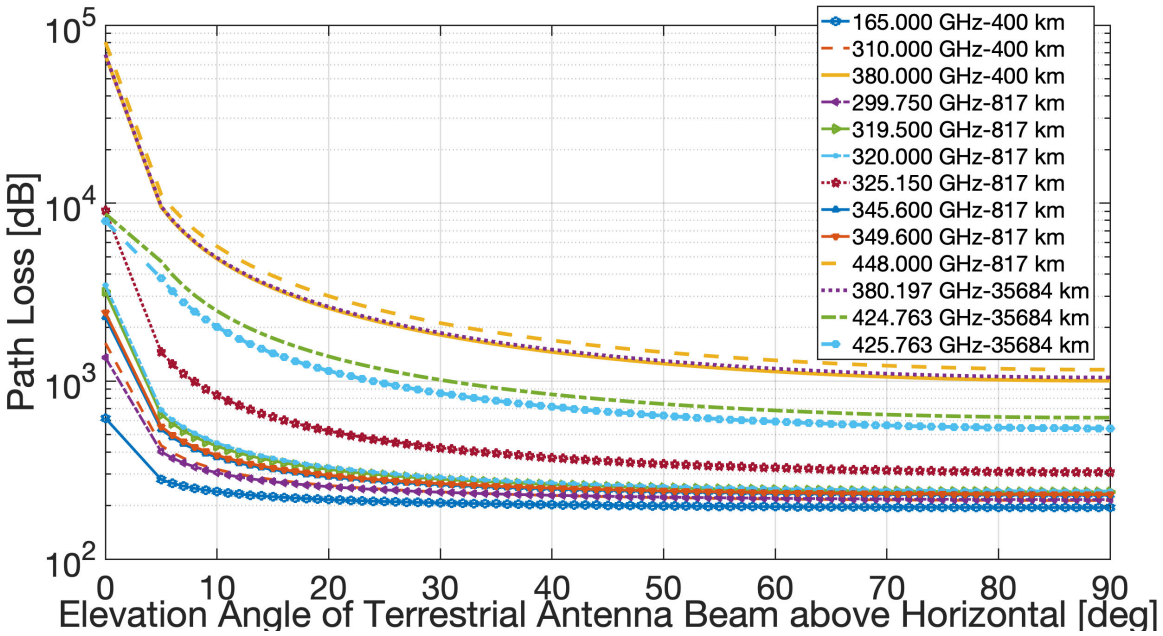

Figure 1.4: Total path loss from ground terminals to satellite NGSO EESS altitudes (without antenna gains) computed from models in [31, 46].

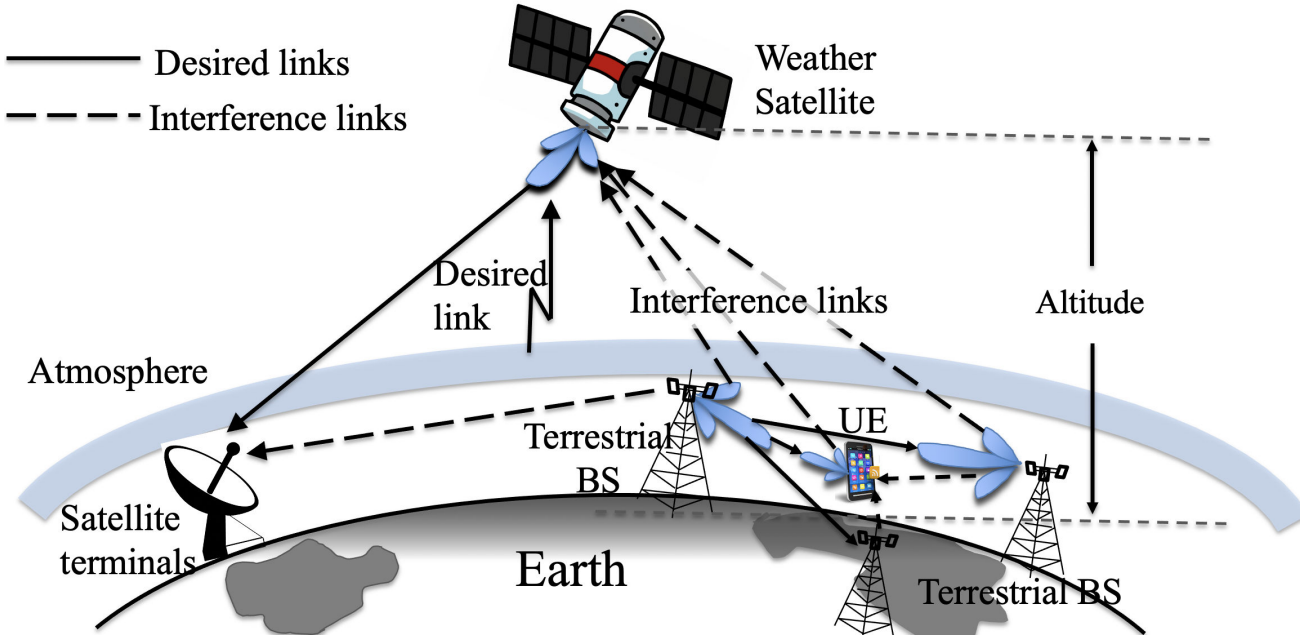

Figure 1.5: Satellite and Terrestrial networks, illustrating the interference between weather satellites (passive) and terrestrial communication (active) systems [32].

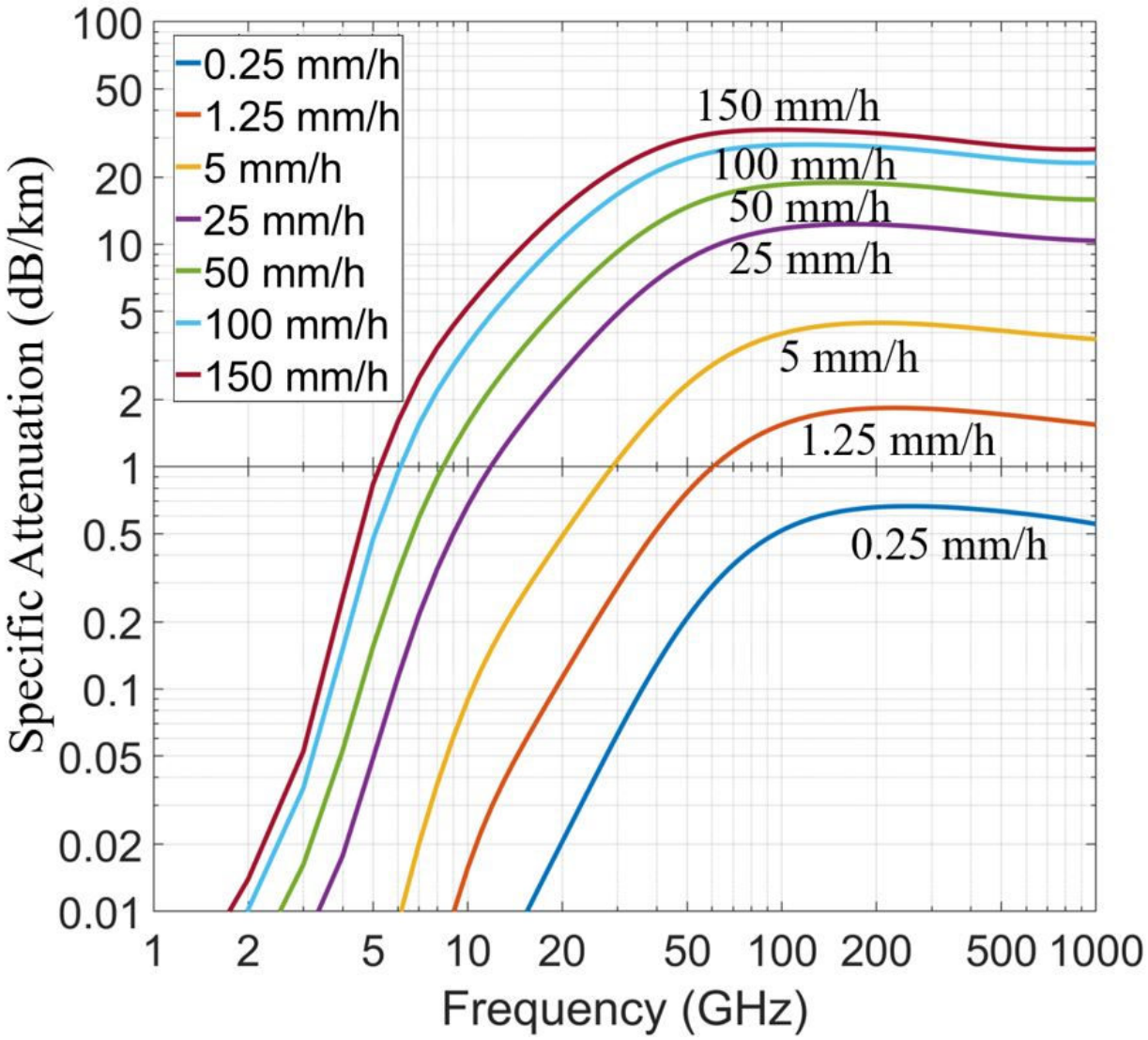

Figure 1.6: Rain attenuation beyond natural FSPL in dB/km over frequency at various rainfall rates using ITU models [31, 32]. Rain attenuation flattens out above 70 GHz. The rain attenuation at 1 THz is 10 dB/km for very heavy rainfall of 25 mm/h, only 5 dB/km more than the rain attenuation experienced at 28 GHz [34, 39, 47].

hundreds and even thousands of dB when low angles are used from earth to orbiting satellites (see Figure 1.4) at various satellite altitudes and frequency bands from 165-425 GHz. This natural attenuation provided by the earth's atmosphere (mainly from the troposphere) to orbiting satellites above 100 GHz is remarkably effective provided that earth emissions are kept low on the horizon (15° or less) as Figure 1.1 and Figure 1.4 demonstrate.

The rain attenuation beyond the natural Friis free space loss [1, 30] across frequency at various rainfall rates is shown in Figure 1.6, indicating that above 70 GHz, further increases in frequencies are *not* further impacted by rain. This is encouraging since coverage distances in today's 5G mmWave networks will not be hampered by rain as carrier frequencies move up to THz [1, 39]. It is worth noting that the ITU-R rain attenuation model [48] is used to compute data shown in Figure 1.6, however, the Crane Model [49] is used in [1], which predicts a 15 dB/km greater loss at extremely

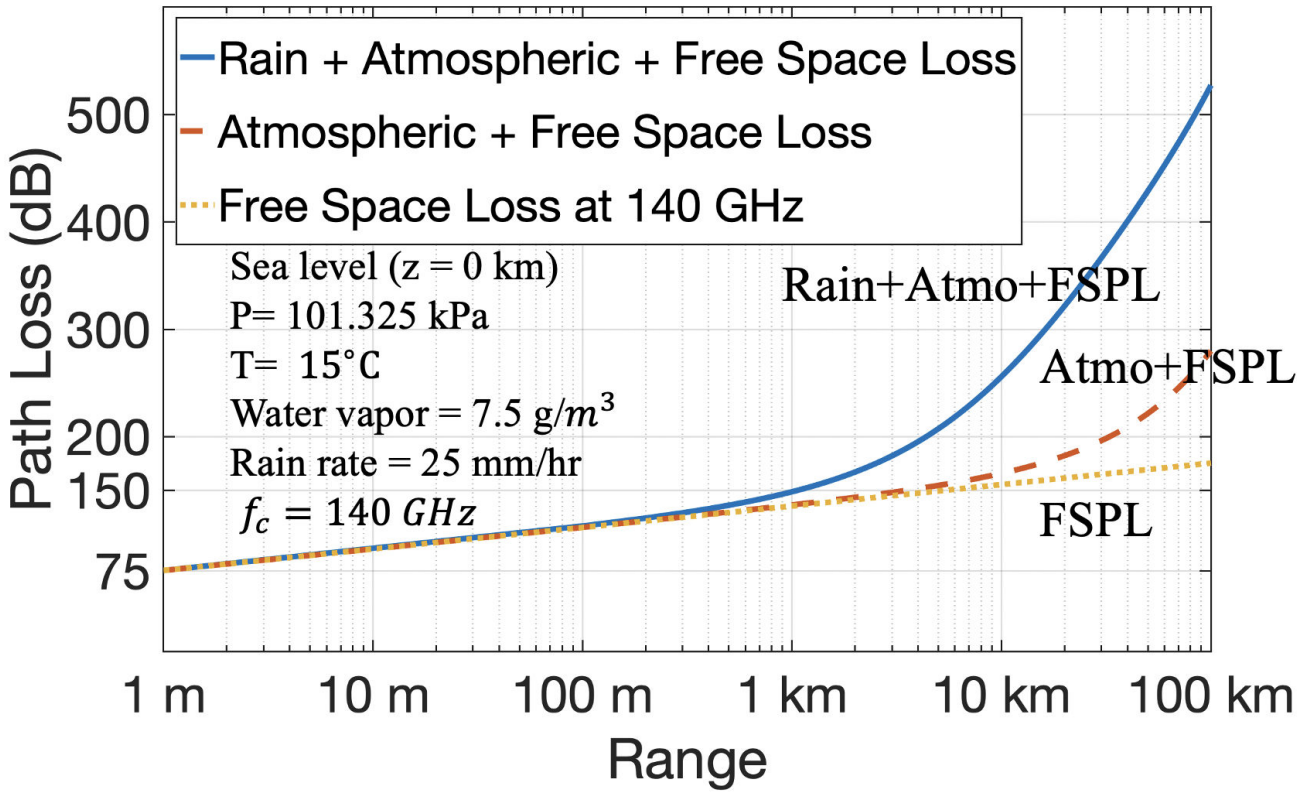

Figure 1.7: Total path loss at 140 GHz (0° elevation angle) without antenna gains including free space path loss (FSPL), rain attenuation, and atmospheric absorption on a terrestrial path using models in [31].

heavy rain rates near 150 mm/hr above 100 GHz. Work in [50] shows the ITU-R model fits well with measurement data at rainfall rate up to 80 mm/h, however, more measurement data are needed at rainfall rates near 150 mm/h.

Total path loss including FSPL, rain attenuation, and atmospheric absorption for fixed backhaul (energy beamed close to the horizon) at 140 GHz (at sea level with the standard conditions) is shown in Figure 1.7, indicating the atmospheric absorption has remarkably little impact on total path loss out to about 10-20 km, although heavy rain will practically limit fixed THz links to several km. It shows that at sea level ($z = 0km$) in standard conditions, with a rain rate of 25mm/hr, the additional loss beyond the FSPL at 140 GHz caused by rain and atmospheric absorption is negligible, proving that small-cell and short-range wireless networks at sub-THz frequencies can work well when it is raining.

Work in [51] showed that particles such as rain drops, snow, and hail caused substantial attenuation at frequencies above 10 GHz. 73 GHz signals attenuate at 10 dB/km when the rain rate is 50 mm/h [38, 39, 48]. Interestingly, as shown in [34, 39, 52] rain attenuation flattens out from 100 GHz to 500 GHz. For all mmWave frequencies where the urban cell sizes are on the order of 200 m, rain or snow attenuation can be overcome with additional antenna gain (obtainable by adding more antenna array elements) [40].

Work in [35, 53, 54, 55, 56, 57] showed effects of rain, fog, dust, and air turbulence at THz and

infrared frequencies based on measurements with less than 10 m links, which indicated a relatively small change (a few dB) in the received power compared to the power received in clear weather. THz outdoor measurements during a snow fall at 200 GHz were presented in [36], and a 2 dB decrease in the received power was observed across an 8 m LOS link indicating that a higher transmitted power was required during a snow fall to maintain the same data rate. MmWave and THz wireless channels are expected to experience ∼30 dB/km of rain attenuation above 100 GHz.

1.3 MmWave and Terahertz Applications

The ultra-high data rate facilitated by mmWave and Terahertz wireless local area networks will enable high-definition holographic video conferencing and high-speed wireless data distribution in data centers [3, 21]. In addition to the extremely high data rate and secure communications, there are promising applications for future mmWave and Terahertz systems that are likely to evolve in 6th generation (6G) of cellular networks, and beyond.

Radar at mmWave and sub-Terahertz frequencies can be used for assisting driving or flying in foul weather, as well as in military and national security [21, 23]. High-definition video resolution radars that operate at several hundred gigahertz will be good enough to provide a TV-like picture and will complement radars at lower frequencies (below 12.5 GHz) that provide longer range detection but with poor resolution [23, 25]. The dual-frequency radar systems will enable driving or flying in very heavy fog or rain [23]. It is worth noting that although Lidar (a use of light detection and ranging) can provide higher resolution, Lidar does not work when it is foggy, raining, or cloudy.

Using mmWave imaging (mmWave camera) to reconstruct 3D maps of the surroundings in an unknown environment will be another application since mmWaves reflect strongly from most building materials which enable imaging of hidden objects (NLOS imaging) [58]. Based on the 3D maps of the surroundings and the time and angular information from a mobile (TOA and AOA), centimeter-level localization and mapping are achievable with the massive bandwidth and large antenna arrays at mmWave and Terahertz frequencies [58, 59].

Other applications enabled by mmWave and Terahertz frequencies, like miniaturized radars for gesture detection and touchless smartphones, spectrometers for explosive detection and gas sensing [60], Terahertz security body scan, air quality detection [26], personal health monitoring system [61], precision time/frequency transfer, and wireless synchronization are receiving rapidly rising attention [21, 24, 62]. These applications can be categorized into wireless cognition (sensing), imaging, wireless communication, and positioning, which are summarized in Table 1.2 (only one or two typical works are cited due to space limitation).

Table 1.2: Promising applications at mmWave and THz

mmWave & THz Applications–the potential for 6G	
Application	**Example Use Cases**
Wireless Cognition	Robotic Control [63, 64], Human Surrogate Drone Fleet Control [63] Autonomous vehicles [65]
Sensing	Air quality detection [26] Personal health monitoring system [61] Gesture detection [24] Explosive detection and gas sensing[60]
Imaging	See in the dark (mmWave Camera) [58] High-definition video resolution radar [23] THz security body scan [25]
Communication	Wireless fiber for backhaul [40] Intra-device radio communication [16] Connectivity in data centers [21] Information shower ($\geq$100 Gbps) [15]
Positioning	Centimeter-level Positioning [58, 59]

1.4 Conclusion

This chapter presents recent global spectrum regulations as well as fundamental atmospheric and rain attenuation considerations at frequencies above 100 GHz which show there is no fundamental physical channel impediment for utilizing sub-THz and THz bands up to 1 THz for future wireless communications. This chapter also explores the fundamental free space and rain-related radio propagation characteristics of the sub-THz and THz frequency bands (see [1, 37, 66, 67, 68, 69] that cover other propagation issues such as scattering, multipath, or path loss at 140 GHz). This chapter demonstrates how the engineering efforts to create mmWave 5G networks will carry forward to frequencies as high as 800-900 GHz, meaning that the engineering developments of adaptive beamforming, wideband channel allocation, and site-specific installation used to create today's 5G networks will hold for the coming several decades as mobile communications move up into the THz range.

Chapter 2

Channel Sounder Systems and Channel Measurements above 100 GHz

The wireless channels at low mmWave (e.g., 28-100 GHz) are well studied and different channel models derived from field measurements at various frequencies have been proposed. Understanding the wireless channels above 100 GHz is the critical first step for researchers to design future THz communication systems for 6G and beyond. This chapter introduces three main THz channel sounding techniques and presents the measurement campaigns at frequencies above 100 GHz from different research groups. Propagation characteristics including reflection, scattering, penetration, and antenna cross-polarization are presented and analyzed as well, which can help the researchers to have a basic understanding of the wireless channels above 100 GHz.

2.1 Channel Sounding Above 100 GHz

Regarding the sounding signal bandwidth, channel sounders can be classified into wideband and narrowband. Narrowband channel sounders usually transmit a sinusoidal continuous wave (CW) at a certain carrier frequency, and at the RX a spectrum analyzer is usually used to capture the received signal (mainly measuring the path loss and multipath distortion effect, no time domain information) within an observation window spanning a few hundred of hertz [70, 71].

Wideband channel sounders are usually used at mmWave and THz frequencies, where the channel bandwidth is large (with both power and delay information,). For wideband channel sounders, there is three main channel sounding techniques in the THz range, namely, THz Time Domain Spectroscopy (THz-TDS), Vector Network Analyzer (VNA) based channel sounding, and correlation-based sounding [38, 71, 71, 72, 73, 74, 75]. The characteristics, strengths, and weakness of different channel sounding techniques are summarized in Table 4.1.

Table 2.1: Channel sounding techniques in THz channel Measurements (frequencies above 100 GHz) [1, 71].

Characteristic	**VNA-based**	**Correlation-based**	**Pulse-based**
Domain	Frequency	Time	Time
Signal	Single carrier	Auto-correlated sequence	THz pulse
Distance	Limited by physical Link length and loss	Relative larger distance compared to VNA and THz-TDS sounders	Limited by pulse power
Synchronization	Implicit	Required	Required
Strengths	Large frequency range and bandwidth	High measuring speed, Large dynamic range, no connection required between TX and RX	Large bandwidth
Weaknesses	Low measuring speed, require cable connected, only work in static environments	High complexity, require synchronization	Large size, low transmit power

2.1.1 THz Pulse-based Channel Sounders

THz-TDS is based on sending ultrashort pulsed laser light from a common source to the transmitter (TX) and the receiver (RX). The TX converts the ultrashort pulse to the THz range and the detector at the RX transforms the received field strength of the THz impulse into an electrical signal when the optical impulse hits the detector [72, 73]. The short THz-TDS pulses cover a huge bandwidth and are excellent for estimating electrical and scattering parameters of sample materials. However, due to the large size of the spectrometer and the limited output power, it is not suitable to be used in any outdoor large scenario or measuring the wireless channels at a large distance.

Measurements at 100, 200, 300, and 400 GHz with a 1 GHz RF bandwidth THz-TDS channel sounder (Prof. Mittleman's group in Brown University) showed that both indoor LOS and NLOS (specular reflection from interior building walls) links could provide a data rate of 1 Gbps [37]. Furthermore, THz-TDS based channel sounders are also used to measure and analyze the weather effect on the THz link [36, 56].

Prof. Kurner's group in TUBS also collaborated with Prof. Mittleman's group at Brown University and used THz-TDS based channel sounder system to analyze reflection and scattering effect at 350 GHz [22, 76].

Hossain *et. al* (with Prof. Jornet's group in University at Buffalo) used THZ-TDS based channel sounder to measure and model the interference between THz devices at the 300 GHz band [77]. THz-TDS pulse-based channel sounder systems at frequencies above 100 GHz and the THz measurement campaigns conducted by different research groups are summarized in Table 2.2. bnv6

2.1.2 VNA-based Channel Sounders

Four-port VNAs are commonly used for THz range channel sounding, where the two additional ports (compared to the traditional 2-port VNA based channel sounder used at lower frequencies) are used to generate a local oscillator (LO) for the mixer in the frequency extensions that are used

Table 2.2: THz-TDS pulse-based channel sounders at frequencies above 100 GHz with the measurement campaigns [1, 71].

THz-TDS pulse-based channel sounders				
Characteristic	**Symbol**	US	US	Germany
		Brown University	University at Buffalo	TUBS
Carrier Frequency	**fc**	100, 200, 300, 400 GHz	300 GHz	350 GHz
Bandwidth	**B**	CW, and 2 GHz		
Dynamic range	**D**			
TX antenna Gain	**Gtx**	21, 21, 26, 26 dBi		
RX antenna Gain	**Grx**	21, 21, 26, 26 dBi		
Transmit Power	**Pt**	24, 20, 8.5, 10 dbm		
TR Separation Dist.	**d**	10-35 m indoor, 1-80 m outdoor	0-1 m	1-10 m
Environment	**Env.**	Indoor office, Outdoor (Reflection, scattering, penetration, weather effect)	Indoor (reflection)	Indoor (Scattering)
Scenarios	**Scen.**	LOS	LOS	LOS

VNA Based Channel Sounding Systems											
		China		US		Finland	Germany		Korea	Turkey	UK
Characteristic	**Symbol**	SJTU & Huawei	SJTU & Huawei	USC	Georgia Tech.	Aalto Univ.	TUBS	Disburg-Essen	POSTECH	Koc Univ.	NPL & univ. of surrey
Carrier Frequency	**fc**	130-143 GHz	201-209 GHz	140-220 GHz	300-320 GHz	141.1-145.1 GHz	300-310 GHz	300-310 GHz	270-330 GHz	260-440 GHz	500-750 GHz
Bandwidth	**B**	13 GHz	8 GHz	80 GHz	60 GHz	4 GHz	10 GHz	10 GHz	60 GHz	19 GHz	250 GHz
Dynamic range	**D**	120 Db	120 Db	140 dB	90 dB	130 Db	85 dB	85 dB		60 dB	80 Db
TX antenna Gain	**Gtx**	15 dBi	15 dBi	21 dBi	23 dBi	0 dBi	26 dBi	26 dBi	25 dBi	25 dBi	26 dBi
RX antenna Gain	**Grx**	25 dBi	25 dBi	21 dBi	23 dBi	19 dBi	26 dBi	26 dBi	25 dBi	25 dBi	26 dBi
Transmit Power	**Pt**	0 dBm	0 dBm		-5 dBm	-7 dBm	-5 dBm	-10 dBm		-10 dBm	-25 dBm
TR Separation Dist.	**d**	1.8-7.3 m	2-30 m	1-35 m/ 100m	0.1-2.1 m	3-65 m, 15-51m	0.1-1.67 m	1-5 m	0.1-1 m	0.01-0.95 m	0-0.2286 m
Environment	**Env.**	Indoor (meeting room)	Indoor (Office room)	Indoor office, Urban	Indoor Desktop, office room	Indoor shopping mall, airport	Desktop, indoor office	Indoor office	Indoor	Indoor	Indoor
Scenarios		LOS	LOS and NLOS	LOS, LOS and NLOS	LOS and NLOS	LOS, afew NLOS	LOS and NLOS	LOS	LOS	LOS	LOS

Figure 2.1: VNA-based channel sounder systems at frequencies above 100 GHz and THz measurement campaigns conducted by various research groups.

to elevate stock VNA's to much higher frequencies through heterodyning[73, 74]. A VNA sweeps discrete narrowband frequency tones across the bandwidth of interest to measure the S_{21} parameter of the wireless channel. Due to the long sweep time across a broad spectrum which can exceed the channel coherence time, VNA based channel sounders are typically used in a static environment and require a cable that can be a tripping hazard [74, 75, 78]. VNAs are widely used by many researchers for mmWave and THz channel measurements because the measurement system is relatively simple. Another challenge for VNA based system is that the cable loss from the LO source to the TX and RX antennas is large for a long TX-RX separation distance. Works in [68, 79, 80] used radio-over-fiber extended VNA based systems, where the TX and RX are connected to the VNA by an optical fiber instead of traditional coaxial cables (LO signals), to overcome this disadvantage. The VNA-based channel sounder systems at frequencies above 100 GHz and the THz measurement campaigns conducted by different research groups are summarized in Figure 2.1.

Propagation measurements in the 140 GHz band were conducted by Aalto University in a shopping mall (3-65 m) [79, 80] using a VNA based channel sounder with a 19 dBi horn antenna at the RX, and a 2 dBi bicone antenna at the TX. It was shown that the numbers of clusters and multipath components (MPCs) in each cluster in the 140 GHz band, an average of 5.9 clusters and 3.8 MPCs/cluster, were fewer compared to the 28 GHz band, which had an average of 7.9 clusters and 5.4 MPCs/cluster [79]. Recently, in 2021, the same group conducted propagation measurements at 140 GHz in an airport check-in hall (15-51 m) with the same system

Work in [81, 82] presented D-band propagation measurements in a very close-in environment around a personal computer using a VNA based sounder. Indoor directional path losses at 30 GHz, 140 GHz, and 300 GHz were compared using different path loss models in [82]. Although the LOS path loss models predicted path loss exponents (PLE) close to 2.0, the multi-frequency close-in free space reference distance model with a frequency-dependent term (CIF) and alpha-beta-gamma (ABG) model had better PLE and standard deviation stability than the single-frequency CI and Floating Interception (FI) models [40, 82, 83, 84].

Indoor channel measurements in the 126-156 GHz frequency band were shown in [85] using a VNA based channel sounder and 20 dBi gain horn antennas at both TX and RX within a T-R separation distance of 10.6 m. The PLE for the measured D band signal was closed to 2 (free space) since the LOS component is much stronger than the secondary paths. The root mean square delay spread was found to be within 15 ns [85].

Propagation loss measurements for estimating the performance of a communication link in the 350 GHz frequency band were presented in [86], where a VNA based system was used with 26 dBi gain co-polarized horn antennas at both the TX and RX. The presence of water absorption lines in the spectra at 380 GHz and 448 GHz was very evident. Data rates of 1 Gbps for an 8.5 m link and 100 Gbps for a 1 m T-R separation distances were shown to be possible via wireless communication links at 350 GHz [86].

Channel and propagation measurements at 300 GHz were presented in [87, 88], where a VNA based channel system with 26 dBi gain horn antennas at both TX and RX was used to analyze the channel characteristics from 300-310 GHz with an IF frequency bandwidth of 10 kHz. Maximum transmission rates of several tens of Gbps for LOS and several Gbps for NLOS paths were shown to be achievable [88].

THz band indoor propagation measurements were conducted in [89] using a VNA based system covering a frequency range from 260 GHz to 400 GHz with 25 dBi gain horn antennas at both TX and RX within a T-R separation range of 0.95 m. Measurement results showed that Tbps throughput was achievable in the THz band. However, robust beam forming algorithms will be required in THz band communications. Acoustic ceiling panels, which serve as a good reflector at THz band, could be used as low-cost components to support NLOS links [89].

2.1.3 Correlation-based Channel Sounders

Correlation based channel sounder systems transmit a known pseudo-random noise (PN) sequence (usually the maximum-length sequences) at a chip rate of f_{chip} over the wireless channels. At the RX, the received signal is cross-correlated with an identical but slightly delayed pseudo-random sequence, providing autocorrelation gain at the expense of a slightly longer acquisition time (on the order of tens of ms) [74, 78, 90]. At the RX side, the same PN sequence will be generated at a slightly lower chip rate f'_{chip}. The received signal will be correlated with the slower signal generated at the RX resulting the impulse response of the wireless channels. The sliding correlation operation compresses

Table 2.3: Sliding-correlation based channel sounding systems at frequencies above 100 GHz and the measurement campaigns conducted by different research groups.

Sliding-Correlation Based Channel Sounding Systems						
Symbol	US	China& Germany	Germany	Finland & Germany	Germany	Germany
	NYU WIRELESS	BJTU & TUBS	TUBS	University of Tampere & TUBS	TU Ilmenau	Heinrich Hertz Institu
fc	142 GHz	300 GHz	300 GHz	300 GHz	190 GHz	300 GHz
B	1 GHz	8 GHz	8 GHz	8 GHz	7.5 GHz	2 GHz
D	150 Db	113 Db	113 Db		NA	120 dB
Gtx	27 dBi	15 dBi	15 dBi	26.4 dBi	NA	6 dBi
Grx	27 dBi	15 dBi	15 dBi	26.4 dBi	NA	20 dBi
Pt	0 dBm			-23.7 dBm	NA	-1.6 dBm
d	1-117.4 m	1-10 m	1-20 m	2-14 m	4-10 m	6-34 m
Env.	Indoor office, Outdoor Urban Microcell	Train-to-Train, T2I, Intra-Wagon (static)	Indoor Conference Room	V2V (Indoor static), Aircraft (indoor to outdoor)	Indoor Conference Room	Outdoor UMi (Parki
Scen.	LOS and NLOS	LOS	LOS	LOS and NLOS	LOS	LOS

the bandwidth of the signal by the sliding factor of $\gamma = f_{chip}/(f_{chip} - f'_{chip})$ which reduces the required sampling rate of the ADC (e.g., oscilloscopes) at the expense of increase the measurement duration (also by a factor of γ). Sliding correlation-based channel sounder systems at frequencies above 100 GHz and the THz measurement campaigns conducted by different research groups are summarized in Table 2.3.

NYU WIRELESS developed the sliding-correlation based channel sounder at 142 GHz with a capability to transmit signal bandwidth of 4 GHz. Using a 0 dBm transmit power and 27 dBi gain horn antennas (8°HPBW) at both the TX and RX, the maximum measurable path loss range (dynamic range) is 150 dB. Radio propagation measurements in indoor office environments (4 - 65 m) and outdoor urban microcell environments (10-117 m) were conducted for both LOS and NLOS scenarios. Channel characteristics including reflection, scattering, diffraction, penetration, and human blockage were also measured and analyzed [1, 43, 66, 67, 75, 91, 92].

Technische Universitat Ilmenau (TU Ilmenau, Germany) developed their sliding-correlation based channel sounder at 190 GHz with 7.5 GHz bandwidth and conducted measurements in a conference room with TR separation distance of 4-10 m [93]. Directional horn antennas with 15°HPBW are used at both the TX and RX. Window frames, walls, tables, and other furniture provide strong reflections (multipath-rich channels). Different polarization combinations were also studied showing that the strongest MPC that is apart from the LOS (reflections from the surroundings) experienced large polarization discrimination which depends on the orientation of the scattering surface. The antenna gains, TX transmit power, and channel sounder dynamic range are not specified in [93].

Heinrich Hertz Institute (HHI, Germany) presented their sliding-correlation based channel sounder at 300 GHz with a null-to-null bandwidth of 2 GHz [94]. The channel sounder used a 6 dBi gain horn antenna (90°HPBW) at the TX and a 20 dBi gain horn antenna (15°HPBW) at the RX. Propagation measurements (LOS) were conducted in a parking lot (6-34 m), and channel characteristics like path loss, delay spread, and angular spread were measured and analyzed [94].

A correlation-based channel sounder at 300 GHz with 8 GHz bandwidth was presented and evaluated by Prof. Kurner's group in Technische Universitat Braunschweig (TUBS) in [73] with

Table 2.4: Summary of channel sounder systems and antennas used in measurements at 28, 73, and 142 GHz [39, 74, 75]. The overall received power does not change with the signal bandwidth but the RX noise power and noise figure change [78]. Thus, higher gain (more directional) antennas were used at both the TX and RX to compensate for noise and greater path loss in the first meter at higher frequencies.

RF Frequency	RF Bandwidth	Antenna HPBW	Antenna Gain	Antenna XPD	A_e
28 GHz [39]	1 GHz	30°	15 dBi	19.30 dB	2.88 cm^2
73 GHz [74]	1 GHz	15°	20 dBi	28.94 dB	1.32 cm^2
142 GHz [75]	1 GHz	8°	27 dBi	30.18 dB	1.83 cm^2

the same wired clock source being connected to both the TX and RX, which use a subsampling technique to avoid the expense of high-speed A/D converters. A 12^{th} order M-sequence was used with a subsampling factor of 128, and the theoretically maximum measurable Doppler frequency was 8.8 kHz, equivalent to a velocity of 31.7 km/h at 300 GHz [73].

Channel modeling and capacity analysis for THz band electromagnetic (EM) wireless nano-networks were explored in [95], where a propagation model accounting for the total path loss and the molecular absorption noise for EM communications in the THz band was developed based on radiative transfer theory. Channel capacity of the THz band was investigated by using the proposed path loss model for different power allocation schemes showing that for several tens of millimeters the THz channel supports very large bit-rates (up to few terabits per second), which enables a radically different communication paradigm for nano-networks [95].

A 140 GHz channel sounder, which consists of sub-harmonic mixers (SHM) based on Schottky barrier diodes, bandpass filters (BPF), Cassegrain antennas (51 dBi gain, 0.6° HPBW in horizontal plane and 0.35° in the vertical plane), and local oscillator (LO) multipliers, was presented in [96]. A 10 Gbps non-real-time link based on a software modulator and a 2 Gbps real-time transmission based on a hardware modulator was realized in 1.5 km far-field tests at 140 GHz with 3.6 GHz bandwidth using 16-QAM modulation scheme, and the spectrum efficiency achieved 2.86 bit/s/Hz [96].

2.2 NYU WIRELESS Channel Sounder Architecture

Sliding correlator chips have recently been produced that offer a 1 Gbps baseband spread spectrum sequence [97], and sliding correlators generally enable cable-free operation over useful mobile communication distances of up to 200 m at sub-THz frequencies, depending on transmit power, bandwidth, and antenna gain [75, 98]. A 140 GHz channel sounder with 1 GHz RF bandwidths has been used to measure indoor channels at NYU [75].

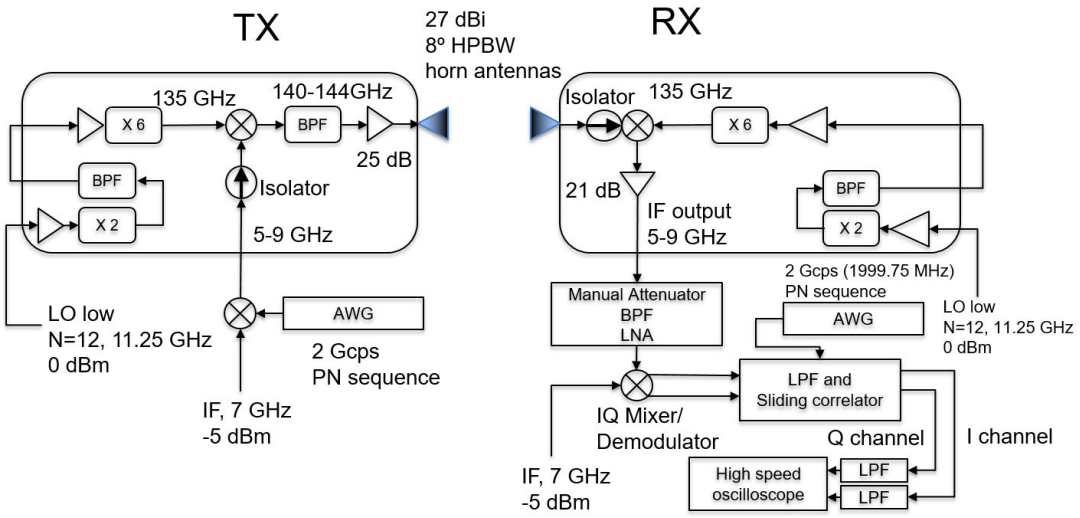

Figure 2.2: Block diagram of NYU's 140 GHz system [75].

2.2.1 A novel 140 GHz channel sounder system

The 140 GHz channel sounding system at NYU WIRELESS can support both a wideband sliding correlator mode and a real-time spread spectrum mode, which are suitable for both long-distance propagation measurements with angular/delay spread and short-range dynamic channel measurements for Doppler and rapidly fading characterization, respectively [74]. The block diagram of the 140 GHz sliding correlator mode system is shown in Figure 2.2, where a 2 Giga-chip-per-second (Gcps) pseudorandom noise (PN) sequence of 2047 chips in length (11 bits) is generated by a Keysight M8195A arbitrary waveform generator (AWG). The PN sequence is modulated by an IF signal centered at 7 GHz, and then the 4 GHz wide null-to-null bandwidth signal at IF enters the RF upconverter. The LO is set at 11.25 GHz, and the LO and IF signals are mixed in the RF upconverter which will generate the RF signal centered at 142 GHz ($11.25 \times 12 + 7 = 142$ GHz).

In the 140 GHz channel sounder system, a 0 dBm LO signal goes through a band path filter (BPF) and the frequency multiplier, and then the LO signal and the IF signal are mixed. The output RF signal from the mixer will pass through a 140 GHz band BPF (140-144 GHz), be amplified by a 25 dB gain power amplifier, and then transmit out through a 27 dBi gain horn antenna with a 8° HPBW in both azimuth and elevation planes. The incoming RF signal is captured by the horn antenna at the RX and then down converted by the LO signal at 135 GHz. The down converted signal will go through a variable attenuator, a BPF, a low noise amplifier (LNA), and will be IQ demodulated to baseband. The demodulated I and Q signal will be correlated with an identical PN sequence but at a slightly offset rate, providing autocorrelation processing gain at the expense of a longer acquisition time [74, 78]. With the processing gain, a sliding correlator based channel sounder usually has a larger dynamic range than the VNA based ones [74]. For the 140 GHz sliding correlator mode, the 11-bit PN sequence provides a 66 dB autocorrelation processing gain ($20 \times \log_{10} 2^{11}$) and the maximum measurable dynamic range is 145 dB with a transmit RF output power of 0 dBm using 27 dBi horn antennas at both TX and RX. Theoretically the path loss in free space decreases

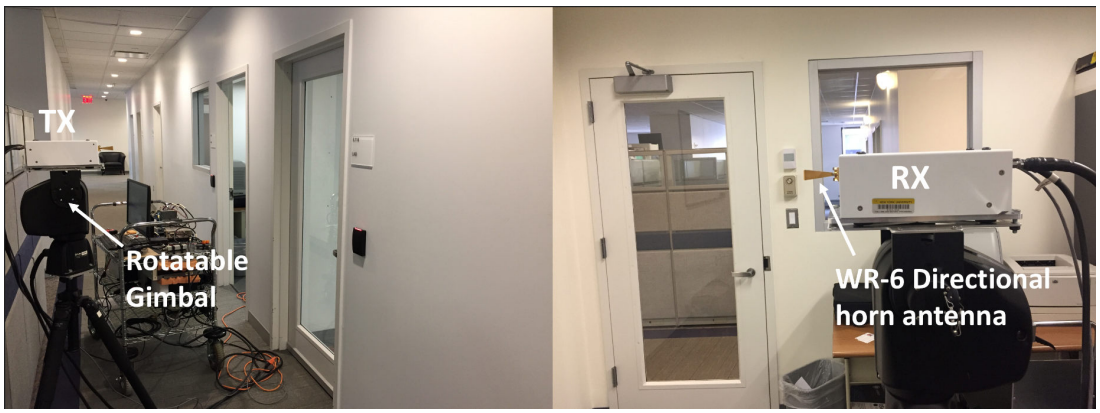

Figure 2.3: 140 GHz channel sounder with directional horn antennas.

quadratically as frequency increases, if the physical size of the antenna (effective aperture) is kept constant over frequency at both link ends [40, 78]. The measurable path loss range of the 140 GHz system is less than that at lower frequencies because of the limited output power (e.g., limited gain) provided by the power amplifier (0 dBm at 140 GHz compared to 30 dBm at 28 GHz [39]).

Two separate high stability Rubidium (Rb) clocks are used at the transmitter (TX) and receiver (RX) for cableless synchronization. The TX and RX are both mounted on a gimbal which can be swept 360° in azimuth plane and 120° in elevation plane in 1°/step, so that dual-directional information (AOA and AOD) can be obtained for MIMO and directionality analysis.

2.3 XPD Measurements

Characterizing the XPD of antenna systems and radio channels for millimeter wave (mmWave) communication systems using directional antennas is vital for properly interpreting measured results and developing proper path loss models for orthogonally-polarized or dual-polarized communication systems. Even though a transmitted signal may be linearly polarized, scattering effects in the propagation channel will induce some ellipticity to the polarization of the received signal, and the antenna itself may not be ideally linear polarized. Accurate measurement and calibration of the XPD for a directional co-polarized communication system are important for separating antenna and channel effects, where the XPD is defined as the ratio (in dB) of the power in the transmitted co-polarized state to the power radiated in the cross-polarized state when transmitted in free space, without channel impairments [78, 99]. XPD may also be applied to path loss models when determining the received power in co- versus cross-polarized states over distance.

XPD of channels has been studied since the early days of cellphones, in the 1990s. Measurement results at 1.3 GHz and 4.0 GHz [100] showed that the line-of-sight (LOS) channels offered significantly more XPD than the non-line-of-sight (NLOS) channels, and the directional circularly polarized antennas greatly reduced root-mean-square (RMS) delay spread. XPD measurements at 2.6 GHz with 200 MHz bandwidth using a multiple-input-multiple-output (MIMO) channel sounder

were presented in [101], and models to describe the dependence of XPD on distance, azimuth and elevation and delay spread were investigated, which concluded that the XPD increased with distance and delay. Measurements at 34 GHz with dual-polarized directional horn antennas were conducted to study the behavior of XPD in mmWave channels [102]. It was observed that the variation of XPD reduced exponentially with an increase in channel bandwidth. Measurements at 73 GHz with 800 MHz bandwidth using dual-polarized directional horn antennas [103] showed that the XPD was constant over the T-R separation distance range from 10 to 40 m.

2.3.1 A standardized verification approach for XPD

Using geometric optics and fundamental propagation theory, we have developed verification procedures that may be applied to verify the XPD and penetration loss and are suitable for use as a standard approach. To approve the efficacy of the verification methods, the XPD and penetration loss measurements at 73 GHz were conducted to verify their consistency across various TX and RX antenna types at different TR separation distances. By measuring consistent values over many different distances, relatively close, between the transmitter and receiver, for different frequencies and bandwidths, verification can be performed, ensuring no multipath or antenna artifacts are contained in the measurement system.

The approach validates the XPD of the system antennas. It is repeatable and has been confirmed by measurements at different distances in a controlled, open, and static environment that attempts to remove channel effects and focuses solely on the antennas used. There are three basic rules to follow when measuring the XPD of a transmit and receive antenna for a channel sounder: a) ensure that the measurement is in LOS free space with a T-R separation distance beyond the far-field or Fraunhofer distance D_f of the antennas while also ensuring that the TX and RX antennas are perfectly boresight-aligned; b) ensure that no nearby reflectors or obstructions are present in the propagation path that might cause multipath reflections or induce fading in the measurement; and c) ensure the heights of the antennas and the T-R separation distance between the antennas are selected so that ground bounces and ceiling bounces do not induce reflection, scattering, or diffraction within or just outside the half-power beamwidth (HPBW) of the main lobe of the TX/RX antenna pattern. As shown subsequently, these three rules guarantee accurate measurements of the antenna XPD since the measurement environment is devoid of reflectors or objects that might cause multipath, especially in the first Fresnel-zone which would induce errors into the XPD [104, 105, 106].

Antenna cross-polarization discrimination (XPD) measurements were conducted at NYU WIRELESS research center to verify the XPD values via different TR separation distances at different frequencies (28, 73, and 142 GHz). Calibration and verification of antenna XPD were first conducted by measuring and calibrating free space path loss at various closely-spaced (but in the far-field region) TR separation distances (e.g., 1, 2, 3, 4, and 5 m) with co-polarized antennas (both for VV and HH), followed by measurements at the same distances but using cross-polarized antennas (both

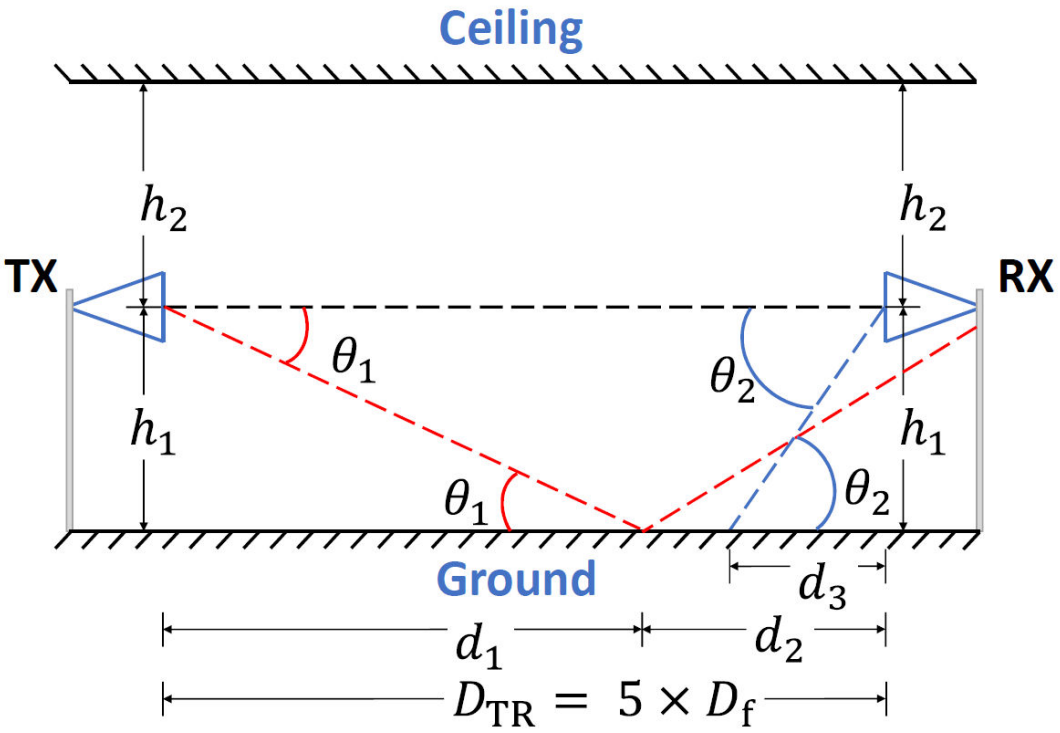

Figure 2.4: Sketch of geometry and test setup for accurately measuring the antenna XPD between two orthogonally-polarized antennas for channel-sounder verification.

for VH and HV), where one antenna was rotated by 90° from the other in a systematic way either electrically or mechanically to make both antennas experience identical cross-polarization from each other.

The three basic rules are further quantified in Figure 2.4:

1. To ensure that a plane-wave is incident on the RX, measurements in free-space should be made with the TX antenna separated by at least one Fraunhofer distances from the RX antenna. A general rule-of-thumb to assure plane-wave propagation is to set the RX antenna at least five Fraunhofer distances from the radiating TX antenna [78]. The Fraunhofer far-field distance D_f is defined as:

$$D_f = \frac{2D^2}{\lambda}, \tag{2.1}$$

where D is the length in meters of the largest linear dimension of the antenna aperture and λ is the carrier wavelength of the radiating signal in meters [78]. Using the rule of thumb of five Fraunhofer lengths, the T-R separation distance D_{TR} used to measure the XPD should obey:

$$D_{\mathrm{TR}} \geqslant 5 \times D_f. \tag{2.2}$$

Several measurements should be taken at different far-field distances that are greater than $5 \times D_f$ and that are far enough from each other to discern an appreciable difference of a few

to several dB of received power in free space, while satisfying (2.2) and the other two rules described below. The additional distances should typically be 20% to 100% greater than the initial distance. For example, if $5 \times D_f$ is 4 meters, then 5, 6, and 8 meters would be good distances, as long as they satisfy the other requirements. Additionally, the TX and RX antennas should be boresight-aligned for both co-polarized and cross-polarized measurements such that their axes of maximum antenna gain align.

2. Following [104, 105, 106], the heights of the TX and RX antennas, and the T-R separation distance between the antennas should be chosen so as to avoid any ground, ceiling, wall, or object reflections. Specifically, the heights and distances should be selected in conjunction with the HPBW of the TX and RX antennas such that the projected ground bounce or other reflection sources from the TX antennas are far outside of the HPBW angular spread of the TX antenna and should not arrive anywhere near the HPBW viewing angle of the RX antenna. If the TX antenna has a HPBW of $2 \cdot \theta_1$ in radians and the RX antenna has a HPBW of $2 \cdot \theta_2$ in radians, and we fix the distance between the TX and RX antennas as $D_{\text{TR}} = 5 \times D_f$, then we can use simple geometry to determine the constraint on the height at which the antennas should be placed to avoid multipath sources. Figure 2.4 shows a sketch of a typical measurement setup. By solving a set of geometry equations pertaining to the sketch above, the relationship of the T-R separation distance, antenna height above ground (h_1) and below the ceiling (h_2) can be defined by:

$$h_1, h_2 > \left(\frac{D_{\text{TR}}}{\left(\frac{1}{\tan(\theta_1)}\right) + \left(\frac{1}{\tan(\theta_2)}\right)} \right), \tag{2.3}$$

where D_{TR} is the T-R separation distance, h_1 is the height of the TX and RX antennas above the ground, and h_2 is the distance of the antennas from the ceiling and any obstructions or walls on either side of the straight line between the TX and RX antennas. A value twice the height specified in (2.3) is used to ensure additional clearance so as to provide sufficient distance, time, and antenna pattern separation between the direct path and any ground, ceiling, or other reflections in the measurement environment:

$$h_1, h_2 > 2 \times \left(\frac{D_{\text{TR}}}{\left(\frac{1}{\tan(\theta_1)}\right) + \left(\frac{1}{\tan(\theta_2)}\right)} \right). \tag{2.4}$$

2.3.2 Measurements to Validate XPD Values at 28, 73, and 142 GHz

Polarization diversity can provide twice as much data rates in dual-polarized communication systems as in the co-polarized system theoretically without any extra bandwidth or spatial separation

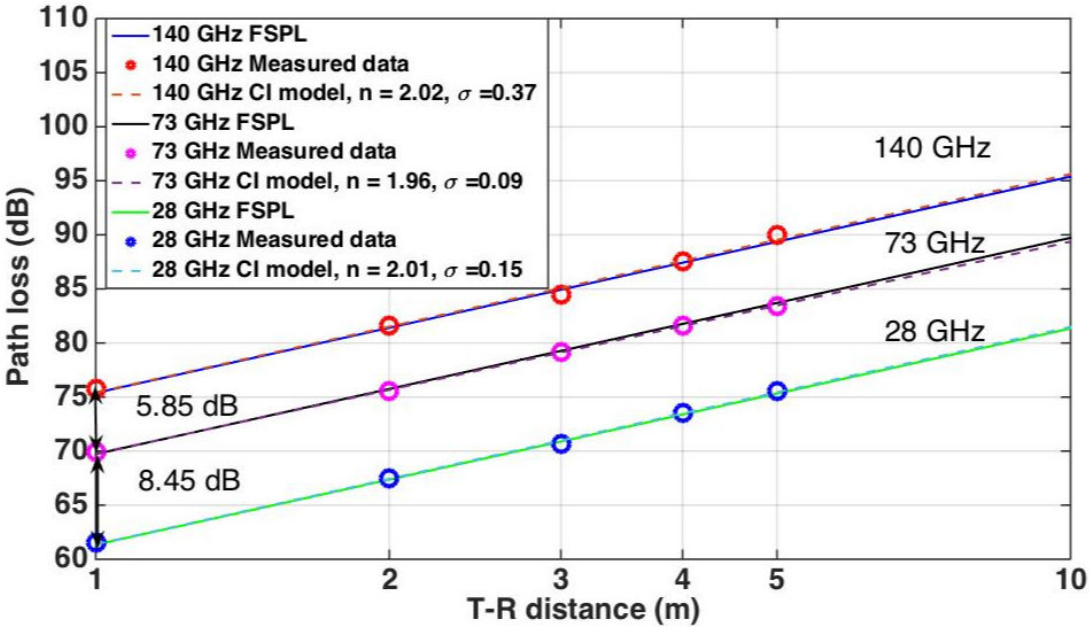

Figure 2.5: 28, 73 and 140 GHz free space path loss (after subtracting out all antenna gains) verification measurements at distances of 1, 2, 3, 4, and 5 m.

between antennas [107]. Measurements for antenna cross-polarization discrimination (XPD) at 28, 73, and 140 GHz were conducted to analyze the polarization characterization of the horn antennas [108, 109]. The XPD values also helped analyze the polarization effects of partitions at different frequencies.

Free space path loss measurements were firstly conducted at 3, 3.5, 4, 4.5, and 5 m, according to the measurements setting procedures aforementioned [108], with vertically polarized horn antennas at both the TX and RX. The free space path loss measurement results after removing the antenna gains are shown in Figure 2.5 and a negligible difference (less than 0.5 dB) from the theoretical Friis free space path loss equation was observed, which validate the accuracy of the channel sounder.

After the free space power measurements with co-polarized antennas, measurements were conducted at the same distances but with cross-polarized antennas (e.g., V-H). Cross-polarization was realized by using a waveguide twist which rotates the antenna by 90°. The insertion loss caused by the twist was measured and calibrated out. The received power for the cross-polarized antennas is shown in Figure 2.6. The XPD was calculated by taking the difference between the path losses of the V-V and V-H antenna configurations at the same distances. A summary of the XPD values measured is provided in Table 2.5. Note that, at a fixed TR separation distance, the free space received powers for the H-H and H-V configurations were within 1 dB of the V-V and V-H received powers respectively.

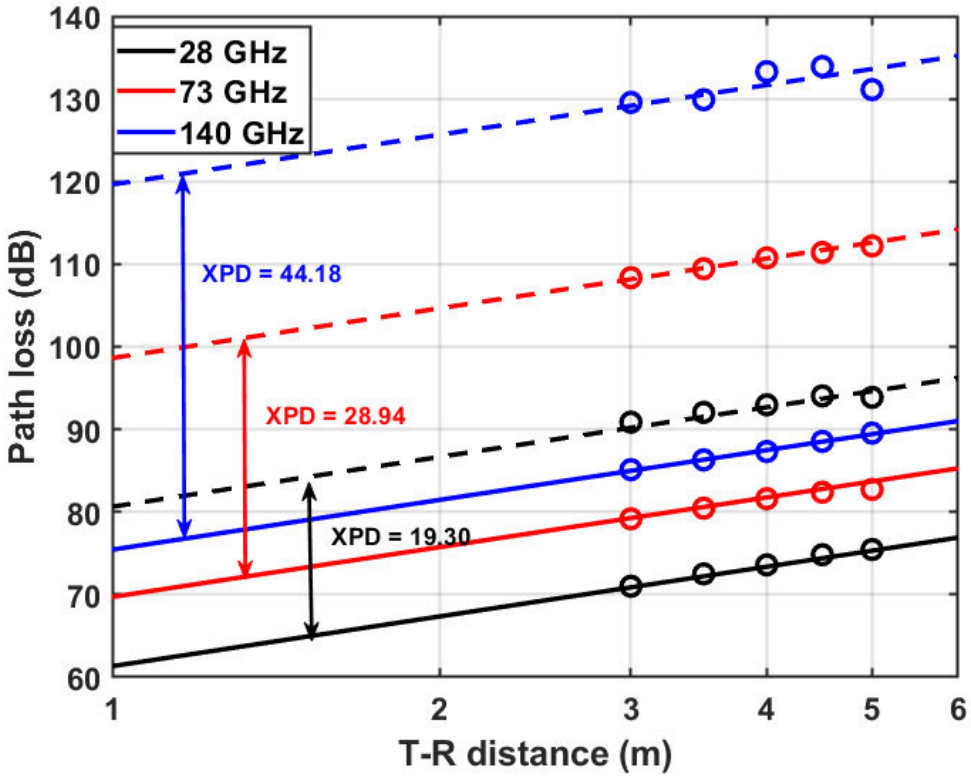

Figure 2.6: Measured antenna XPD at 28, 73, and 140 GHz. The solid lines and the dash lines represent the path loss measured with co-polarized and cross-polarized antennas, respectively. The XPD values calculated across five distances are within 1 dB at each frequency, which verifies the XPD measurement procedure is correct.

Table 2.5: XPD Measurement Results at 28, 73 and 140 GHz

Distance (m)	XPD at 28 GHz (dB)	XPD at 73 GHz (dB)	XPD at 140 GHz (dB)
3	19.86	29.17	44.44
3.5	19.54	28.98	43.58
4	19.37	28.98	45.97
4.5	19.22	28.79	45.36
5	18.41	28.79	41.57
mean	19.30	28.94	44.18
std	0.54	0.19	1.72

2.3.3 Documentation of XPD Measurement Data

XPD measurements at 28 GHz were conducted on 11.06.2018 with 15 dBi gain horn antennas and the measurement data was saved in `euler:\PropDataBackup\XPDMeasurements\11.06.2018`. Calibrations before and after the measurements were recorded in the "Calibration Area". Ten measurements were recorded corresponding to VV and VH polarization combinations at 3, 3.5, 4, 4.5, and 5 m. At each distance, five PDPs (five rots) were recorded, taking the average of the power in the first arriving multipath component of the recorded PDPs, to calibrate out the variation caused by the channel sounder. Static information is saved in the "pdpLogFile" and the PDP is saved in the "IQsquaredXXX" file. Excel tables named "XPD28", "XPD73", and "XPD140" are also saved for records.

XPD measurements at 73 GHz were conducted on 12.26.2017 and the measurement data was saved in `euler:\PropDataBackup\XPDMeasurements\12.26.2017`. The only difference from 28 GHz is that 30 measurements were recorded with measurement number 1-10 for wide-wide (20 dBi gain horn antennas at both the TX and RX), 11-20 for narrow-wide (27 dBi gain horn antenna at the TX and 20 dBi gain horn antenna at the RX), and 21-30 for narrow-narrow (27 dBi gain horn antennas at both sides).

XPD measurements at 140 GHz were conducted on 09.16.2018 and the measurement data was saved in `euler:\PropDataBackup\XPDMeasurements\09.16.2018` (L1-RX1). Same as 28 GHz, 10 measurements were recorded using the 27 dBi gain horns at both sides. Calibration 1 and 2 were conducted before and after XPD measurements and Calibration 3 is conducted after the partition loss measurements of clear glass at 140 GHz (L2-RX2).

2.4 Partition Loss Measurements and Analysis

The partition loss is defined as the difference between signal power right before the partition and the signal power right after the partition [110, 111], which includes reflection/scattering loss and the material absorption loss.

2.4.1 Variation of Electrical Parameters at 140 GHz

One of the earliest studies of differences between microwave and mmWave frequencies (1.7 GHz and 60 GHz) was presented in [112], which showed the variation of the electrical parameters (reflection coefficient, conductivity, etc.) of the building materials with frequencies. The permittivity (ϵ_r) of drywall was measured to be 2.4 at 3 GHz in [113].

Since little is known of the electrical parameters at frequencies above 100 GHz, reflection/scattering measurements of drywall at 140 GHz were conducted using the channel sounder system with specifications summarized in Table 2.4, and the measurement setup is shown in Figure. 2.12. During the measurements, both the heights of TX and RX were set at 1.2 m to make sure there was no

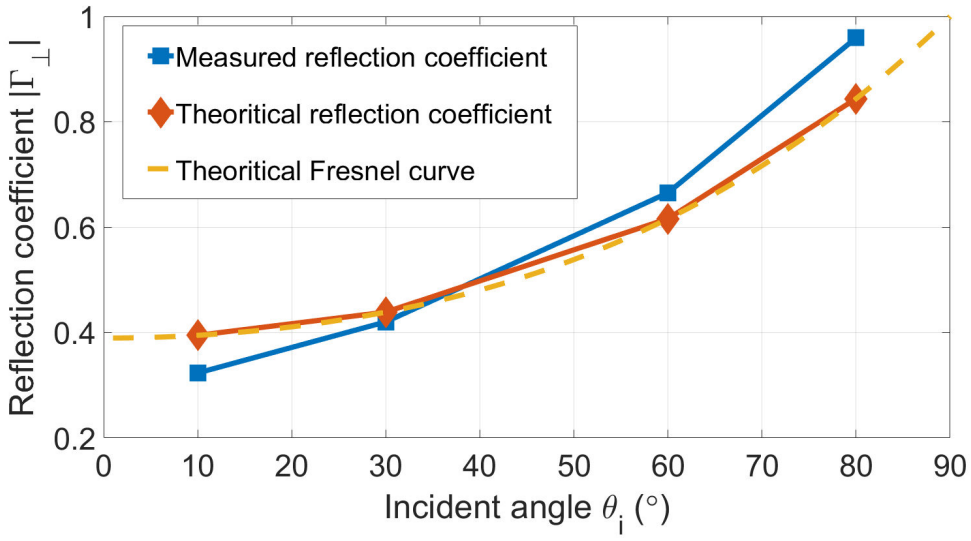

Figure 2.7: Measured magnitude of reflection coefficients of drywall at 140 GHz, with $\epsilon_r = 6.4$ by MMSE estimation.

ground/ceiling bounces happening within or just outside the HPBW of the main lobe of the TX/RX antenna patterns, and on an arc with a radius of 1.5 m which is greater than the Fraunhofer distance to ensure the propagation is happened in far field [108]. Vertically polarized horn antennas were used at both TX and RX. Incident angles of $\theta_i = 10°, 30°, 60°, 80°$ (with respect to the normal) were chosen to measure the reflection coefficient of the drywall from small incident angles to large angles. The RX power was measured in the plane of the incident ray and the norm of the surface from $10°$ to $170°$ in $10°$/step (the RX power at $0°$ and $180°$ was not able to be measured due to the physical size of the channel sounder system).

The Fresnel reflection coefficient $\Gamma_\perp$ (E-field normal to the plane of incidence) is given by [78]:

$$\Gamma_\perp = \frac{E_r}{E_i} = \frac{\cos\theta_i - \sqrt{\epsilon_r - \sin^2\theta_i}}{\cos\theta_i + \sqrt{\epsilon_r - \sin^2\theta_i}}, \tag{2.5}$$

where E_r and E_i are the electric fields of the reflected wave and the incident wave with units of V/m respectively, ϵ_r is the permittivity of the reflecting surface, and θ_i is defined as the angle between the incident direction and normal direction.

Based on the measured data and the Fresnel equation (2.5), a permittivity of $\epsilon_r = 6.4$ was obtained through a minimum mean square error (MMSE) estimator of $|\Gamma_\perp|^2$. As shown in Figure 2.7, the blue line indicates the measured reflection coefficient and the yellow dashed line is the theoretical Fresnel curve through MMSE estimation. A maximum gap of 0.1 was observed over incident angles of $10°$ and $80°$.

2.4.2 Partition Loss Measurements

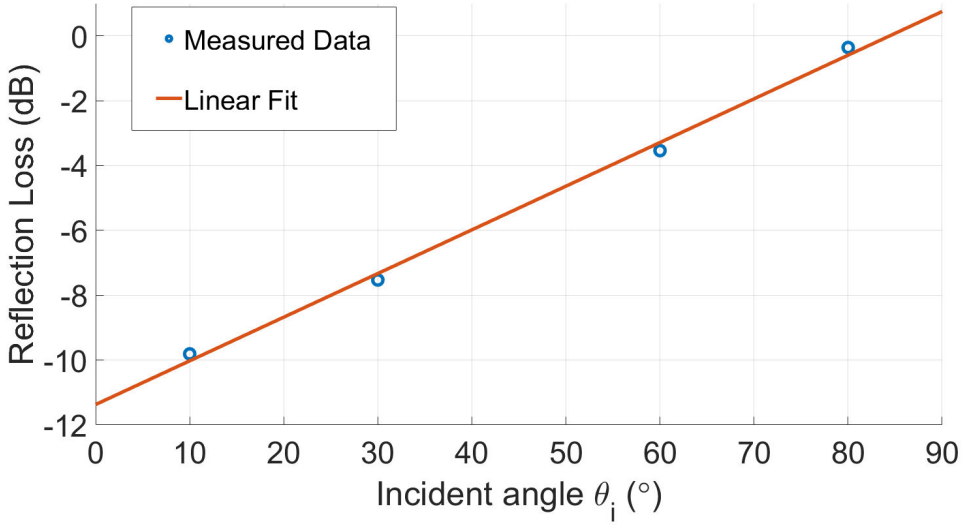

Figure 2.8: Measured reflection loss with a linear prediction.

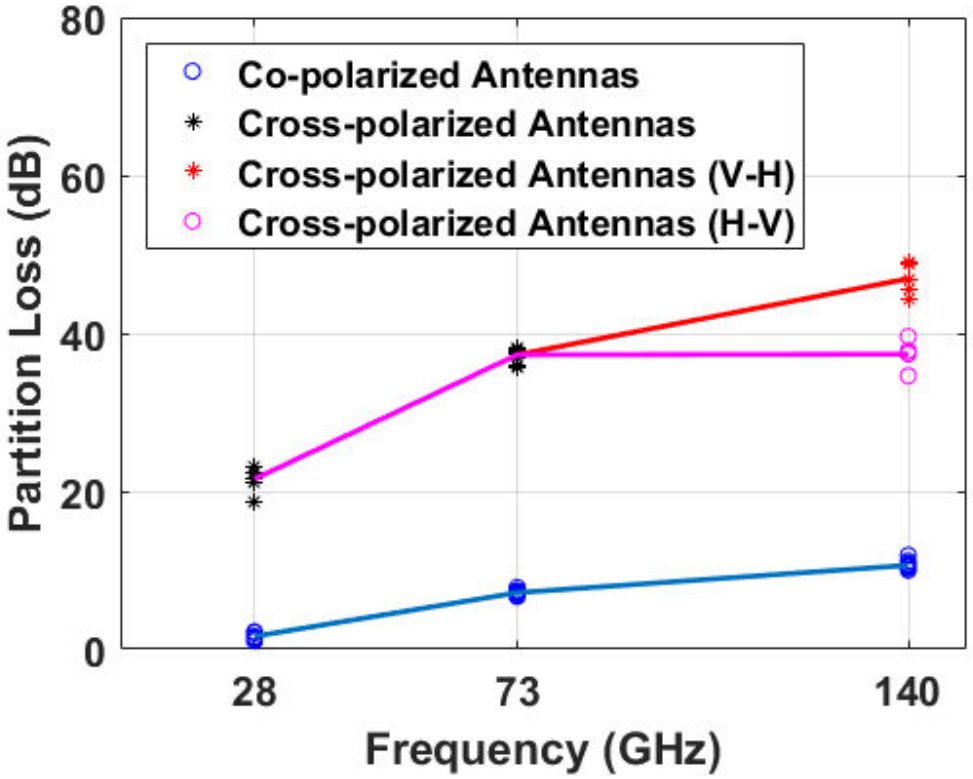

Figure 2.9: Partition loss measurement results of clear glass with a thickness of 0.6 cm at 28, 73, and 140 GHz. Partition loss trends to increase with frequencies for both co-polarized and cross-polarized antenna configurations.

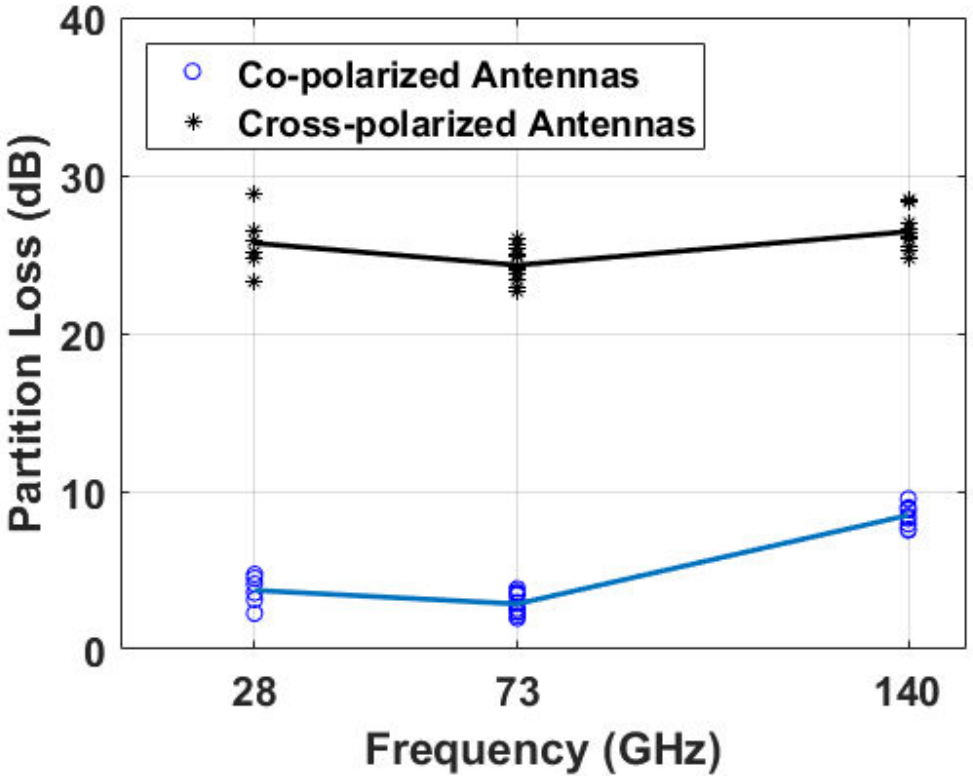

Figure 2.10: Partition loss measurement results of drywall with a thickness of 14.5 cm at 28, 73, and 140 GHz.

Partition loss measurements at 28, 73, and 140 GHz were conducted using the channel sounder systems summarized in Table 2.4. T-R separation distances of 3, 3.5, 4, 4.5, and 5 m were used and the TX/RX antenna heights were 1.6 m (see Figure 3 in [108]). The separation distances were greater than $5 \times D_f$, where D_f is the Fraunhofer distance to ensure that the measured material is in the far-field of the TX and a plane wave is incident upon the material under test (MUT). The dimensions of the MUT were large enough to guarantee that the radiating wavefront from the TX antenna is illuminated on the material without exceeding the physical dimensions of the MUT [108]. At each distance, 5 measurements were recorded with slight movement in the order of half a wavelength, taking the average of the power in the first arriving multipath component of the recorded PDPs, to exclude the multipath constructive or destructive effects. Four antenna polarization configurations (all possible linear polarization combinations of the TX and RX: V-V, V-H, H-V, and H-H) were measured to characterize the polarization effects of the MUT on partition loss. The channel sounder systems used in this work had an RF bandwidth of 1 GHz and a time resolution of 2 ns ($\Delta t = 1/B =$), which means multipath components having more than 0.6 m difference of link length can be resolved.

Common building construction materials, drywall (with a thickness of 14.5 cm) and clear glass (with a thickness of 0.6 cm), were selected and measured at 28, 73, and 140 GHz, with measurement results listed in Table 2.6 and Table 2.7, respectively. The partition losses were measured and calculated as:

$$L_{XY}[\text{dB}] = P_{tX}[\text{dBm}] - P_{rY}(d)[\text{dBm}] - \text{FSPL}(d)[\text{dB}], \tag{2.6}$$

where $L_{XY}[\text{dB}]$ is the material partition loss, X, and Y can be either V or H, corresponding to vertically polarized or horizontally polarized antenna configuration at the link ends, $P_{rY}(d)$ is the RX received power in dBm at distance d in meters with the MUT between the TX and RX, $P_{tX}[\text{dBm}]$ is the transmitted power from the TX , and $\text{FSPL}(d)[\text{dB}]$ is the free space path loss at distance d [30, 108].

The measured mean partition loss of clear glass at 28 GHz for co-polarized situation (V-V or H-H), see Table 2.6, is 1.50 dB with a standard deviation (STD) of 0.50 dB. The mean partition loss for co-polarized situation (V-V and H-H) is 7.16 dB with a STD of 0.15 dB at 73 GHz, and 10.33 dB with a STD of 0.24 dB at 140 GHz. According to the measurement results, the partition loss of clear glass increases with the frequencies moderately, as expected, rising from 1.50 dB at 28 GHz to 10.33 dB at 140 GHz.

At 28 and 73 GHz, the difference of clear glass partition losses in the cross-polarization situation (V-H and H-V) are negligible. However, at 140 GHz, the mean partition loss of clear glass with V-H configuration is 9.55 dB higher than that with H-V configuration, which means the material has different polarization effects at higher frequencies. It's worth noting that the XPD is not subtracted from the cross-polarized partition loss measurements shown in Table 2.6 and Table 2.7. Subtracting the XPD results in a negative value of partition loss due to the polarization coupling effects (depolarization) of the building materials. Figure 2.9 illustrates how that the partition loss of clear glass tends to increase with frequencies for both co-polarized and cross-polarized antenna configurations.

As shown in Figure 2.10 and Table 2.7, the mean partition loss of drywall for co-polarization configuration (V-V and H-H) is 3.73 dB at 28 GHz and 2.87 dB at 73 GHz, respectively. However, the mean partition loss increases to 8.89 dB at 140 GHz.

For cross-polarization configuration (H-V or V-H), the mean partition losses of drywall at 28, 73 GHz, and 140 GHz are 25.70 dB, 24.18 dB, and 26.64 dB, respectively. There is a negligible difference between the partition loss of V-H and H-V configurations. After subtracting the measured XPD values (as shown in Figure 2.6), we get 6.40 dB, -4.76 dB, and -17.54 dB, where the negative value means the drywall induce polarization coupling effects (depolarization) at 73 and 140 GHz.

Work in [37] showed that absorption imposed a ∼8dB penalty to the reflection power (nearly 16% of the signal power imping on the reflection surface is reflected and about 84% of the power is absorbed) from an indoor painted cinderblock wall at 100 GHz and the effect of scattering from the painted cinderblock wall is significantly smaller than the effect of absorption. It is worth noting that the absorption mentioned in [37] includes the power penetrating through the wall and the power absorbed by the wall.

Using the predicted permittivity of drywall at 140 GHz ($\epsilon_r = 6.4$ from Section 2.4.1), a reflection loss of 7.25 dB is predicted (∼18.8% of the power is reflected), which is comparable to the reflected

Table 2.6: Partition Loss Measurement Results at 28, 73, and 140 GHz for Clear Glass.

Polarization	Partition Loss at 28 GHz		Partition Loss at 73 GHz		Partition Loss at 140 GHz	
	Mean (dB)	std (dB)	Mean (dB)	std (dB)	Mean (dB)	std (dB)
V-V	1.53	0.60	7.17	0.17	10.22	0.22
V-H	1.33	1.32	8.71	0.53	2.74	2.05
H-V	2.95	0.88	7.98	1.11	- 6.81	1.79
H-H	1.48	0.54	7.15	0.44	11.04	0.55

Table 2.7: Partition Loss Measurement Results at 28, 73, and 140 GHz for Drywall.

Polarization	Partition Loss at 28 GHz		Partition Loss at 73 GHz		Partition Loss at 140 GHz	
	Mean (dB)	std (dB)	Mean (dB)	std (dB)	Mean (dB)	std (dB)
V-V	4.15	0.59	2.57	0.61	8.46	1.22
V-H	6.29	2.85	-3.97	0.58	-16.9	1.77
H-V	6.51	0.65	-5.56	0.65	-18.18	1.42
H-H	3.31	1.13	3.17	0.68	9.31	0.61

power (∼8 dB) measured in [37] at 100 GHz. In addition, as seen in Section 2.4.2, 14.3% of the incident power is transmitted through the drywall at 140 GHz (8.46 dB partition loss was measured). Thus, we can conclude that there is about 66.9% (100% -18.8% -14.3%) of the power impinging on the surface (∼4.8 dB real absorption loss) was absorbed by drywall at 140 GHz.

2.4.3 Partition Loss Measurements in the Literature

Wideband mmWave and THz networks, as well as precise ray-tracer algorithms [122, 123], will require accurate channel models that accurately represent the partition losses induced by common building objects[59, 108]. Therefore, partition loss of common building materials needs to be extensively investigated for 5G mmWave wireless systems and future THz wireless communications in and

Table 2.8: Partition Loss of Common Outdoor Materials [1].

Material	Material Thickness	Average Attenuation	Standard Deviation	Frequency	Polarization	Ref.
Brick Pillar	185.4 cm	28.3 dB	–	28 GHz	V-V	[114]
Brick Wall	–	12.5 dB	2.4 dB	5.85 GHz	V-V	[115]
	–	16.4 dB	3.3 dB	5.85 GHz	V-V	[115]
Cinderblock Wall	–	22.0 dB	3.5 dB	5.85 GHz	V-V	[115]
Wood siding exterior	–	8.8 dB	3.5 dB	5.85 GHz	V-V	[115]
Tinted Glass	3.8 cm	40.1 dB	–	28 GHz	V-V	[114]
	1.2 cm	24.5 dB	–	28 GHz	V-V	[114]
Mesh Glass	0.3 cm	7.7 dB	1.4 dB	2.5 GHz	V-V	[110]
	0.3 cm	10.2 dB	2.1 dB	60 GHz	V-V	[110]

Table 2.9: Partition Loss of Common Indoor Materials [1].

Material	Thickness (cm)	Attenuation (dB)	std (dB)	Frequency	Polarization	Ref.
Drywall	2.5	5.4	2.1	2.5 GHz	V-V	[110]
	2.5	6.0	3.4	60 GHz	V-V	[110]
	38.1	6.8	—-	28 GHz	V-V	[114]
	13.3	10.6	5.6	73 GHz	V-V	[116]
	13.3	11.7	6.2	73 GHz	V-H	[116]
	14.5	15.0	–	140 GHz	V-V	[75]
Clear Glass	0.3	6.4	1.9	2.5 GHz	V-V	[110]
	1.2	3.9	–	28 GHz	V-V	[114]
	1.2	3.6	–	28 GHz	V-V	[114]
	0.3	3.6	2.2	60 GHz	V-V	[110]
	0.6	8.6	1.3	140 GHz	V-V	[75]
	1.3	16.2	–	140 GHz	V-V	[75]
	2.5	86.7	–	300 GHz	V-V/H-H	[75]
	0.16-0.48	15-26.5	–	0.1-10 THz	V-V	[117]
Steel Door	5.3	52.2	4.0	73 GHz	V-V	[116]
	5.3	48.3	4.6	73 GHz	V-H	[116]
Office Whiteboard	1.9	0.5	2.3	2.5 GHz	V-V	[110]
	1.9	9.6	1.3	60 GHz	V-V	[110]
Heavily reinforced uniform concrete wall	35.0	22.0	–	1-4 GHz	V-V	[118]
	35.0	35.0	–	6 GHz	V-V	[118]
	35.0	64.0	–	9 GHz	V-V	[118]
Slightly reinforced uniform concrete wall	20.3	2.0-4.0	–	900 MHz	V-V/H-H	[119]
	12.0	8.0	–	1-3 GHz	V-V	[118]
	12.0	13.0	–	3-7 GHz	H-H	[118]
	12.0	17.0	–	5 GHz	V-V	[118]
	12.0	27.0	–	10 GHz	V-V	[118]
	12.0	32.0	–	8-12.0 GHz	H-H	[118]
	12.0	27.0	–	15 GHz	V-V	[118]
	12.0	23.0	–	12-18 GHz	H-H	[118]
Concrete slab	3.0	13.1	–	45 GHz	H-H	[120]
	3.0	13.9	–	45 GHz	V-V	[120]
Solid wood	2.0	4.8	–	45 GHz	H-H	[120]
	2.0	8.4	–	45 GHz	V-V	[120]
	2.0	19.0	–	100 GHz	H-H	[121]
	2.0	20.4	–	100 GHz	V-V	[121]
	4.0	41.6	–	100 GHz	V-V	[121]
	3.5	65.5	–	300 GHz	V-V/H-H	[87]
	0.25-0.75	14.0-26.0	–	0.1-10 THz	V-V	[117]
Cement tile	2.5	39.5	–	100 GHz	H-H	[121]
	2.5	39.3	–	100 GHz	V-V	[121]
Gypsum board	1.2	3.5	–	100 GHz	–	[121]
Plastic	0.2-1.2	8.0-20.0	–	0.1-10 THz	–	[117]
Paper	0.25-1.0	12.0-24.0	–	0.1-10 THz	–	[117]
Uniform plasterboard wall	12.0	4.0	–	1-3 GHz	V-V	[118]
	12.0	10.0	–	5 GHz	V-V	[118]
	–	4.7	2.6	5.85 GHz	V-V	[115]
	12.0	6.0	–	6-7 GHz	V-V	[118]
	12.0	18.0	–	15 GHz	V-V	[118]
	12.0	11.0	–	18 GHz	V-V	[118]

around buildings.

Partition loss measurements at 2.5 and 60 GHz of a variety of materials like drywall, office whiteboard, clear glass, mesh glass, using a wideband channel sounder with vertically polarized antennas at both TX and RX were presented in [110], where root mean square (RMS) delay spreads were found to be much lower at 60 GHz than at 2.5 GHz. Based on the measured data, a partition-based path loss model which provided fast and accurate link budget predictions in a multipath-rich environment was developed in [110, 115]. Partition loss measurements at 73 GHz for V-V and V-H polarization configurations for glass doors, drywall, steel doors, and clear glass were conducted in [116]. The co-polarized partition loss for glass doors and windows was found to be 5-7 dB at 73 GHz, and steel doors induced a partition loss as large as 40-50 dB, showing that different materials could be properly chosen for propagation or interference isolation between neighboring rooms [75, 108, 116]. The partition loss of common outdoor and indoor materials are summarized in Table 2.8 and 2.9, respectively, and reveal that not much is known above 100 GHz.

Effective attenuation of typical building materials such as concrete bricks, wood, tiles, and a gypsum plate were measured at 100 GHz with the TX and RX boresight-aligned [121]. The co-polarization situations (both TX and RX were vertically or horizontally polarized) were analyzed, and the effective attenuation of most of the building materials was observed to be polarization sensitive [121].

Work in [118] presented penetration loss measurements of concrete walls and plasterboard walls over the frequency range of 900 MHz to 18 GHz, as shown in Table 2.9, and the penetration loss was shown to not necessarily increase monotonically with respect to frequency. A comparison of measured partition loss versus frequency for a variety of different common building materials was shown in [119].

As measured in [119], an 8-inch concrete wall had a typical partition loss of 2 to 4 dB at 900 MHz for both V-V and H-H antenna configurations. The attenuation through solid wood, having a thickness of 2 cm, was measured to be about 5 dB and 8 dB at 45 GHz for both H-H and V-V antenna configurations, respectively, while the attenuation through a concrete slab having a thickness of 3 cm was measured to be about 13 dB at 45 GHz for both H-H and V-V antenna configurations [120]. Penetration loss measurements in THz band (0.1 - 10 THz) of plastic board, paper, and glass which had losses of 12.47 dB/cm, 15.82 dB/cm, and 35.99 dB/cm were presented in [117]. However, the measurements in [117] were conducted in a very short range (less than 10 cm) and the thicknesses of sample materials were less than 1 cm which may cause large uncertainty or error.

Absorption coefficients of glass, medium density fiberboard, and plexiglass were measured where the S_{21} parameter was recorded at a T-R separation distance of 10 cm with and without the obstructions brought into the ray path, showing that a 2.5 cm thick window and a 3.5 cm thick fiberboard door would induce absorption attenuation of approximately 65.5 dB and 86.7 dB at 300 GHz [87], respectively.

2.4.4 Documentation of Partition Loss Measurements

Partition loss measurements of drywall (14.5 cm) at 28 GHz were conducted on 11.09.2018 with 15 dBi gain, 28.8° HPBW horn antennas at both the TX and RX. Four antenna polarization configurations (VV, VH, HV, and HH) were used to study the polarization effects of the partition. The measurement data was saved in `euler:\PropDataBackup\PartitionLossMeasurements\11.09.2018`. Calibrations before and after the measurements were recorded in the "Calibration Area". Forty measurements were recorded corresponding to VV, VH, HV, and HH polarization combinations at 3, 3.5, 4, 4.5, and 5 m with drywall and drywall plus whiteboard. Measurements 1, 3, 5, ...40 were the partition loss measurements of drywall. At each distance, five PDPs (five rots) were recorded, taking the average of the power in the first arriving multipath component of the recorded PDPs, to calibrate out the variation caused by the channel sounder. Static information is saved in the "pdpLogFile" and the PDP is saved in the "IQsquaredXXX" file. Excel tables named "28 PartitionLoss", "73 PartitionLoss", and "140 PartitionLoss" are also saved for records.

Partition loss measurements of clear glass (0.6 cm) at 28 GHz were conducted on 11.13.2018 with the same measurement setups as described above. The only difference is that only 16 measurements were recorded corresponding to VV, VH, HV, and HH polarization configurations at TR separation distances of 1, 1.5, 2, and 2.5m, due to the limit of the physical size of the clear glass (ensuring the MUT have dimensions large enough such that the radiating wavefront from the TX antenna is illuminated on the MUT without exceeding the projected HPBW angle spread from the TX antenna [108]).

Partition loss measurements of drywall and clear glass at 73 GHz were conducted on 11.01.2018 and the measurement data was saved in `euler:\PropDataBackup\PartitionLossMeasurements\11.01.2018` (L1-RX1). Measurements 1-4 were XPD measurements with statistic information recorded in the PDP log file. Measurements 5-24 were partition loss measurements of drywall and Measurements 25-44 were partition loss measurements of clear glass.

Partition loss measurements of clear glass at 140 GHz were conducted on 09.16.2018 and the measurement data was saved in `euler:\PropDataBackup\PartitionLossMeasurements\09.16.2018` (L2-RX2). Same as 28 and 73 GHz , 20 measurements were recorded using the 27 dBi gain horns at both sides with different polarizations. Calibration 1 and 2 were conducted before and after XPD measurements and Calibration 3 is conducted after the partition loss measurements of clear glass at 140 GHz (L2-RX2).

Partition loss measurements of drywall at 140 GHz were conducted on 10.30.2018 and the measurement data was saved in `euler:\PropDataBackup\PartitionLossMeasurements\10.30.2018` (L1-RX1). Twenty measurements were recorded at distances of 3, 3.5, 4, 4.5, and 5 m with all the polarization combinations.

2.5 Scattering Measurements

Scattering at mmWave and THz frequencies is an important propagation mechanism [38]. The surfaces of buildings, terrain, walls, and ceilings have usually been assumed to be electrically smooth since their surface height variations are small compared to the carrier wavelength at lower frequencies (e.g., greater than 5 cm at below 6 GHz) [124]. At today's 1-5 GHz cellular and WLAN systems, the reflection process is dominated by a strong specular path at an angle of reflection equal to the angle of incidence, and scattering, being a weaker propagation phenomenon, is negligible. However, in mmWave bands and above, the roughness of surfaces are comparable to the carrier wavelength and the illuminated scatterers may actually create signal paths that are as substantial as (or even occasionally stronger than reflected paths) [38, 124].

A smooth metal plate or a conformal metal foil attached on the wall (having a size much larger than the radius of the first Fresnel zone for frequencies of 100, 200, 300, and 400 GHz) was shown to provide 6-10 dB more power from specular reflection (at an incident angle of 50°) than the bare painted cinderblock wall did [37], indicating that the effect of scattering from the rough surface was significantly smaller than the effect of absorption from the bare painted cinderblock wall, even at 400 GHz. Specular reflection loss with varied incident angles measurements at 400 GHz was also conducted in [37] with 5 different incident angles ranging from 20° to 60° which showed that when the incident angle is large, reflection loss is small (absorption loss plus the scattering loss) and the scattering loss is negligible. However when the incident angle is small (e.g., incident ray impinges the wall perpendicularly), the scattering loss is not negligible (4 dB difference than predicted result when scattering losses are neglected) [37].

Scattering measurements at 60 GHz were presented in [124] using a 2 GHz wide baseband sounder to measure the non-specular diffuse scattering with an incident angle of 15°, 30°, and 45°. Two types of building materials were used: a red stone wall (a rough wall surface) and a concrete pillar (a smooth wall surface). The received power was measured in the range of 0° to 90° from the normal to the wall and the term of power concentration was defined as the angular span corresponding to 90% of the received power. It was shown that the angular span is centered at the incident angle and higher incident angles lead to smaller angular spread [124]. The power concentration of the rough wall surface was shown to be significantly larger than the case of a smooth wall surface and the coupling effects (depolarization) are more severe when reflecting/scattering from rough wall surface [124].

Diffuse scattering measurements at 100, 200, 300, and 400 GHz were presented in [125] to study the scattering effect with different surface roughness. The bistatic scattering integral equation method (IEM) model was shown to predict the properties of the scattered wave well, and NLOS paths from specular reflection or diffuse nonspecular scattering can be valuable for establishing a link [125].

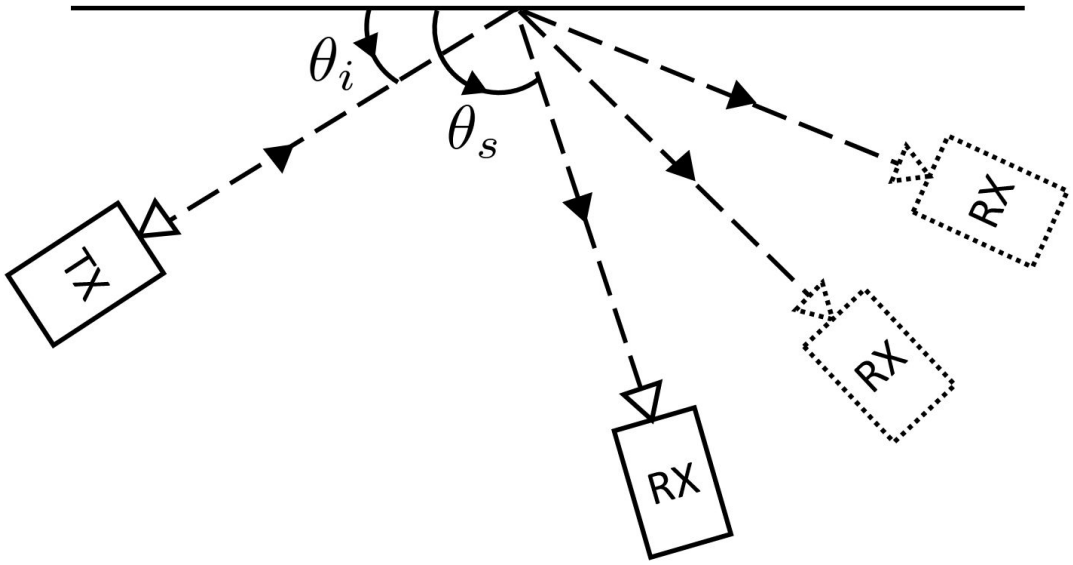

Figure 2.11: Setup for scattering measurements. θ_i is the angle the incident ray makes with the wall and θ_s is the scattered angle.

2.5.1 Scattering Measurements at 142 GHz by NYU WIRELESS

Scattering measurements of drywall were conducted at 142 GHz, and the measurement setups and photos are shown in Figure 2.11 and 2.12. During the scattering measurements, both the TX and RX heights were set at 1.2 m on an arc with a radius of 1.5 m using TX output power of -2.35 dBm with 27 dBi gain and 8° HPBW horn antennas at both ends of the link. Incident angles θ_i = 10°, 30°, 60°, 80° were chosen to study the scattering performance from a small incident angle θ_i to a large angle with respect to the scattered/reflected surface. The RX power was measured in the same plane of the incident ray and the norm of the surface from 0°to 180°in 10°/step (0°and 180°cannot be measured due to the physical size of the channel sounder system). Five PDPs were recorded and averaged at each RX location to calibrate the power fluctuation (within 0.3 dB).

The path loss was calculated by:

$$\text{PL[dB]} = P_{\text{TX}}[\text{dBm}] - P_{\text{RX}}[\text{dBm}] + G_{\text{TX}}[\text{dBi}] + G_{\text{RX}}[\text{dBi}],$$

where P_{TX} [dBm] is the true transmit power in dBm, P_{RX} [dBm] is the record received power by the channel sounder system, G_{TX} [dBi] and G_{RX} [dBi] are the TX and RX antenna gain in dB, respectively. The scattered power was then normalized with respect to the free space path loss:

$$\text{SP} = \text{PL[dB]} - \text{FSPL}(f, d)[\text{dB}], \tag{2.7}$$

$$\text{FSPL}(f, d)[\text{dB}] = 32.4 + 20\log_{10}(f) + 20\log_{10} d, \tag{2.8}$$

where SP is the scattered power in dBm, f is the carrier frequency in GHz and d is the TR separation distance in meter.

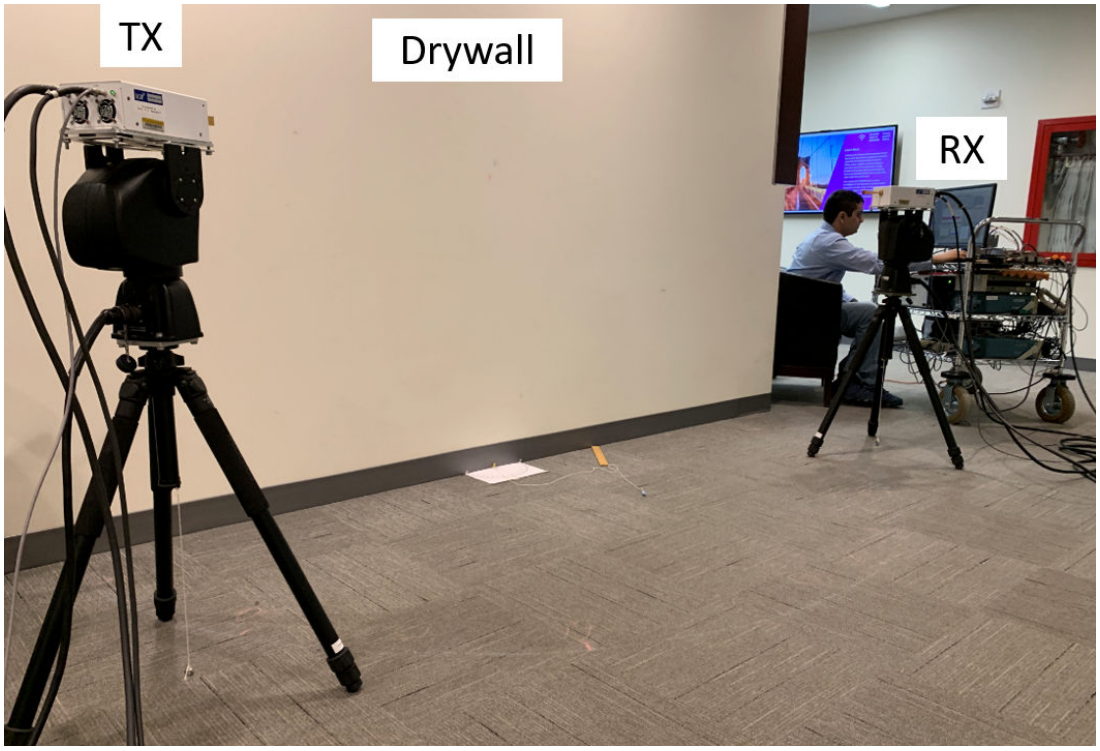

Figure 2.12: Photograph of the scattering measurement setup. The reflected/scattered power of drywall was measured at a distance 1.5 m away from the wall, in angular increments of 10°.

The scatter patterns of different incident angles are shown in Figure 2.13. The blue dashed line is a prediction of the scattered power when the TX was at an incident angle $\theta_i = 10°$. The peak scattered power is observed at the specular reflected angle (Snell's law), and peak scattered power is larger at small incident angles than at large incident angles (9.4 dB difference between 10° and 80°). Scattered power is within 10 dB below the peak power in a $\pm$ 10° angle range of the specular reflection angle. In addition, back scattered are also observed (RX angles above 90°) when the incident angle is large (e.g., 60°and 80°) but relatively less than the front scattered power.

2.5.2 Directive Scattering model

The directive scattering (DS) model is widely used to predict the scattered power in optics [126]. The single lobe DS model [127, 128] assumes that the main scattering lobe is steered in the direction of the specular reflection (θ_r shown in Fig. 2.14). The DS model has been used in [128] to model the RF propagation environment of a hospital room at 60 GHz. The PDP of the environment agreed well with simulations using the DS model, up to an excess delay of 30 ns. The DS model has also been tested at 1.296 GHz in [127], where the DS model agreed with the scattering from rural and suburban buildings. When an electromagnetic wave impinges upon a surface at an incident angle θ_i, the scattered electric field at any particular scattering angle θ_s can be calculated using the DS

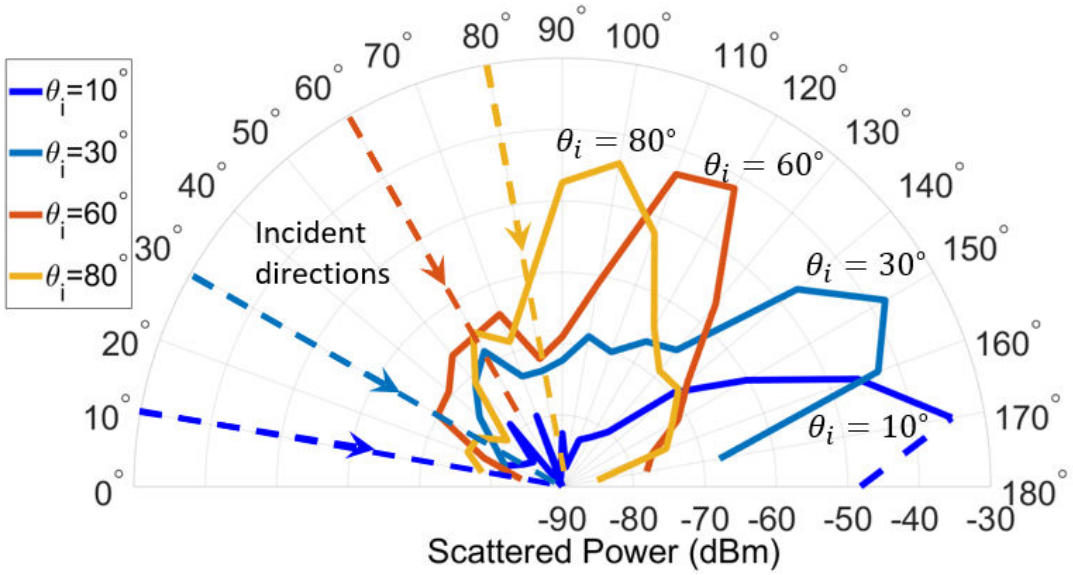

Figure 2.13: Polar plots of the scattered power off drywall, measured at four incident angles. Power at scattered angles is measured in 10° increments.

model. The DS scattered electric field in the incident plane is given by:

$$\begin{aligned} |\mathbf{E}_s|^2 &= |\mathbf{E}_{s0}|^2 \cdot \left(\frac{1+\cos(\Psi)}{2}\right)^{\alpha_R} \\ &= \left(\frac{SK}{d_t d_r}\right)^2 \frac{l\cos\theta_i}{F_{\alpha_R}} \cdot \left(\frac{1+\cos(\Psi)}{2}\right)^{\alpha_i} \end{aligned} \tag{2.9}$$

where $\mathbf{E}_s$ is the scattered electric field at the scattering angle Ψ. $\mathbf{E}_{s0}$ is the maximum scattered electric field, which is adopted from an effective roughness model[127]. K is given by $\sqrt{60P_tG_t}$ which is a constant depending on the transmitted power and the transmitter antenna gain [129]. d_t and d_r are the distances between the scatterer and the transmitter and receiver, respectively. l is the length of the scattering object. Ψ is the angle between the reflected wave and the scattered wave, as shown in Fig. 2.14. α_R determines the width of the scattering lobe with higher values of α_R implying a narrower scattering lobe.

The received power at the receiver can then be calculated as [78]:

$$P_r = P_d A_e = \frac{|\mathbf{E}_s|^2}{120\pi} \cdot \frac{G_r\lambda^2}{4\pi} = \frac{|\mathbf{E}_s|^2 G_r\lambda^2}{480\pi^2} \tag{2.10}$$

where P_d is the power flux density of the scattered wave, and A_e is receiver antenna aperture [78]. G_r is the receiver antenna gain, and λ is the wavelength of the radio wave. The scattered power is calculated using (2.9)-(2.10), and the reflected power is calculated using:

$$\Gamma_{\text{rough}} = \rho_s \cdot \Gamma_{\text{smooth}}, \tag{2.11}$$

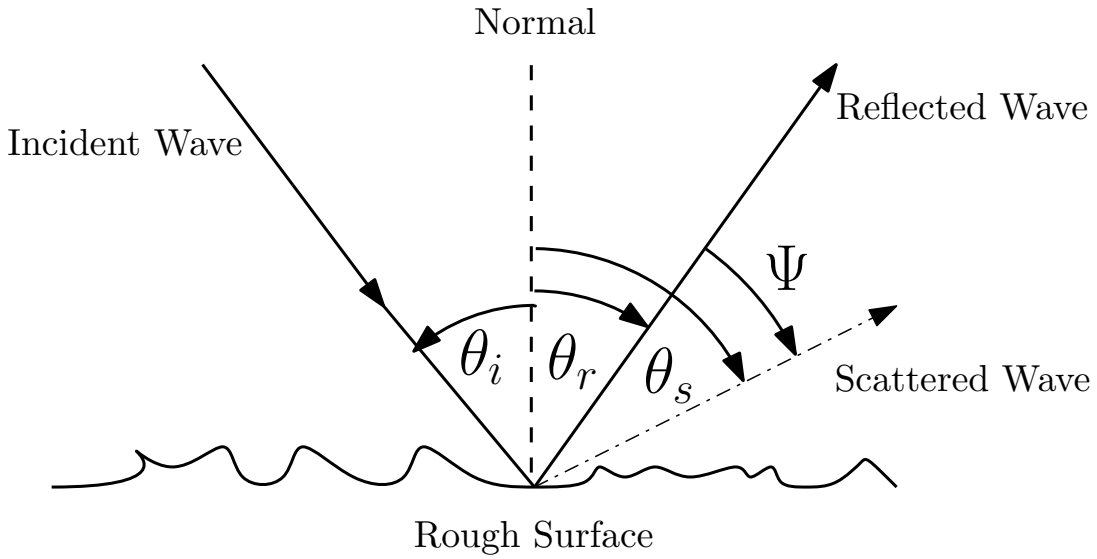

Figure 2.14: A radio wave incident at an angle θ_i with respect to the normal to the targeted rough surface. θ_r and θ_s are reflected and scattered angle, respectively. From Snell's law, reflections obey $\theta_i = \theta_r$. Ψ is the angle between reflected and scattered waves.

where ρ_s is the scattering loss factor and

$$\rho_s = \exp\Big[-8\left(\frac{\pi h_{\text{rms}}\cos\theta_i}{\lambda}\right)^2\Big] I_0\Big[8\left(\frac{\pi h_{\text{rms}}\cos\theta_i}{\lambda}\right)\Big], \tag{2.12}$$

where I_0 is the zero-order Bessel function of the first kind. When $\theta_i = 1°$, 30°, and 45° (small incident angles), it was shown in [130] that *the maximum scattered power (in the reflection direction as in Snell's law) computed by the DS model is stronger than the reflected power obtained from the rough surface reflection model for a rough surface.*

Simulations were performed using three materials with incident angle θ_i ranging from 10° to 90°and over frequencies from 1 GHz to 1 THz [130]. It was shown that as the frequency increases, the received scattered power increases, which can be expected since the surfaces tend to be rough as the frequency increases and rougher surfaces cause greater scattered power (even greater than the reflected power). Moreover, the maximum scattered power is received when the incident wave impinges upon the surface along the normal direction. The scattered power falls off sharply when the incident wave becomes grazing, and most of the incident power is reflected [130].

The single lobe DS model may be modified to incorporate power an additional back-scatter lobe[127]. The DS scattered electric field taking into account for backscattering is given by:

$$|E_s|^2 = |\mathbf{E}_{s0}|^2\Bigg[\Lambda\cdot\left(\frac{1+\cos(\Psi)}{2}\right)^{\alpha_R} + (1-\Lambda)\cdot\left(\frac{1+\cos(\Psi_i)}{2}\right)^{\alpha_R}\Bigg] \tag{2.13}$$

where Ψ_i is the angle between the scattered ray and the incident ray and Λ determines the relative

strength of the back scattered lobe with respect to the main scattered lobe.

A Comparison between measurements and predictions made by the dual-lobe DS model [130, 131] with TX incident angle θ_i= 10°, 30°, 60°, and 80° is shown in Figure 2.15. It is shown that the peak received power of the simulation at the specular reflection angle agrees well with the measured data (within 2 dB). The received power (measured and simulated) changes versus the RX pointing angle (θ_r as shown in Figure2.11). A back-scattered peak is observed in both the measurement data and the dual-lobe DS model prediction for all the incident angles, and the back-scattered power could be used for imaging around the corner [58].

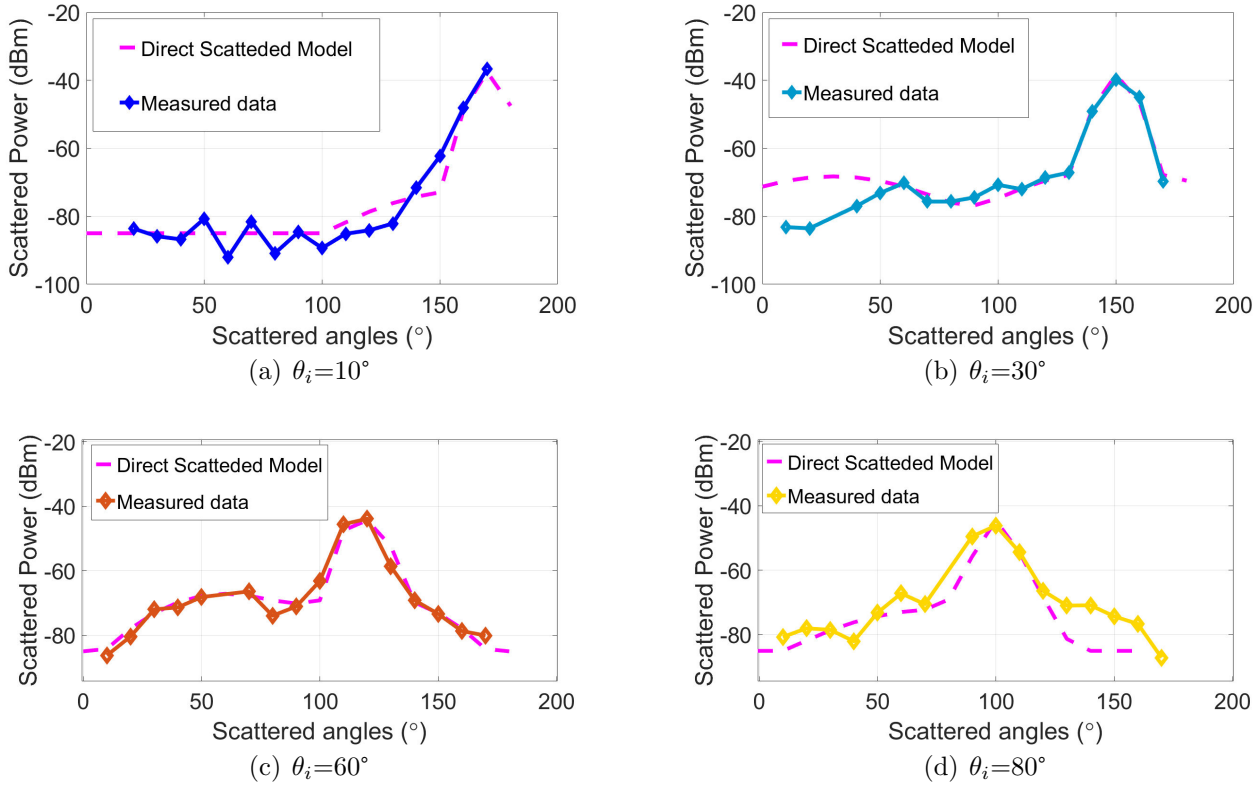

(a) θ_i=10° (b) θ_i=30°

(c) θ_i=60° (d) θ_i=80°

Figure 2.15: Comparison between measured data and the dual-lobe Directive Scattering model with TX incident angle θ_i= 10°, 30°, 60°, and 80°at 142 GHz.

2.5.3 Documentation of Scattering Measurements

Scattering measurements of a drywall for co-polarized and cross-polarized antennas were conducted on 12.02.2018 and 02.10.2019 respectively. The description of system parameter settings for measurement numbers are summarized in the Log sheet named '12.02.2018ScatteringVV.jpg' and '02.10.2019ScatteringVH.jpg'. Calibrations were conducted before and after the measurements to make sure accuracy of the measurements. The scattering measurement data are saved in `euler:\PropDataBackup\140GHzScatteringMeasurements`. The static information is stored in 'pdpLogFile.txt' and the PDPs are saved in 'IQsquared' files.

2.6 Conclusion

This chapter presented different channel sounding techniques for frequencies above 100 GHz and the state-of-the-art channel sounding measurements, channel modeling research in the literature, and elaborates the sub-THz channel sounder system at NYU WIRELESS. This chapter also introduced propagation characteristics such as antenna cross polarization discrimination (XPD), partition loss (penetration loss), reflection, and scattering at sub-THz frequencies, which provided a basic understanding of the wireless channels above 100 GHz.

Chapter 3

Indoor Office Propagation Measurements and Modeling at 142 GHz

The use of wide bandwidths (e.g., ≥100 MHz) in 5G and future wireless communication systems will enable multi-Gbps data rates for mobile devices and will usher in many new applications such as wireless cognition and centimeter-level positioning [1, 32, 132]. Highly directional electronically-steered antenna arrays will be used by both handset terminals and base stations, resulting in directional wireless channels at mmWave, a significant departure from sub-6 GHz frequencies that use less directional antennas but undergo less penetration and diffraction loss from obstacles [1, 32, 39]. FCC has recently opened up spectrum above 95 GHz with four new unlicensed bands from 116 GHz to 246 GHz, ushering in a new era of wireless networks that will have hundreds of Gbps of throughput [32].

Propagation channels at mmWave frequencies in the 24-73 GHz range are somewhat different from sub-6 GHz channels in transmission properties yet are viable through the use of directional antennas on both ends of the link [39, 44, 66, 92, 133, 134]. However, there is very little known about indoor channels above 100 GHz that have a coverage range of 30-40 m. Furthermore, it is currently unknown whether sub-THz wireless networks (i.e., 100-300 GHz) have similar or contrasting propagation characteristics compared to radio channels at lower frequencies. Knowledge of channel characteristics at frequencies above 100 GHz, as well as key differences from lower frequencies, is vital for the creation of frequency-dependent channel models that can be applied over vast frequency ranges (e.g., from 1-300 GHz) to support the design of multi-band indoor wireless modems in global standard bodies such as 3GPP and IEEE [135]. Also, knowledge of how channel characteristics vary over wide frequency ranges can be useful for futuristic applications such as intelligent reflecting surfaces [136] and precise position location [132]. Therefore, this work provides needed insights on indoor wireless channels from mmWave to sub-THz frequencies for futuristic wireless system designs.

Previous channel measurements in frequency bands from 28 to 380 GHz [137, 138, 139] have mostly focused on very close ranges (less than 10 m) due to the difficulty in achieving sufficient transmit power and large measurable path loss range [1]. Prior measurements at frequencies above

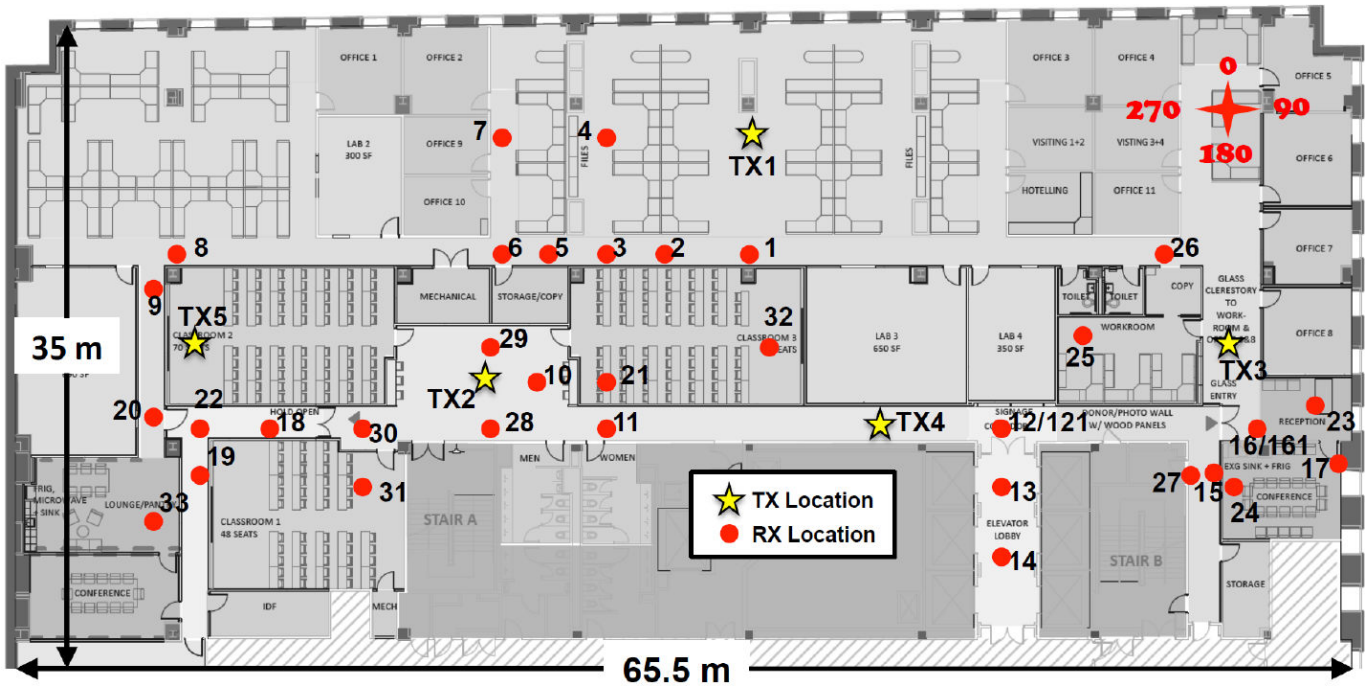

Figure 3.1: Maps of 2 MetroTech Center 9^{th} floor. There were five TX locations (stars) and 33 RX locations (dots) measured at 28 and 73 GHz providing 33 TX-RX combinations ranging from 4 to 48 m.

100 GHz [37, 68, 69] focused on line-of-sight (LOS) propagation using either reflective materials [37] or an RF-over-fiber extension [68, 69] of a VNA based system achieving over 100 m distance. However, no prior work has performed extensive indoor measurements wherein the same environment is used over a vast frequency range with commercially relevant distances of many tens of meters to provide comparisons of channel characteristics.

3.1 Indoor Propagation Measurements at 142 GHz

Above 100 GHz, high phase noise and Doppler spread, limited output power due to device limitations, and the need to fabricate more compact directional phased arrays present challenges for the deployment of future wireless networks above 100 GHz [1, 2, 4, 37]. To overcome these challenges, it is critical that designers first understand the channel characteristics for radio frequencies above 100 GHz.

140 GHz wideband wireless propagation measurements were conducted in 2019-2021 in a multipath rich indoor environment on the 9th floor of 2 MetroTech Center, Brooklyn, which is a typical indoor environment including the hallway, meeting rooms, cubical office, laboratory, and open area [75]. The purpose of the 140 GHz indoor measurement campaign was to collect data from various field propagation measurements and to build statistical indoor channel models for various TX and RX antenna configurations at multiple frequencies [140] (together with the existing 28 and 73 GHz indoor data [83, 141]), and to learn how much difference is there in the channels below and above 100 GHz. The measurements and resulting models will help with mmWave indoor wireless access net-

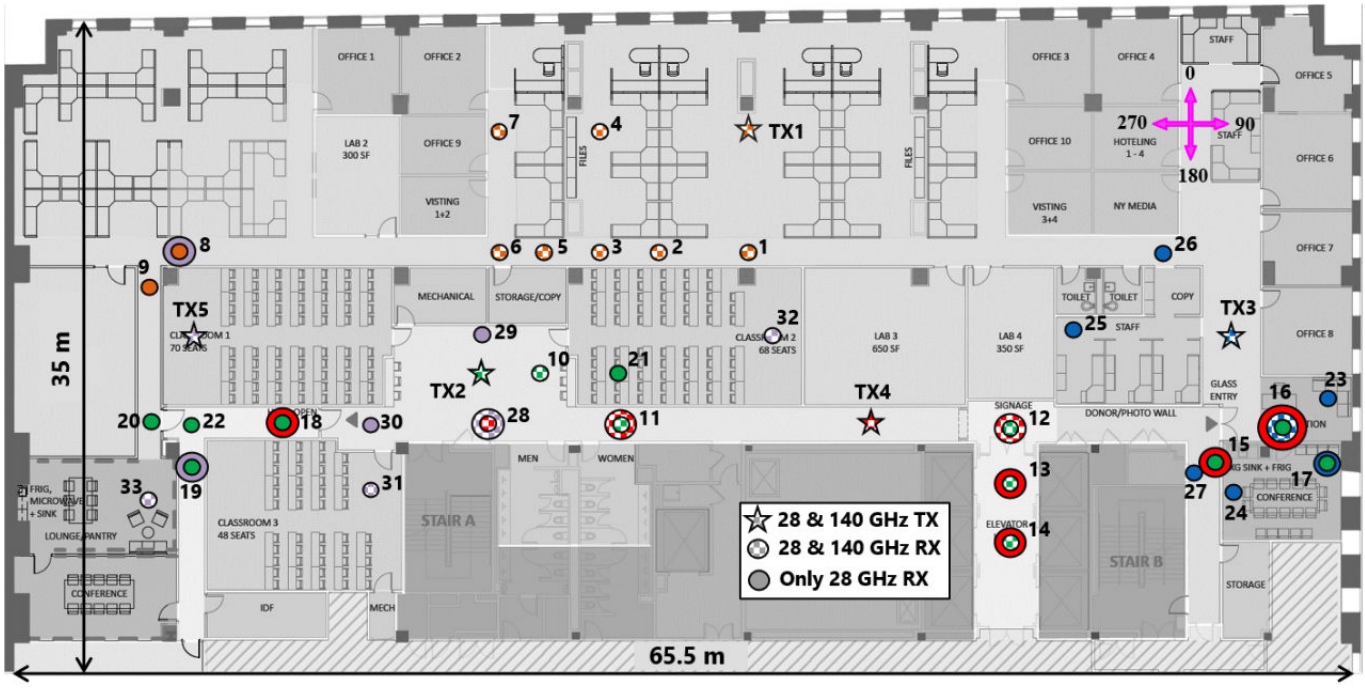

Figure 3.2: Map displaying 5 TX locations with the corresponding RX locations at 140 GHz, providing 22 TX-RX combinations ranging from 4 to 40 m with both LOS and NLOS situations. TX and RX locations measured at both 28 GHz and 140 GHz are denoted as stars and circles with checkerboard texture, respectively. RX locations only measured at 28 GHz are denoted as solid circles. Each of the five TX locations is denoted in a different color, and the RX locations paired with a TX location is denoted in the same color. Detailed specifications are provided in Tables 3.1, 3.2, 3.3, 3.4 and 3.5 [92].

works, gigabyte WiFi (WiGig), Internet of things (IoT), and future Terahertz (THz) communications for 6G [1].

The 140 GHz indoor measurement campaign was planned to use exactly the same measurement locations as used at 28 and 73 GHz (see Figure 3.1) [140, 141, 142, 143, 144], providing 33 TX-RX combinations ranging from 3.9 to 45.9 m.

However due to the entire department of NYU WIRELESS are moving to a new building in the summer of 2019 and 2 Metrotech center will be not available after July 2019, the most important 19 TX-RX combinations are selected, providing 5 LOS (there is no obstruction between TX and RX antennas), and 14 NLOS (common obstructions including desks, chairs, cubicle, drywall, glass doors, and glass windows) TX-RX combinations. Two of the 14 NLOS TX-RX combinations were outage (can not receive signals other than noise). The range of T-R separation distance is from 4 m to 40 m including both LOS and NLOS situations, see Figure 3.2.

Three TX locations and 16 RX locations were selected to study specific indoor environments such as cubical office, conference room (classroom), hallways, and corridors. Propagation effects like reflections, scattering, penetration (partition loss), and diffraction were included and analyzed.

The TX antenna was set at 2.5 m near the ceiling (2.7 m) to emulate current indoor wireless access points and the RX antennas were set at heights of 1.5 m which are typical heights of mobile devices. Both TX and RX antennas were horns with 27 dBi gain and 8° half power beam width (HPBW). For each TX-RX combination, 3 elevation angles at both TX and RX were chosen (boresight, uptilted by 8°, and down tilted by 8°) and both TX and RX rotated 360° in azimuth by 8°/step which is the HPBW.

In the meantime, indoor ray tracing techniques will be used to assist the measurements and will produce more simulations together with the measurements to provide an accurate stochastic indoor channel model across different frequencies and various bandwidths.

Measured environment types were categorized according to the following definitions for each unique antenna direction (both TX and RX) in both the azimuth and elevation planes.

1. **Line-of-Sight Boresight (LOS_B):** when both the TX and RX antennas are pointing directly towards each other on boresight and aligned in both the azimuth and elevation planes with no obstructions between the antennas.

2. **Line-of-Sight Non-Boresight (LOS_NB):** when the TX and RX antennas have no obstructions between them, but the antennas are not pointed directly towards each other in either the azimuth or elevation plane, or both, commonly known as *off-boresight*.

3. **Non-Line-of-Sight (NLOS):** when the TX and RX antennas are in an environment with obstructions between each other, with no clear optical path between the two.

3.2 Measurement Procedures

Channel sounder calibration is crucial for reliable measurements and the interpretation of the measurement data. Before each set of measurements, the two Rubidium clocks at both the TX and RX were connected for more than 4 hours to synchronize the system, and the channel sounding system was running for more than half an hour to warm up.

A calibration routine was performed at the start and end of each measurement day, which determined the linear range and gain of the RX system and ensured the system gain did not fluctuate (within 1 dB). The calibration routine was performed at a T-R separation distance of 4 meters in a LOS environment (free space, Fraunhofer far-field regions) with vertically-polarized TX and RX antennas (1.5 m high from the ground) perfectly boresight aligned to each other. During the calibration routine, a power delay profile (PDP) was acquired for different attenuator settings ranging from 0 to 90 dB in steps of 10 dB. Therefore, 10 PDPs were acquired and the measured received power in the LOS component (the first arrived multi-path component) was plotted against the corresponding variable attenuator settings to find the linear range and RX system gain of the channel sounder. The linear region was determined by finding the slope most close to -1, using line fitting across different attenuation ranges. With the linear equation determined by the linear region, the RX system gain was easily recovered by taking the difference between the theoretical free space received power at the calibration distance and the intercept of the linear fit.

It should be noted that the RX system gain included gains from the amplifiers and processing gain induced by the sliding correlator operation [74]. The noise floor was obtained by taking the mean of the last 5000 samples from each PDP and setting a threshold of 5 dB above the mean noise floor such that all signal components recorded to have at least a 5 dB SNR (valid signal samples). All the samples of a PDP below the threshold were manually given a low value of -200 dBm which effectively means setting them to 0 power. For the cross-polarization measurements (V-H), a 90°waveguide twist was used to change the polarization of the RX antenna from vertical, to horizontal.

For each TX-RX location combination, 16 measurements were measured for various TX and RX antenna elevation angle combinations and both co-polarization and cross-polarization. Measurements 1 through 8 correspond to co-polarized configuration (V-V), whereas Measurements 9 through 16 correspond to cross-polarized configuration (V-H). The TX antenna angle is set to be 0° when pointing to the true north, and it can rotate from 0 to 360° (correspond to clockwise) in the azimuth plane. For each RX location, the TX and RX were pointed directly towards each other for the initial azimuth and elevation angle setup (recorded as Measurement 1, Rotation (Rot) 0), and then the TX or RX antenna swept in the azimuth plane in 8° step increments which is the HPBW of the antenna. A PDP was recorded at each step (named by a specific rotation number), and 45 PDPs were recorded for one measurement to cover the entire 360° azimuth plane. In NLOS environments, the TX and RX antennas were also pointed directly toward each other in the azimuth plane for the initial angle positions, regardless of the obstructions between the two. The measurement procedures are described below:

1. **Measurement 1 (RX sweep):** The TX and RX antennas were pointed directly towards each other on boresight in both the azimuth and elevation planes (for LOS or NLOS environments). The RX antenna was then swept in the azimuth plane in steps of 8°, while the TX antenna was fixed at the boresight azimuth and elevation angles.

2. **Measurement 2 (RX sweep):** With respect to the boresight angle in elevation, the RX antenna was uptilted by 8° and then swept in the azimuth plane in steps of 8°, for a fixed TX antenna at the boresight azimuth and elevation angles.

3. **Measurement 3 (RX sweep):** With respect to the boresight angle in elevation, the RX antenna was downtilted by 8° and then swept in the azimuth plane in steps of 8°, for a fixed TX antenna at the boresight azimuth and elevation angles.

4. **Measurement 4 (RX sweep):** With respect to the boresight angle in elevation, the TX antenna was uptilted by 8°. The RX antenna was fixed at the boresight elevation angle and then swept in the azimuth plane in steps of 8°.

5. **Measurement 5 (RX sweep):** With respect to the boresight angle in elevation, the TX antenna was downtilted by 8°. The RX antenna was fixed at the boresight elevation angle and then swept in the azimuth plane in steps of 8°.

6. **Measurement 6 (TX sweep):** The TX and RX antennas were pointed directly towards each other on boresight in both the azimuth and elevation planes. The TX antenna was then swept in the azimuth plane in steps of 8°, for a fixed RX antenna at the boresight azimuth and elevation angles.

7. **Measurement 7 (RX sweep):** This measurement was an RX sweep with the TX antenna set to the second strongest AOD in the azimuth and elevation planes. The second strongest AOD was determined by comparing the power level from all the AODs during Measurement 6, except for the angles corresponding to the main angle of arrival. The RX antenna was fixed at the boresight elevation angle and then swept in steps of 8° in the azimuth plane.

8. **Measurement 8 (TX sweep):** This measurement was a TX sweep with TX antenna either uptilted or downtilted by 8° after determining the elevation plane with the strongest received power from Measurement 4 and Measurement 5 during field measurements. The RX antenna was pointed towards the initial boresight azimuth and elevation angles, and the TX was uptilted or downtilted by 8°, and then swept in steps of 8° in the azimuth plane.

When recording the PDPs, several steps need to be followed to make sure all the information is accurate and recorded/named properly, which is important for post processing. First, the measurement number needs to be changed which should agree with the number in the measurement log sheet. Then, the RX elevation needs to be changed to the aimed value according to the setup. After

Table 3.1: Specifications for TX1 and the corresponding RX locations.

TX	RX	T-R Distance (m)	TX Azi. (°)	TX Ele. (°)	RX Azi. (°)	RX Ele. (°)	Env.
TX1	1	6.48	180	-9	0	9	LOS
	2	7.86	216	-6	38	11	NLOS
	3	10.15	231	-6	51	5	NLOS
	4	7.96	270	-6	90	7	LOS
	5	11.94	238	-4	60	5	NLOS
	6	14.43	234	-3	58	4	NLOS
	7	12.94	269	-3	90	5	LOS

resetting the bad PDPs (the power in the PDPs is not in the linear range determined in the calibration), change the sweep direction and check if the recording TX azimuth and elevation angle agree with the field measurements. If all these information and settings are correct, the channel sounder can automatically sweep and record the measurement data. Finally, check if there is any bad PDP (adjust the attenuation at the RX to make the received power in the linear range of the channel sounder), and record the last one.

3.3 Measurement Locations and Environment Descriptions

3.3.1 TX1 and the Corresponding RX Locations

The first TX location (TX1) was placed in the center of an open area office space as shown in Figure 3.2. Seven RX locations (RX1 to RX7) were identified with T-R separation distance ranging from 6.4 m to 15 m with RX1, 4, and 7 to be LOS. For the NLOS locations (RX2, 3, 5, and 6) there were various combinations of offices partitions and walls between the TX and RX. The cubicle partition heights were 1.7 m relative to the floor, which was slightly higher than the RX height.

The T-R separation distances, initial TX and RX antenna azimuth and elevation pointing angles, and environments for both co-polarized and cross-polarized antenna configurations are listed in Table 3.1.

3.3.2 TX2 and the Corresponding RX Locations

The second TX location (TX2) was located in the center of a lobby outside of two classrooms and at one end of a long corridor, as shown in Figure 3.2. There was one RX location (RX10) in the LOS environment, and 6 RX locations in the NLOS environment with 2 of them (RX13 and RX14) were outage, with a link range of 4.12 m to 39.21 m. The blockage materials include drywall outside

Table 3.2: Specifications for TX2 and the corresponding RX locations.

TX	RX	T-R Distance (m)	TX Azi. (°)	TX Ele. (°)	RX Azi. (°)	RX Ele. (°)	Env.
TX2	10	4.12	90	-14	270	14	LOS
	11	9.06	103	-6	282	6	NLOS
	12	28.52	93	-2	277	2	NLOS
	13	29.22	104	-2	284	2	Outage
	14	30.4	111	-2	291	2	Outage
	15	39.21	99	-1	286	1	NLOS
	21	8.42	90	-6	266	6	NLOS

Table 3.3: Specifications for TX3 and the corresponding RX locations with the initial TX and RX antenna pointing angles in both azimuth and elevation planes.

TX	RX	T-R Distance (m)	TX Azi. (°)	TX Ele. (°)	RX Azi. (°)	RX Ele. (°)	Env.
TX3	16	5.30	156	-10	335	10	NLOS

the classrooms and along with the corridor, glass doors, and plastic boards. The RX locations were chosen with various combinations of partitions to study the loss caused by multiple obstructions and reflections for NLOS indoor environments.

The T-R separation distances, initial TX and RX antenna azimuth and elevation pointing angles, and environments for both co-polarized and cross-polarized antenna configurations are listed in Table 3.2

3.3.3 TX3 and the Corresponding RX Locations

The third TX location (TX3) was located in the center of a corridor outside of an office, as shown in Figure 3.2. There was only one RX location (RX16) in the NLOS environment with a T-R separation distance of 5.3 m. The blockage materials include drywall, glass doors, and glass windows.

3.3.4 TX4 and the Corresponding RX Locations

The fourth TX location (TX4) was located in the center of a corridor close to the glass-door entrance of the 9th floor of 2 MTC, as shown in Figure 3.2. There were three RX locations (RX11, 12, 28) in the LOS environment with T-R separation distances of 12.7, 7.1, and 21.3 m, respectively. The blockage materials include drywall, plastic boards, glass doors, and metal plate (the display

Table 3.4: Specifications for TX4 and the corresponding RX locations with the initial TX and RX antenna pointing angles in both azimuth and elevation planes.

TX	RX	T-R Distance (m)	TX Azi. (°)	TX Ele. (°)	RX Azi. (°)	RX Ele. (°)	Env.
TX4	11	12.70	269	-4	89	4	LOS
	12	7.10	89	-7	270	7	LOS
	28	21.30	270	-2	90	2	LOS

Table 3.5: Specifications for TX5 and the corresponding RX locations.

TX	RX	T-R Distance (m)	TX Azi. (°)	TX Ele. (°)	RX Azi. (°)	RX Ele. (°)	Env.
TX5	28	15.63	105	-4	285	4	NLOS
	31	13.94	137	-5	320	4	NLOS
	32	31.22	90	-2	270	2	NLOS
	321	31.22	90	-2	270	2	NLOS
	322	31.22	90	-2	270	2	LOS
	33	9.15	198	-7	15	8	NLOS
	331	9.15	198	-7	15	8	NLOS

board of NYU industry affiliates).

3.3.5 TX5 and the Corresponding RX Locations

The third TX location (TX5) was located in a classroom adjacent to the long corridor. There were 4 RX locations chosen but with 7 different link situations, where the link distances were from 9.15 m to 31.22 m. As shown in Figure 3.2, RX32, RX321, and RX322 shared the same location but RX32 was with two glass doors closed (NLOS), RX321 was with one glass door open and the other closed (NLOS), and RX322 was with two glass doors open (LOS). RX33 and RX331 shared the same location as seen in Figure 3.2, but RX33 was with the metal door closed and RX331 was with the metal door open. However, RX33 and RX331 were both in NLOS of TX5, since there was one drywall of the classroom between the link. The environmental obstructions include drywall, glass doors, and metal doors.

The T-R separation distances, initial TX and RX antenna azimuth and elevation pointing angles, and environments for both co-polarized and cross-polarized antenna configurations are listed in Table 3.5

3.4 Path Loss Models at 142 GHz

Radio propagation in mmWave and THz bands is range limited due to the severe path loss in the first meter and the limited output power of amplifiers, which are compensated by using directional antennas/arrays [1, 32]. The measured path loss in this work is calculated by:

$$PL\ [\text{dB}] = P_t + G_t + G_r - P_r + G_{sym}, \tag{3.1}$$

where P_t is the output power fed into the TX antenna in dBm, G_t and G_r are TX and RX antennas gains in dBi, respectively, P_r is the measured received power in dBm, and G_{sym} is the processing gain of the channel sounder system in dB.

There are three basic types of large-scale path loss models to predict mmWave signal strength over distance for the vast mmWave frequency range (with antenna gains included in the link budget and not in the slope of path loss as shown in Eq. (3.9) of [38], also see p.3040 in [145]). These include the close-in (CI) free space reference distance model (with a 1 m reference distance) [44, 145, 146, 147], the CI model with a frequency-weighted or height weighted path loss exponent (CIF and CIH models) [83, 148, 149], and the floating intercept (FI) path loss model, also known as the ABG model because of its use of three parameters α, β, and γ [83, 145, 148, 150, 151, 152].

The CI path loss model accounts for the frequency dependency of path loss by using a close-in reference distance based on Friis' law as given by [44, 83, 149, 153]:

$$PL^{CI}(f_c, d_{3D})\ [\text{dB}] = \text{FSPL}(f_c, 1\text{ m}) + 10n\log_{10}(d_{3D}) + \chi_\sigma^{CI} \tag{3.2}$$

where χ_σ^{CI} is the shadow fading (SF) that is modeled as a zero-mean Gaussian random variable with a standard deviation in dB, n is the path loss exponent (PLE) found by minimizing the error of the measured data to (4.1), $d_{3D} > 1m$, FSPL(f, 1 m) is the free space path loss (FSPL) at frequency f_c in GHz at 1 m and is calculated by [30]:

$$\text{FSPL}(f_c, 1\text{ m}) = 20\log_{10}\left(\frac{4\pi f_c \times 10^9}{c}\right) = 32.4 + 20\log_{10}(f_c)\ [\text{dB}] \tag{3.3}$$

where c is the speed of light, 3×10^8 m/s. The standard deviation σ yields insight into the statistical variation about the distant-dependent mean path loss [38].

The CI model ties path loss at any frequency to the physical free space path loss at 1 m according to Friis' free space equation [30], and has been shown to be robust and accurate in various scenarios [44, 149, 154]. Indoor environments, however, were found to have frequency-dependent loss beyond the first meter, due to the surrounding environment, and work in [155] extended the CI model to the CIF model where the PLE has a frequency-dependent term.

The close-in free space reference distance with frequency weighting (CIF) path loss model is a multi-frequency model presented in [44, 155], which is an extension of the CI model with a frequency

dependent term:

$$PL^{CIF}(f_c, d)\ [\text{dB}] = 32.4 + 20\log_{10}(f_c) + 10n\left(1 + b\left(\frac{f_c - f_0}{f_0}\right)\right)\log_{10}(d) + \chi_\sigma^{CIF} \tag{3.4}$$

The FI/ABG path loss model is given as:

$$PL^{ABG}(f_c, d)\ [\text{dB}] = 10\alpha\log_{10}(d) + \beta + 10\gamma\log_{10}(f_c) + \chi_\sigma^{ABG} \tag{3.5}$$

where three model parameters α, β and γ are determined by finding the best fit values to minimize the error between the model and the measured data. In (3.5), α indicates the slope of path loss with log distance, β is the floating offset value in dB, and γ models the frequency dependence of path loss, where f_c is in GHz.

The CI path loss model is one of the most commonly used large-scale path loss model to predict the mmWave signal strength over distance for multi-frequency bands. Directional path loss models are useful for future 5G and 6G communication systems with directional antennas or antenna arrays for beam steering and beam combining techniques [141].

Figure 3.3 shows the directional path loss scatter plots and the best fit directional CI path loss model (4.1) at 140 GHz for both LOS and NLOS environments. The LOS path loss exponent (PLE) is 1.7 at 28 GHz, 1.6 at 73 GHz, and is 1.99 at 142 GHz, as presented in Table 4.2, showing that there is a bit more loss at 142 GHz likely due to atmospheric attenuation [1]. The NLOS Best (the situation where the RX is pointing to the direction with maximum received power) PLEs and NLOS PLEs are similar over all three frequencies, respectively, with NLOS Best at 142 GHz having slightly less loss than the lower frequencies, likely due to greater reflected power as frequencies increases.

Table 3.6: Indoor Directional CI path loss model at 28, 73, and 142 GHz for both LOS and NLOS environment [141, 156].

Env.	28 GHz [141]		73 GHz [141]		142 GHz	
	n (dB)	σ (dB)	n (dB)	σ (dB)	n (dB)	σ (dB)
LOS	1.7	2.5	1.6	3.2	1.99	2.7
NLOS_{Best}	3.0	10.8	3.4	11.8	3.0	6.9
NLOS	4.4	11.6	5.3	15.7	4.7	14.1

The omnidirectional Indoor-Office path loss models used for frequencies below 100 GHz in 3GPP TR 38.901 Release 15 [157] are shown in Table. 3.7. Figure 3.4 shows the 3GPP omni-directional Indoor-Office path loss model at 142 GHz (even though 142 GHz is out of the application range), the NYU best-fit omni-directional CI path loss model at 142 GHz, and the scatter plot of synthesized omni-directional measured path loss at 142 GHz. It is worth noting that in the NLOS case, there are

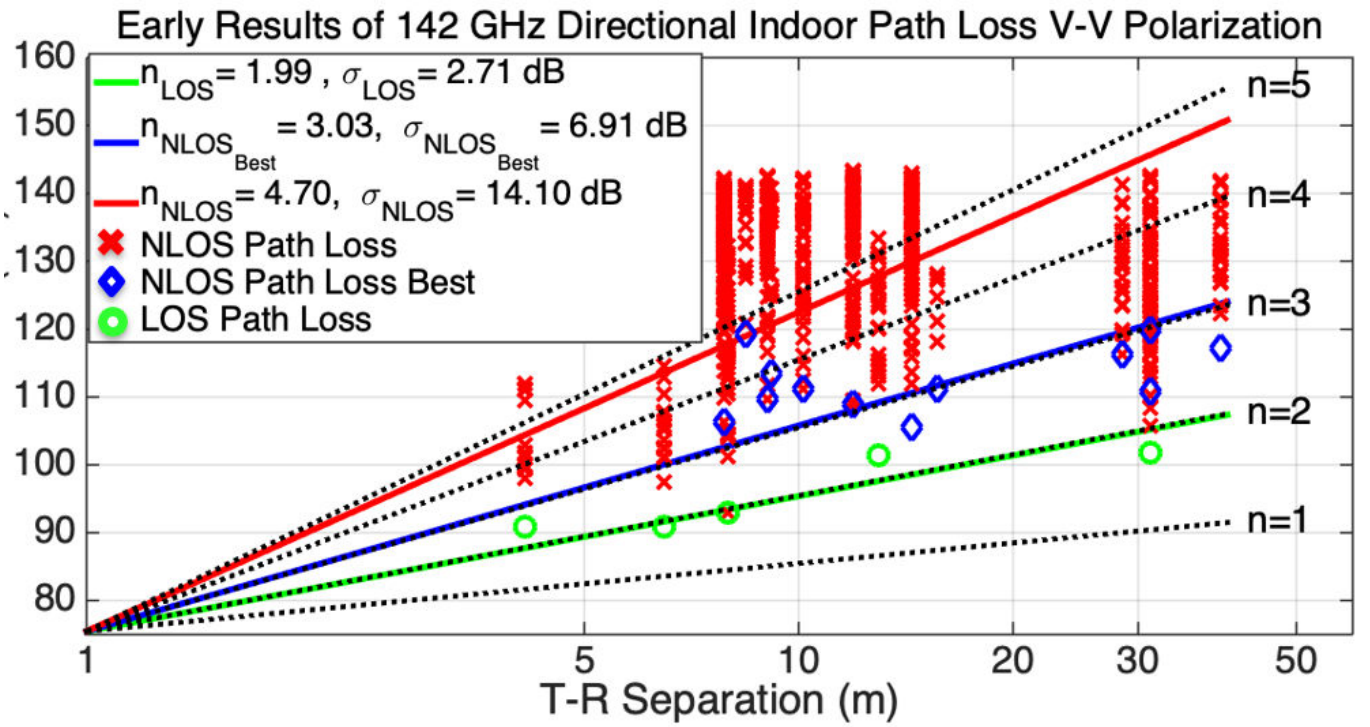

Figure 3.3: 142 GHz directional path loss scatter plot and indoor directional CI ($d_0 = 1$ m) path loss model for both LOS and NLOS scenarios. Each green circle represents LOS path loss values, red crosses represent NLOS path loss values measured at arbitrary antenna pointing angles between the TX and RX, and blue diamonds represent angles with the lowest path loss measured for each NLOS TX-RX location combination.

two kinds of path loss models, the NLOS ABG path loss model, and NLOS CI path loss model, in the 3GPP document [157], as shown as the magenta and red dashed lines in Figure 3.4, respectively.

In Figure 3.4, the LOS PLEs of the omni-directional 3GPP path loss model [157] and the omni-directional NYU best fit CI path loss model [141] are 1.75 and 1.73, respectively, and with standard deviations of 2.88 dB and 2.9 dB, respectively. Both models agree with each other and fit well with the measured data, which shows the 3GPP omni-directional path loss model can still work at frequencies above 100 GHz in LOS environments, and LOS path loss at frequencies above 100 GHz is not much different from frequencies below 100 GHz, except for a constant path loss gap due to the difference of frequencies [75], see Figure 2.5. In the NLOS case, the PLEs of the omni-directional ABG and CI path loss models are 3.83 and 3.19, respectively, and the PLE of the omni-directional NYU best-fit CI path loss model is 2.69, which is a slightly lower (less path loss than expected), possibly due to the less reflection loss at higher frequencies [66]. Corrections should be made in the 3GPP omni-directional path loss models in the NLOS case for frequencies above 100 GHz. Figure 3.4 shows that signals at 140 GHz could be used for indoor wireless communications and the coverage is better than expected.

The indoor directional LOS PLE for the best-fit CI path loss model is $n = 1.90$ at 28 GHz, $n = 1.63$ at 73 GHz, and is $n = 2.05$ at 142 GHz with a shadow fading standard deviation of $\sigma = 3.38$ dB, 3.06 dB, and 2.89 dB, respectively, as presented in Table 4.2. These values all are close to the theoretical free space PLE value of 2.0, with lower mmWave frequencies experiencing waveguiding

Table 3.7: 3GPP TR 38.901 omni-directional path loss models in Indoor-Office scenarios [158].

3GPP TR 38.901 V15.0.0 [157]			
Env.	**PL [dB], f_c is in GHz, d is in meters**	**Shadow fading std [dB]**	**Applicability range and Parameters**
LOS	$PL_{InH-LOS} = 32.4 + 17.3\log_{10}(d_{3D}) + 20\log_{10}(f_c)$	$\sigma_{SF} = 3.0$	$0.5 < f_c < 100$ GHz $1 \leq d_{3D} \leq 150$ m
NLOS	$PL = \max\left(PL_{InH-LOS}(d_{3D}), PL_{InH-NLOS}(d_{3D})\right)$ $PL_{InH-NLOS} = 17.30 + 38.3\log_{10}(d_{3D}) + 24.9\log_{10}(f_c)$	$\sigma_{SF} = 8.03$	$0.5 < f_c < 100$ GHz $1 < d_{3D} < 150$ m
	Option: CI model with 1 m reference distance		
	$PL = 32.4 + 20\log_{10}(f_c) + 31.9\log_{10}(d_{3D})$	$\sigma_{SF} = 8.29$	$1 \leq d_{3D} \leq 150$ m

Table 3.8: Directional InH-Office channel parameters of CI and CIF path loss models, RMS delay spread, the number of clusters, and the number of MPCs per cluster in both LOS and NLOS environments at 28, 73, and 142 GHz [44, 45, 92, 135, 141, 145].

Environment type		**LOS**			**NLOS$_{\text{Best}}$**			**NLOS**		
Frequency [GHz]		**28**	**73**	**142**	**28**	**73**	**142**	**28**	**73**	**142**
Dir. Ant. HPBW		30°	15°	8°	30°	15°	8°	30°	15°	8°
Single-Band PL CI [44, 45, 141]	n	1.9	1.6	2.1	2.8	3.3	3.2	4.4	5.5	4.6
	σ^{CI} [dB]	3.4	3.1	2.9	7.0	8.8	6.0	7.3	8.9	13.8
Multi-Band PL CI [44, 45, 141]	n	1.86			3.07			5.02		
	σ^{CI} [dB]	3.45			7.67			13.97		
Multi-Band PL CIF [44, 45, 141]	$[n, b]$	$[1.86, 0.07]$			$[3.07, 0.05]$			$[5.02, 0.03]$		
	σ^{CIF} [dB]	3.45			7.67			13.85		
RMS DS [141, 145]	$\min_{DS}$ [ns]	0.9	0.8	0.7	0.9	3.7	0.6	0.6	0.5	0.3
	$\max_{DS}$ [ns]	5.5	5.3	11.9	44.5	31.4	10.8	198.6	142.0	92.5
	μ_{DS} [ns]	3.9	3.5	2.7	10.2	7.4	5.7	17.6	12.5	8.9
NumCluster [92]	μ_{NC}	1.4	1.3	1.3	1.7	1.5	1.2	3.4	2.6	2.4
	σ_{NC}	0.9	1.0	0.9	0.8	0.9	0.7	2.0	1.7	1.5
NumMPCperCluster [92]	μ_{MPC}	2.5	2.5	2.1	2.6	2.4	2.0	3.2	2.8	1.2
	σ_{MPC}	2.2	2.3	1.4	1.5	2.2	2.3	4.6	5.2	2.2

effects and a PLE less than 2.0. This hints at the fact that higher sub-THz frequencies have fewer reflections in LOS directional channels (e.g., less waveguiding) due to narrower beam antennas at both ends of the link that attenuate energy toward the reflecting surfaces of walls, ceiling, and floor. The LOS measurements show that there is 2-4 dB more average loss at 10 m and 3-7 dB more average

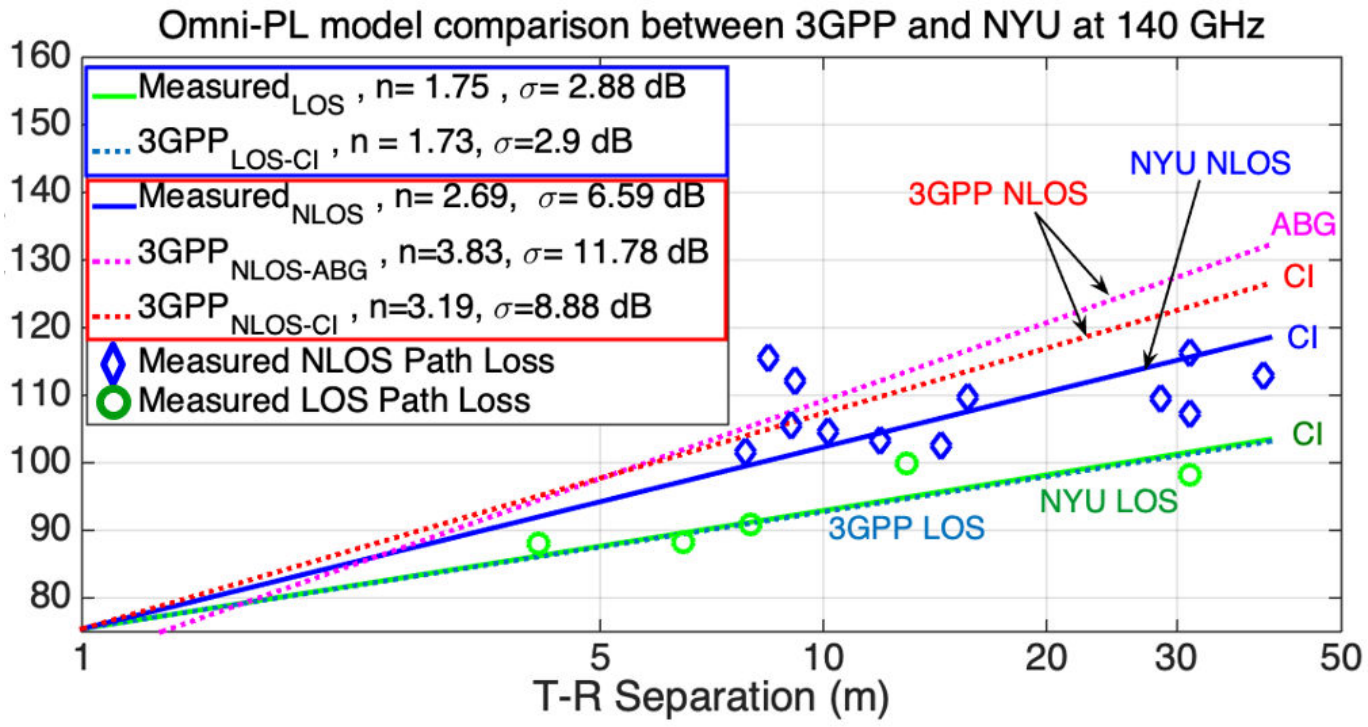

Figure 3.4: Comparison between 3GPP TR 38.901 [157] path loss models (currently valid for frequencies below 100 GHz) vs. the NYU best fit omni-directional CI path loss model at 142 GHz.

loss at 40 m at 142 GHz compared to the average loss at 28 and 73 GHz when referenced to a one meter free space reference distance [1, 44, 159].

The $\text{NLOS}_{\text{Best}}$ is defined as the best pointing direction of both the TX and RX antennas for which the maximum power is received at the RX at each of the NLOS measurement locations. The best-fit $\text{NLOS}_{\text{Best}}$ PLEs are $n = 2.75$, 3.30, and 3.21 at 28, 73, and 142 GHz, respectively, with shadow fading standard deviations of $\sigma = 7.00$, 8.76, and 6.03 dB, respectively, showing that the indoor $\text{NLOS}_{\text{Best}}$ channels at 73 and 142 GHz are more lossy (higher PLEs) than the channels at 28 GHz.

Two transmission properties, reflections and penetrations, appear to cause the slight difference of the NLOS PLEs at 28 and 142 GHz [1, 66], since it is known that as frequencies increase, there is less transmissivity through reflecting objects and more power is reflected (i.e., greater power in the reflection direction but less penetrated power is observed at 142 GHz compared to 28 and 73 GHz)[66, 130]. However, the surfaces are relatively rough at higher frequencies, and indoor reflection and scattering measurements at 28, 73, and 142 GHz show that the scattered power is negligible (more than 20 dB less) compared to the signal power in the reflection direction for most indoor materials (e.g., drywall and clear glass) [66, 130].

Omnidirectional path loss models were developed from the directional measurements by synthesizing omnidirectional antenna patterns, received power, and path loss from directional antennas [145, 160]. The LOS omnidirectional PLE at 142 GHz is 1.74 with a shadow fading standard deviation of 3.62 dB, which, as expected, is less than the LOS directional PLE of 2.05 at the same 142 GHz due to the capture of energy over the entire horizon using an omnidirectional pattern [145, 160].

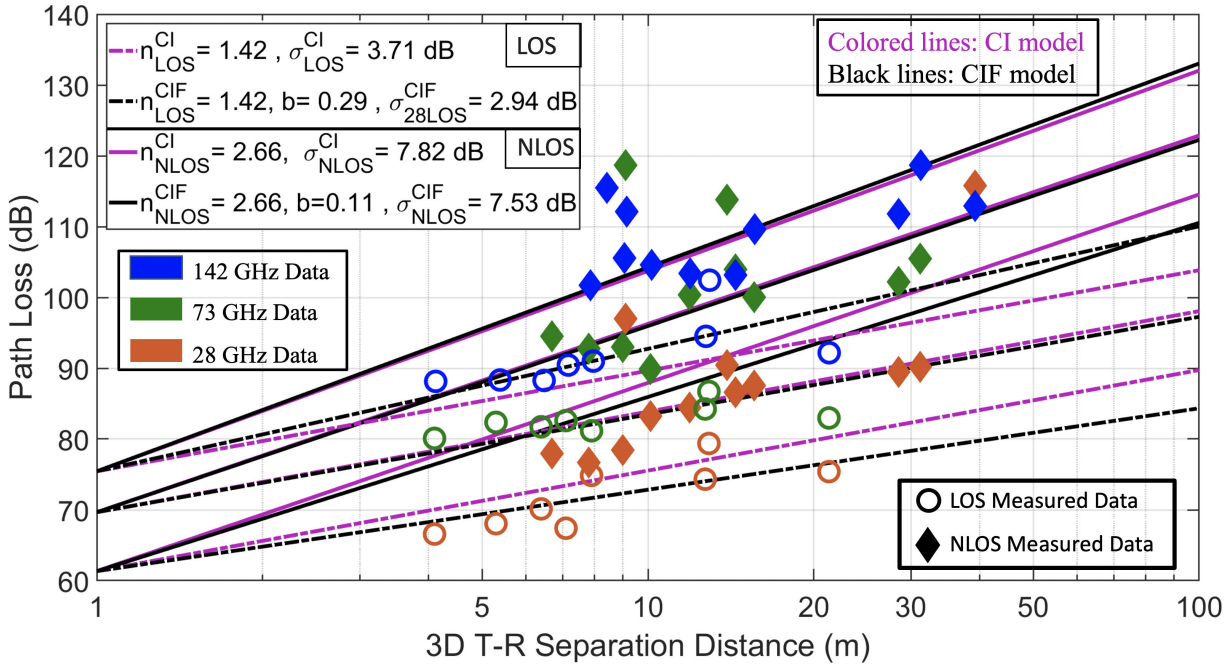

Figure 3.5: InH-Office 28, 73, and 142 GHz multi-band omnidirectional CI and CIF path loss models for both LOS and NLOS scenarios with antenna gains removed and with respect to a 1 m free space reference [44, 45, 141]. The diamonds and circles represent measured omnidirectional path loss in NLOS and LOS locations, respectively [66, 92, 141]. The fixed reference frequency f_0 for the CIF path loss model is 81 GHz for both LOS and NLOS conditions. Results here and Table 4.4 show the 142 GHz band is lossier in NLOS conditions, with the CI and CIF models being remarkably similar [44, 141].

The LOS omnidirectional channel offers 3.1 dB less average loss at 10 m and 5.0 dB less average loss at 40 m than the LOS directional channel at 142 GHz (with antenna gains removed). However, in practice, omnidirectional antennas cover a shorter link range due to the lower antenna gain. The NLOS omnidirectional PLE at 142 GHz is 2.83 with a shadow fading standard deviation of 6.07 dB which is a much lossier channel than LOS, yet offers better link coverage than the $\text{NLOS}_{\text{Best}}$ PLE of 3.21 and the arbitrary directional NLOS PLE of 4.60 at 142 GHz as shown in Tables 4.2 and 4.4. The higher PLE in NLOS at higher frequencies suggests accurate beamforming algorithms will be needed to find, capture, and combine the most dominant multipath energy to maintain indoor NLOS communication links above 100 GHz [1, 134, 159].

The omnidirectional PLE and shadowing parameters of the CI path loss model with 1 m free space reference distance for both LOS and NLOS over each of the three bands and for all bands combined are summarized in Table 4.4. The indoor omnidirectional LOS PLEs and shadow fading standard deviations (n, σ) are (1.17, 2.72 dB), (1.36, 2.30 dB), and (1.74, 3.62 dB) at 28, 73, and 142 GHz bands, respectively, and the higher LOS PLE at 142 GHz indicates that the MPCs undergo penetration, reflection, and absorption with more loss at 142 GHz than at 28 and 73 GHz [38, 66]. In the NLOS omnidirectional case, the PLEs and shadow fading standard deviations (n, σ) are (2.37, 7.22 dB), (2.81, 8.71 dB), and (2.83, 6.07 dB) at 28, 73, and 142 GHz, respectively, showing that 28 GHz is less lossy than both 73 and 142 GHz, with the two higher bands behaving very similarly, except for the first meter loss.

The CI model with a frequency-weighted PLE (CIF) path loss model [44, 141] was proposed as a viable multi-band model for indoor path loss and can be considered as an extension of the CI path loss model to offer an extra degree of freedom for more accurate statistical modeling over a wide range of frequencies:

$$PL^{CIF}(f_c, d_{3D})\ [\text{dB}] = \text{FSPL}(f_c, 1\ \text{m}) + 10n\left(1 + b\left(\frac{f - f_0}{f_0}\right)\right)\log_{10}\left(\frac{d}{1\ \text{m}}\right) + \chi_\sigma^{CIF}, \tag{3.6}$$

where n is the PLE at the weighted frequency average f_0 of all measurements for each specific environments, b is a model fitting parameter that presents the slope of linear frequency dependency of path loss, and $n\,(1 + b(f - f_0)/f_0)$ represents the frequency-dependent PLE at frequency f. The weighted average frequency f_0 is computed over K frequency bands as $f_0 = \sum_{k=1}^{K} f_k N_k / \sum_{k=1}^{K} N_k$, where N_k is the number of measurements at a particular frequency f [44, 141].

In this chapter, we used the data to calculate $f_0 = 81$ GHz for both LOS and NLOS scenarios. In LOS omnidirectional scenarios, $n_{LOS}^{CIF} = 1.42$ and $b_{LOS}^{CIF} = 0.29$ are the best-fit parameters of the omnidirectional CIF path loss model with a shadow fading standard deviation of $\sigma_{LOS}^{CIF} = 2.94$ dB, as shown in Table 4.4, when applied to all measurements across 28, 73, and 142 GHz. In NLOS omnidirectional scenarios, $n_{NLOS}^{CIF} = 2.66$ and $b_{NLOS}^{CIF} = 0.11$ are the best-fit parameters of the omnidirectional CIF path loss model with a shadow fading standard deviation of $\sigma_{NLOS}^{CIF} = 7.53$ dB.

Note that the CI path loss model (4.1) can also be used as a multi-band path loss model, using only a single parameter PLE [44, 45, 141]. Figure 4.17 shows the indoor office 28, 73, and 142 GHz multi-band omnidirectional CI and CIF path loss models for both LOS and NLOS scenarios with antenna gains removed at both ends of the link and with respect to a 1 m free space reference. CI and CIF path loss models show remarkable similarity in terms of path loss exponents over 28, 73, and 142 GHz bands, when referenced to the first meter free space reference distance [44, 45, 141], implying the extra parameter in the CIF model may not be necessary over wide frequency bands. This illuminates the fact that an identical PLE may accurately model path loss over a vast range of frequencies, with the only frequency-dependent effect being *the path loss in the first meter of propagation as energy spreads into the far field* [32, 44, 45, 141].

3.5 Multipath Statistics at 28, 73, and 142 GHz

The indoor wireless channel statistics at 28, 73, and 142 GHz bands are summarized in Tables 4.2 and 4.4 for directional and omnidirectional channels, respectively. The spatial statistical channel modeling approach introduced in [92] is used here. The large-scale path loss, shadow fading, root mean square delay spread (RMS DS), the number of time clusters, as well as the number of MPCs per cluster were evaluated from the measured data.

Table 3.9: Omnidirectional InH-Office channel parameters of CI and CIF path loss models, RMS delay spread, the number of clusters, and the number of MPCs per cluster at 28, 73, and 142 GHz [44, 45, 92, 135, 141, 145].

Environment type		**InH-Office LOS**			**InH-Office NLOS**		
Frequency [GHz]		**28**	**73**	**142**	**28**	**73**	**142**
Single-Band Path Loss CI [44, 45, 141]	n	1.17	1.36	1.74	2.37	2.81	2.83
	σ^{CI} [dB]	2.72	2.30	3.62	7.22	8.71	6.07
Multi-Band Path Loss CI [44, 45, 141]	n	1.42			2.66		
	σ^{CI} [dB]	3.71			7.82		
Multi-Band Path Loss CIF [44, 45, 141]	n, b	$n = 1.42, b = 0.29$			$n = 2.66, b = 0.11$		
	σ^{CIF} [dB]	2.94			7.53		
RMS Delay Spread [141, 145]	$\min_{DS}$ [ns]	0.70	0.60	0.71	0.60	0.50	0.60
	$\max_{DS}$ [ns]	134.40	101.90	11.94	198.50	142.00	60.87
	μ_{DS} [ns]	10.80	6.24	3.00	17.10	12.30	9.20
NumCluster [92]	μ_{NC}	4.60	2.76	1.90	5.40	3.20	2.80
	σ_{NC}	1.94	2.32	1.30	1.96	1.70	1.65
NumMPCperCluster [92]	μ_{MPC}	4.70	3.43	2.40	6.40	3.20	2.20
	σ_{MPC}	3.65	2.86	2.20	4.58	5.20	2.47

3.5.1 RMS Delay Spread

RMS Delay spread characterizes the multipath richness, time dispersion, and coherence bandwidth of a radio propagation channel, depending on the signal's bandwidth [38, 78]. A 5 dB SNR threshold relative to the mean thermal noise floor of a raw PDP was used for detecting and keeping the MPCs in each PDP [145]. The number of MPCs are computed by peak tracking algorithms as illustrated in [92] that one peak in a PDP is counted as a valid MPC if the time delay between its next adjacent peak (above the 5 dB SNR threshold) is larger than the channel sounder time resolution (the inverse of the channel bandwidth).

The minimum, maximum, and mean of RMS delay spread values from measurements in an identical indoor office setting at 28, 73, and 142 GHz are presented in Table 4.2 and 4.4 for both directional and omnidirectional indoor channels, respectively, in both LOS and NLOS scenarios [145].

As shown in Table 4.2, there is negligible RMS DS in LOS directional scenarios with a mean of 3-4 ns, which is close to the width of the channel sounder's probing signal across these three frequency bands when directional antennas are used to line up antenna boresights (our probe had a 3 dB power width of 2.5 ns at 28 and 73 GHz and 2 ns at 142 GHz as shown in Table 4.1). The excess delays of the multipath components reflected from the walls, ceiling, and floor would be within (and cause a spread of) the original pulse width.

In $\text{NLOS}_{\text{Best}}$ scenarios, the minimum RMS DS ($\min_{DS}$) is extremely small (e.g., 0.5 ns) and similar to the minimum RMS DS in LOS directional environments across 28, 73, and 142 GHz bands, however, the mean RMS DS (μ_{DS}) increases by a few ns (e.g., 3-6 ns) at all frequencies compared to LOS directional scenarios, and the maximum RMS DS ($\max_{DS}$) was observed to be 44 ns at 28 GHz, 31 ns at 73 GHz, and 11 ns at 142 GHz, with 90% of the RMS DS less than 40 ns, 25 ns, and 9 ns at 28, 73, and 142 GHz bands, respectively. The data clearly show maximum observable RMS DS is frequency dependent, with much less maximum delay spread at higher frequencies.

In NLOS directional scenarios where the directional antenna at the RX was arbitrarily pointed, the maximum delay spread was observed to be more than 90 ns with only 3%, 2%, and 1% of the RMS DS larger than 90 ns at 28, 73, and 142 GHz bands [92, 141], respectively. The mean RMS DS decreases as frequency increases with 18 ns at 28 GHz, 13 ns at 73 GHz, and 9 ns at 142 GHz, indicating that the time dispersion is smaller at higher frequencies, likely due to the narrower beam antennas used at higher frequencies that fail to capture all the multipath in the environment and miss reflected multipath from directions out of antenna pointing beam [92, 141, 145].

The omnidirectional RMS DS obtained from measurements for both the LOS and NLOS scenarios at 28, 73, and 142 GHz bands [92, 141] are presented in Table 4.4 and are compared with mean μ_{DS} and standard deviation σ_{DS} values from 3GPP TR 38.901 Release 16 (see Table 7.5-6 in [135]). Note that 3GPP does not specify the RMS DS for channels above 100 GHz.

In LOS omnidirectional scenarios, the mean RMS DS decreases with increasing frequency and is 11, 6, and 3 ns at 28, 73, and 142 GHz bands, respectively. By contrast, the mean RMS DS predicted by the 3GPP InH channel model is virtually identical at 28 and 73 GHz (20.40 ns and 20.21 ns,

respectively), however, in our work the measured mean RMS DS at 73 GHz decreases by 40% (about 5 ns lower) than the measured mean RMS DS at 28 GHz, and the mean RMS DS decreases by 50% further to a very small 3 ns at 142 GHz.

In NLOS omnidirectional scenarios, when compared to LOS omnidirectional channels, the mean RMS DS increases by 60%, 100%, and 200% at 28, 73, and 142 GHz, respectively, with mean values of 17, 12, and 9 ns at 28, 73, and 142 GHz bands, respectively, indicating a wider time spread of multipath energy that is frequency dependent in NLOS environments. The free space path loss in the first meter and partition losses are larger at higher frequencies, such that the signal power of MPCs with large time delays (longer propagation distances and are more likely to be blocked, and hence have weaker power) may be below the noise floor and not detected by the channel sounder RX [145]. This is one cause for why the RMS DS at 142 GHz is lower than the RMS DSs at 73 and 28 GHz.

In general, the RMS DS in NLOS locations is larger than LOS locations, since obstructions in NLOS locations block or severely attenuate the direct path, leading to larger RMS DSs [92, 141, 145].

3.5.2 The Numbers of Time Clusters and MPCs per Cluster

The numbers of time clusters and MPCs per cluster depends on the minimum inter-cluster time void interval (MTI), which is the minimum time interval between two separate time clusters [39, 92, 161]. There are fewer time clusters but more MPCs per cluster when the MTI is larger. An MTI of 6 ns [92] (determined by the width of corridors, 2 m) is used in this letter, based on the idea that the physical environment helps delineate the observed temporal cluster partitions of multipath energy arriving at a receiver [39, 161]. The number of time clusters follows a Poisson distribution at all three frequencies as shown in [92]. The omnidirectional mean numbers of time clusters are found to decrease with increasing frequency and are 4.60, 2.76, and 1.90 at 28, 73, and 142 GHz, respectively, in indoor LOS scenarios, and are 5.40, 3.20, and 2.80 at 28, 73, and 142 GHz in indoor NLOS scenarios, again showing the frequency dependent nature of multipath. The channels are more sparse in both LOS and NLOS omnidirectional scenarios at higher frequencies due to the larger partition loss (e.g., 4-8 dB higher loss at 142 GHz than 28 GHz for different materials [66]) which cause MPCs with longer propagation times and weaker power to fall below the noise floor. Using smart antennas to capture the most dominant multipath energy for beam combining to achieve range extension is needed as wireless moves into the THz regime [1, 45, 134, 159].

The number of MPCs per cluster follows a composite of a delta function $\delta(n-1)$ and a discrete exponential distribution at all three frequencies [92]. At 28 GHz, the mean number of MPCs per cluster in the NLOS omnidirectional scenarios is larger than in the LOS omnidirectional scenarios. However, there are fewer MPCs per cluster in the NLOS scenarios than in the LOS scenarios at 73 and 142 GHz, since the larger partition loss in NLOS scenarios makes the channels more sparse at higher frequencies [66, 92].

Step Index	Channel Parameters	28 - 73 GHz UMi [38]	28 - 140 GHz InO
Step 1	**# Time clusters** N	$N \sim \text{DU}(1, N_c)$	$N \sim \text{Poisson}(\lambda_c)$
Step 2	**# Cluster subpaths** M_n	$M_n \sim \text{DU}(1, M_s)$	$M_n \sim (1-\beta)\delta(M_n) + \text{DE}(\mu_s)$
Step 3	**Cluster delay** τ_n **(ns)**	$\tau_n'' \sim \text{Exp}(\mu_\tau)$ or $\text{Logn}(\mu_\tau, \sigma_\tau)$ $\Delta\tau_n = \text{sort}(\tau_n'') - \min(\tau_n'')$ $\tau_n = \begin{cases} 0 & , n = 1 \\ \tau_{n-1} + \rho_{M_{n-1},n-1} + \Delta\tau_n + \text{MTI} & , n = 2, ...N \end{cases}$	
Step 4	**Intra-cluster delay** $\rho_{m,n}$ **(ns)**	$\rho_{m,n} = \left[\frac{1}{B_{bb}} \times (m-1)\right]^{1+X_n}$, $m = 1, 2, ..., M_n,\ n = 1, 2, ..., N$	$\rho_{m,n} \sim \text{Exp}(\mu_\rho)$
Step 5	**Cluster power** P_n **(mW)**	$P_n' = \bar{P}_0 e^{-\frac{\tau_n}{\Gamma}} 10^{\frac{Z_n}{10}}$, $P_n = \frac{P_n'}{\sum_{k=1}^{N} P_k'} \times P_r[mW]$, $Z_n \sim \mathcal{N}(0, \sigma_Z),\ n = 1, 2, ..., N$	
Step 6	**Subpath power** $\Pi_{m,n}$**(mW)**	$\Pi_{m,n}' = \bar{\Pi}_0 e^{-\frac{\rho_{m,n}}{\gamma}} 10^{\frac{U_{m,n}}{10}}$, $\Pi_{m,n} = \frac{\Pi_{m,n}'}{\sum_{k=1}^{M_n} \Pi_{k,n}'} \times P_n[mW]$, $U_{m,n} \sim \mathcal{N}(0, \sigma_U),\ m = 1, 2, ..., M_n$	
Step 7	**Subpath phase** φ **(rad)**	Uniform(0, 2π)	
Step 8	**# Spatial lobes** L	$L_{\text{AOD}} \sim \min\{L_{\max}, \max\{1, \text{Poisson}(\mu_{\text{AOD}})\}\}$ $L_{\text{AOA}} \sim \min\{L_{\max}, \max\{1, \text{Poisson}(\mu_{\text{AOA}})\}\}$	$L_{\text{AOD}} \sim \text{DU}(1, L_{\text{AOD,max}})$ $L_{\text{AOA}} \sim \text{DU}(1, L_{\text{AOA,max}})$
Step 9	**Spatial lobe mean angle** ϕ_i, θ_i **(°)**	$\phi_i \sim U(\phi_{\min}, \phi_{\max}), \phi_{\min} = \frac{360(i-1)}{L}, \phi_{\max} = \frac{360i}{L}, i = 1, 2, ..., L$ $\theta_i \sim \mathcal{N}(\mu_l, \sigma_l)$	
Step 10	**Subpath angle offset** $\Delta\phi_i, \Delta\theta_i$ **w.r.t** ϕ_i, θ_i **(°)**	$i \sim \text{DU}[1, L_{\text{AOD}}], j \sim \text{DU}[1, L_{\text{AOA}}]$ $(\Delta\phi_i)_{m,n,\text{AOD}} \sim \mathcal{N}(0, \sigma_{\phi,\text{AOD}})$ $(\Delta\theta_i)_{m,n,\text{ZOD}} \sim \mathcal{N}(0, \sigma_{\theta,\text{ZOD}})$ $(\Delta\phi_j)_{m,n,\text{AOA}} \sim \mathcal{N}(0, \sigma_{\phi,\text{AOA}})$ $(\Delta\theta_j)_{m,n,\text{ZOA}} \sim \mathcal{N}(0, \sigma_{\theta,\text{ZOA}})$	

Figure 3.6: Statistical distributions of different channel models for 28-73 GHz outdoor UMi scenarios, and 28-140 GHz indoor scenarios [92].

3.5.3 Statistical Indoor Models at 28-142 GHz

As discussed before, temporal and spatial channel parameters are extracted from the measurements. Temporal parameters are the number of time clusters (TCs) (N) and subpaths within each TC (M_n), cluster excess delay (τ_n) and intra- cluster subpath excess delay ($\rho_{m,n}$), cluster power (P_n) and subpath power ($\Omega_{m,n}$) [92]. Spatial parameters are the number of spatial lobes (SLs) (L), the mean azimuth and elevation angle of an SL (ϕ and θ), and the azimuth and elevation angular offset of a subpath ($\delta\theta$ and $\delta\phi$) with respect to the mean angle of an SL [92]. The statistical distribution of each channel parameters are summarized in Figure 3.6 and the corresponding values for each channel parameter are presented in Figure 3.7 [92].

The number of TCs follows the Poisson distribution of a mean of N, and since the Poisson distribution starts from zero while the number of TCs starts from one, the number of TCs is $N + 1$ [92]. The number of cluster subpaths M_n a composite distribution with a δ-function at $M_n = 1$ and a discrete exponential (DE) distribution after that. The inter-cluster excess delay τ_n is defined as the time difference between the first arriving subpath in the PDP and the first arriving subpath in a cluster. Inter-cluster delays at 140 GHz can be well fitted using an exponential distribution for both

LOS and NLOS scenarios. The distributions for the 28 GHz and 140 GHz LOS scenarios are different (lognormal and exponential), likely due to the higher partition loss and the smaller measurable range at 140 GHz. The intra-cluster excess delay is defined as the time difference between the first arriving subpath and the targeted arriving subpath within the same TC, and it can be modeled as an exponential distribution. Cluster power is defined as the sum of the subpath powers in the cluster, and the normalized cluster power over the total received power in the PDP can be well modeled by an exponentially decaying function of cluster excess delay with a lognormal-distributed shadowing term [43, 92].

An SL represents the main direction of arrival or departure. The angular resolution of the measured APS depends on the antenna HPBW, which are 30°and 8°in 28 and 140 GHz measurements, respectively [92]. A simple discrete uniform (DU) distribution is used to characterize the number of spatial lobes. For each spatial lobe, the RMS lobe AS is extracted from the partitioned AOA and AOD APSs. A generated subpath is randomly assigned to one of the generated SLs, and the angles of this subpath (i.e., AOD, ZOD, AOA, and ZOA) are calculated by adding angular offsets with respect to the mean angle of the SL. The angular offset follows a normal distribution with zero mean and a standard deviation of the median of the measured RMS lobe AS. Such angular offset generation deviates from the 3GPP TR 38.901 channel model where angular offsets of 20 MPCs in a cluster are constant [92, 157].

From the measurements, we find that the statistical distributions for each channel parameter are the same at frequencies from 28-140 GHz, and only the values of each parameter for different frequencies are different. In general, the channel is sparse at higher frequencies. The channel at 140 GHz has fewer time clusters and fewer subpaths within each cluster than the channel at 28 GHz. Greater partition loss and higher path loss in the first meter of propagation distance at 140 GHz cause a smaller signal propagation range (the difference of maximum measurable path loss between two frequencies has been considered); thus, some of RX locations that could receive signals at 28 GHz were in an outage at 140 GHz [43, 92].

3.6 Ray Tracing VS. Measurements

Since the field measurements are expensive and time-consuming, ray tracer is an important tool that can provide accurate power and coverage prediction saving the effort to conduct field measurements, assisting wireless network deployment [59]. Currently, the application range of most ray tracers is below 6 GHz and several of them are extended to frequencies below 100 GHz. WinProp, one of the most commonly used ray tracer designed for frequencies below 100 GHz, is used and modified to extend its application range to frequencies above 100 GHz in this work.

Channels are not much different between frequencies below and above 100 GHz. To verify this statement, modifications were made to WinProp to enable it to be used at 142 GHz. 3D map/environment of 2 Metrotech center was created with drywall, glass door, office soft partition, ceiling, and

Input Parameters	28 LOS all	28 NLOS all	28 LOS common	28 NLOS common	140 LOS common	140 NLOS common
λ_c	3.6	5.1	3.6	4.4	0.9	1.8
β_s	0.7	0.7	0.7	0.7	1.0	1.0
μ_s	3.7	5.3	3.4	4.6	1.4	1.2
μ_τ[**ns**]	logn(2.1, 1.6)	10.9	logn(1.9,1.6)	9.8	14.6	21.0
μ_ρ[**ns**]	3.4	22.7	3.4	14.2	1.1	2.7
Γ[**ns**], σ_Z[**dB**]	20.7, 15.4	23.6, 9.6	20.6, 15.9	22.5, 11.3	18.2, 9.1	16.1, 12.8
γ[**ns**], σ_U[**dB**]	2.0, 5.2	9.2, 6.0	2.0, 5.0	9.9, 5.7	2.0, 4.6	2.4, 5.8
$L_{\text{AOD,max}}$, $L_{\text{AOA,max}}$	2, 2	3, 3	2, 2	3, 3	2, 2	2, 2
$\mu_{l,\text{ZOD}}$[°], $\sigma_{l,\text{ZOD}}$[°]	-7.3, 3.8	-5.5, 2.9	-7.2, 3.5	-5.8, 2.6	-6.8, 4.9	-2.5, 2.7
$\mu_{l,\text{ZOA}}$[°], $\sigma_{l,\text{ZOA}}$[°]	7.4, 3.8	5.5, 2.9	7.2, 3.5	5.8, 2.6	7.4, 4.5	4.8, 2.8
$\sigma_{\phi,\text{AOD}}$[°], $\sigma_{\theta,\text{AOD}}$[°]	7.1, 13.0	17.6, 13.0	7.0, 12.9	16.1, 12.9	4.3, 3.4	4.0, 3.3
$\sigma_{\phi,\text{AOA}}$[°], $\sigma_{\theta,\text{AOA}}$[°]	19.3, 11.3	20.2, 11.6	19.9, 11.8	19.0, 11.6	4.4, 3.3	5.6, 3.3

Figure 3.7: Values of different channel parameters for NYUSIM indoor InH channel models [92].

ground floor, as shown in Figure 3.8.

With the aim to validate the ray tracer, modifications are needed to fit the ray tracing simulations with the real world measurements at 142 GHz. Since the FSPL at 142 GHz is 6 dB higher than that at 71 GHz [1, 75], the frequency was set to be 71 GHz, and the transmit power was set to be 6 dB lower in the ray tracer. The 2D antenna pattern of the D-band 261D-27/387 horn antenna was measured at 142 GHz and a 3D pattern was simulated at 142 GHz, as shown in Figure 3.9, which was used in WinProp.

At most of 3 transmissions and 3 reflections were set in the ray tracing simulations which agree with the real world observation, and the path loss range of the rays was set to be 150 dB according to the measurement system [75]. Ray optical propagation model was used, where free space propagation plus reflection, scattering, transmission, diffraction, and air absorption were considered, and the coverage of the ray tracing simulations are shown in Figure3.10.

The ray tracing simulated PDPs and the measured PDPs of RX1 are shown in Figure 3.11. There are about 8 rays predicted by the ray tracer and 5 of them are captured by the measurements. A couple of simulated rays are not captured by the measurements which are possibly because these rays are blocked by the physical size of the channel sounder system. As shown in Figure 3.11, Ray 1 is the direct LOS path from TX1 to RX1 and Ray 2 is a ray with one reflection from drywall. Ray 3, 4, and 5 are rays with two reflections, where one is from drywall and the other is from the surface of wood closets. Figure 3.11 shows that the number of predicted rays from ray tracing simulations agrees well with the measured rays at 142 GHz, and the power of each simulated ray also fits closely with the measurements which indicate that with some necessary modifications, ray tracer like WinProp could be extended to higher frequencies (e.g., 140 GHz band).

Another example of the simulated PDP and measured PDP is shown in Figure 3.12, which shows the simulated and measured rays at RX5. There are 6 main rays predicted and measured. Ray 1 is the direct path from TX1 to RX5 penetrating through one office soft partition and Ray 2 and Ray 4 are the paths with one reflection from drywall. Ray 3, 5, and 6 are rays with more than two

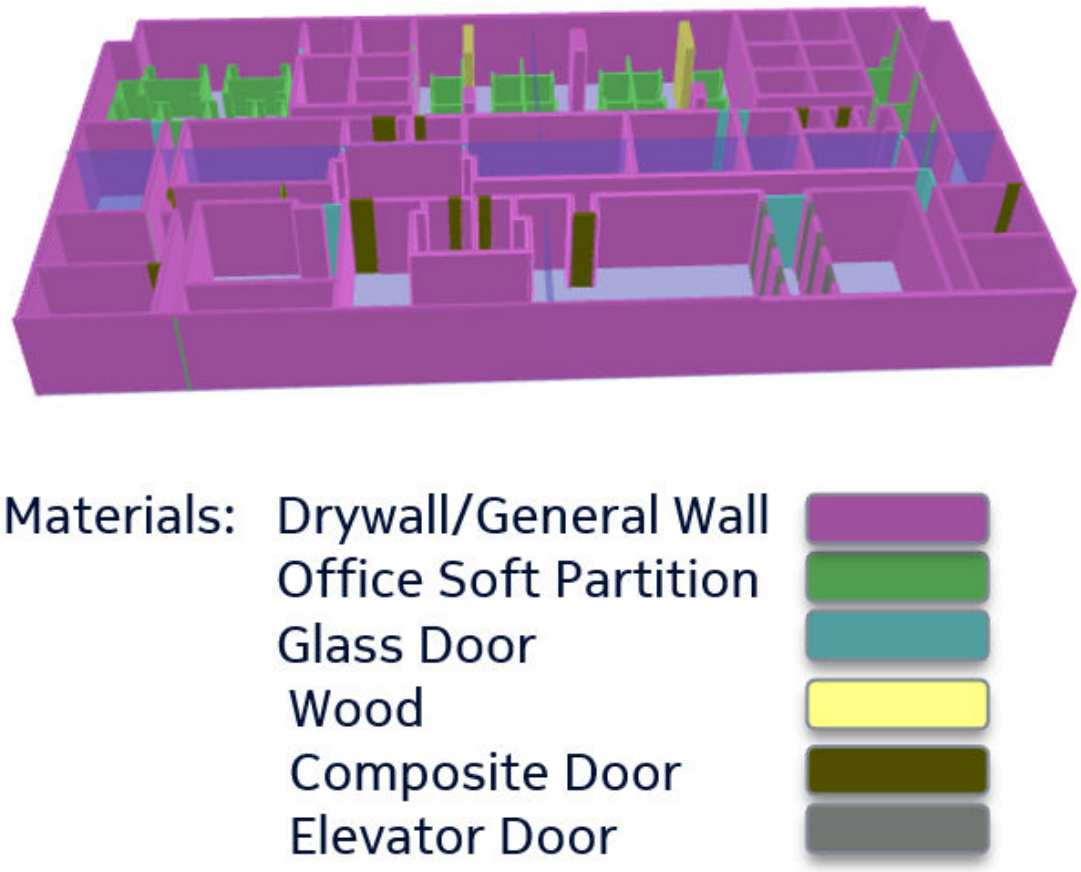

Figure 3.8: 3D map of 2 Metrotech center. Material proprieties like the reflection loss, penetration loss, and scattering were chosen based on the measurements in [66, 75].

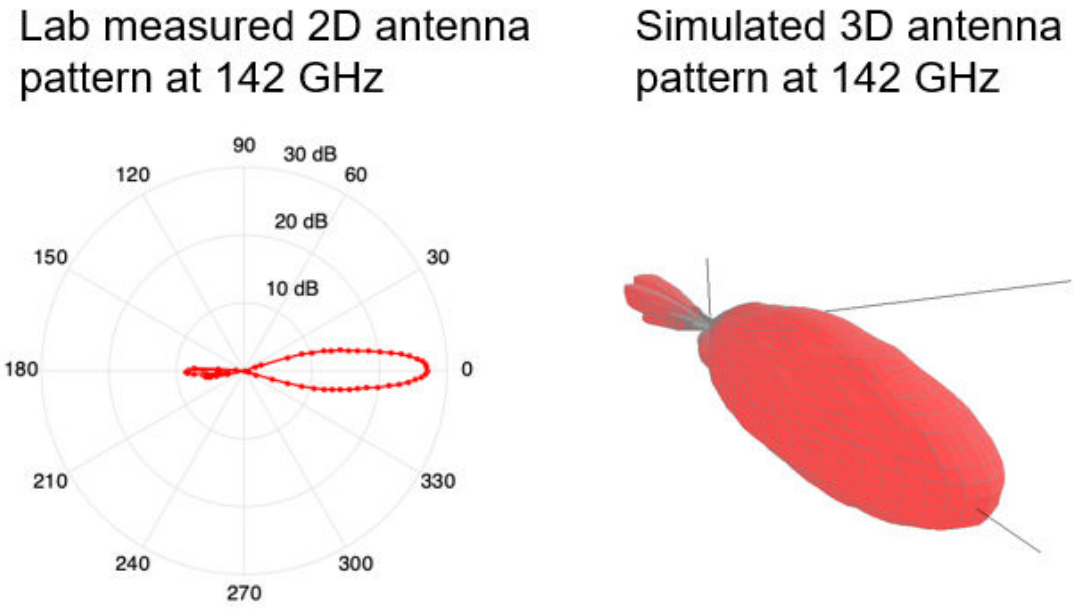

Figure 3.9: The antenna pattern of MI-Wave D-band 261D-27/387 horn antenna which has 27 dBi gain and 8° HPBW.

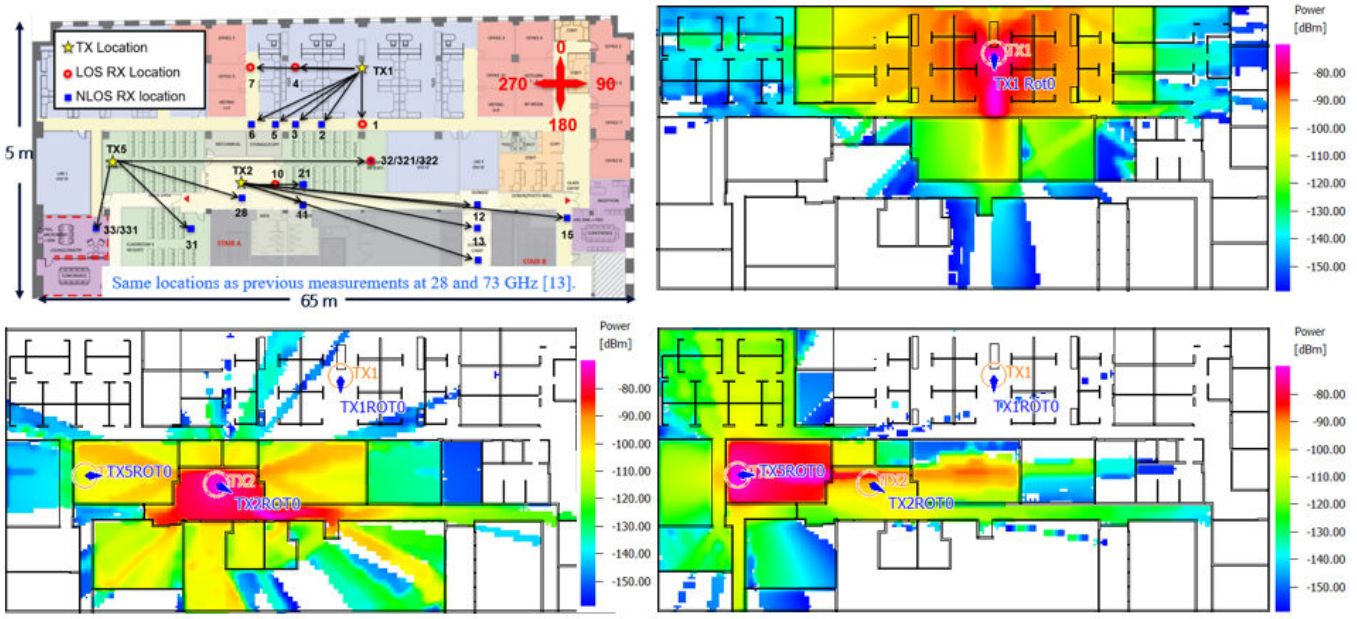

Figure 3.10: Ray tracing coverage simulations at the same TX locations of TX1, TX2, and TX5 as in the 142 GHz measurements.

interactions (reflections + penetrations) as shown in Figure 3.12. The simulated PDP agrees well with the measured PDP indicating that the ray tracer works at 142 GHz.

3.7 Simulation Results

After validating the ray tracer, 10000 simulations (e.g., randomly choose RX locations and simulate the channels between the RX and the certain TX) were performed to study the indoor channels at 142 GHz assuming the Equivalent Isotropically Radiated Power(EIRP) of 18 dBm with a noise floor of -100 dBm over a 1 GHz RF bandwidth. A dynamic range of 30 dB is used which means at a certain location signal within 30 dB from the peak signal power can be detected. The simulation results are shown in Figure 3.13-3.16.

Figure 3.13 shows the pdf and cdf of the simulated RMS delay spread, and same as the channels below 100 GHz, the RMS delay spread above 100 GHz also follows an exponential distribution with a mean $\mu = 5.6$ ns and a standard deviation σ=7.4 ns.

The statistics of the number of clusters per omnidirectional PDP (per RX location) is presented in Figure 3.14. In 3GPP TR 38.901 Release 15 [157], the number of clusters follows a Poisson distribution or a discrete uniform distribution. However, at 142 GHz, it shows that the Poisson distribution does not describe the statistics of the number of clusters well. Most RX locations (nearly 50% of the total locations) only have one cluster which means, in most locations, the received signal only comes from one direction. It agrees with the expectation of the high directionality at frequencies above 100 GHz. The percentage of cluster numbers more than 5 is below 5 % and a maximum number of 11 clusters is observed in the simulations.

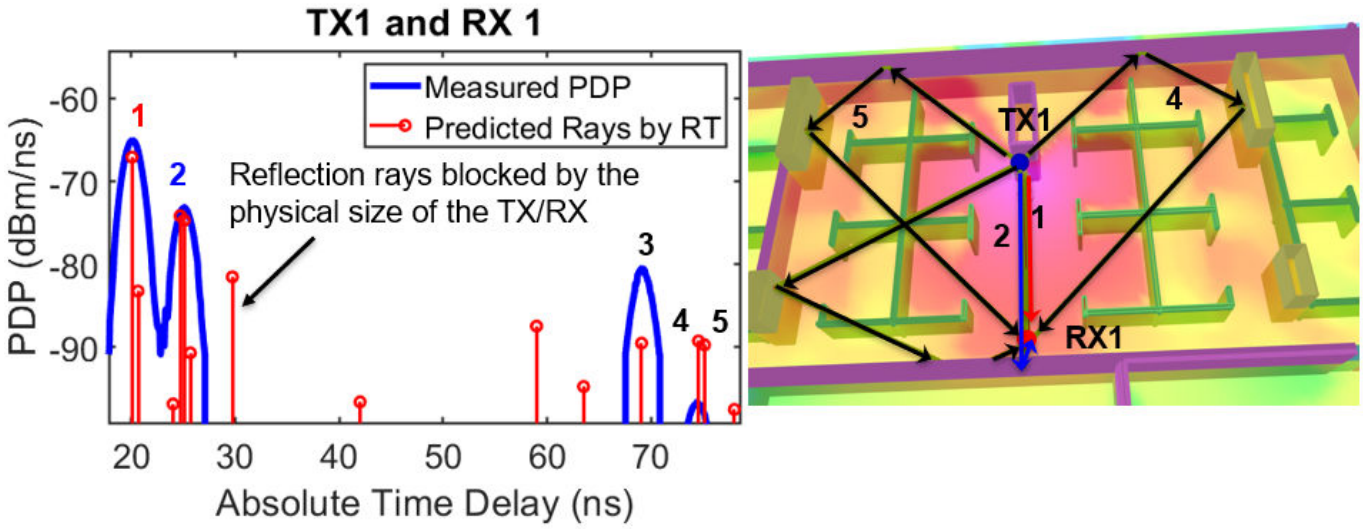

Figure 3.11: The simulated PDP of RX1 vs. the measured PDP at 142 GHz. A couple of simulated rays are not captured by the measurements which are possibly due to these rays are blocked by the physical size of the channel sounder system.

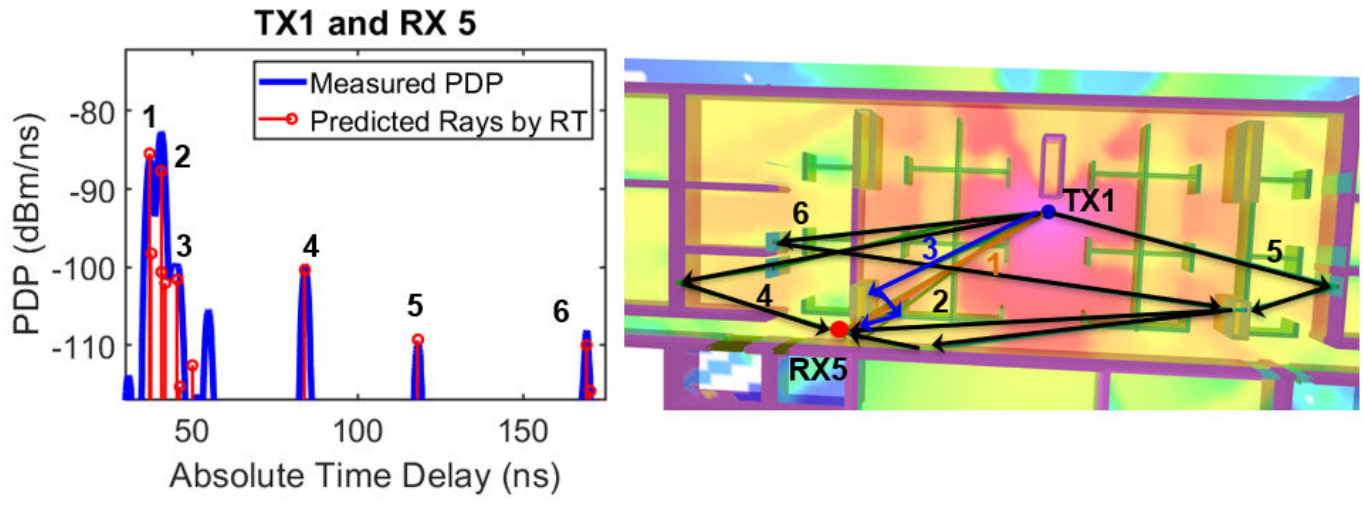

Figure 3.12: The simulated PDP of RX5 vs. the measured PDP at 142 GHz.

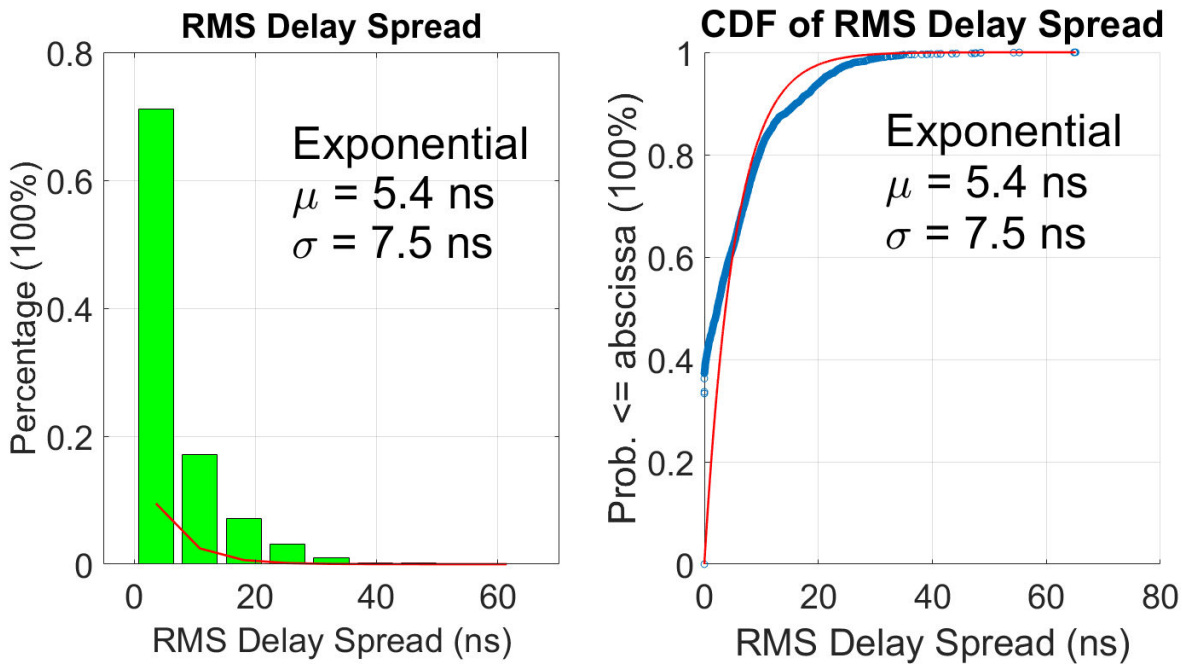

Figure 3.13: The simulated PDF and CDF of RMS delay spread vs. the theoretical exponential distribution with mean $\mu = 5.4$ ns and standard deviations $\sigma = 7.5$ ns.

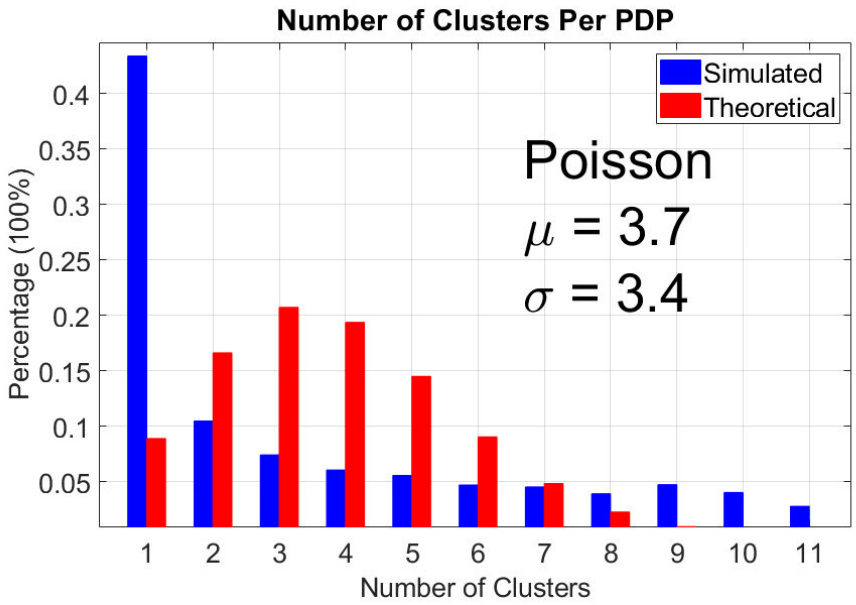

Figure 3.14: The simulated number of clusters per omnidirectional PDP vs. the theoretical Poisson distribution with a mean μ of 3.7 and a standard deviation σ of 3.4 at 142 GHz.

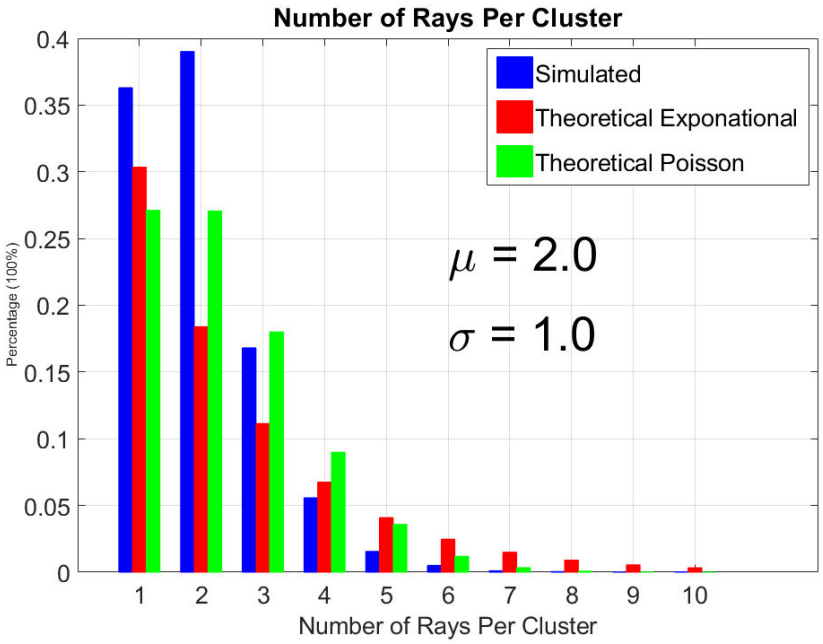

Figure 3.15: The simulated number of rays/subpaths per cluster vs. theoretical Exponential and Poisson distributions with a mean $\mu = 2.0$ and a standard deviation $\sigma = 1.0$ at 142 GHz.

The statistics of the number of rays/subpaths per cluster is shown in Figure 3.15 with most clusters (more than 70%) having only one or two rays/subpaths. Less than 2% of the clusters have more than 6 subpaths. Both an exponential distribution and a Poisson distribution with a mean $\mu = 2.0$ and a standard deviation $\sigma = 1.0$ are presented in Figure 3.15, and the Poisson distribution seems to have a better description of the channel statistics than the Exponential distribution.

Similar to the frequencies below 100 GHz, the cluster excess time delay at frequencies above also follows an exponential decaying distribution with a mean μ of 46.8 ns and a standard deviation σ of 37.1 ns.

3.8 Phase Noise and Modulation Schemes Analysis at THz

There are many applications and usages enabled by the vast bandwidth at mmWave and THz as discussed in Section 1.3, however, there are also notable differences and challenges seen for frequencies beyond 100 GHz, which make propagation more challenging.

First, at higher frequencies, the transmit power as well as the power efficiency is limited by the power amplifiers (PA) [1] capabilities since the year 2000 is given in [162]. The channel will be noise-limited because the larger bandwidth used will increase the noise floor. Beamforming and beam alignment algorithms are needed since the propagation is more challenging and more directional antennas/arrays will be used at these frequencies. Phase noise will be worse and Doppler frequencies will be higher due to the high carrier frequencies. Actually, the phase noise (PN) could increase by 6 dB every time when the carrier frequency f_c doubles (assuming the other things do not change)

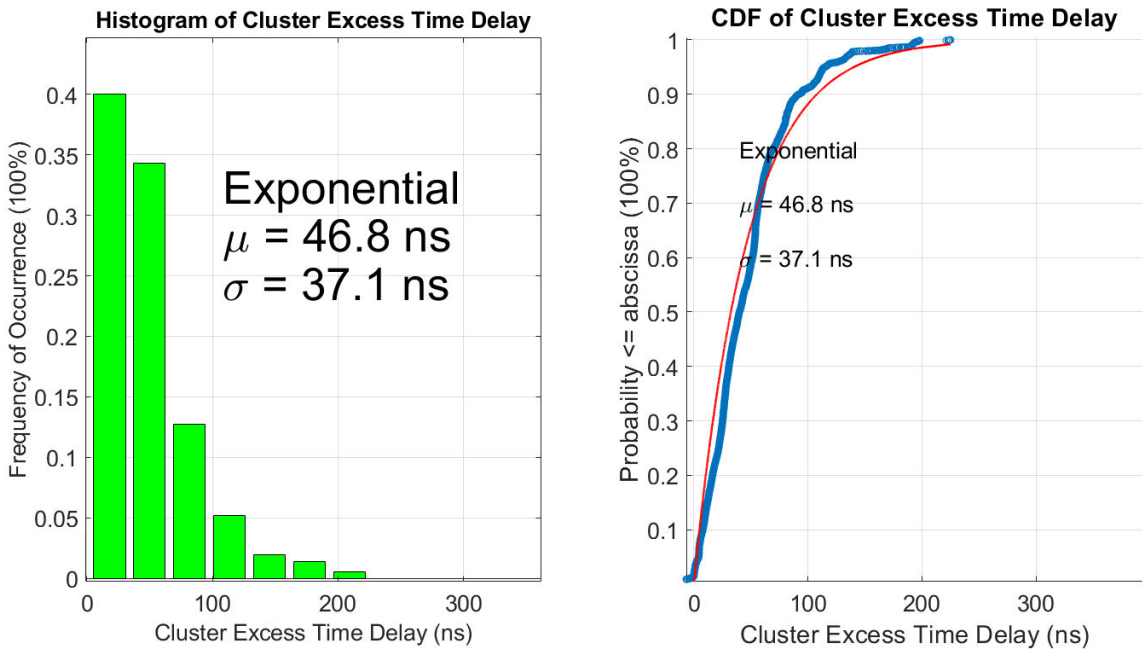

Figure 3.16: The simulated pdf and cdf of cluster RMS excess time delay vs. the theoretical exponential distribution with a mean $\mu = 46.8$ ns and a standard deviation $\sigma = 37.1$ ns at 142 GHz.

and the PN is inversely proportional to the square of the loaded quality factor of the resonator [163]. Phase noise is also an important parameter in relation to the choice of sub-carrier spacing and achievable signal quality.

Basically, PN is caused by noise in the active components ends and lossy elements which is up-converted to the carrier frequency (e.g., oscillator). Frequency synthesizers generally consist of a reference oscillator (or clock), a voltage-controlled oscillator (VCO), and a phase-locked loop (PLL) with a frequency divider, a phase-frequency detector charge pump, and loop filter. Noise is the sum of an infinite number of infinitesimal components spread over a range of frequencies, so the signal it mixes into the IF is spread into an infinite number of small replicas, all at different frequencies. The characteristic of PN is usually explained by its power spectrum.

3.8.1 Phase Noise Model

There are several models to simulate the practical PN spectra, for example, a simple single pole/zero model is adopted in IEEE P802.15 [164] which is a linear model that describes the PN caused by the PLL. As an extension, a multi-pole/zero model which provides a good approximation to reflect practical PN characteristic is adopted in the 3GPP TR 38.803 (R1-163984, 3GPP TSG RA#71) [163, 165] as follow:

$$S(f) = PSD_0 \prod_{n=1}^{N} \frac{1 + (\frac{f}{f_{z,n}})^2}{1 + (\frac{f}{f_{p,n}})^2}, \tag{3.7}$$

where PSD0 is the power spectral density for zero frequency ($f = 0$) in dBc/Hz (dB relative to the carrier), $f_{z,n}$ and $f_{p,n}$ are zero and pole frequencies. There are two parameters sets which are obtained from filed measurements and are adopted in the 3GPP TR 38.803 [163, 165] listed in Table 3.10.

Table 3.10: Parameter sets for PN models at 30 GHz and 60 GHz [163, 165].

	Parameter Set-A	Parameter Set-B
Carrier frequency ($f_{c,\mathbf{base}}$)	30 GHz	60 GHz
PSD0 (dBc/Hz)	-79.4	-70
F_P(**MHz**)	[0.1, 0.2, 8]	[0.005, 0.4, 0.6]
F_Z(**MHz**)	[1.8, 2.2, 40]	[0.02, 6, 10]

If the operating carrier frequency is changed, the PSD will be shifted by $20\log_{10}(f_c/f_{c,base})$ dBc/Hz, which means the PN could increase by 6 dB every time when $f_{c,base}$ doubles assuming the other things do not change. Parameter Set-A is used to generate the PN and Figure. 3.17 shows the PSDs at 4, 30, 70, 140 GHz.

Figure. 3.18 and 3.19 show the impact of PN on the 16-QAM constellations at 140 GHz. Clearly, without correction, PN will make distortions to the constellation map which impairs the channel performance.

3.8.2 Single Carrier Waveform

To analyze the impact of PN at frequencies above 100 GHz, an end-to-end wireless communication system is simulated using Null Cyclic Prefix-Single Carrier (NCP-SC) waveform with 16-QAM modulation scheme. As discussed before, when frequencies go beyond 52.6 GHz (which is an important 3GPP work item in Release 17) the power amplifier is less efficient and the performance will be noise-limited. Therefore, the lower Peak to Average Power Ratio (PAPR) enabled by single carrier frequency-division multiplexing (SC-FDM) over Orthogonal frequency-division multiplexing (OFDM) is more critical to maximize the coverage and power amplifier efficiency.

In this work, the same null-cyclic-prefix single carrier (NCP-SC) waveform structure as introduced in [166, 167] was used. As shown in Figure 3.20, there are 512 symbols in a NCP-SC block where there are $M_{data} = 480$ data symbols and $M_{cp} = 32$ padding symbols. 150 NCP-SC blocks form a time slot where there are 138 data blocks, 1 control block, 1 pilot block, and 10 reserved blocks for future use such as positioning reference signal [166, 167]. 5 slots form a TDM frame and 40 frames form a TDM superframe. At a 1.536 GHz sampling rate, one slot period is 100 us, which is one tenth of 4G, and one superframe is 20 ms.

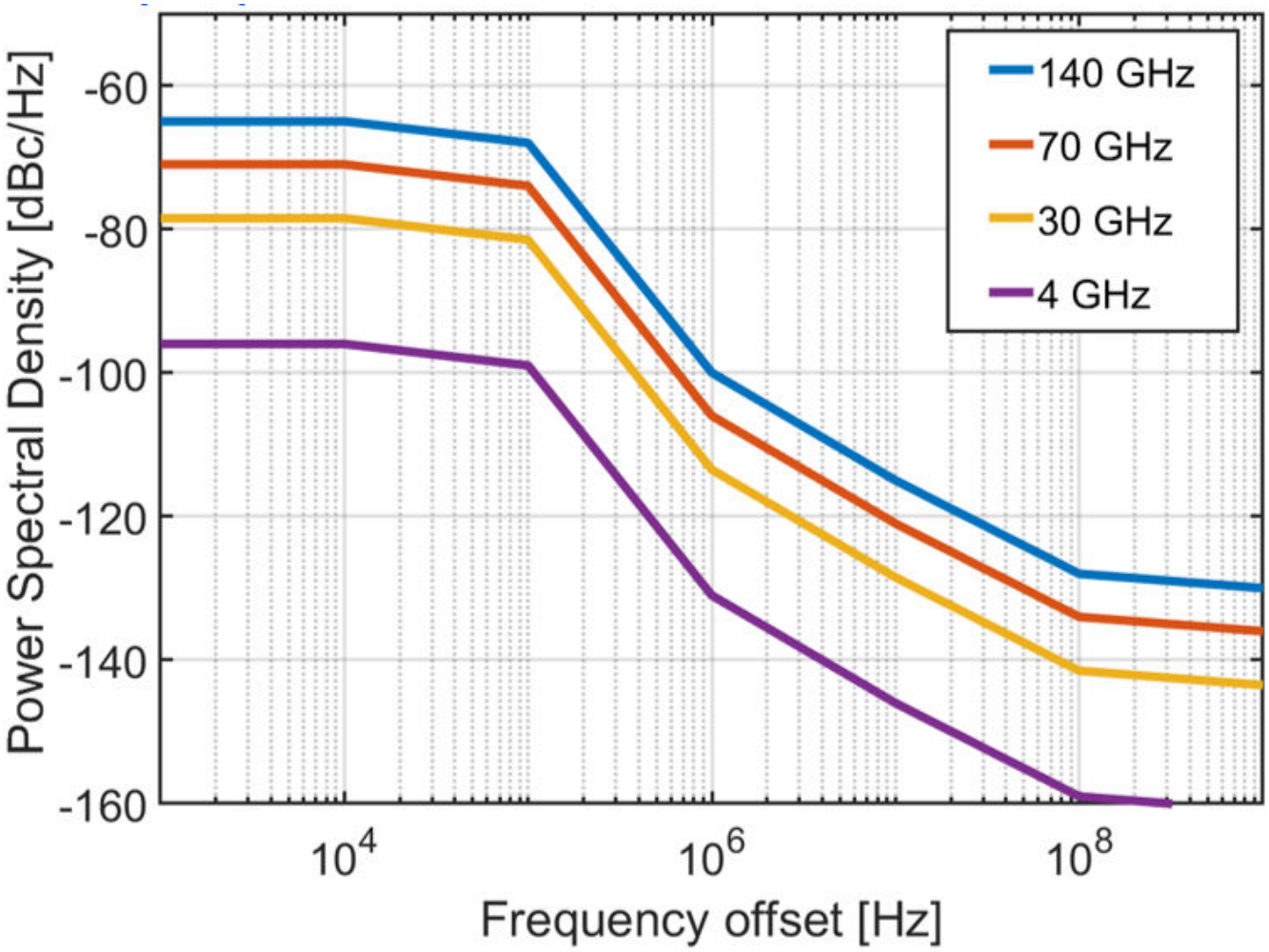

Figure 3.17: Phase noise spectral density using Parameter Set-A in Table 3.10.

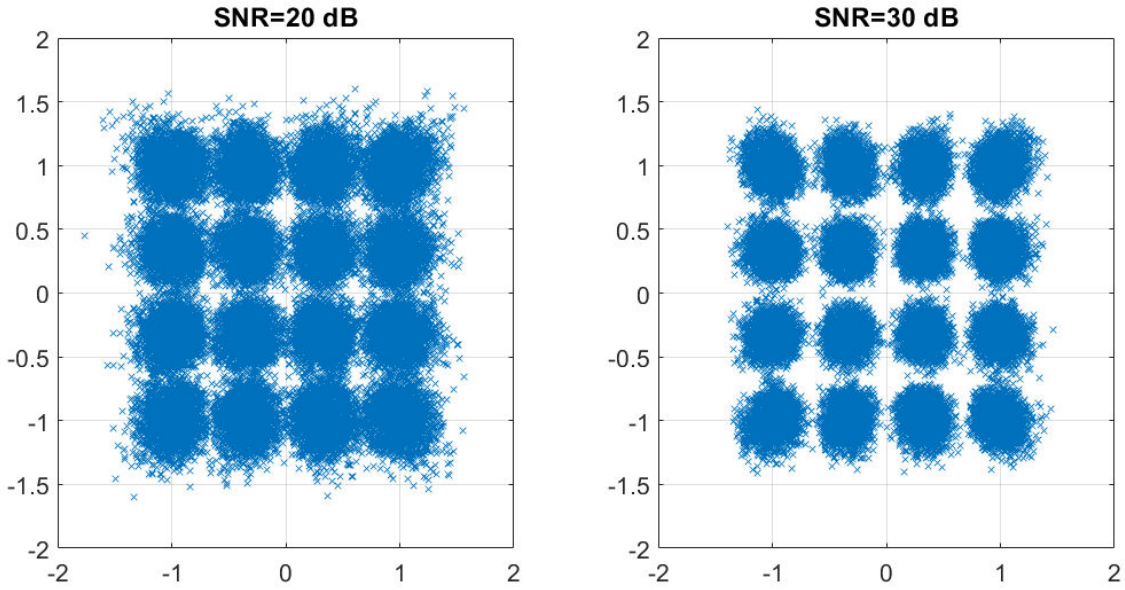

Figure 3.18: 16-QAM constellation without PN at 140 GHz.

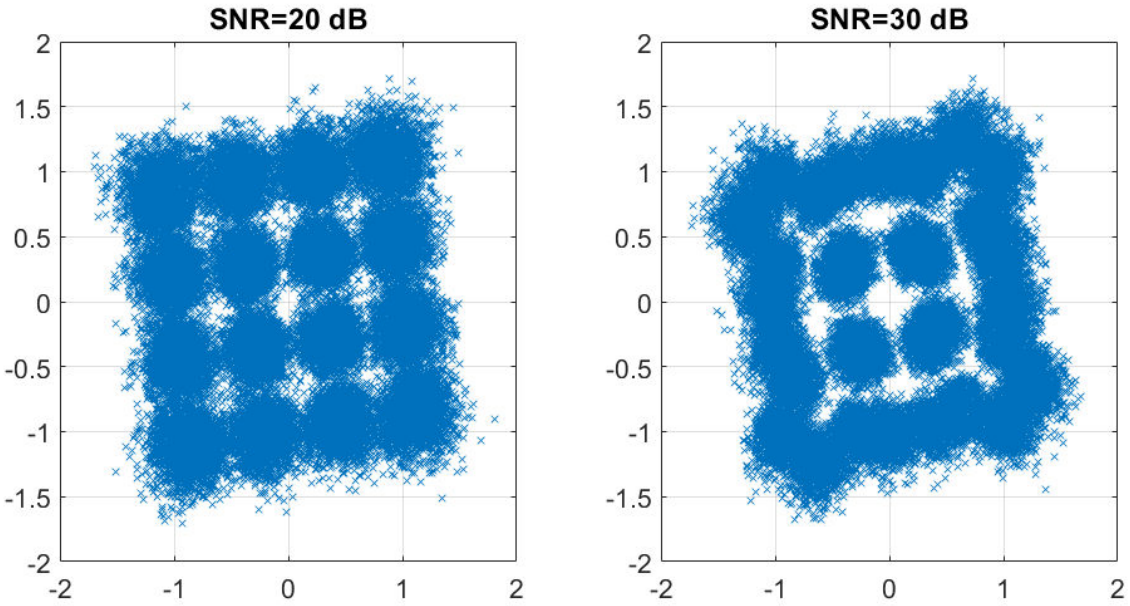

Figure 3.19: Phase noise impact on constellations at 140 GHz.

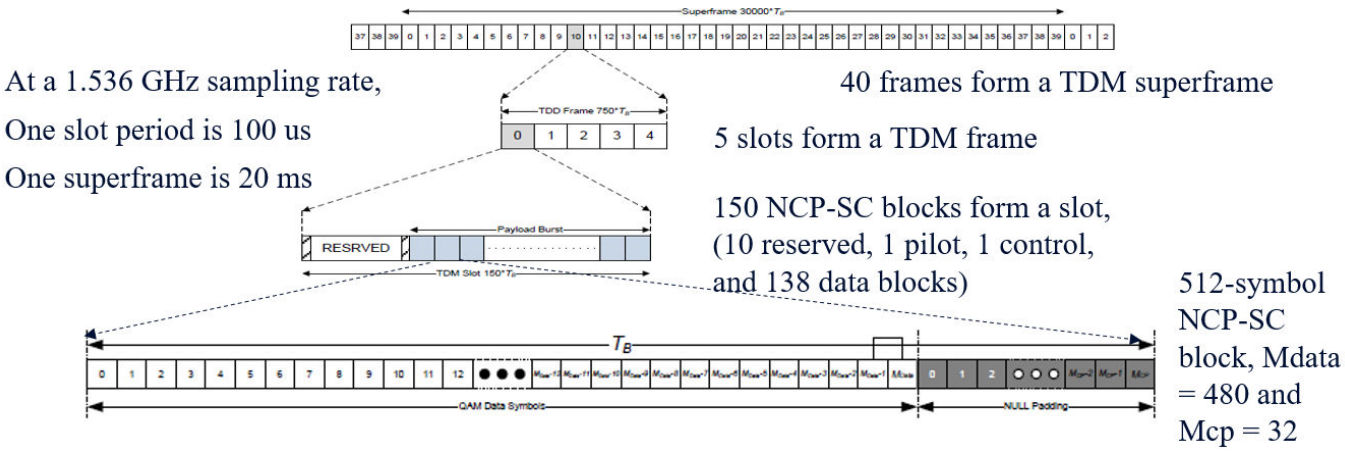

Figure 3.20: Waveform structure of the NCP-SC system [166, 167]

3.8.3 Blind Phase Noise Estimation

There are many existing blind PN estimation algorithms that can be used to estimate the PN [167, 168, 169]. In this work, we will use a relatively straight-forward method called the power law estimator for BPSK and QAM constellations, which is given as:

$$\hat{\theta} = \frac{1}{2}\tan^{-1}\left(\frac{2\mathbf{r}_R^T\mathbf{r}_I}{\mathbf{r}_R^T\mathbf{r}_R - \mathbf{r}_I^T\mathbf{r}_I}\right), \tag{3.8}$$

where $\mathbf{r}_R = [r_R(0), ..., r_R(M_{data}-1)]^T$ and $\mathbf{r}_I = [r_I(0), ..., r_I(M_{data}-1)]^T$ are the real part and image part of the received equalized symbols for a given NCP-SC block (M_{data} of which are data symbols and the remaining are null symbols). Before applying the formula, $r(l)$ should be multiplied by $(1-j)/\sqrt{2}$ to convert from the standard BPSK symbol +1 or -1 to the LTE definition $(1+j)/\sqrt{2}$ or $(1-j)/\sqrt{2}$ [167]. Although the power law estimator is designed for BPSK, it can also be extended to QAM symbols by mapping the equalized symbols in the second and fourth quadrants to the first or thrid quadrants by multiplying these symbols by $-j$, as discussed in [167].

Since the block size of a NCP-SC system will be designed to be small enough that the phase changes relatively slowly from block to block and the phase offset within a block can be assumed to be the same [167].

3.8.4 Simulation Results

Simulation settings are summarized in Table 3.11. The carrier frequency is 140 GHz with 1 GHz RF bandwidth. According to the aforementioned model shown in Figure 3.17 [163], the PN power spectral density is about -65 dBc/Hz at 100 kHz offset frequency. AWGN channel was first simulated with one transmit antenna and one receive antenna. 16-QAM modulation was used and the simulation results were shown in Figure 3.21 and 3.22.

Table 3.11: Simulation Parameters Setting

Parameter	**Value**
Carrier Frequency	140 GHz
RF Bandwidth	1 GHz
PN Model	3GPP TR38.803 [163] Parameter Set A
Waveform	NCP-SC (Figure 3.20)
Modulation Scheme	16-QAM
Channel	AWGN
Subcarrier Spacing	960 kHz

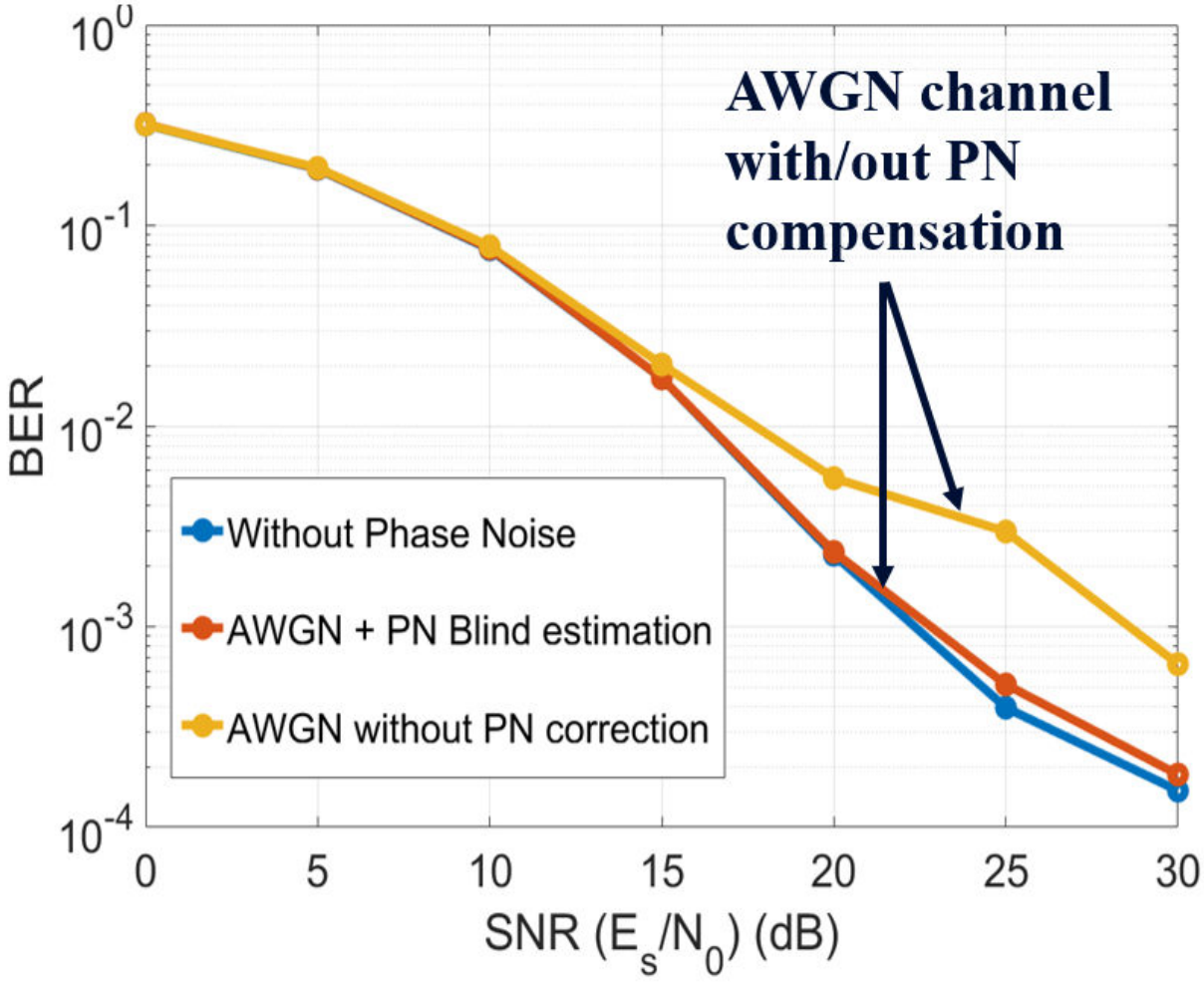

Figure 3.21: 16 QAM BERs in AWGN channel with and without PN compensation at 140 GHz, where the PN power spectral density is -65dBc/Hz at 100 kHz offset.

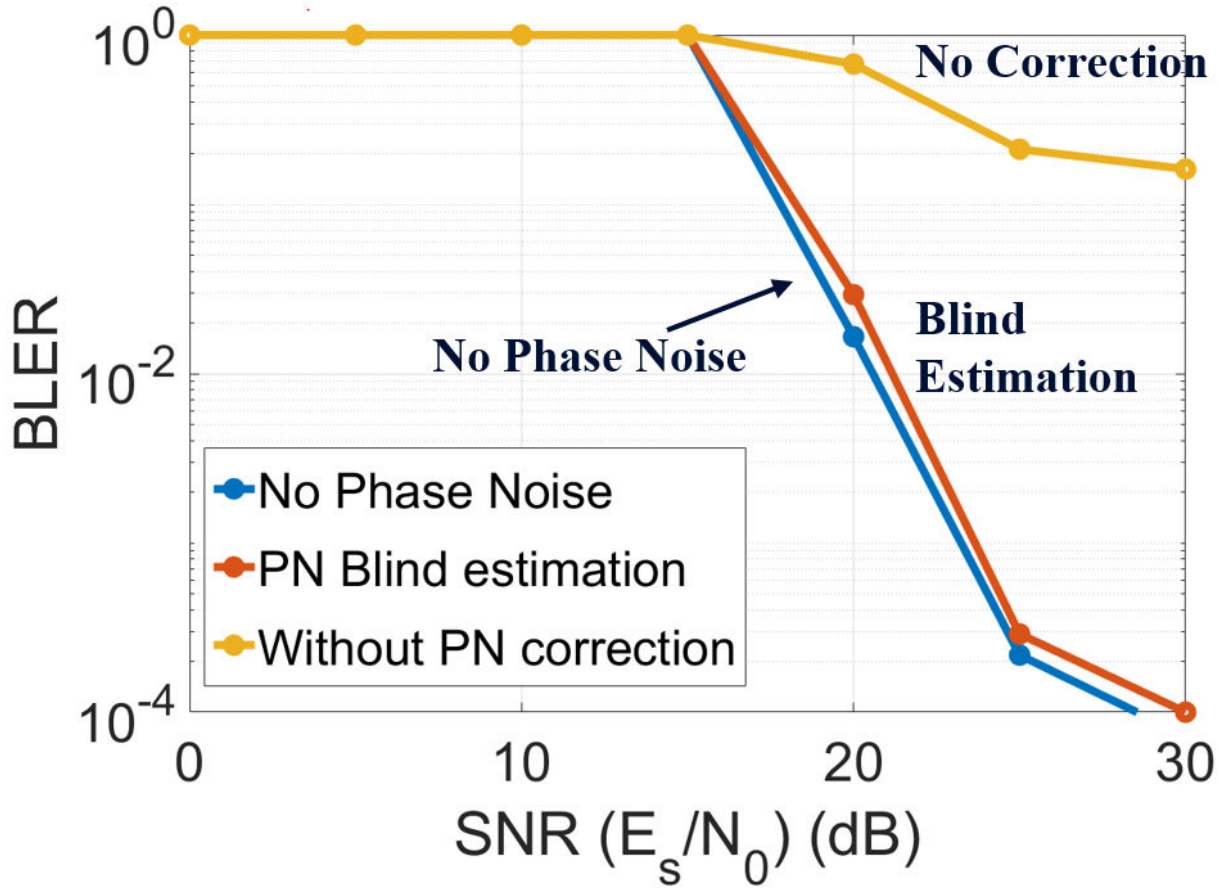

Figure 3.22: 16 QAM BLER in AWGN channel with and without PN compensation at 140 GHz, where the PN power spectral density is -65dBc/Hz at 100 kHz offset.

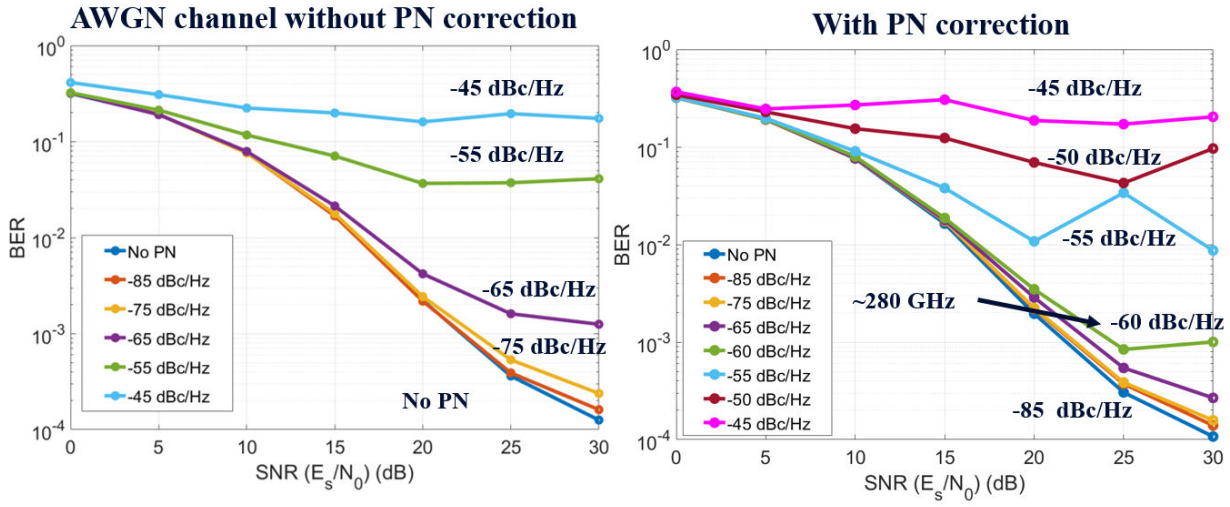

Figure 3.23: 16 QAM BERs in AWGN channel with and without PN compensation for different PN levels which are equivalent to different carrier frequencies.

The blue line is the bit error rate (BER)/block error rate (BLER) in the ideal situation where there is no PN, the yellow line is the BER/BLER with PN but without PN compensation, and the red line is the BER/BLER with blind PN estimation (3.8). As shown in both Figure 3.21 and 3.22, with no PN correction the system performance in terms of both BER and BLER is bad compared to the ideal case (without PN). With blind PN estimation, the system performs as well as the ideal case which shows that blink PN compensation greatly improves the system performance without any expense for phase tracking signals.

To explore how well does the blind PN compensation method work for different frequencies, which are equivalent to different PN levels, simulations are made using the same settings in Table 3.11 but with different carrier frequencies (PN levels). As shown in Figure 3.23, the blind PN compensation method works well till -60 dBc/Hz which is approximately the PN level at the carrier frequency of 240 GHz. However, when the PN levels are higher than -60 dBc/Hz, the blind PN estimation method does not work that well since the blind PN estimation method used in this chapter can only estimate phase offsets less than $pi/2$. To improve the system performance, a shorter block length of the NCP-SC waveform (e.g., 256 or 128 NCP-SC symbols per block) can be used for better PN estimation.

As shown in Figure 3.24, the power law blind PN estimator improves the system performance a lot in terms of BLER at different PN levels. With a block size of 512 NCP-SC symbols, the carrier frequency range for the best performance is 0-280 GHz.

3.9 Conclusion

Channel differences between frequencies below and above 100 GHz are studied based on both measurements and simulations. Real-world measurements conducted in an indoor office environment

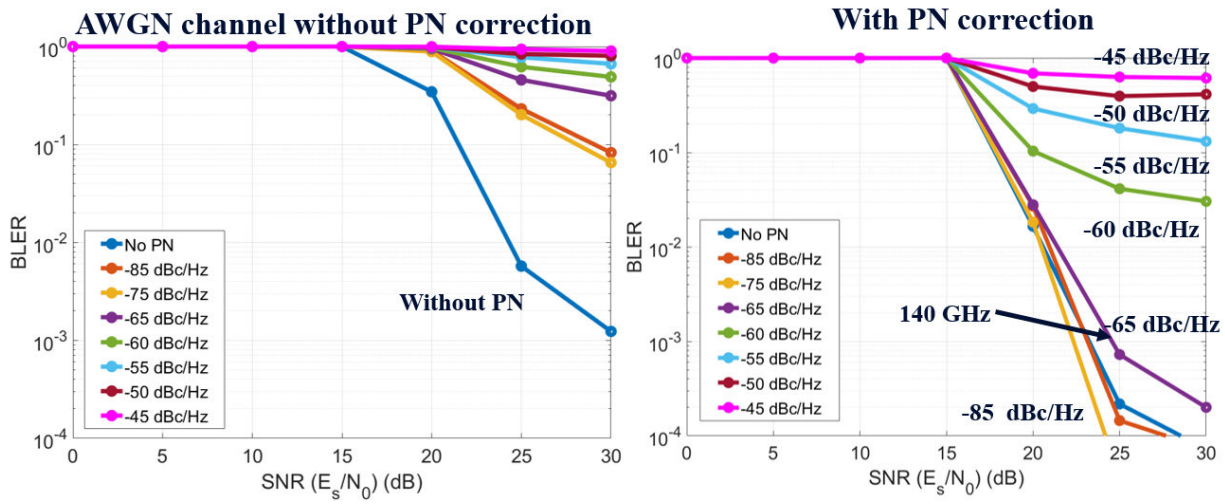

Figure 3.24: 16 QAM BLERs in AWGN channel with and without PN compensation for different PN levels which are equivalent to different carrier frequencies.

at NYU WIRELESS at 140 GHz together with ray-tracing simulations show that there is not much difference between the channels below and above 100 GHz. The statistical distribution at higher frequencies (e.g., 140 GHz) for important channel parameters like the number of clusters, delay spread, number of subpaths per cluster is the same as frequencies below 100 GHz (e.g., 28 and 73 GHz), which means with some modification to the distribution parameters, the channel models developed for frequencies below 100 GHz can still be used at higher frequencies.

Phase noise impact at 140 GHz is studied using a null cyclic prefix single carrier system since high phase noise is a key issue for high frequencies systems. Simulation results show that the blind phase noise estimation method (without any design of phase tracking signals) can greatly improve the system performance at 140 GHz with a block length of 512 NCP-SC symbols. Shorter block length can be used at higher frequencies to ensure a good performance of the blind phase noise compensation method.

Chapter 4

Outdoor Measurements and Modeling at 142 GHz

One of the most prominent advancements in the fifth generation (5G) of mobile communications, over prior generations (e.g., 4G LTE), is the use of much wider bandwidth at millimeter wave (mmWave, 30-300 GHz) in comparison to the limited spectrum available at sub-6 GHz frequencies [1, 2, 4]. The vast bandwidth enables multi-Gbps data rate operations at mobile devices and various new applications like wireless cognition and centimeter-level positioning [1, 132]. Both handset terminals and base stations will use highly directional antenna arrays, resulting in huge differences in antenna beamforming and adaptation to wireless channels at mmWave compared to sub-6 GHz frequencies (e.g., narrower antenna beamwidth, higher penetration loss, stronger reflections but much lossier diffractions) [1, 2, 134]. Extensive research has been conducted at frequencies below 100 GHz and several channel models have been developed by standards and different research organizations such as 3GPP, 5GCM, NYU WIRELESS, METIS, and mmMAGIC, which has helped to facilitate the deployment of 5G networks [157, 158, 170, 171, 172, 173].

Terahertz (THz) frequency bands (e.g., frequencies from 100 GHz to 3 THz) are promising bands for the next generation of wireless communications (6G). However, there are notable challenges seen for frequencies above 100 GHz (e.g., high phase noise and Doppler shift, limited output power, and more directional beams), which makes communications in THz bands more challenging [1, 66]. Propagation measurements at THz frequency bands are imperative to provide knowledge and understanding of the wireless channels above 100 GHz [140, 174].

Most of the measurements at THz bands are focused on short-range indoor scenarios [69, 137, 138, 139], which are limited by the dynamic range and the cable connected between the transmitter (TX) and receiver (RX) of the vector network analyzer (VNA) based system. Work in [43, 92, 140] presented an indoor wideband measurement campaign at 142 GHz looking at large indoor radio propagation distances up to 40 m. There are very few outdoor measurement campaigns at frequencies above 100 GHz [37, 68] and they primarily focus on line-of-sight (LOS) propagation using either reflected materials [37] or a RF-over-fiber extension [68] of a VNA based system.

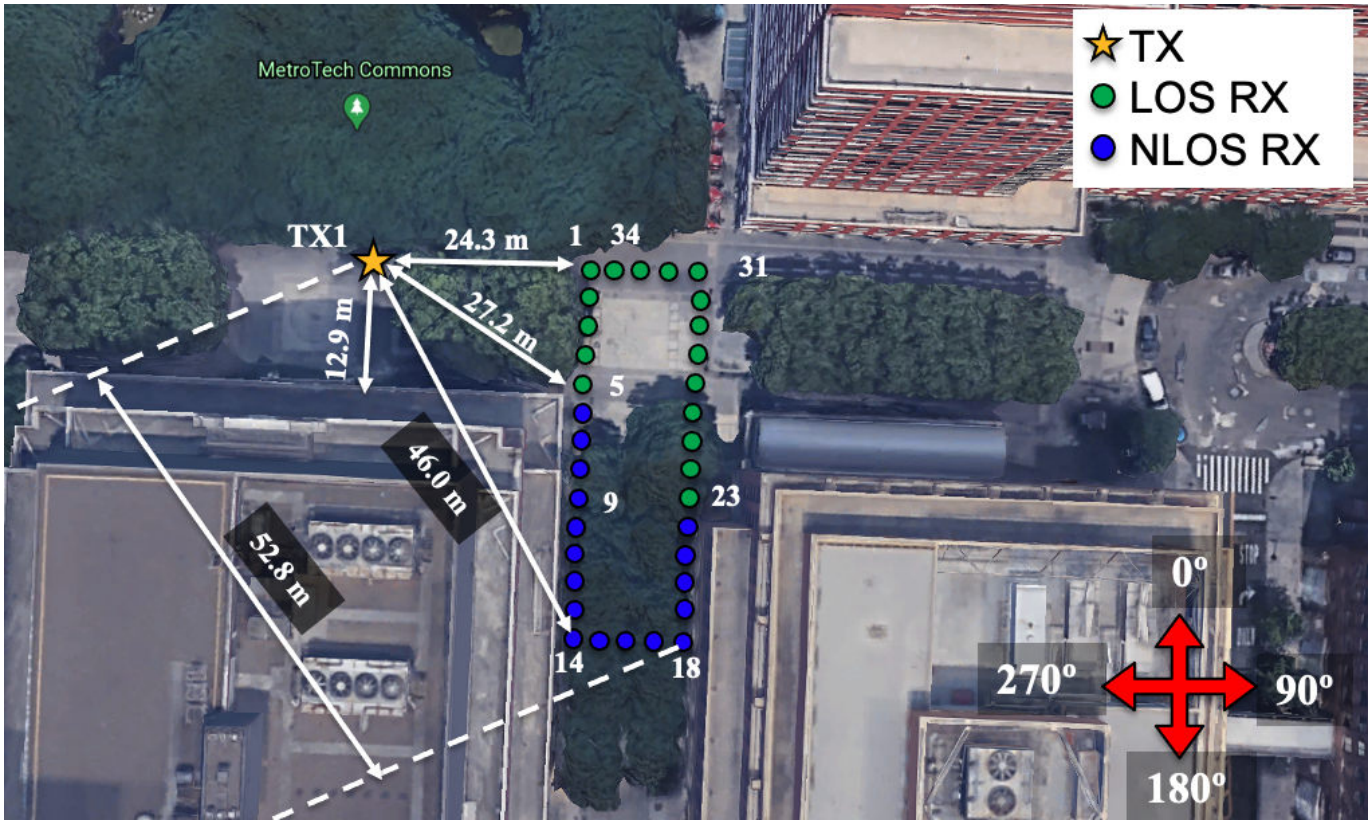

Figure 4.1: 142 GHz outdoor UMi Local Area measurement locations [175].

4.1 Terrestrial UMi Local Area Measurement Locations and Procedures

The terrestrial UMi local area measurements were designed to study the spatial characteristics of the UMi wireless channels at sub-THz frequencies. The TX was set at 4 m above ground to emulate a small-cell base station in front of 2 MTC building, as shown in Figure 4.1. The RXs were set at 1.5 m above ground level to emulate mobile terminals. There were 34 RX locations which form a rectangular shape of 39 m $\times$ 12 m as shown in Figure 4.1, and each adjacent RX pair was separated by 3 m. RX locations RX1-RX5 and RX23-RX34 were in LOS scenarios (17 locations marked as green dots in Figure 4.1), and RX locations RX6-RX22 were in NLOS scenarios (17 locations marked as blue dots in Figure 4.1).

There were metal lamppost, concrete walls, glass windows, marble pillars, trees, foliage, and pedestrians in the surrounding environment, as shown in Figure 4.7. The reflections were observed mainly from surrounding buildings and metal lampposts during the measurements.

At each TX-RX location, the strongest pointing angles in both azimuth and elevation were searched for both TX and RX antennas, where the TX and RX antennas were pointing boresight to each other in LOS scenarios, and the TX and RX antennas were pointing to the best reflection direction found by manual search. Then, the TX pointing direction was fixed, and RX swept in the azimuth plane in steps equal to the antenna HPBW (8°). 45 stepped-rotations (360/8=45) were per-

formed, and 45 directional PDPs were measured in one azimuth sweep. The RX was then downtilted and uptilted by the antenna HPBW, and we performed the same extensive azimuth sweeps. Overall, three RX sweeps with 135 directional PDPs were recorded for one TX pointing angle. The TX was then pointed to some manually selected directions which have appreciable energy, and the identical three RX azimuth sweeps were performed for each of the different TX pointing angles. Most RX locations received signals from between one to three TX pointing directions. For each unique TX pointing angle, typically one to three different RX pointing angles are able to provide detectable energy [175].

4.1.1 Spatial Consistency at 142 GHz based on Local Area Measurements

Figure 4.2 shows omnidirectional path loss of the terrestrial local area measurements at 142 GHz versus different separation distances over 34 locations. RX 2 and RX 29 were partially blocked by trees from the TX, resulting in an abrupt increase in path loss from its adjacent RX locations (in LOS scenarios). Using the CI path loss model, the PLE for the LOS scenario is 2.01 which is very close to the free space propagation, and the PLE for the NLOS scenario is 3.20.

Analysis of spatial autocorrelation of large-scale and small-scale parameters is crucial for wireless system design. The spatial autocorrelation function models the channel correlation property over distance in terms of channel parameters such as shadow fading, delay spread, angular spread [175]. Figures 4.3 and 4.4 show the spatial autocorrelation coefficients of shadow fading (SF) and delay spread (DS) and angular angular spread (AS). The correlation distance is defined as the distance where the correlation coefficient first drops below $1/e$ ($\tilde{0}.37$). The correlation distance of SF at 142 GHz is 3.8 m, which means if two RX locations are separated more than 3.8 m the SF of them at 142 GHz are uncorrelated [175]. The correlation distances for the delay spread and angular spread are 11.8 m and 12.0 m at 142 GHz, respectively, indicating that the delay spread and angular spread show a similar decaying trend in the UMi street canyon scenario [175]. Results show that the correlation distances of delay spread and angular spread measured at 142 GHz are close to the values (7-10 m) proposed for frequencies below 100 GHz by 3GPP [157].

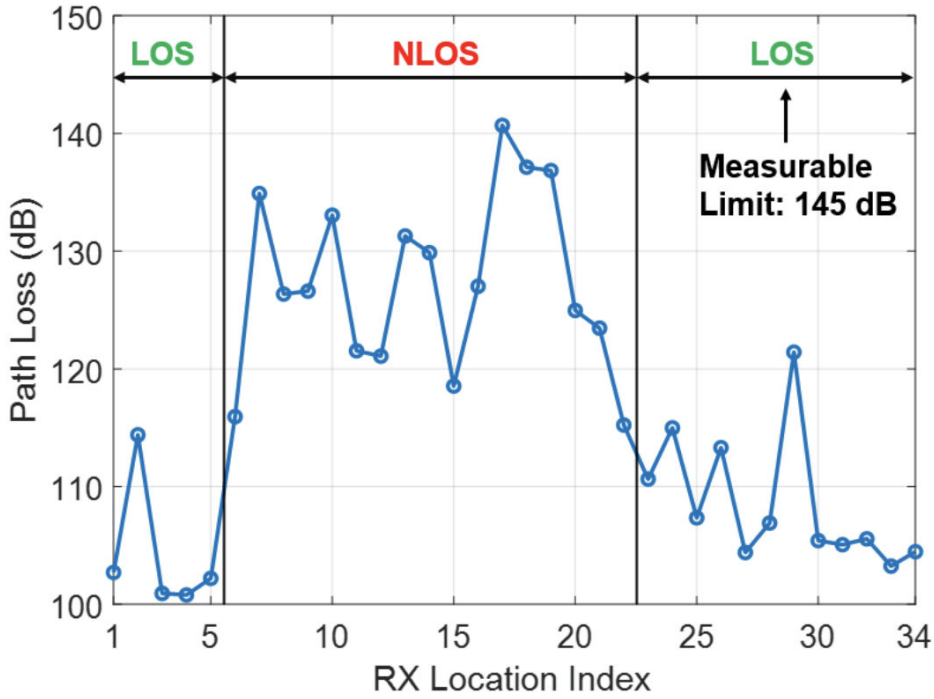

(a) 142 GHz omnidirectional path loss variation over 34 RX locations in LOS and NLOS environments.

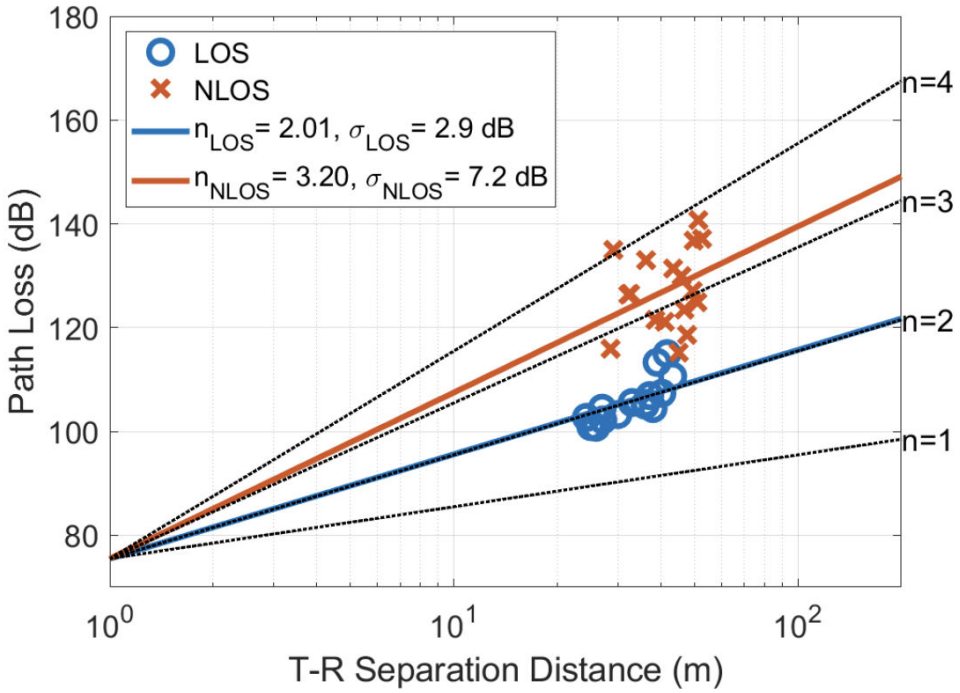

(b) 142 GHz omnidirectional path loss scatter plot and CI models for LOS and NLOS measurements.

Figure 4.2: Omnidirectional path loss for terrestrial local area measurements at 142 GHz [175].

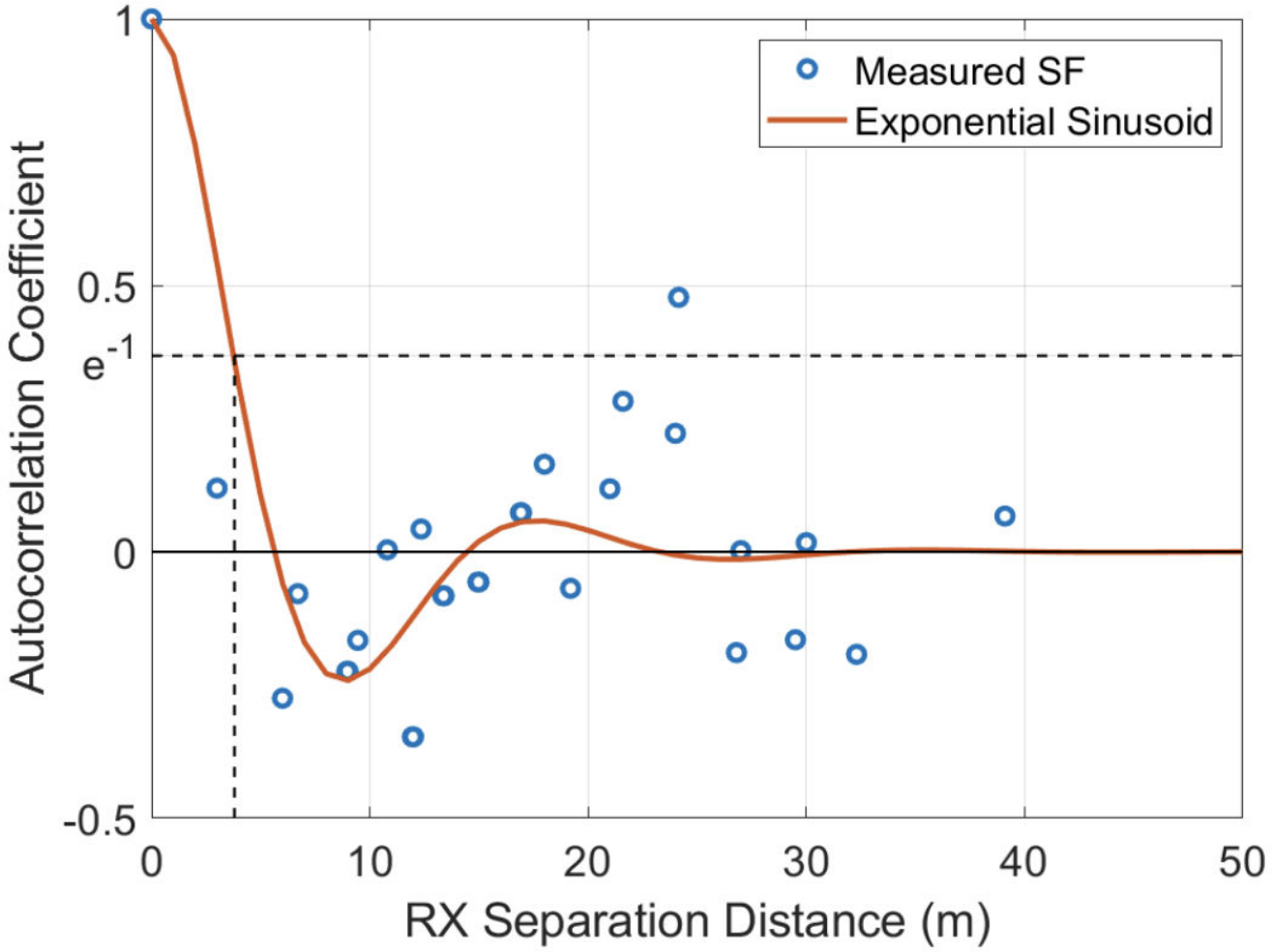

Figure 4.3: The exponential decaying sinusoid function fit to the spatial autocorrelation function of shadow fading with $D_1 = 6.2$ m and $D_2 = 2.8$ m, with a correlation distance of shadow fading of 3.8 m [175].

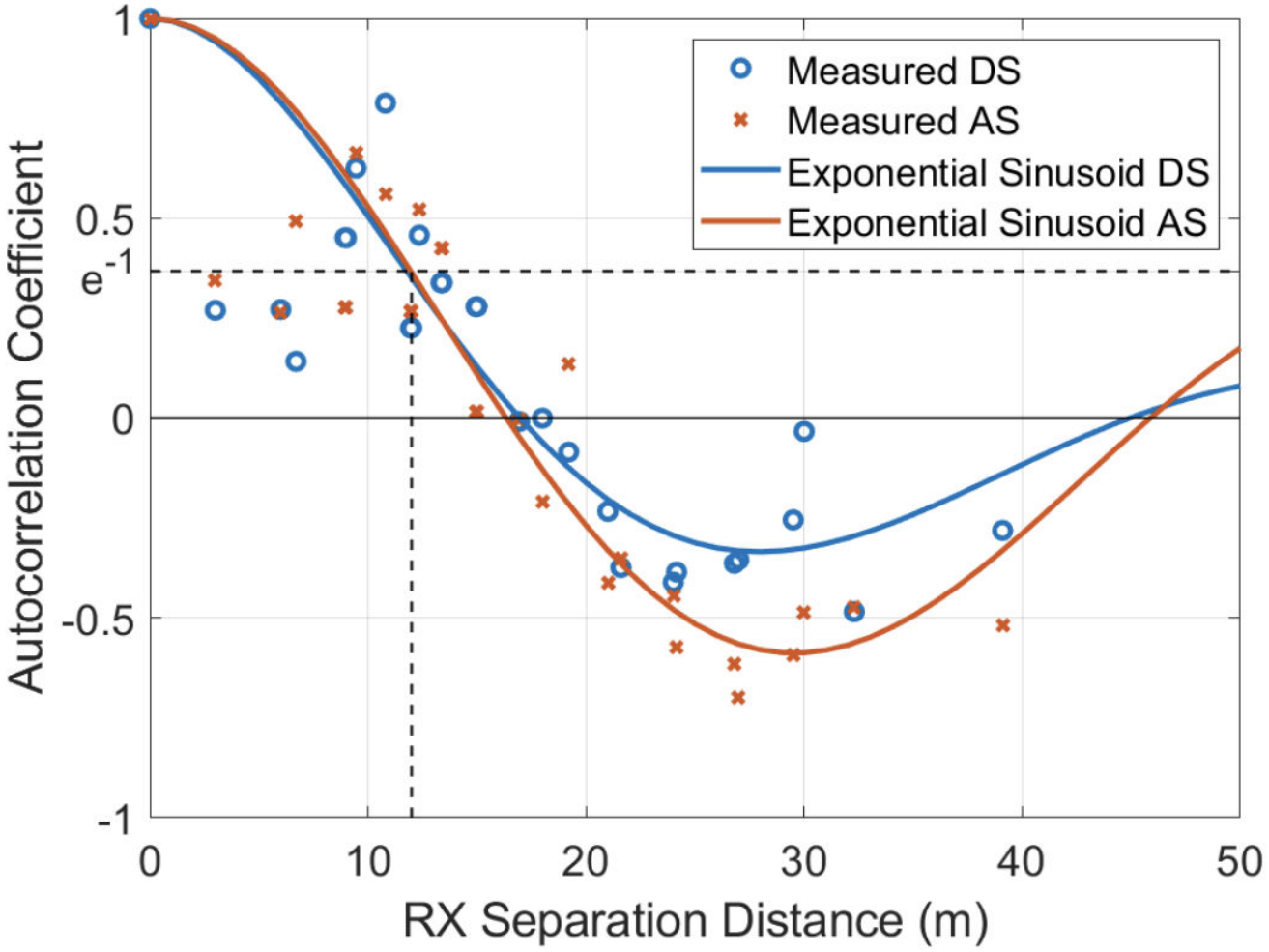

Figure 4.4: The exponential decaying sinusoid function fitS to the spatial autocorrelation function of delay spread (DS) and angular spread (AS) where $D_1 = 25.5$ m and $D_2 = 8.9$ m for the DS; $D_1 = 55.6$ m and $D_2 = 9.4$ m for the AS. The correlation distances of DS and AS are 11.8 m and 12.0 m [175].

4.2 Outdoor 142 GHz Terrestrial Urban Microcell Measurement Campaign

The terrestrial UMi measurement campaign was designed to study the wireless channels and propagation characteristics in the sub-THz bands for 6G cellular communications in urban microcell and small-cell scenarios. Figure 4.6 shows a map of six TX locations and 17 RX locations (with some RX locations reused for more than one TX location, such as RX1) around NYU's downtown Brooklyn campus. TX1 serves nine RX locations, where five of them are LOS (RX1, RX5, RX 23, RX 27, and RX31) and four of them are NLOS (RX9, RX14, RX16, and RX18). TX2 serves four RX locations, where three of them are LOS (RX1, RX35, and RX36) and one of them is NLOS (RX14). TX3 serves four RX locations, where three of them are LOS (RX35, RX36, and RX37) and the other one is NLOS (RX1). TX4 serves four RX locations, where two of them are LOS (RX3 and RX37) and the other two are NLOS (RX1 and RX38). TX5 serves four RX locations, where two of them are LOS (RX3 and RX35) and the other two are NLOS (RX1 and RX10). TX6 serves three RX locations, where one of them is LOS (RX1) and two of them are NLOS (RX39 and RX40). In total, there are 16 LOS TX-RX location combinations and 12 NLOS TX-RX location combinations with TX-RX separation distances up to 117.4 m. All the 16 LOS locations and 11 out of 12 NLOS locations could successfully receive a signal and measure a power delay profile (PDP) through the channel.

During the measurements, TXs were set at heights of 4 m above the ground (similar heights as lampposts) to emulate small-cell base stations (BS), and the RXs were set at heights of 1.5 m above the ground to emulate mobile user receivers. In the surrounding environment, there are metal lampposts, concrete building walls, paved roads, trees, pedestrians, bare soil ground, concrete pillars, glass windows, vehicles, and glass doors, as shown in Figures 4.7, 4.8, 4.9, 4.10, 4.12, and 4.11.

At the beginning and the end of each measurement day, routine calibrations [108] were conducted to make sure all the measurements were valid and accurate [39, 74, 145]. For each TX-RX combination, two elevation angles were used at the BS TX (the TX best pointing elevation angle that the maximum power is received at the RX, and TX antenna downtilts 8° from the best TX pointing elevation angle) and three elevation angles were used at each RX (the best RX pointing elevation angle, and RX antenna uptilts and downtilts 8° from the best RX pointing elevation angle). For each TX and RX elevation angle combination, the antennas at both the TX and RX were exhaustively rotated by 8° HPBW in the azimuth plane (e.g., 45 rotations to cover the 360° plane in azimuth) to capture all the possible multipaths in any azimuth directions. A PDP was recorded for each and every unique TX and RX pointing angle, and omnidirectional PDPs were synthesized as introduced in [176]. Each measured PDP consisted of an average of 20 consecutive instantaneous PDPs to reduce the noise floor, and the averaging factor can be increased at the expense of longer recording time [78].

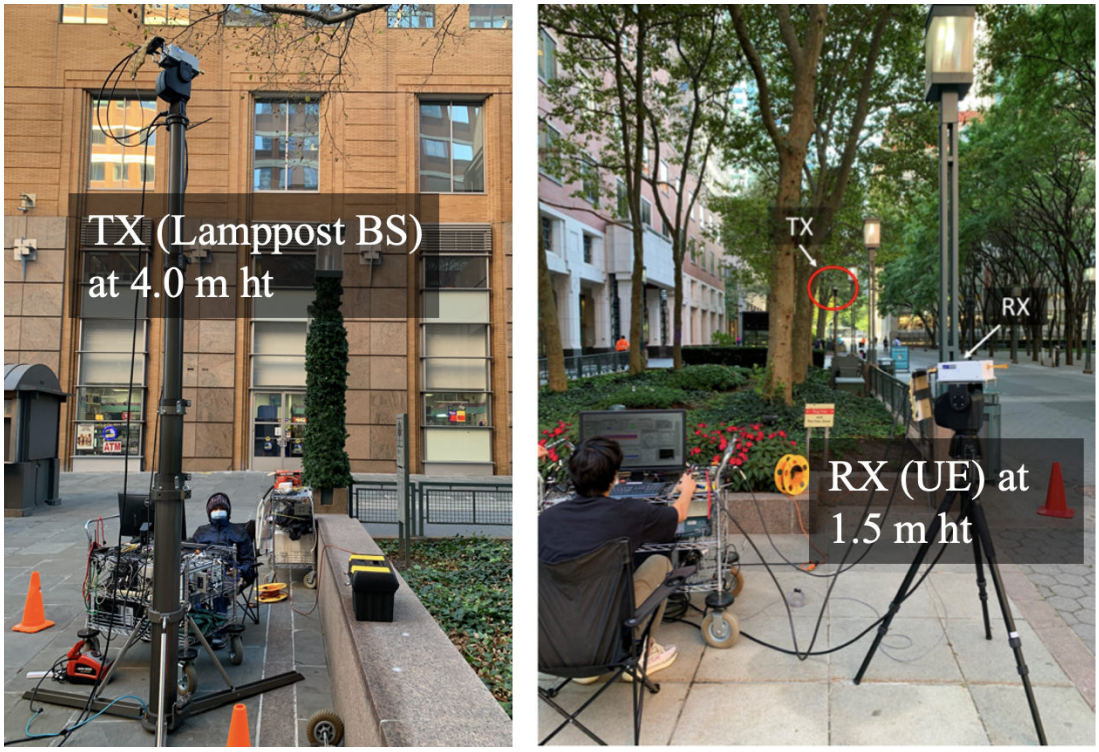

Figure 4.5: The 142 GHz channel sounder system and outdoor UMi measurements in NYU courtyard in Brooklyn, with the TX antenna at 4.0 m above ground level to emulate outdoor small-cell lamppost base stations (BS) and the RX antenna positioned 1.5 m above ground level, similar to the height of a handset terminal [67].

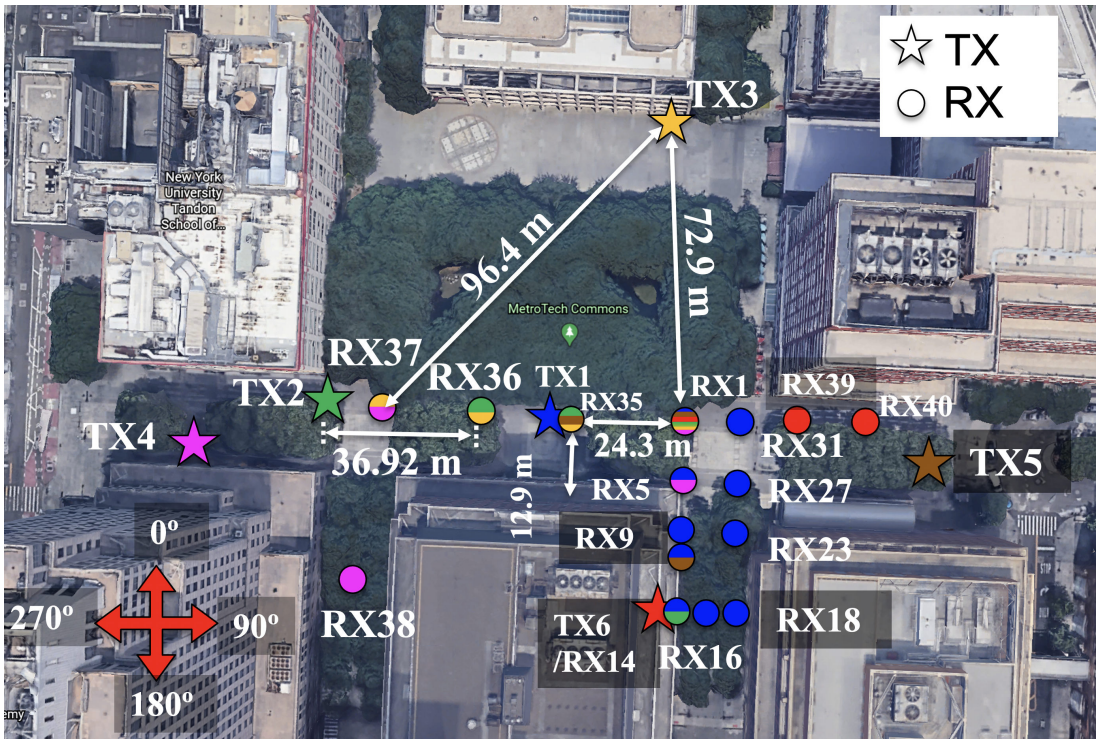

Figure 4.6: Terrestrial urban microcell measurement campaign in NYU's downtown Brooklyn campus. Six TX locations are identified as stars with different colors and the corresponding RX locations are identified as the same color circles.

Figure 4.7: Surrounding environments of the 142 GHz UMi measurements in NYU courtyard, Brooklyn, NY.

Figure 4.8: TX1-RX14 location pair in NLOS scenarios with the surrounding environments.

Figure 4.9: TX1-RX5 location pair in LOS scenarios with the surrounding environments.

Figure 4.10: The surrounding environments of the TX6-RX1 location pair.

Figure 4.11: The surrounding environments of TX5.

Figure 4.12: The surrounding environments of TX2.

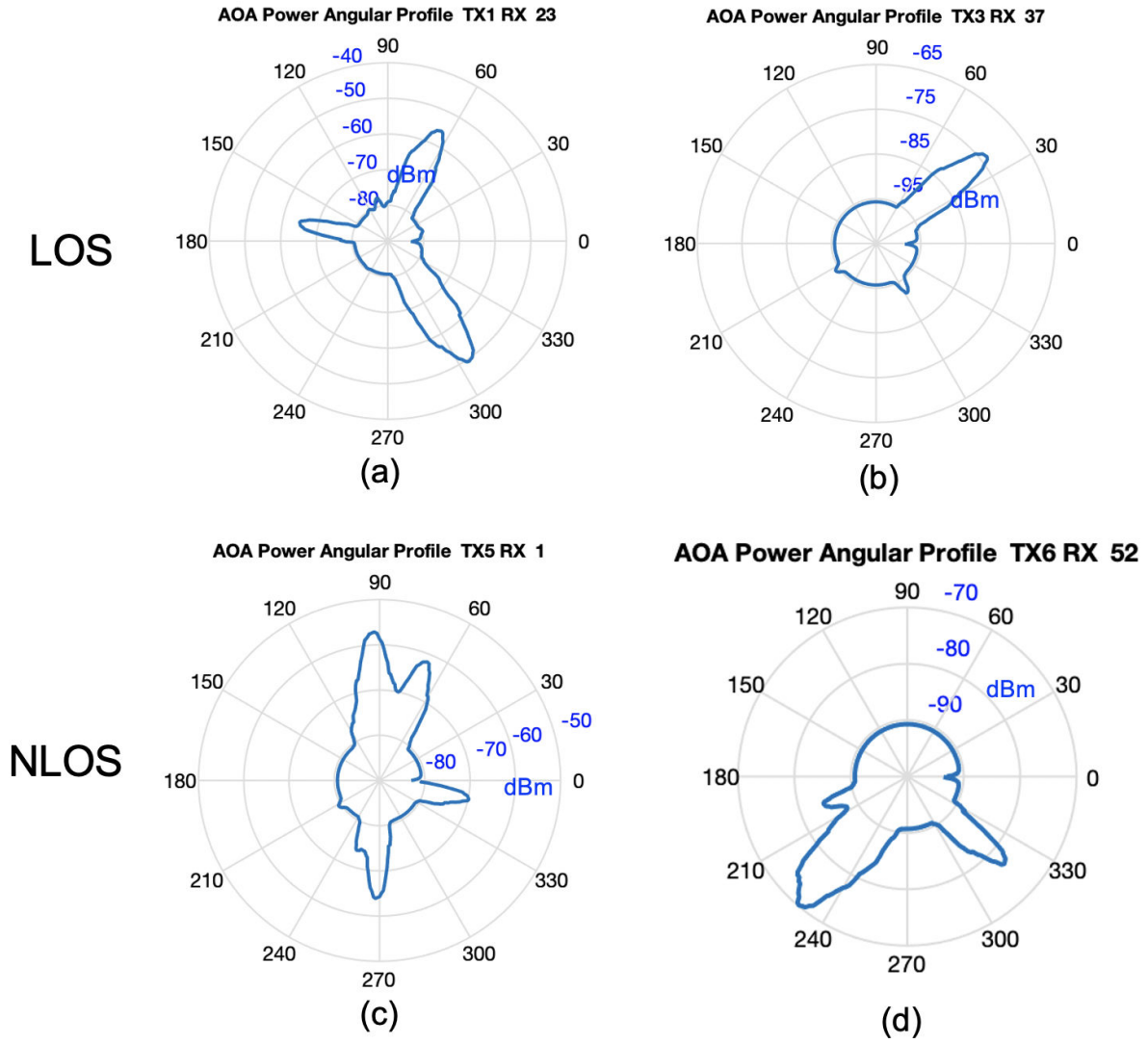

Figure 4.13: 142 GHz UMi Sample Power Angular Profiles in both LOS and NLOS scenarios.

Table 4.1: Outdoor UMi measurement campaigns at 28, 38, 73, and 142 GHz [39, 43, 74, 75].

RF Freq. (GHz)	**RF Bandwidth**	**Antenna HPBW**	**Ant. Gain (dBi)**	**Campaign (UMi)**
28 [39]	0.8 GHz	10.9°	24.5	Manhattan 2012
38 [145]	0.8 GHz	7.8°	25.0	Austin 2011
73 [74]	1.0 GHz	7.0/15.0°	27.0/20.0	Brooklyn 2016
142 [67]	1.0 GHz	8.0°	27.0	Brooklyn 2020

As wireless channels become more sparse and antenna beamwidth is narrower at higher frequencies, rapid beamforming and beam tracking algorithms are required in MIMO systems, which require accurate channel angular information. A 30 dB down from the peak power threshold was used at 142 GHz to detect and keep the MPCs in each power angular profile to study the channel angular statistics.

Figure 4.13 presents four sample AOA power angular profiles in both LOS and NLOS scenarios at 142 GHz. There are three and one distinct AOA directions observed in LOS scenarios as shown in Figure 4.13 (a) and (b), respectively, and there are four and two separated AOA directions observed in NLOS scenarios as shown in Figure 4.13 (c) and (d).

4.3 Comparisons between 28, 38, 73, and 142 GHz in outdoor UMi environments

4.3.1 28 GHz Outdoor UMi Measurements in Manhattan

The 28 GHz outdoor UMi measurements [39, 145, 177] were conducted in downtown Manhattan (a street canyon environment) in 2012 using 24.5 dBi gain, 10.9° Az./El. HPBW steerable horn antennas at both the TX and RX, with a maximum RF transmit power of 30.1 dBm fed to the TX antennas over an 800 MHz RF null-to-null bandwidth. There were three TX locations (two were 7 m and one was 17 m above ground level) and 27 RX locations (1.5 m above ground level) where 74 total TX-RX location combinations were measured ranging from 31 m to 187 m (26 location combinations could receive signals, with 5 LOS and 21 NLOS locations). For each TX-RX location combination, nine RX antenna azimuth sweeps were performed at three distinct RX antenna elevation planes of 0° and ±20° in steps of the 11° HPBW for three distinct fixed TX antenna azimuth angles (the TX pointing directions with the first, second, and third strongest received powers) with a downtilt of −10°.

4.3.2 38 GHz Outdoor UMi Measurements in Austin

The 38 GHz outdoor UMi measurements [39, 145, 177] were conducted in the University of Texas at Austin campus in 2011 using 25.0 dBi gain, 7.8° Az./El. HPBW steerable horn antennas at both the TX and RX, with a maximum RF transmit power of 21.2 dBm fed to the TX antennas over an 800 MHz null-to-null RF bandwidth. There were four rooftop TX locations (one was 8 m, one was 23 m, and two were 36 m above ground level) and 36 RX locations (1.5 m above ground level), yielding 43 total TX-RX combinations (seven RX locations were measured from two different TX locations) ranging from 29 m to 930 m (24 LOS and 19 NLOS location combinations). For each TX-RX combination, the TX and RX antennas were systematically and iteratively steered in both azimuth and elevation directions to capture various multipath components (MPCs).

4.3.3 73 GHz Outdoor UMi Measurements in Brooklyn

The 73 GHz outdoor UMi measurements [178] were conducted in the New York University courtyard in Brooklyn in 2016 with 27.0 dBi gain, 7° Az./El. HPBW steerable directional horn antennas at the TX with a maximum RF transmit power of 14.9 dBm fed to the TX antennas over a 1 GHz null-to-null RF bandwidth, and 20.0 dBi gain, 15° Az./El. HPBW steerable directional horn antennas at the RX. There were 10 TX locations (4 m above ground level) and 11 RX locations (1.5 m above ground level), yielding 36 total measured TX-RX location combinations ranging from 21 m to 140 m (11 LOS and 25 NLOS locations). For each TX-RX location combination, the TX antennas were scanned 120° sectors in azimuth by steps of 8° with the strongest TX pointing angle (when the RX received the maximum power) at the center of the sector (TX elevation angles were fixed), and for each TX pointing angle, the RX antenna was scanned in steps of the 15° HPBW across the entire 360° azimuth at three distinct RX antenna elevation planes (the elevation angle with the strongest RX power and ± 15°on either side of the strongest elevation angle).

4.3.4 142 GHz Outdoor UMi Measurements in Brooklyn

The 142 GHz outdoor UMi measurements [178] were conducted in the identical environment as 73 GHz in New York University Brooklyn courtyard in 2020 using 27.0 dBi gain, 8° Az./El. HPBW steerable directional horn antennas at both the TX and RX, with a maximum RF transmit power of 0 dBm fed to the TX antennas over a 1 GHz null-to-null RF bandwidth. There were six TX locations (4 m above ground level) and 17 RX locations (1.5 m above ground level), yielding 28 total measured TX-RX location combinations ranging from 21 m to 117 m (16 LOS and 12 NLOS locations). Two elevation angles were used for each TX-RX combination at the BS TX (the best TX elevation pointing angle and a downtilt of 8° from the best TX elevation angle) and three elevation angles were used at each RX location (the best RX elevation pointing angle, and uptilts or downtilts of 8° from the best RX elevation angle). For each TX and RX elevation angle combination, the antennas at both the TX and RX were swept 360° in the azimuth plane by 8° steps to exhaustively

search any MPCs.

4.3.5 UMi Large-Scale Path Loss and Models in 28, 38, 73, 142 GHz Bands

Understanding the wireless channels above 100 GHz is the critical first step for researchers to design future THz communication systems for 6G and beyond. This section analyzes and compares outdoor UMi propagation measurements at 28 GHz [39] (Manhattan, New York), 38 GHz (Texas, Austin) [177], 73 GHz (Brooklyn, New York) [178], and most recently 142 GHz (Brooklyn, New York) [67], conducted over a nine-year period since 2011 with communication ranges up to 930 m [39, 44, 67, 83, 145, 159, 178]. Compared to previous measurements at frequencies below 100 GHz, more challenges exist when building channel sounders at 142 GHz [75]. The limited transmit power and severe free space path loss in the first meter at higher frequencies require the channel sounder system to use high gain directional antennas/arrays which need a longer scan time to capture signals from all possible directions. The detailed measurement locations and procedures at each frequency can be found in [39, 44, 67, 83, 145, 159, 178]. Wideband sliding correlation-based (time domain spread spectrum) channel sounding systems with identical rotatable horn antennas for each frequency at both link ends were used, as shown in Table 4.1.

The 1 m close-in (CI) free space reference distance model (4.1) is one of the most commonly used large-scale path loss models to predict the signal strength over distance, and is valid over different frequency bands [92, 135, 141, 145, 147]:

$$\begin{aligned} PL^{CI}(f_c, d_{3\text{D}}) \ &= \text{FSPL}(f_c, 1\text{ m}) + 10n\log_{10}\left(\frac{d_{3D}}{1\text{ m}}\right) + \chi_\sigma, \\ \text{FSPL}(f_c, 1\text{ m}) &= 32.4 + 20\log_{10}(\frac{f_c}{1\text{ GHz}}), \end{aligned} \tag{4.1}$$

where $d_{3\text{D}}$ is the 3D separation distance between the TX and RX antennas, $\text{FSPL}(f_c, 1\text{ m})$ is the free space path loss at carrier frequency f_c in GHz at 1 m in dB, n is the path loss exponent (PLE), and χ_σ is the shadow fading in dB (a zero mean Gaussian random variable with a standard deviation σ in dB) [38, 44, 78, 145, 147].

In prior work [39, 177] at 28 and 38 GHz, the close-in (CI) free space reference distance path loss model with free space reference distances of $d_0 = 3$ m and 5 m were used. Subsequent work in [44, 145] studied the optimized reference distance d_{opt} and showed using a $d_0 = 1$ m free space reference distance has negligible difference in accuracy when compared to the optimal d_{opt}, and is more sensible for a universal standard for comparing path loss among different frequencies, locations, and researchers [44]. In addition, using the 1 m close-in free space reference distance (a leverage point) assures path loss has a continuous physical tie to signal strength over distance for multi-frequency bands and wide ranges of environments [44]. Therefore, the CI path loss model with a $d_0 = 1$ m reference distance (the equations could be found in [44, 92, 135, 141, 145, 158]) is used to present

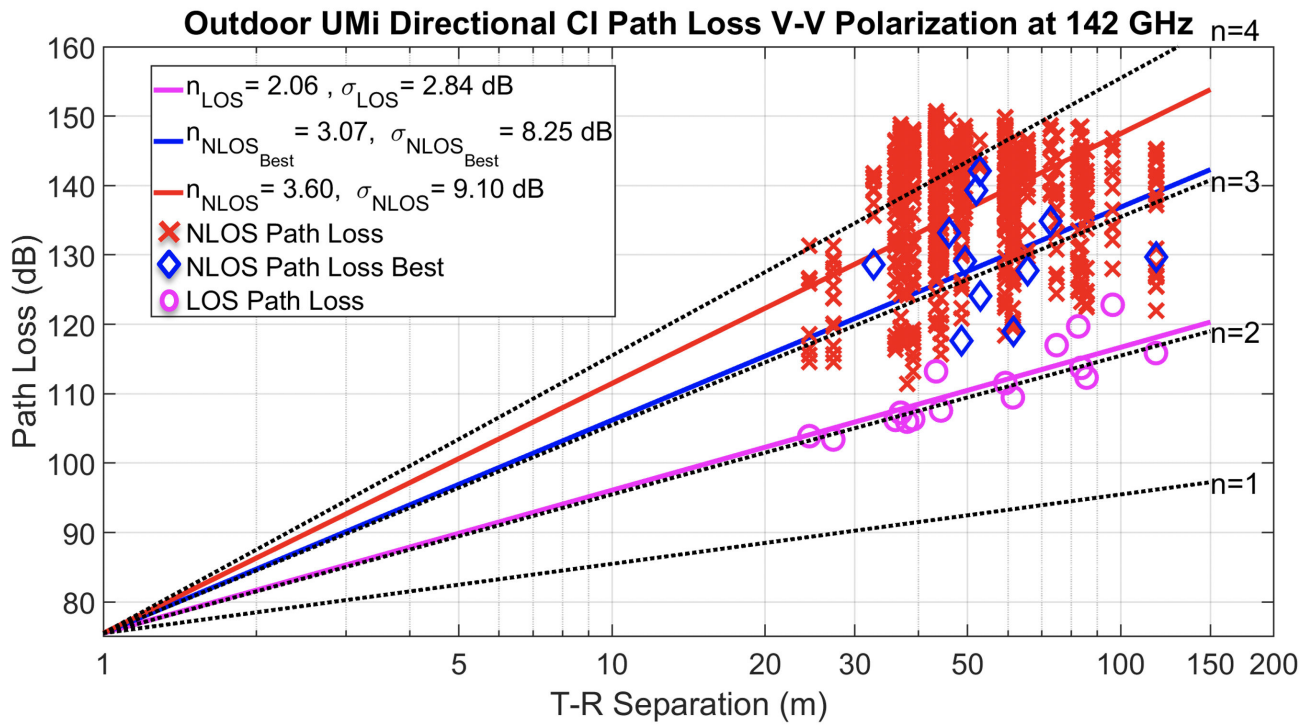

Figure 4.14: Urban UMi 142 GHz directional path loss scatter plot and outdoor directional CI (d_0= 1 m) path loss model for both LOS and NLOS scenarios using 27 dBi gain and 8° HPBW horn antennas at both the TX and RX (without antenna gains included for path loss calculations). Each green circle represents the LOS path loss at a LOS location, red crosses represent NLOS path losses measured at arbitrary antenna pointing angles between the TX and RX for NLOS scenarios, and each blue diamond represents the best antenna pointing angles of both the TX and RX to receive the maximum power at the RX for each NLOS TX-RX location combination [67].

the measured path loss and shadow fading in this paper. The methods to compute the multipath numbers, the corresponding channel-gain, RMS delay spread, and RMS angular spread can be found in [92].

4.3.6 UMi CI Path Loss Model in a Single Frequency Band

The outdoor UMi LOS directional path loss exponent (PLE) for the single-frequency CI model is n = 2.3 at 28 GHz, n = 1.9 at 38 GHz, n = 2.0 at 73 GHz, and n = 2.1 at 142 GHz with shadow fading standard deviations of σ = 4.3 dB, 3.5 dB, 1.9 dB, and 2.8 dB as shown in Table 4.2, respectively. The higher PLE at 28 GHz is because of antenna misalignment or foliage attenuation between the TX and RX, indicating that accurate beam searching and beam steering algorithms are needed for directional antennas. The LOS measurements show that there is only 1-2 dB larger average loss per decade of distance in the 142 GHz band compared to the average path loss in the 38 and 73 GHz bands when referenced to the first meter free space path loss [1, 44, 159], which can be easily compensated for in a practical system by higher antenna gains.

The higher gain antennas will not take a larger physical area since the antenna gain increases quadratically as frequency increases if the physical size of the antenna (effective aperture) is kept

constant over frequency [1, 74, 75]. Thus, the infrastructure spacing in mobile systems will not have to change as frequencies increase up to THz scale, since increased bandwidth channels at higher frequencies can serve over similar distances if the antenna area remains constant [1, 74, 75].

The PLE increasing slightly to 2.0 and 2.1 at 73 and 142 GHz, respectively, hints at the fact that higher sub-THz frequencies have fewer reflections in LOS directional channels (e.g., less waveguiding) due to narrower beam antennas (as shown in Table 4.1) at both ends of the link that attenuate energy that would otherwise reflect off of surfaces of building walls and ground. The slightly higher path loss and fewer reflections at higher frequencies are also observed in indoor radio propagation [43, 92].

$\text{NLOS}_{\text{Best}}$ denotes the optimal situation at each NLOS measurement location that antennas of the TX and RX are pointing in the best direction when the RX captures the maximum power [43, 92, 141]. This measurement approach emulates how practical systems would employ directional beamforming in a real-world link to maximize the signal-to-noise ratio (SNR).

The $\text{NLOS}_{\text{Best}}$ PLEs of the CI model are n = 3.8, 2.7, 3.1, and 3.1 at 28, 38, 73, and 142 GHz, respectively, as shown in Table 4.2. The buildings are less dense in Austin (38 GHz) than in downtown Manhattan (28 GHz) and Brooklyn (73 and 142 GHz), thus the transmitted signal at 38 GHz did not encounter as many physical obstructions (blockages) as in Manhattan and Brooklyn, resulting in a substantially lower PLE of 2.7 at 38 GHz compared to the PLEs at the other three frequencies. However, the $\text{NLOS}_{\text{Best}}$ PLEs at 28, 73, and 142 GHz are remarkably similar to one another with slightly lower PLEs at higher frequencies, which is because of the stronger reflections at higher frequencies (which is also observed in indoor measurements at 28, 73, and 142 GHz [43, 66]).

Omnidirectional antenna pattern and received power were synthesized by summing the received powers from every measured non-overlapping directional HPBW antenna pointing angle combination [176]. Figure 4.17 shows the scatter plot of synthesized omnidirectional measured path loss (without antenna gains) at 28, 38, 73, and 142 GHz in outdoor UMi environments ranging from 20-930 m, where the LOS and NLOS path loss data are denoted as circles and diamonds, respectively, and different frequency bands are marked with various colors [44, 45, 67, 83, 145, 178].

A typical omnidirectional PDP measured between TX1 and RX23 in the LOS scenario with a TX-RX separation distance of 43.34 m is shown in Figure4.15 (omnidirectional PDPs in NLOS scenarios are being synthesized with the help of the NYURay ray-tracer [132], and will be available in future work). Figure 4.15 shows four time clusters [179], where there are between 1 to 4 multipath components in each time cluster and 10 multipath components in total. The first multipath component is the boresight LOS path from TX1 to RX23 with a propagation time delay of 144.47 ns. The other multipath components are either reflected from the neighboring buildings, pillars, or surrounding lampposts, resulting in a root mean square delay spread of 37.6 ns.

Conventional wisdom before this work is that LOS communication would be the main use case (e.g., 6G cellular and backhaul) at 142 GHz in outdoor environments. However, we observed that many outdoor construction materials (e.g., metal lamppost, concrete building walls, and tinted glass) served as excellent reflectors at 142 GHz which enabled good NLOS coverage up to 117.4 m, as shown

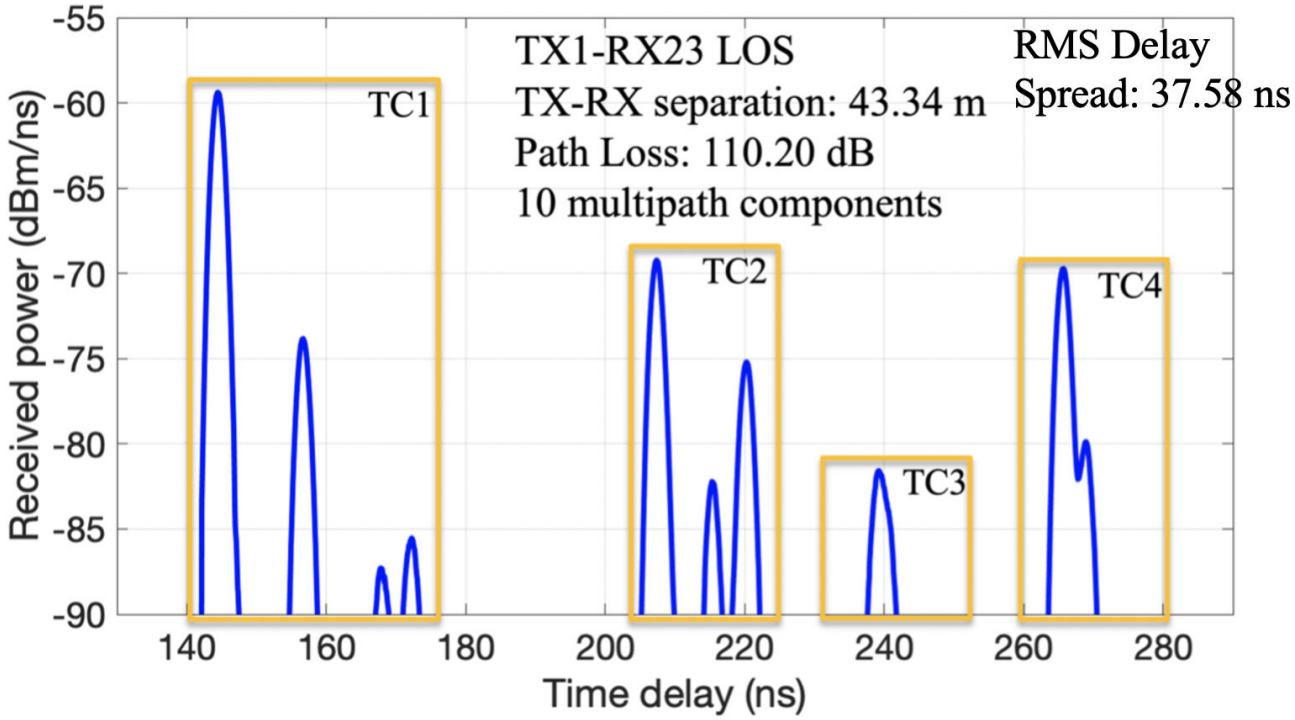

Figure 4.15: Omnidirectional PDP of TX1-RX23 which is in the LOS scenario with a separation distance of 43.34 m. There are 10 multipath components in four time clusters (TC), where the first multipath component is the LOS path, and the others are reflected paths from the neighbor buildings and surrounding lampposts as shown in Figure 4.6 [67].

in Figs. 4.14 and 4.16.

Figure 4.17 shows the scatter plot of synthesized omnidirectional measured path loss (without antenna gains) at 28, 38, 73, and 142 GHz in outdoor UMi environments ranging from 20-930 m, where the LOS and NLOS path loss data are denoted as circles and diamonds, respectively, and different frequency bands are marked with various colors [44, 45, 67, 83, 145, 178].

4.3.7 UMi CI and CIF Models in Multi-Frequency Bands

The multi-frequency CI model with a frequency-weighted PLE (CIF) [44, 141] was proposed as a viable multi-band path loss model valid across various frequency bands [43, 44, 158]:

$$\begin{aligned} PL^{CIF}(f_c,d_{3\mathrm{D}}) &= \mathrm{FSPL}(f_c, d_0)+ \\ &\quad 10n\left(1+b\left(\frac{f-f_0}{f_0}\right)\right)\log_{10}\left(\frac{d}{d_0}\right)+\chi_\sigma^{CIF}, \\ &\quad \text{where } f_0 = \sum_{k=1}^{K} f_k N_k / \sum_{k=1}^{K} N_k. \end{aligned} \tag{4.2}$$

In addition to the PLE n, the two-parameter CIF path loss model (4.2) uses another parameter b to present the frequency dependency of path loss, and a large absolute value of b (e.g., $b = 0.5$) means the PLE is highly dependent on frequencies, vice versa.

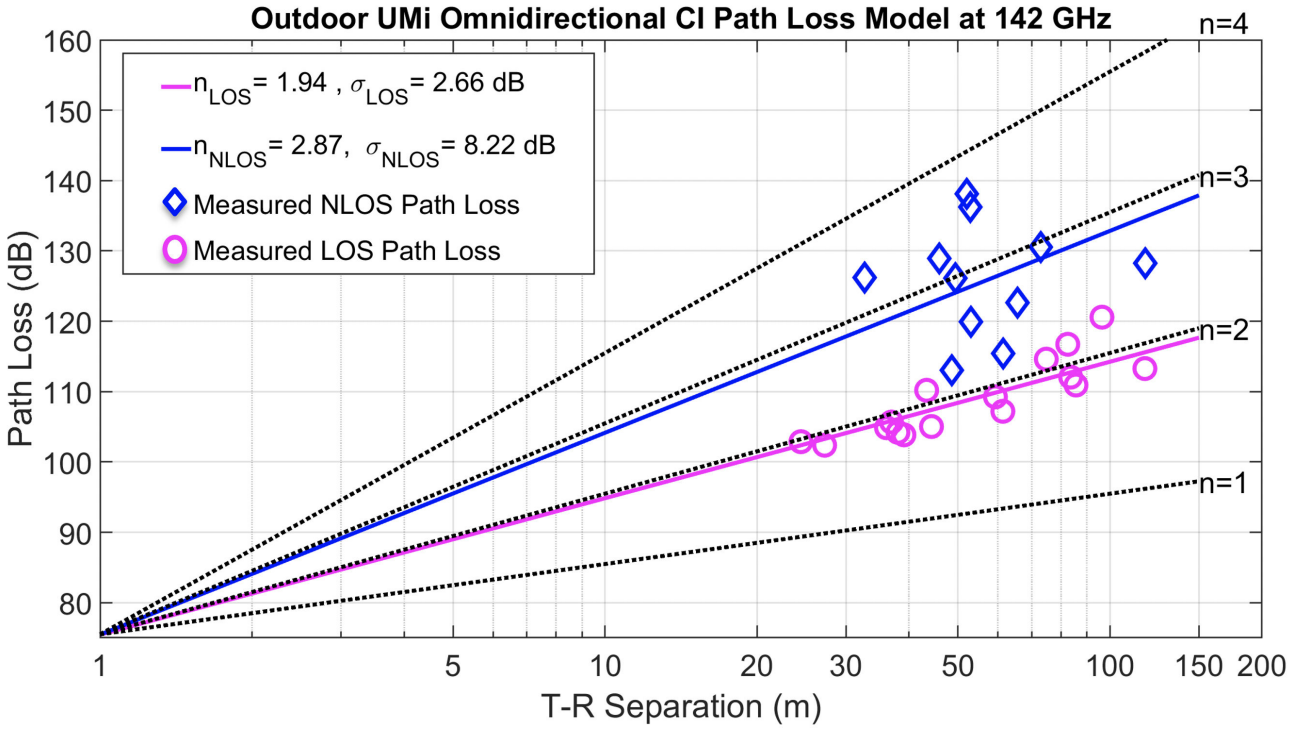

Figure 4.16: Urban UMi best-fit omnidirectional CI path loss model (without antenna gains) at 142 GHz for both LOS and NLOS situations. The blue diamonds represent the measured omnidirectional path loss at 142 GHz in the NLOS environment and the green circles, conversely, represent the LOS situation.

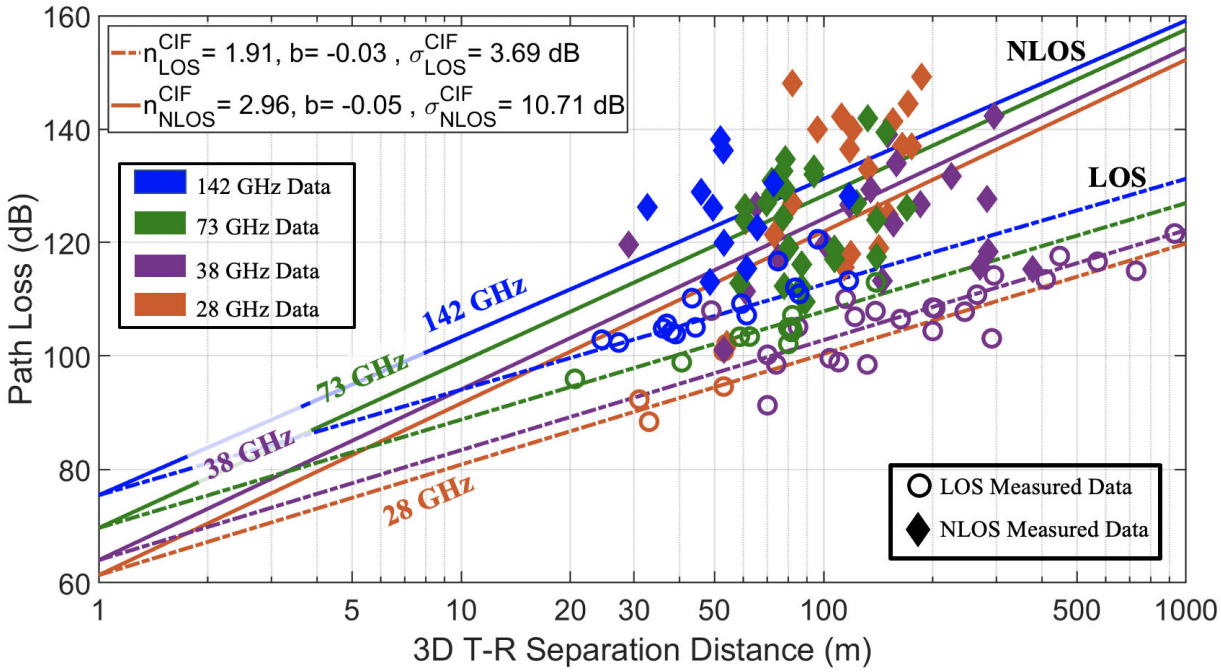

Figure 4.17: Outdoor UMi 28, 38, 73, and 142 GHz multi-band omnidirectional CIF path loss models with 1 m free space reference distance and without antenna gains [44, 45, 67, 83, 145, 178]. The f_0 computed by (4.2) is 73 and 62 GHz for LOS and NLOS conditions, respectively (more NLOS locations were measured at lower frequencies).

Table 4.2: Directional UMi CI and CIF path loss models and RMS delay spread in both LOS (boresight), NLOS Best, and NLOS Arbitrary pointing directions at 28 GHz (Manhattan, 31-187m), 38 GHz (Austin, 29-930m), 73 GHz (Brooklyn, 21-170m), and 142 GHz (Brooklyn, 24-117m) [44, 45, 83, 145, 178]. The weighted average frequency f_0 is 73 GHz for LOS scenarios and 62 GHz for NLOS scenarios.

Urban Microcell		**Directional-LOS**				**Directional-NLOS$_{\textbf{Best}}$**			
Frequency [GHz]		**28**	**38**	**73**	**142**	**28**	**38**	**73**	**142**
Directional Antenna HPBW		11°	8°	7/15°	8°	11°	8°	7/15°	8°
Single-Band PL CI	n	2.3	1.9	2.0	2.1	3.8	2.7	3.1	3.1
	σ^{CI} [dB]	4.3	3.5	1.9	2.8	9.3	7.9	10.5	8.3
Multi-Band PL CI	n	2.07				3.21			
	σ^{CI} [dB]	3.6				9.8			
Multi-Band PL CIF	n, b	$n = 2.07, b = -0.10$				$n = 3.21, b = -0.03$			
	σ^{CIF} [dB]	3.5				9.6			
RMS DS [145]	$\min_{DS}$ [ns]	0.8	N/A	0.7	0.7	1.0	N/A	0.6	0.6
	$\max_{DS}$ [ns]	2.6	N/A	0.7	13.9	165.1	N/A	77.0	32.7
	μ_{DS} [ns]	0.9	N/A	0.7	1.7	17.9	N/A	10.3	4.5
	σ_{DS} [ns]	1.0	N/A	0.1	3.4	13.0	N/A	18.7	9.7

The CIF model (4.2) can be considered as an extension of the CI model (4.1) to offer an extra degree of freedom for accurate statistical modeling.

The CIF path loss model (4.2) uses two parameters to model average path loss over distance over multiple frequency bands, and reverts to the single-parameter CI model (4.1) when $b = 0$ or when using data from just one frequency band [44, 45, 141]. The introduction and closed-form expressions for the best-fit model parameters of the CIF model can be found in [44, 141] and is expected to be useful over the wide swath for bands going up to THz [32, 141].

The weighted average frequency f_0 is computed over K frequency bands as in (4.2), where N_k is the number of measurements at a particular frequency f_k [44, 141]. In this paper, we used the path loss data at 28, 38, 73, and 142 GHz to calculate $f_0 = 73$ GHz for LOS scenarios, and $f_0 = 62$ GHz for NLOS scenarios (there are 21 NLOS locations compared to 5 LOS locations at 28 GHz which moved f_0 lower for NLOS scenarios).

In outdoor UMI scenarios, the LOS best-fit omnidirectional CIF model are $n_{LOS}^{CIF} = 1.91$ and $b_{LOS}^{CIF} = -0.03$ with $\sigma_{LOS}^{CIF} = 3.72$ dB across 28, 38, 73, and 142 GHz as presented in Table 4.4. The NLOS omnidirectional CIF model are $n_{NLOS}^{CIF} = 2.96$ and $b_{NLOS}^{CIF} = -0.05$ with $\sigma_{NLOS}^{CIF} = 10.93$ dB.

Remarkable similarities in terms of PLEs are observed for CI and CIF path loss models over 28, 38, 73, and 142 GHz bands (n is the same and b is remarkably small) [44, 45, 141], which indicates

Table 4.3: **Continue of Table 4.2**. Directional UMi CI and CIF path loss models and RMS delay spread in NLOS Arbitrary pointing directions at 28 GHz (Manhattan, 31-187m), 38 GHz (Austin, 29-930m), 73 GHz (Brooklyn, 21-170m), and 142 GHz (Brooklyn, 24-117m) [44, 45, 83, 145, 178]. The weighted average frequency f_0 is 62 GHz for NLOS scenarios.

Urban Microcell		**Directional-NLOS**			
Frequency [GHz]		**28**	**38**	**73**	**142**
Directional Antenna HPBW		11°	8°	7/15°	8°
Single-Band PL CI	n	4.5	3.3	4.6	3.60
	σ^{CI} [dB]	10.0	10.3	10.5	9.1
Multi-Band PL CI	n	3.96			
	σ^{CI} [dB]	11.5			
Multi-Band PL CIF	n, b	$n = 3.96, b = -0.05$			
	σ^{CIF} [dB]	11.5			
RMS DS [145]	$\min_{DS}$ [ns]	0.5	1.0	0.5	0.6
	$\max_{DS}$ [ns]	420.0	180.0	290.1	53.0
	μ_{DS} [ns]	25.7	11.4	23.4	9.2
	σ_{DS} [ns]	25.0	N/A	31.6	17.4

the extra parameter b in the CIF model may not be needed for outdoor UMi environment over a wide range of frequencies from the mmWave to THz bands. This presents that an identical PLE may accurately model path loss over a vast range of frequencies in UMi environments, with the only frequency-dependent effect happening in the first meter of propagation [32, 44, 45, 141].

In UMi LOS omnidirectional scenarios, $n^{CIF}_{LOS} = 1.91$ and $b^{CIF}_{LOS} = -0.03$ are the best-fit parameters of the omnidirectional CIF path loss model with a shadow fading standard deviation of $\sigma^{CIF}_{LOS} = 3.72$ dB across 28, 38, 73, and 142 GHz, as presented in Table 4.4. In UMi NLOS omnidirectional scenarios, $n^{CIF}_{NLOS} = 2.96$ and $b^{CIF}_{NLOS} = -0.05$ are the best-fit parameters of the omnidirectional CIF path loss model with a shadow fading standard deviation of $\sigma^{CIF}_{NLOS} = 10.93$ dB, when applied to all NLOS measurements across 28, 38, 73, and 142 GHz, as shown in Table 4.4.

The CI path loss model (4.1) can also serve as a multi-band path loss model, using only a single parameter PLE n [44, 45, 141].

Table 4.2 and 4.4 summarize directional and omnidirectional multi-band CI and CIF path loss models for both LOS and NLOS scenarios, and both models provide nearly identical results in terms of the path loss and shadow fading over four frequency bands, as also shown in Figure 4.17. The 3GPP UMi omnidirectional path loss models [135] which are proposed for frequencies from 0.5-100 GHz are also presented in Table 4.4 for comparisons. In general, the 3GPP UMi CI path loss models

Table 4.4: Omnidirectional UMi path loss CI and CIF models, RMS angle of arrival spread (ASA) and RMS angle of departure spread (ASD) at 28 GHz (Manhattan, 31-187 m), 38 GHz (Austin, 29-930 m), 73 GHz (Brooklyn. 21-170 m), and 142 GHz (Brooklyn, 24-117m) [44, 45, 83, 135, 145, 178]. The weighted average frequency f_0 of CIF path loss models is 73 GHz for LOS and 62 GHz for NLOS scenarios. A 30 dB down threshold from the peak MPC power at each RX location was used to detect MPCs.

Urban Microcell		**Omnidirectional-LOS**				**Omnidirectional-NLOS**			
Frequency [GHz]		**28**	**38**	**73**	**142**	**28**	**38**	**73**	**142**
Single-Band PL CI	n	2.1	1.9	1.9	1.9	3.4	2.7	2.8	2.9
	σ^{CI} [dB]	3.6	4.4	1.7	2.7	9.7	10.1	8.7	8.2
Multi-Band PL CI	n	1.91				2.96			
	σ^{CI} [dB]	3.72				10.93			
Multi-Band PL CIF	n, b	$n = 1.91, b = -0.03$				$n = 2.96, b = -0.05$			
	σ^{CIF} [dB]	3.69				10.71			
RMS AOA spread	$\min_{ASA}$ [ns]	0°	N/A	8.8°	3.2°	2.6°	N/A	15.3°	3.4°
	$\max_{ASA}$ [ns]	58.4°	N/A	36.3°	15.3°	62.2°	N/A	65.6°	59.2°
	μ_{ASA} [ns]	30.8°	N/A	19.3°	10.1°	32.5°	N/A	33.5°	32.5°
	σ_{ASA} [ns]	26.2 °	N/A	8.9°	3.1°	23.8°	N/A	12.3°	18.2 °
RMS AOD spread	$\min_{ASD}$ [ns]	0°	N/A	3.2°	0.6°	4.0°	N/A	7.0°	0°
	$\max_{ASD}$ [ns]	42.9°	N/A	10.8°	21.7°	40.4°	N/A	33.7°	18.0°
	μ_{ASD} [ns]	12.5°	N/A	5.3°	6.0°	22.4°	N/A	15.8°	6.3°
	σ_{ASD} [ns]	16.0 °	N/A	2.4°	5.3°	12.0°	N/A	8.4°	6.5 °
Number of AOA Directions	n_{AOA}	3.6	N/A	2.8	1.9	4.7	N/A	4.3	4.1
	σ_{AOA}	3.4	N/A	3.2	1.1	3.0	N/A	2.8	2.6
Number of AOD Directions	n_{AOD}	2.1	N/A	1.6	1.3	3.3	N/A	2.2	1.6
	σ_{AOD}	2.6	N/A	1.0	1.3	2.5	N/A	1.9	2.1
RMS DS [145]	$\min_{DS}$ [ns]	0.70	0.60	0.71	N/A	0.60	0.50	0.60	N/A
	$\max_{DS}$ [ns]	134.40	101.90	11.94	N/A	198.50	142.00	60.87	N/A
	μ_{DS} [ns]	10.80	6.24	3.00	20.40	17.10	12.30	9.20	27.40
	σ_{DS} [ns]	4.24	4.11	2.14	5.68	13.80	14.2	8.74	8.57

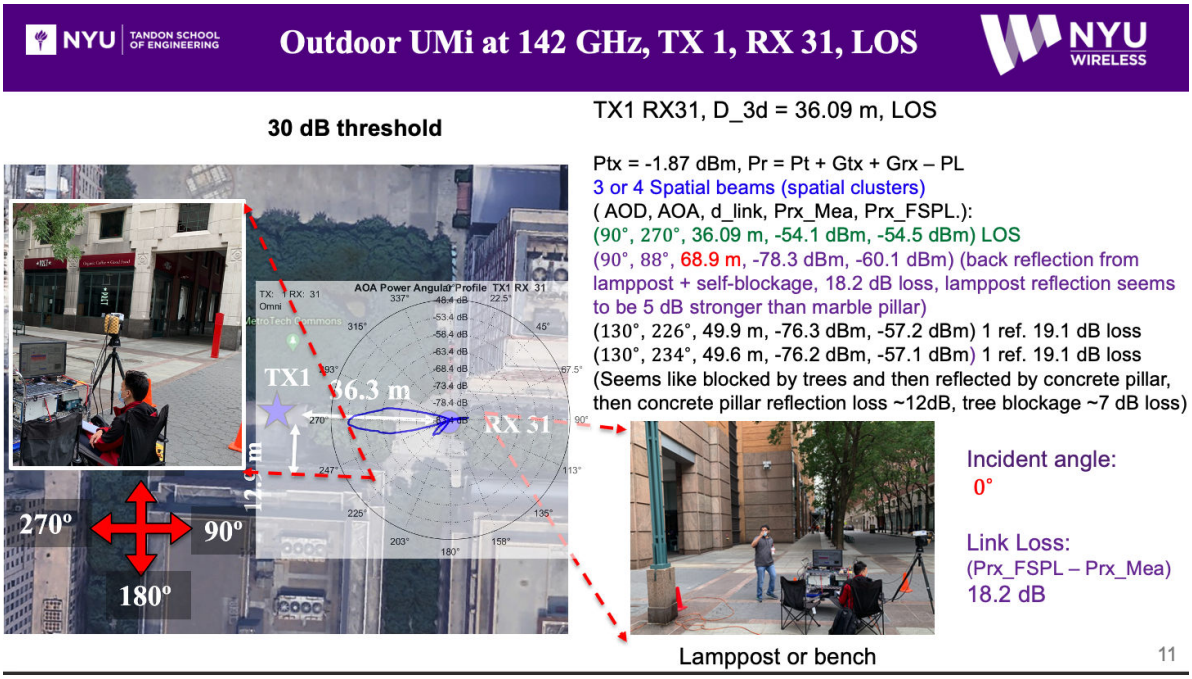

Figure 4.18: Outdoor 142 GHz UMi propagation between TX1 and RX31 which is in LOS scenarios.

are close to the multi-frequency path loss models presented in this letter in terms of PLEs and shadow fading standard deviations in both LOS and NLOS scenarios. The PLEs of the 3GPP UMi path loss models are close to the PLEs at 28 GHz and overestimate the path loss at higher frequencies, which may be due to the fact that 3GPP models are developed from a large number of measurements around 28 GHz but few measurements at higher frequencies up to 100 GHz [158].

Some samples of measured AOA directions for different TX-RX pairs are shown in Figures 4.18 and 4.19. A 30 dB threshold down from the peak is applied to detect the spatial multipath components (spatial clusters). The distinguishable TX-RX links are shown in the form of AOD, AOA, link distances, RX measured received power, and the theoretical free space path loss. For example, as shown in Figure 4.18, there are 4 distinguishable (3 strong spatial directions and one weak spatial direction) spatial directions at RX 31 that can receive signals from TX1. The LOS link (the strongest path) is when the TX antenna is pointing at 90°and the RX antenna is pointing at 270°in azimuth. The LOS link length is 36.09 m (physically measured and then used this measured distance to validate ray tracer). The measured received power after the RX antenna (27 dBi gain) is -54.1 dBm (with TX transmit power of -1.87 dBm feed into the TX antenna, 23 dBi gain), and the theoretical received power assuming free space propagation is -54.5 dBm, as shown by the green text in Figure 4.18. Similarly, the other three spatial links are presented in the same way, and predictions of reflection losses of different surfaces from the surrounding environments are also shown.

Empirical reflection loss and blockage loss (penetration loss) from the measurements are presented in Figure 4.20. For example, a 12 dB reflection loss is observed for concrete pillars at an incident angle of 45°, and 3-7 dB tree blockage loss is observed from the measurements. These values are useful for ray tracer predictions of the power of each MPC at frequencies above 100 GHz.

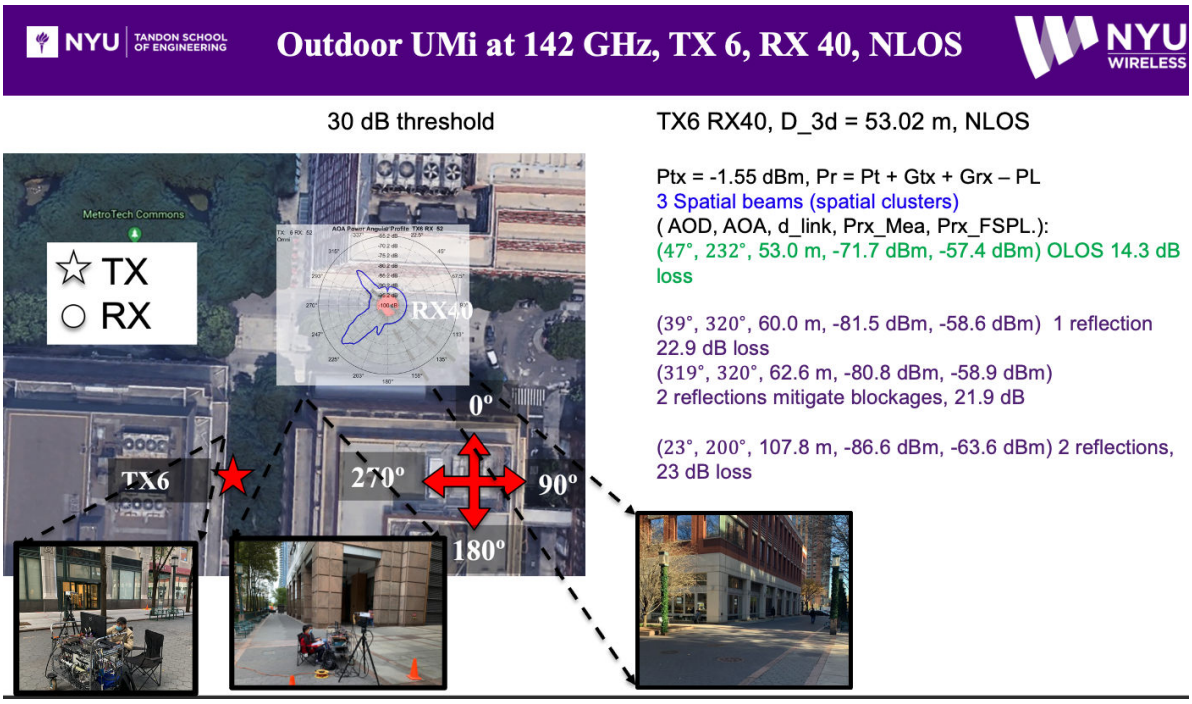

Figure 4.19: Outdoor 142 GHz UMi propagation between TX6 and RX40 which is in NLOS scenarios.

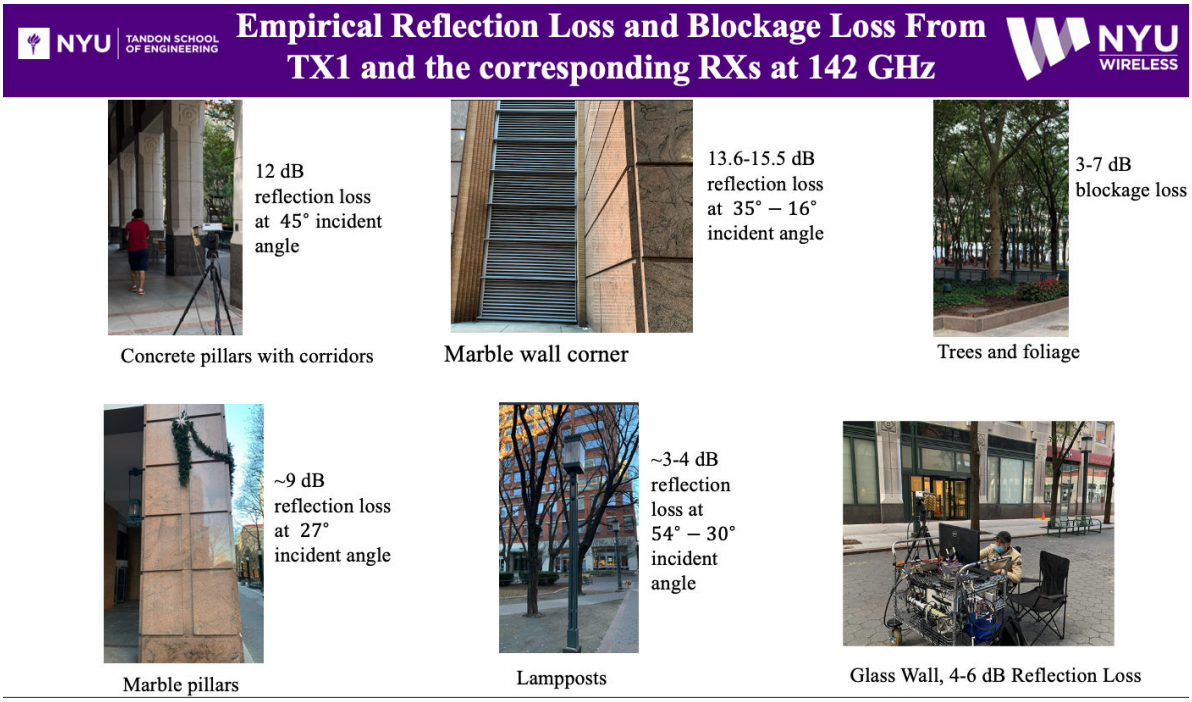

Figure 4.20: Empirical reflection loss, penetration loss, and foliage loss at 142 GHz from field measurements in outdoor Urban Microcell environments.

4.4 RMS Delay Spreads at 28, 38, 73, and 142 GHz

The minimum, maximum, and mean of RMS delay spreads from the aforementioned outdoor UMi measurements at 28, 38, 73, and 142 GHz are presented in Table 4.2 for directional outdoor UMi channels [39, 145, 177]. A 5 dB SNR threshold was used in this letter for all four bands to detect and keep the MPCs in each power delay profile [145].

Table 4.2 shows that the UMi directional LOS RMS DS is negligible with a mean of 1-2 ns from 28 to 142 GHz, indicating the fact that the LOS multipath component is the only dominant path (no other MPCs or powers of other MPCs are negligible) when narrow-beam directional antennas are pointing in the boresight direction in LOS scenarios in mmWave and sub-THz bands.

For UMi directional $\text{NLOS}_{\text{Best}}$ scenarios, the mean RMS DS (μ_{DS}) is 18 ns, 10 ns, and 5 ns at 28, 73, and 142 GHz, respectively, which implies more than one multipath components can be received in NLOS scenarios with directional antennas. The maximum RMS DS ($\max_{DS}$) decreases as frequency increases and is 165 ns at 28 GHz, 77 ns at 73 GHz, and 32 ns at 142 GHz, with only 10% of the RMS DS larger than 88 ns, 37 ns, and 15 ns in 28, 73, and 142 GHz bands, respectively. The mean and maximum RMS delay spread decreases as frequency increases, which is likely due to there are higher losses introduced by obstructions and foliage, and fewer reflections captured by the directional antennas at higher frequencies.

When the RX antenna was not pointing to the $\text{NLOS}_{\text{Best}}$ direction in NLOS scenarios or to the LOS boresight direction in LOS scenarios (arbitrarily pointing), the maximum delay spread was observed to be 420 ns, 180 ns, 290 ns, and 53 ns at 28, 38, 73, and 142 GHz, respectively, with only 10%, 6%, 6%, and 1% of the RMS DS larger than 50 ns at 28, 73, and 142 GHz bands [92, 141], respectively. The mean RMS delay spread is 26 ns at 28 GHz, 11 ns at 38 GHz, 23 ns at 73 GHz, and 9 ns at 142 GHz, which are all larger than the RMS delay spreads in $\text{NLOS}_{\text{Best}}$ and LOS boresight scenarios across all four frequencies bands, since for UMi NLOS scenarios there is likely more than one dominant multipath. The lower RMS DS at 38 GHz is due to there are less dense buildings and obstructions in Austin as compared to Manhattan and Brooklyn. The dropping RMS DS at higher frequencies indicates fewer multipath components at higher frequencies, which is likely because of the higher loss introduced by obstructions and foliage.

4.5 Angular Statistics at 28, 38, 73, and 142 GHz

As wireless channels become more sparse and antenna beamwidth is narrower at higher frequencies, rapid beamforming and beam tracking algorithms are required in MIMO systems, which require accurate channel angular information. Channel angular statistics including the RMS angle of arrival (AOA) spread, RMS angle of departure (AOD) spread, and the average number of AOA and AOD directions extracted from the aforementioned outdoor UMi measurements at 28, 38, 73, and 142 GHz are summarized in Table 4.4 [39, 145, 177]. A 30 dB down from the peak power threshold was used in this letter at 28, 73, and 142 GHz to detect and keep the MPCs in each power angular profile.

Figure 4.13 presents four sample AOA power angular profiles in both LOS and NLOS scenarios at 142 GHz. There are three and one distinct AOA directions observed in LOS scenarios as shown in Figure 4.13 (a) and (b), respectively, and there are four and two separated AOA directions observed in NLOS scenarios as shown in Figure 4.13 (c) and (d). Counting the number of AOA and AOD directions for each location pair at different frequencies, the average number AOA and AOD directions are presented in Table 4.4.

The mean of RMS AOA and AOD spread tends to decrease with increasing frequencies in both LOS and NLOS scenarios, and at the same frequency, the mean of RMS AOA spread is generally larger than the mean of RMS AOD spread, indicating there are more AOA directions than AOD directions. In our measurements, relatively the same beamwidth antennas (7-10°) were used at different frequencies as shown in Table 4.1, and any spatial paths within the antenna beamwidth could not be resolved (e.g., 8°). If a narrower beam antenna was used, there might be more AOA or AOD directions resolved, and if a wider beam antenna was used, some AOA or AOD directions might be lost (not resolvable). However, the angular statistics will not change with the transmission bandwidth unless the bandwidth is huge (e.g., 10 or 20 GHz) which increases the thermal noise of the channel, and some weak spatial directions will not be detected.

The number of AOA and AOD directions decreases with the increasing frequency in both LOS and NLOS scenarios, which shows the wireless channels are more sparse at higher frequencies. Threshold level greatly impacts statistics such as the number of AOA/AOD directions but has negligible impact on path loss and RMS time/angular spreads (stronger MPCs contribute more). If a power threshold of 20 dB down from the peak MPC is used, the mean number of AOA directions at 142 GHz decreases to 1.7 and 2.8 in LOS and NLOS scenarios [180], respectively, since some of the AOA directions with weak powers are filtered out by thresholding. The spatial statistics (e.g., RMS angular spread, number of distinct AOA and AOD directions) will be useful for MIMO channel rank (the number of beams that can be supported by the MIMO matrix) analysis.

4.6 Sub-Terahertz Wireless Coverage Analysis at 142 GHz in Urban Microcell

Radio frequencies above 100 GHz (e.g., sub-THz) are promising candidates for future communication systems to provide multi-Gbps average data rates, rapid streaming (e.g., the peak data rate on the order of Tbps) with extremely low latency (e.g., less than 1 ms), fiber-like fronthaul and backhaul in rural areas for fiber replacement and edge data centers replacements [1, 2, 4, 6]. Spectrum regulators (e.g., Japanese MIAC, European CEPT, and FCC in the US) have instituted their views and provisions on frequencies above 100 GHz during the past few years, and possible coexistence and spectrum sharing techniques above 100 GHz are presented in [5, 32].

The smaller wavelength (e.g., 1 mm) and wider available bandwidth (e.g., 1-40 GHz) at frequencies above 100 GHz will enable new techniques and applications like centimeter level precise position

location [132, 181], wireless cognition (e.g., robotic control, human surrogate) [1, 4, 182], and joint communication and sensing [183, 184]. Learning the characteristics of the wireless propagation channel at frequencies above 100 GHz is the initial step for researchers to design future communications systems to realize the aforementioned applications.

Many universities and research centers all over the world have conducted channel sounding measurements and research at frequencies above 100 GHz, including Aalto University [79], New York University (NYU) [67], University of Southern California (USC) [68], Beijing Jiao Tong University (BJTU) [182], Shanghai Jiao Tong University (SJTU) [185], Georgia Institute of Technology [186], Brown University [37], Technische University Braunschweig (TUBS) [87], Koc University [89], University of Surrey [187], and Pohang University of Science and Technology [188]. These works have proven that sub-THz and THz frequencies can be used for future 6G wireless communications as the current mmWave 5G networks. However, what is the coverage for sub-THz communication systems and how is the system performance is still a question mark.

This Section analyzes the small-cell base station coverage and the system performance in terms of spectral efficiency (SE) at sub-THz frequencies in an Urban Microcell (UMi) environment, using realistic channel models derived from field measurements at 142 GHz conducted in downtown Brooklyn, New York.

4.6.1 System Settings and Propagation Models

Small-cell architecture (shrinking the cell size from a few kilometers to a few hundreds of meters) is a promising means to increase area spectral efficiency and energy efficiency in future sub-THz and THz communications [158, 189]. In this paper, small cell coverage is studied for both single-cell and multi-cell cases (7 cells in particular) in UMi scenarios at 142 GHz.

The base stations (BS) are set at 4 m above the ground, working as small-cell lamppost BS. The carrier frequency f_c is at 142 GHz with 1 GHz null-to-null bandwidth, since 1 GHz to a few GHz bandwidths will be used for future sub-THz and THz communications [1, 32]. The UEs are set at 1.5 m above the ground with 15 dBi gain antennas and a 7 dB noise figure, as shown in Table 4.5.

The theoretical CI path loss models and measured path loss data of outdoor field measurements at 142 GHz [43, 67] in downtown Brooklyn, New York, are presented in Figure4.21. Additional simulated path loss data are generated by NYUSIM [190] which is an open source channel simulator based on field measurements from mmWave to sub-THz frequencies.

For radio propagation at frequencies above 100 GHz, there is still a myth that the wireless channels at higher frequencies would experience more path loss as only omni-directional antennas are considered at both the link ends [1]. If the effective aperture is kept constant over frequencies at both the TX and RX, the path loss decrease quadratically as frequency increases, although the current antenna techniques may not be able to keep the effective aperture constant at sub-THz frequencies compared to mmWave or lower frequencies.

Work in [43, 91] shows that path loss exponents (PLEs) are remarkably similar over frequencies

Table 4.5: System parameters for uplink and downlink propagation.

Environment	Outdoor Urban Microcell (UMi) area
BS Height	4.0 m above the ground
Carrier Frequency	DL: 142 GHz, UL: 140 GHz
DL Channel Bandwidth	1 GHz null-to-null
UL Channel Bandwidth	100 MHz null-to-null
LOS Probability Model	NYU (squared) Model (5GCM)
Path Loss Model	NYU CI Path Loss Model (n, σ): Directional LOS: (2.1, 2.8 dB) Directional $\text{NLOS}_{\text{Best}}$ (3.1, 8.3 dB)
BS Transmit Power	15 dBm (DL)
BS Antenna Gain	40 dBi
BS Noise Figure	5 dB
UE Transmit Power	0 dBm (UL)
UE Antenna Gain	15 dBi
UE Noise Figure	7 dB
Single-cell UE Distribution	250 UEs uniformly distributed
7-cell UE Distribution	1000 UEs uniformly distributed

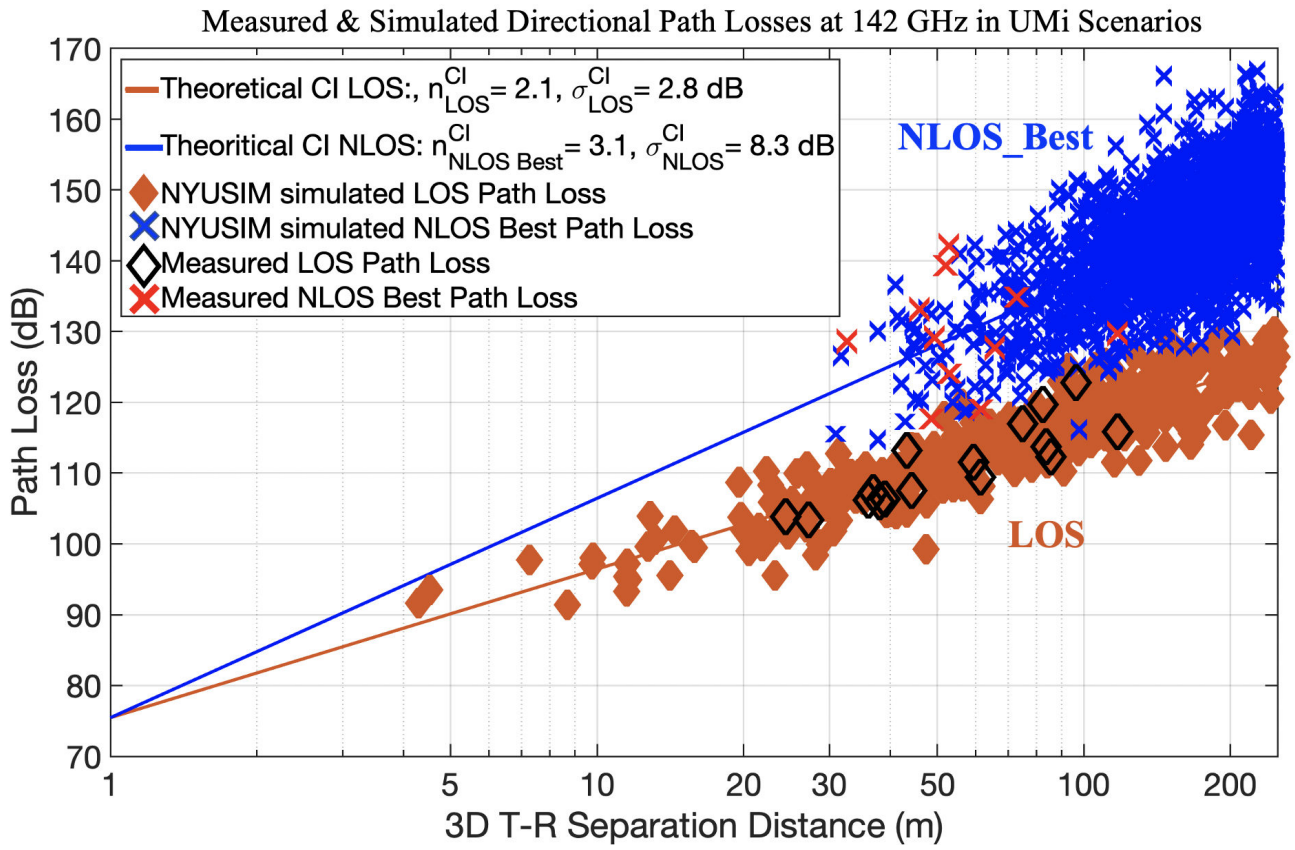

Figure 4.21: Measured and simulated directional path loss (with antenna gains removed) at 142 GHz in UMi environment. The LOS and NLOS Best path loss data (black diamonds and red crosses) are from outdoor field measurements at 142 GHz in downtown Brooklyn [43, 67]. The simulated path loss data are generated by NYUSIM [190].

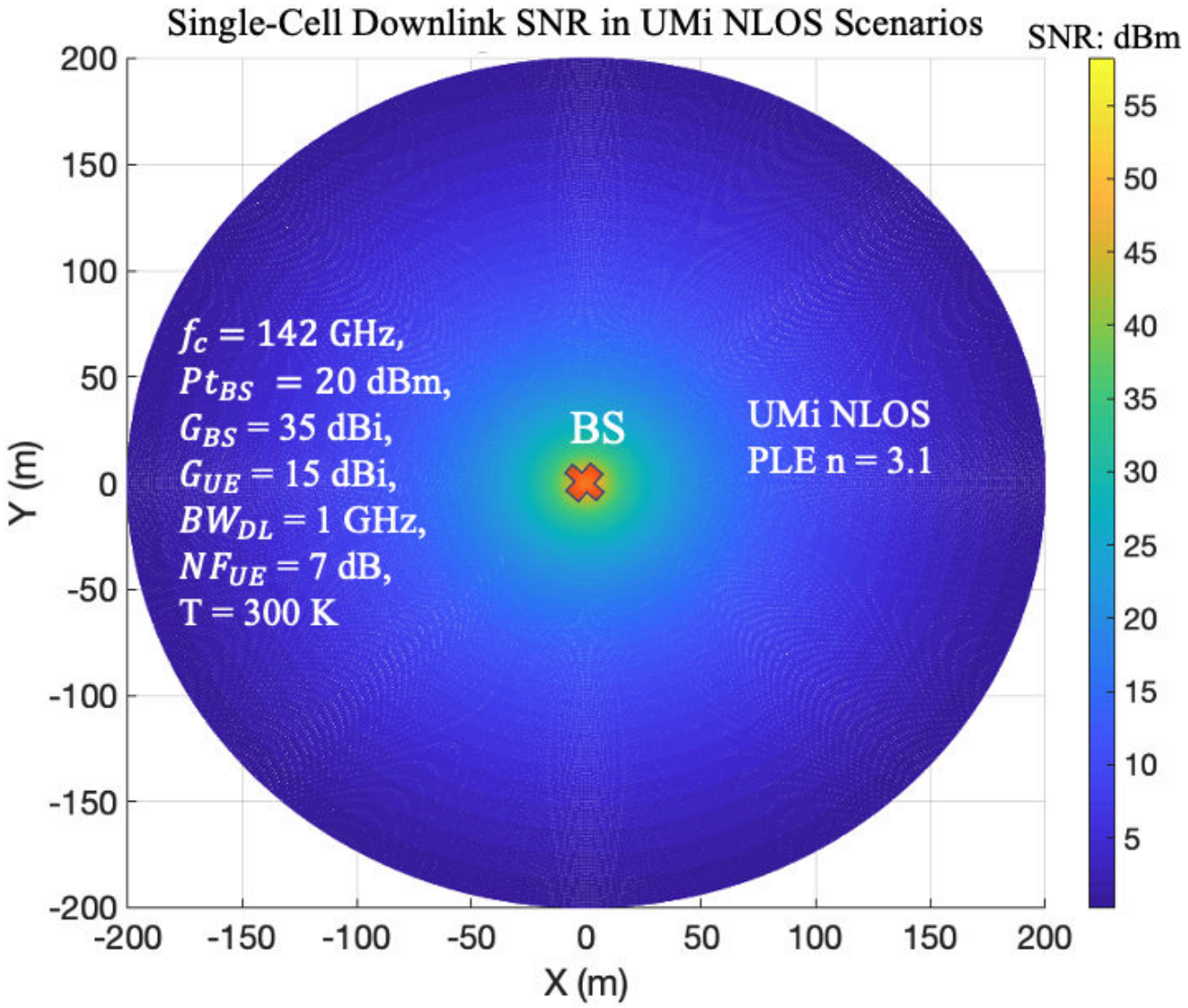

Figure 4.22: Single-Cell downlink coverage with SNR larger than 0 dB in UMi NLOS scenarios, assuming both BS and UE point to the $\text{NLOS}_{\text{Best}}$ direction.

from 28 GHz to 142 GHz, when referenced to the first meter free space path loss. This means after the first meter propagation, wireless channels at sub-THz frequencies do not provide more loss to signals than the channels at mmWave frequencies. Measurements at 142 GHz have shown that metal surfaces, metal lampposts, glass walls, concrete walls, and marble pillars are good reflectors at sub-THz frequencies. Additionally, work in [92, 180] shows that 1-6 spatial clusters observed at 142 GHz with a 20 dB threshold form the peak for both LOS and NLOS scenarios in an UMi environment, and the number of spatial clusters follows Poisson distributions (statistics are sensitive to noise threshold).

In our simulation, the BS EIRP (effective isotropic radiated power) is set the same as the current BS working at low mmWave frequencies (e.g., 28 GHz with an EIRP of 55 dBm), which is smaller than the maximum EIRP regulated by FCC (e.g., maximum average EIRP of 60 dBm for BS and 40 dBm for mobile). The BS is set at the origin in the single-cell case with a radius of 200 m coverage for a signal to noise ratio (SNR) larger than 0 dB in UMi NLOS scenarios. Figure 4.22 shows the

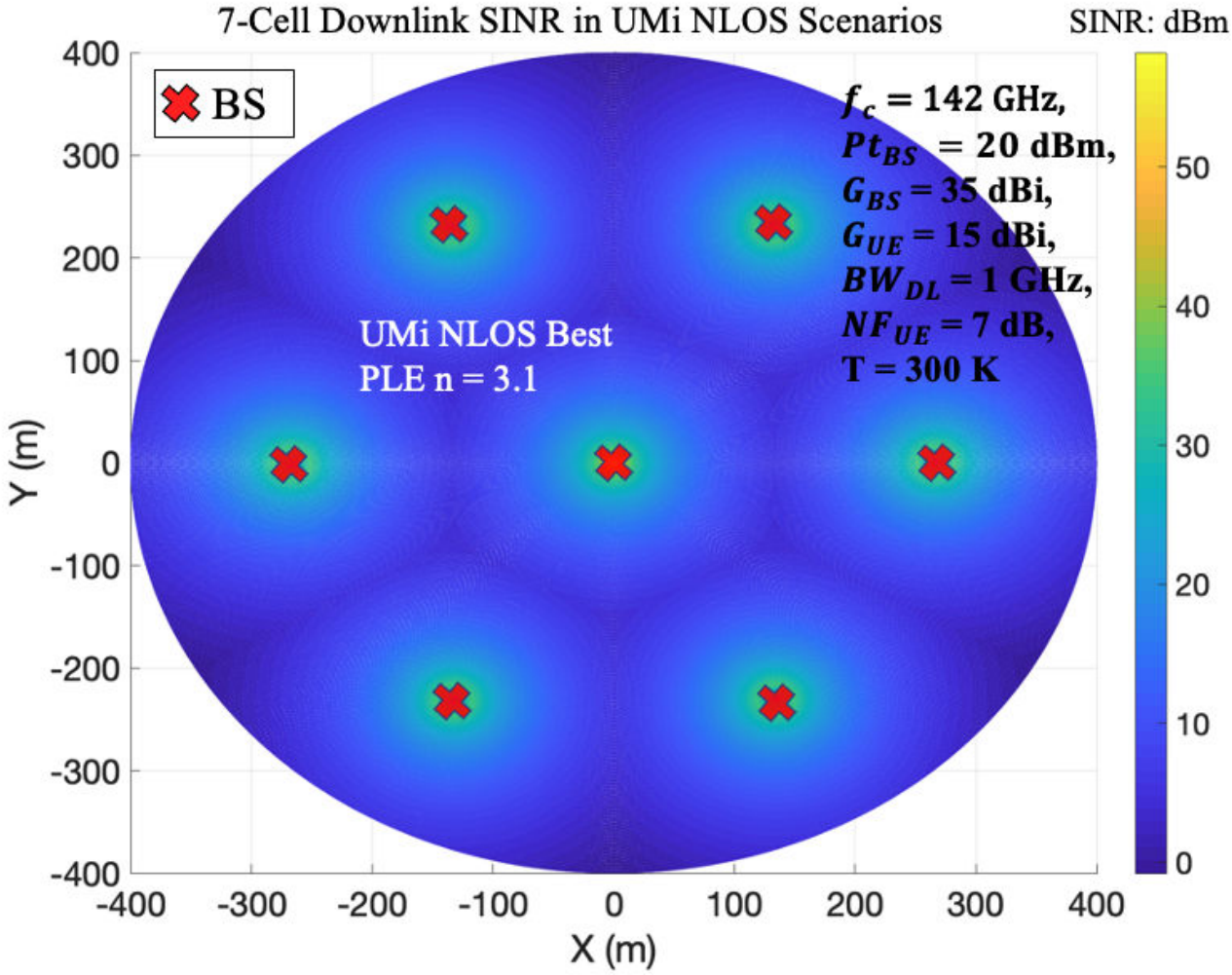

Figure 4.23: 7-Cell downlink coverage with SINR larger than 0 dB in UMi NLOS scenarios, assuming the UE points to the $\text{NLOS}_{\text{Best}}$ direction of the closest BS, and the signal powers from other BS are considered as interference.

single-cell downlink coverage calculated using (4.1) with PLE $n = 3.1$ for $\text{NLOS}_{\text{Best}}$ scenarios (average path loss without fading). A single base station with an EIRP of 55 dBm at 142 GHz can cover an area with a radius of 200 m even in NLOS scenarios.

For the multi-cell case (7-cell in particular), a BS is set at the origin with six other BS equally spaced, as shown in Figure 4.23. Considering NLOS scenarios, the UEs point to the $\text{NLOS}_{\text{Best}}$ direction where the maximum power is received, and the signal powers from other BS are considered as interference. It shows that 7-cell architecture can provide a coverage area (with SINR larger than 0 dB) with a radius of 400 m in NLOS scenarios. The LOS coverage areas of both single-cell and 7-cell architectures are much larger than in NLOS environments. Thus, to study the coverage and system performance at 142 GHz, 1000 UEs are uniformly distributed in areas with a radius of 200 m and 400 m for single-cell and 7-cell cases, respectively.

The NYU (squared) LOS probability model (4.3) (a statistical model derived from a real-world database in downtown New York City [158, 170]) is used to predict whether the UE is within a clear LOS of the BS or in an NLOS region due to obstructions:

$$\begin{aligned} P_{LOS}(d_{2D}) =& (\min(d_1/d_{2D}, 1)(1 - \exp(-d_{2D}/d_2)) \\ &+ \exp(-d_{2D}/d_2))^2, \end{aligned} \tag{4.3}$$

where $P_{LOS}(d_{2D})$ is the likelihood that a UE is in a clear LOS of the BS, d_{2D} is the 2D Euclidean separation distance between the BS and UE in meters, $d_1 = 22$ m, and $d_2 = 100$ m.

Figure 4.24 shows the distribution of UE for both single-cell and 7-cell scenarios. The LOS status of each UE is determined by (4.3) and about 20% of the UE is in LOS of the BS in the single-cell case, as shown in Figure 4.24(a). It is worth noting that, in the 7-cell case, a UE is determined the LOS status of each BS based on the BS-UE separation distance using (4.3), and about 37% of UEs are in LOS of at least one BS, as shown in Figure 4.24(b).

In the single-cell case, the UEs in LOS of the BS point to the LOS boresight directions to the BS and the UEs in NLOS region point to the $\text{NLOS}_{\text{Best}}$ directions. The downlink (DL) received power is calculated by:

$$Pr_{dl} = Pt_{bs} + G_{bs} + G_{ue} - PL^{CI}(f_c, d_{\text{3D}}), \tag{4.4}$$

where the PLE and shadow fading of (2.1, 2.8 dB) and (3.1, 8.3 dB) are used for directional path loss models in LOS and $\text{NLOS}_{\text{Best}}$ scenarios. As shown in Figure 4.24(a), there are 10% of the UEs are out of coverage (with an SNR lower than 0 dB).

In the multi-cell case, the UEs point to the directions where the maximum powers are received (i.e., the LOS boresight directions or the strongest $\text{NLOS}_{\text{Best}}$ directions to a certain BS). The signal powers from the rest six BS are considered as interference. As shown in Figure 4.24(b), there are 15% of the UEs are out of coverage (with an SINR lower than 0 dB).

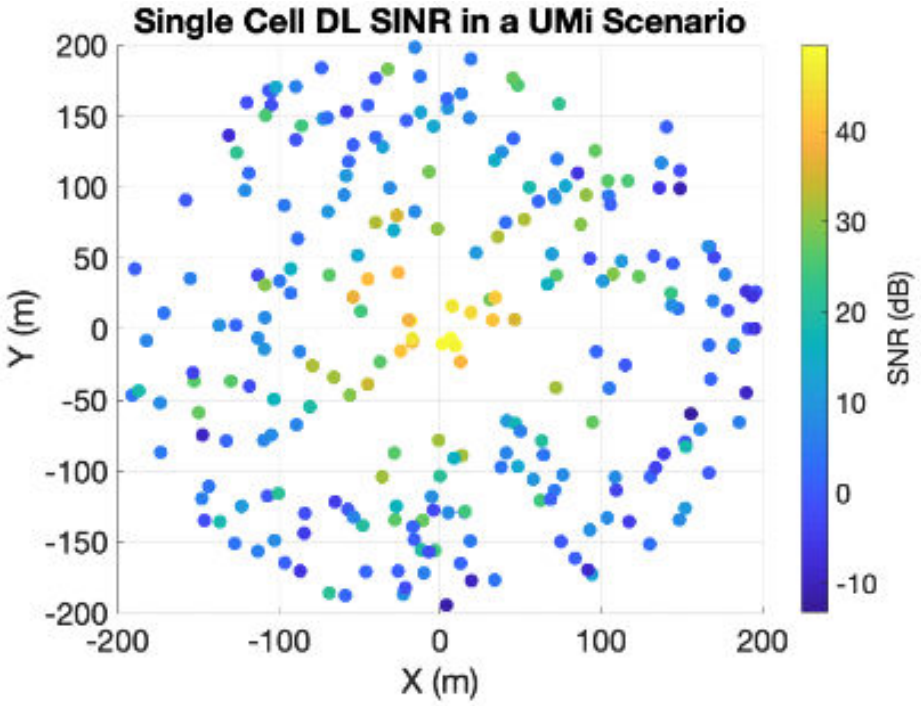

(a) Single-cell with a 200 m radius coverage

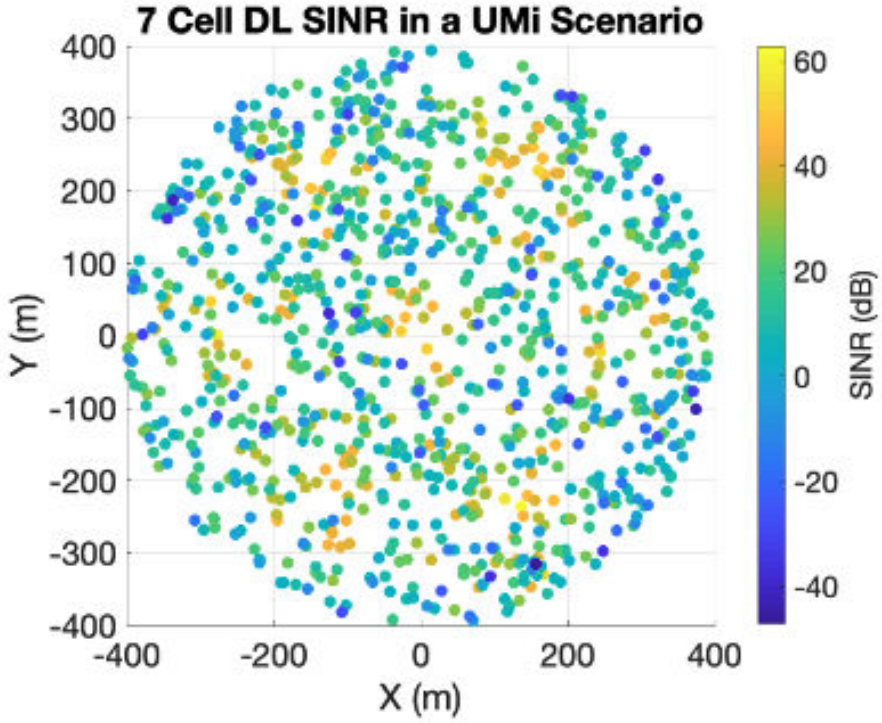

(b) 7-cell with a 400 m radius coverage

Figure 4.24: UE distributions for single-cell and 7-cell scenarios.

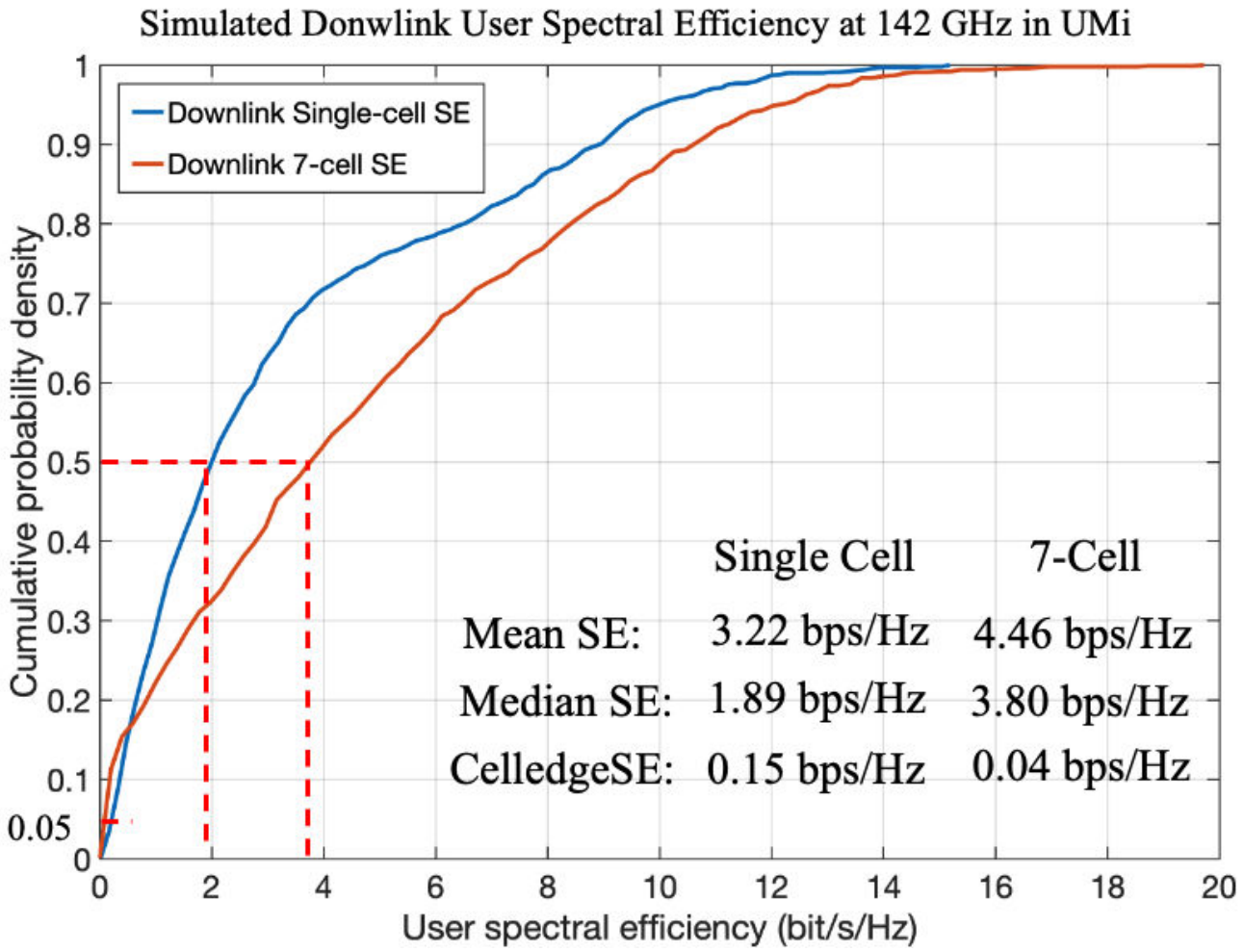

Figure 4.25: Simulated downlink User Spectral Efficiency at 142 GHz in UMi environment with a downlink channel bandwidth of 1 GHz.

4.7 Simulation Results of Single Cell and Multicell Cases

The spectral efficiency (SE) of data transmission is an important performance of communication systems, which usually varies across the service and depends on the UE locations as well as channel conditions [191]. The user SE is defined as the amount of data transferred to (DL) or from (UL) the user normalized by the time-frequency resources used by the system for data transfer. Suppose M_u packets have been transmitted for user u, the SE η_u is calculated as:

$$\eta_u = \left(\sum_{i=1}^{M_u} N_{u,i} \right) / \left(\sum_{i=1}^{M_u} T_{u,i} B_{u,i} \right), \tag{4.5}$$

where $N_{u,i}, T_{u,i}, B_{u,i}$ are respectively the number of information bits, transmission time, and allocated bandwidth for the i-th packet of user u.

Figure 4.25 presents the downlink spectral efficiency (SE) distribution at 142 GHz for both the single-cell case (with a radius of 200 m) and 7-cell case (with a radius of 400 m) with the BS and

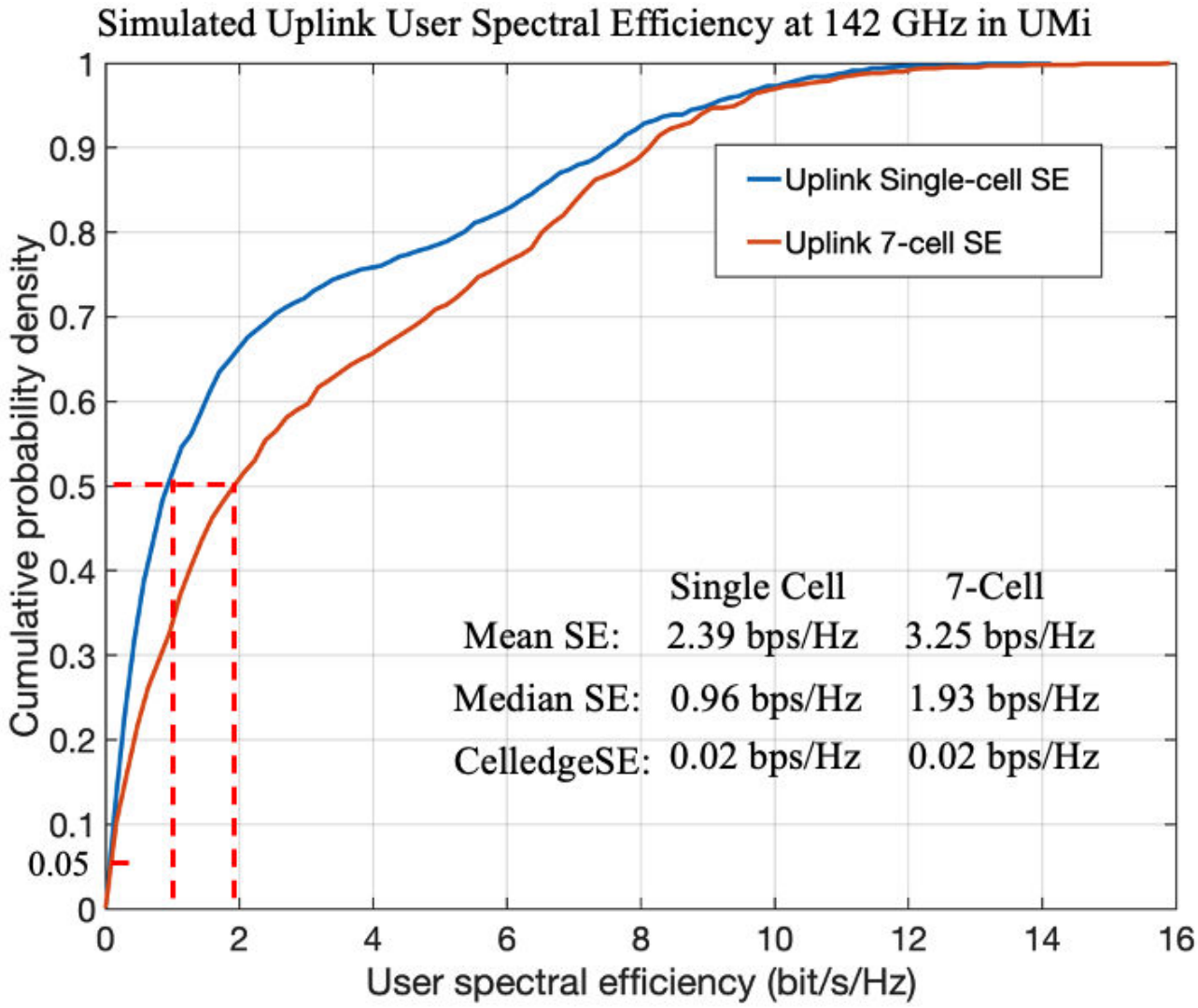

Figure 4.26: Simulated uplink user spectral efficiency at 140 GHz in UMi environment with an uplink channel bandwidth of 100 MHz.

UEs using directional antennas, as shown in Table 4.5. In the single-cell case (blue link in Figure 4.25), the average user SE is 3.22 bps/Hz, the median user SE is 1.89 bps/Hz, and the cell-edge user (5% of the users either at the edge of the cells or in deep fading area) SE is 0.15 bps/Hz. With a 1 GHz bandwidth, the average downlink data rate is 3.22 Gbps and the cell-edge users experience an average downlink date of 150 Mbps. The 7-cell architecture can increase the total coverage to a radius of 400 m (by adding six more BS and shrinking the cell size of each BS), with the average user SE of 4.46 bps/Hz, the median user SE of 3.80 bps/Hz, and the cell-edge user SE of 0.04 bps/Hz. With a 1 GHz bandwidth, the average downlink data rate for the 7-cell case is 4.46 Gbps and the cell-edge users experience an average downlink date of 40 Mbps.

It shows that using the 7-cell architecture can greatly improve the average (+40%) and median user SE (+100%) compared to the single-cell architecture, however, the cell-edge users experience worse service (-75%) due to the interference.

Figure 4.26 shows the uplink user spectral efficiency distribution at 142 GHz for both the single-

cell case (with a radius of 200 m) and the 7-cell case (with a radius of 400 m) with the BS and UEs using directional antennas. In the single-cell case, the uplink SE decrease significantly compared to the downlink SEs, with the mean SE of 2.39 bps/Hz (-26%), the median SE of 1.93 bps/Hz (-50%), and the cell-edge SE of 0.02 bps/Hz (-87%). The uplink coverage is limited by the low EIRP of the UE devices (15 dBm). With a 100 MHz bandwidth, the average data rate in the sing-cell case is 239 Mbps and the cell-edge data rate is 20 Mbps.

In the 7-cell case, the uplink SEs also decrease (compared to the downlink SEs) due to the limited UE EIRP, with the mean SE of 3.25 bps/Hz (-27%), the median SE of 1.93 bps/Hz (-49%), and the cell-edge SE of 0.02 bps/Hz (-50%). In general, using the 7-cell architecture can greatly improve the average and median SE compared to using the single-cell architecture, but have a worse performance for the cell-edge users.

4.8 Conclusion

Two outdoor radio propagation measurement campaigns in urban microcells at 142 GHz are presented in this Chapter, using a wideband sliding correlation-based channel sounder with identical narrow-beam 27 dBi gain horn antennas at both the TX and RX. Omnidirectional and directional CI path loss models with a 1 m reference distance are provided for both LOS and NLOS scenarios in the outdoor terrestrial urban microcell environment at 142 GHz. The path loss results are very encouraging and show that in NLOS scenarios there is usually one or a few dominant paths (e.g., the best pointing beam $NLOS_{\text{Best}}$) compared to the other multipath components (e.g., reflected or scattered), and accurate beamforming algorithms will be needed to find, capture, and combine the most dominant multipath energy to maintain and extend the outdoor NLOS communication range at frequencies above 100 GHz. Surprisingly, metal lamppost, concrete walls, and tinted glass perform as good reflectors at 142 GHz (providing only 2-8 dB loss to the reflected multipath) which provide good coverage using only moderate TX power up to 117.4 m in NLOS scenarios.

Comparisons of outdoor wireless channels (LOS and NLOS) in UMi environments at 28, 38, 73, and 142 GHz are presented in this Chapter, based on four different measurement campaigns conducted from 2011-2020 in downtown Austin, Manhattan, and Brooklyn. The path loss components of both CI and CIF models in both LOS and NLOS scenarios are notably similar over four frequency bands from mmWave to sub-THz frequencies, when referenced to the free space path loss in the first meter (near field) [39, 44, 141], implying the outdoor UMi channels at THz frequencies are not that different from today's mmWave channels with the exception of the first meter path loss. The RMS delay spread and angular spread in outdoor UMi environments decrease as frequency increases when using directional antennas from 28 to 142 GHz. The comparisons of channel characteristics and models in this letter will support outdoor multi-band wireless system designs above 100 GHz for 6G and beyond.

We also analyzed both the single-cell and multi-cell base station coverage of sub-THz systems at 142 GHz in outdoor UMi scenarios based on realistic channel models derived from field measurements.

The single-cell base station can provide coverage of a 200 m radius, and the 7-cell base stations can provide total coverage of a 400 m radius. Uplink and downlink system performances in terms of spectral efficiency are studied for both single-cell and multi-cell cases. The 7-cell architecture can greatly improve the coverage and system performance in terms of the average and median SE compared to the single-cell case but has a worse performance to the cell-edge users. In the 7-cell case, with a 1 GHz bandwidth, DL sector throughput is 4.5 Gbps and DL cell-edge throughput is 40 Mbps. The uplink coverage is limited by UE transmit power and UE antenna gain. Dynamic blockages (e.g., human and vehicle blockages) and fast beam switching (when there is an obstruction block the link) algorithms will be studied for future work.

Chapter 5

Non-Terrestrial Networks (NTN)

Inspired by the success of 5G commercial deployments at millimeter wave (mmWave) and sub-6 GHz frequencies, futuristic wireless communication systems (e.g., 6G and beyond) will likely utilize sub-THz and THz frequencies above 100 GHz to provide not only much higher data rates (Tbps) with near-zero latency [1, 6, 32], but also global coverage with unmanned aerial vehicles (UAV), high altitude platform stations (HAPS), satellites, terrestrial and maritime stations [192], ushering in innovative applications such as autonomous vehicles/drones, wireless cognition, and precise localization with centimeter-level accuracy [132, 192]. Fixed point-to-point communications such as wireless fronthaul and backhaul (e.g., integrated access and backhaul, and Xhaul), operating at data rates on the order of Tbps, will enable fiber replacement in rural areas to provide wireless coverage and services to the less populated areas, and enable wireless replacements of edge data centers [1, 2, 4, 158].

Joint communication and radar sensing [183, 184] will be an important feature of 6G wireless communication systems, where both active sensors such as radar/Lidar and passive sensors like cameras and spectroscopy [1] will support new applications like automotive radars, gesture and activity recognition, and contextual awareness [192, 193]. Sensing aided communications will support beam configuration and alignment, as well as challenging mobility applications like autonomous systems, and communication functionality in radar sensing will help with high-resolution imaging and precise localization with centimeter-level accuracy [132, 183].

The folks in earth observation and radio astronomy are nervous about terrestrial networks moving to higher frequencies (above 100 GHz) causing possible interference to satellite systems [32]. Interference between the joint communication systems and the radar sensing systems will be a key issue, and the corresponding spectrum coexistence techniques developed for joint communication and sensing will help with the possible interference concern with the radio astronomy.

5.1 Spectrum Sharing between Terrestrial and Satellite Networks

Spectrum sharing techniques are expected to play a key role in improving spectrum efficiency and in ensuring coexistence between active systems (e.g., mobile broadband wireless, fixed wireless fiber replacements, futuristic WiFi, terrestrial-based sensing, and spectroscopy) and passive systems (e.g., radio astronomy, atmospheric and geo-space sciences, and climatological observations) [1, 194]. Current spectrum sharing techniques such as adjacent channel or partial channel spectrum masks, cognitive radio, and database management are introduced herein.

A glimpse of the struggles and tensions between satellites and ground-based wireless networks was seen during 2019 in the debate between the National Oceanic and Atmospheric Administration (NOAA) and FCC, when weather satellite advocates complained of the consequences of interference if the 24.250 GHz 5G mobile bands did not provide adequate out-of-band spectrum containment so as to avoid interfering with the 23.835 GHz satellite measurement frequency. This problem sparked a battle raged across the globe, as both sides attempted to define a proper spectrum mask that 5G mobile systems would require in order to assure out-of-band energy did not interfere with the space-based weather sensors.

A final resolution was reached in the ITU World Radio-communication Conference 2019 (WRC-19 [195]) with a -29 dBw total power limit for mobile terminals (-33 dBw for base stations) in any 200 MHz of the satellite passive band spectrum mask. What was not made known to the public was that mmWave measurements used by weather satellites actually use 5 different frequencies (called "channels") between 22 and 30 GHz, and that the models for detecting moisture content, and thus weather effects, are somewhat noisy and variable such that the small incremental additional energy from ground-based radiators was not likely to impact the weather predictions significantly [1].

The extent of "noise" in the existing weather models, and the use of multiple channels to detect moisture content by NOAA is given in [197], where the measurements and resulting models are noisy with much variation (this helps explain why weather predictions are quite often inaccurate, even without any adjacent channel interference). The 24 GHz 5G tussle dealt with just one of the five different frequencies measured in order to create weather models. Having knowledge of how the passive space-based sensors use their energy measurements, and how the radiometer data is used for the ultimate end purpose is critical for determining ultimate sensing performance and degradation due to ground-based interference, if any even exists.

Another example of relatively recent adjacent channel coexistence issues was experienced in the Sirius XM satellite radio system (2320 MHz to 2345 MHz), and the potential interference caused to it by adjacent channel mobile radio systems as satellite radio listeners drove along the highway [198]. The FCC eventually arbitrated a suitable adjacent channel spectrum requirement to allow both systems to thrive, even given the very sensitive receiver signal levels needed by the satellite radio system [198, 199]. In this study, massive simulation studies were conducted, which helped

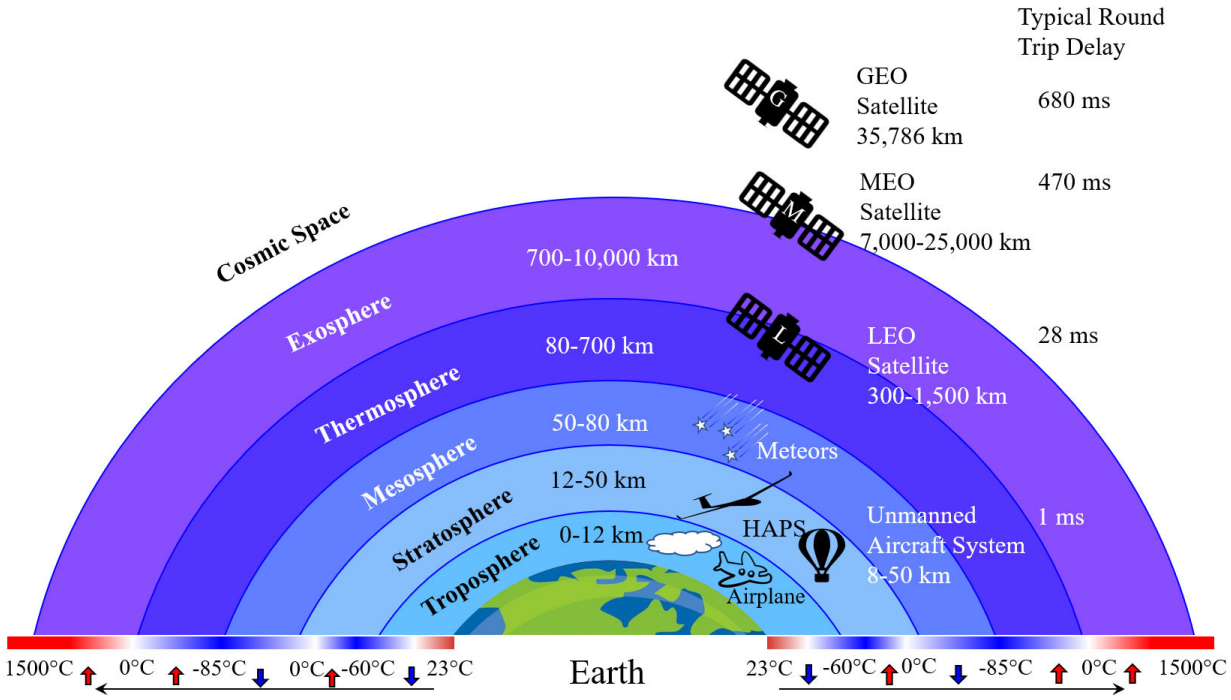

Figure 5.1: Different atmosphere layers of earth and the corresponding satellite services and other communication applications. The typical round trip delays (proportional to the altitudes) are for transparent payload (e.g., satellites or UAS serving as a repeater or relay), which are four times the link distances between the satellites and ground terminals with a 45° average elevation angle over the speed of light [196].

convince the FCC of the appropriate spectrum mask to enable coexistence, and similar approaches will be valuable for, and employed in, the presently proposed research program.

Current means of spectrum sharing are mostly limited to sensing and database management around mostly active users (e.g., the Citizens Broadband Radio Service (CBRS) at 3.5 GHz and its use of a Spectrum Access System, SAS [200]). Modern spectrum sharing techniques like cellular's LTE License Assisted Access (LAA), which has been standardized by 3GPP (TR 36.889 Release 13 [201]) in 2015, enables LTE to leverage the unlicensed 5 GHz WiFi band in combination with licensed LTE spectrum, using carrier aggregation (a contention protocol known as listen-before-talk [202], LBT) to combine unlicensed 5 GHz WiFi band with licensed LTE band to provide better data rates and better user experience, to deliver a performance boost for mobile device users [202].

5G New Radio (NR) in unlicensed spectrum (NR-U), which also relies on the LBT feature, is currently being studied in 3GPP Release 16 (a study item called Integrated Access Backhaul, IAB) aiming to fully integrate the unlicensed spectrum at 70 GHz into 5G networks (promoted by one of the mmWave Coalition members, Nokia), enabling efficient spectrum coexistence [163, 203]. Exploring new spectrum utilization and sharing paradigms for bidirectional active sharing with passive space-based sensors (such as radio astronomy) have been largely unexplored, and require attention and focused research as proposed herein [194].

5.1.1 Atmosphere and Air-to-ground Communications

The atmosphere of Earth can be divided into five main layers according to the altitudes and temperature profiles, with various satellite systems and applications working in different layers, see Figure 5.1. Air-to-ground communications such as satellite communications and unmanned aircraft systems (UAS) are providing coverage and connection all over the world with different use cases including mobile broadband service, IoT connectivity, backhauling, position location, disaster relief, and public safety.

The atmosphere of Earth is the layer of gases, commonly known as air, and the air pressure and density generally decrease with altitude in the atmosphere. However the temperature has a more complicated profile with altitude and may remain relatively constant or even increase with altitude in some regions, the temperature behavior provides a useful metric to distinguish atmospheric layers. The atmosphere of Earth can be divided (also called atmospheric stratification) into five main layers [204], including troposphere (0-12 km), stratosphere (12 to 50 km), mesosphere (50 to 80 km), thermosphere (80 to 700 km), and exosphere (700 to 10,000 km), as shown in Figure 5.1.

The troposphere (0-12 km) is the lowest and thinnest layer which is close to Earth's surface but it contains 80% of the mass of atmosphere since the troposphere is much denser than all its overlying atmospheric layers [204]. Both the air pressure and temperature decline with increasing altitude (heated by the energy from the Earth surface) [204], and nearly all atmospheric water vapor or moisture or cloud is in the troposphere. As shown in Figure 5.1, commercial airplanes and UAVs are operating in the troposphere.

The stratosphere (12 to 50 km) is the second-lowest layer of the atmosphere, which contains the ozone layer (15-35 km). The temperature in the stratosphere rises with increasing altitude due to the absorption of ultraviolet radiation from the Sun by the ozone layer, and the stratosphere lacks the weather-producing air turbulence which is prevalent in the troposphere [204]. Therefore, the stratosphere is almost free of clouds and the wind speed is relatively low, with the minimum wind speed at an altitude of 20 to 25 km, where the high-altitude platform stations (also called high-altitude pseudo-satellite, HAPS) operates [205] (e.g., Airbus Zephyr, Google Loon).

The mesosphere (50 to 80 km) is the third-lowest layer of the atmosphere above Earth, where the temperature drops with increasing altitude (the coldest place in the atmosphere). The mesosphere is too high above Earth to be accessible to jet-powered aircraft and balloons (very low air density), and too low to permit orbital spacecraft, and it is the layer where most meteors burn up [204].

The thermosphere (80 to 700 km) is the second-highest layer of the atmosphere and the temperature gradually increases with altitude (extremely low air density) [204]. This layer is completely cloudless and free of water vapor. The international space station (ISS) orbits in this layer (between 340 to 420 km) and some of the weather satellites, which is a kind of low earth orbit (LEO) satellites, work in this layer (e.g., 400 km)[206]. This layer is also marked as the beginning of space since 99.99997% of the mass of the atmosphere is contained below 100 km (also called Karman line) [204], which also explains why the atmosphere attenuation only happens within the altitude of 100 km [31].

The exosphere (700 to 10,000 km) is the outermost layer of the atmosphere and there are nearly no meteorological phenomena. Most of the satellites orbit in the exosphere, including LEO satellites (e.g., high speed and low latency communication satellites) and medium earth orbit (MEO) satellites (e.g., GPS, Glonass, and Galileo). Some equatorial low Earth orbit and polar satellites (e.g., weather satellites), which are subsets of LEO, also work at the top of the Thermosphere.

The size of communication satellites varies, which can be as big as a school bus and weigh up to several tons (e.g., Telstar 19V, GEO, 7,075 kg) and some can be small as a 4-inch cube and weigh about 10 kg (e.g., TEMPEST-D, LEO CubeSat, 14 kg). The orbiting altitudes and typical round trip time delays for different satellite systems and other communication applications such as UAS are presented in Figure 5.1. It is worth noting that the typical round trip delays are for transparent payload (i.e., satellites or UAS serving as a repeater or relay), which are four times the link distance between the satellites and ground terminals with a 45° average elevation angle [196]. The round trip delay for a regenerative payload (i.e., having all or part of base station functions on board the satellite or UAS platform) is two times the link distances between the satellites and ground terminals (half of the values provided in Figure 5.1).

5.1.2 Air-to-ground Communications

The concept of satellite communications (geostationary communications satellites) was first presented by Clarke in his early work [207] in 1945, and after several decades till now, about 2,000 communications satellites are orbiting Earth including both passive and active systems orbiting at different altitudes from LEO to GEO. There are many private and government organizations launching communication satellites and providing satellite broadband services and secure networking systems covering military and commercial markets (e.g., Viasat, Airbus, SpaceX, Telesat, NASA).

Since the 1990s, the research interests on air-to-ground or space-to-earth communications have not only been on satellites, but increasingly on UAS (including HAPS) operating in the troposphere and stratosphere (8-50 km), which have advantages concerning satellites in terms of the reduced cost of implementation, deployment, and launch, and also low latency [205, 208]. With the development in solar panel power efficiency, battery energy density, and autonomous aviation, unmanned aircraft or balloon serving as HAPS can operate in the stratosphere for months [208], which enable HAPS to provide Internet of Things (IoT) connectivity and 5G services to the sparsely populated areas and disaster relief [209].

Unmanned aerial vehicles (UAVs), which are commonly referred as drones, have attracted major attention from the industry for uses from delivery to communications [210]. In 2018, 3GPP started a feasibility study on non-terrestrial networks (NTN) in TR 38.811 [211] and TR 38.821 [196], where satellites, HAPS, and UAVs are utilized to provide 5G NR communication services for both air-to-ground and air-to-air applications [196, 211].

Some unique features distinguish air-to-ground communications from conventional terrestrial networks, including the highly dynamic wireless channels due to the air station (e.g., satellites, HAPSs,

UAVs) velocity and the high atmosphere attenuation and refraction/scattering due to the variation in air density as a function of altitude [212].

Khawaja provides a comprehensive survey of air-to-ground propagation measurements and modeling for in his recent work [210] including different air-to-ground channel sounding measurements in various scenarios (e.g., urban, suburban, rural, hilly, forest, and sea) across the frequency range from 1 to 6 GHz, generally with omnidirectional antennas at the air stations and directional antennas at ground stations. Channel statistics as large-scale path loss, power delay profile (PDP), root mean square (RMS) delay spread, and Doppler were studied, indicating free space path loss model and a 2-ray model are suitable for LOS path loss, and Rician fading with a K factor of 4-28 dB or a Nakagami-M distribution describes the fading distribution well [210, 212].

The NTN networks consist of a service link (i.e., access link, the radio link between satellite or UAS and user terminals) usually working at sub-6 GHz (e.g., 2 GHz) and a feeder link (i.e., the wireless link between NTN gateway and satellite) working at sub-6 GHz or mmWave (e.g., DL 20 GHz, UL 30 GHz) [196, 211]. The air-to-ground channel has not been studied extensively compared to the terrestrial channels, and other than raytracing simulations, there are few real-world measurements for air-to-ground communications at mmWave frequencies or above.

Propagation models for HAPS (at 20 km altitude) including line of sight (LOS) probability models and path loss models at 2 GHz and 20 GHz in dense urban and sub-urban scenarios in both LOS and non-line of sight (NLOS) conditions based on raytracing simulations were presented in [209, 211]. The LOS probability and path loss were shown to be dependent on the elevation angle of the RX antenna above the horizon. The free space path loss model was shown to be a good prediction in the LOS condition but a frequency selective fast fading model is still required for the NLOS condition. Raytracing simulations for mmWave UAV (below 2 km altitude) air-to-ground propagation channels at 28 GHz and 60 GHz were provided in [213]. It showed that a two ray propagation model could be applicable for urban, suburban, rural, and overseas scenarios, and the RMS delay spread behaved highly dependent on the height of UAV as well as the density/height of the scatters (different scenarios) around UAV.

5.2 Design Spectrum Masks between Satellite and Terrestrial Applications at Frequencies above 100 GHz

Co-channel and adjacent channel interference between satellites and ground terminals in the frequency bands allocated to satellite services above 100 GHz is analyzed in this section. Spectrum masks design methods are provided, showing that with proper transmit power limits and antenna designs, active terrestrial mobile communications could be made to not interfere with the passive satellite applications at frequencies above 100 GHz.

5.2.1 Satellite Systems Working at Sub-THz

Considerations of sharing and adjacent-band compatibility between active ground-based and passive services such as space-based satellites are urgently needed for frequencies above 100 GHz as specified in Resolution 731 of ITU WRC-19 [195]. Key ITU bands identified include 100-102 GHz, 116-122.25 GHz, 148.5-151.5 GHz, 174.8-191.8 GHz, 226-321.5 GHz, and 235-238 GHz as these are allocated to radio astronomy, weather radar satellites.

To understand the coexistence issue between space-based sensors and terrestrial networks, its first important to understand the types of satellites and their distances from the earth, as well as their receiver and antenna characterization.

To understand the coexistence issue between space-based sensors and terrestrial networks, its first important to understand the types of satellites and their distances from the earth, as well as their receiver and antenna characterization.

Geostationary orbit (GSO) satellites, also referred to as a geosynchronous equatorial orbit (GEO), occupy an orbital position 35,786 km above the earth, and remain in a stationary position relative to the Earth itself. The world's major existing telecommunications and broadcasting satellites fall into this category [214]. Non-geostationary orbit (NGSO) satellites occupy a range of orbital positions whereby LEO satellites are located between 300 km-1,500 km from the Earth, and MEO satellites are located at 7,000-25,000 km from the Earth, and do not maintain a stationary position but instead move in relation to the Earth's surface [214], as shown in Figure 5.1.

We focus on the types of satellites used at sub-THz, which are generally NGSO at altitudes of about 2,000 km or less, orbiting at different heights. Many sub-THz satellites may use backhaul links (feeder links) with highly directional antennas (1° half power beam width) to make backhaul connections with the ground. On the other hand, sensors that detect energy are focused on making radiometric energy measurements such as noise temperature and are very sensitive [206].

Three major satellite systems working at sub-THz frequency bands are well documented in the public domain and enable fruitful study for potentially acceptable in-band and out-of-band emission limits (e.g., spectrum mask and receiver front end/antenna designs) which are critical for understanding the coexistence of satellite and terrestrial applications at frequencies above 100 GHz. These well-documented satellites are: (i) Temporal Experiment for Storms and Tropical Systems Technology-Demonstration (TEMPEST-D) [215]; (ii) Time-Resolved Observations of Precipitation structure and storm Intensity with a Constellation of Smallsats (TROPICS) [216]; and (iii) Advanced Technology Microwave Sounder (ATMS) [217].

TEMPEST-D is a CubeSat project of Colorado State University with the objective to demonstrate the ability to monitor the atmosphere with small NGSO satellites, working at near circular orbit with an altitude of 400 km [215]. TEMPEST-D provides passive millimeter-wave observations using a compact radiometer (90-183 GHz) at five frequencies, 89, 165, 176, 180, and 182 GHz [206], and the radiometer performs cross-track scanning, measuring the Earth scene between -45° and +45° nadir angles, providing an 825-km wide swath from a 400-km nominal orbit altitude [206, 215]. The receiver

system can ideally achieve a noise figure of 2 dB with a null-to-null bandwidth of 4±1 GHz at 165 GHz. The measured receiver noise temperature is 300 K at 160 GHz [206].

TROPICS (NGSO at an orbit height of 550 km altitude) measures temperature profiles using seven channels near the 118.75 GHz oxygen absorption line, water vapor profiles using 3 channels near the 183 GHz water vapor absorption line, imagery in a single channel near 90 GHz for precipitation measurements, and a single channel at 206 GHz for cloud ice measurements [216].

ATMS works in a NGSO joint polar satellite system (JPSS) at an orbit height of 824 km [217], and is assimilated into NOAA's National Weather Service numerical weather prediction models. ATMS is a key instrument that collects microwave radiation from the Earth's atmosphere covering 22 bands from 23.8 GHz to 183.3 GHz to provide atmospheric temperature and moisture for operational weather and climate applications [217]. Papers have allowed us to learn about the receiver and antenna designs used by typical passive sensor satellites, which is a vital first step to quantifying interference and ultimate coexistence potential.

5.3 Possible spectrum coexistence techniques

Directional antennas (phased antenna array or fixed antennas for stationary point-to-point use) are needed at frequencies above 100 GHz for mobile communications to provide high EIRP in the desired direction to compensate for the high path loss. Antenna patterns at both the terrestrial base stations and mobile stations can be carefully designed to reduce the EIRP at high elevation angles which will ensure there is no co-channel interference between the satellite and terrestrial systems, meanwhile providing sufficient coverage for mobile communications.

Since the satellites have known orbits and receiver frequencies, the time when a certain satellite will rise above the horizon of the fixed terrestrial stations is available. Therefore, adaptive antenna techniques could be designed to place a null in the direction of a particular satellite as it rises above the horizon, and future phones and base stations could maintain real time tracking of key co-channel satellites to adapt their beam patterns in real time to assure nulls are placed at particular places in the sky.

Because the building partition loss at mmWave is generally very large (e.g., 40-60 dB at 28 GHz for concrete walls) [40, 157], it is a virtual certainty that indoor sub-THz systems will have even greater isolation from space-based sensors that transmitters operating outside of buildings, and thus are highly likely to be able to coexist today with passive satellites (indicating again how current spectrum policy under US246 may be too restrictive for enabling indoor sub-THz markets).

Nevertheless, it is important to know the penetration loss of different materials at frequencies above 100 GHz [66, 108], in order to design the spectrum mask for unprotected indoor passive systems that will coexist with active indoor systems. Thus, this research area will provide important knowledge that is not just useful for space-based receivers, but also for ground based passive sensors, and will help with isolating the indoor and outdoor applications (e.g., factory IoT and 5G/6G/7G

mobile) and provide a fundamental understanding of penetration loss above 100 GHz that will be highly valued by industry and academia as this field opens up.

If the antenna cross polarization discrimination is large enough (e.g., 20 dB), and if multipath is minimal, cross-polarization antennas could be used for different systems or applications for spectrum co-existence which provides efficient spectrum utilization. However, extensive measurements are needed for a better understanding of the XPD at frequencies above 100 GHz as depolarization effects may happen after reflection, scattering, or penetration [66, 218].

5.4 Rooftop Surrogate Satellite Measurements at 142 GHz

To our knowledge, the world's first air-to-ground measurements at 142 GHz were conducted in Downtown Brooklyn from September 2020 to December 2020, which can be used for emulating satellite-to-ground and UAS/HAPS-to-ground communications. This measurement campaign was designed to give early insights for spectrum sharing/coexistence techniques and interference between terrestrial networks and surrogate satellite systems (or for terrestrial networks that will use mobiles and tall base stations for integrated access and backhaul). This measurement campaign used the channel sounder system described in [66]. Figure 5.2 shows the rooftop base station (BS) receiver and ground user equipment (UE) transmitter locations on NYU's downtown Brooklyn campus.

In the rooftop surrogate satellite measurements, the BS (RX) was placed on the rooftop of a nine-story building which is 38.2 m above ground, emulating a passive satellite receiver. Horn antennas with 8° half power beam width (HPBW) were used at both the rooftop RX and ground-based TX, where the antennas were mechanically steered and extensively rotated to consider all possible pointing combinations in the search of energy. In satellite communications, the received interference power level will be highly dependent on the ground-based transmitter's radiation pattern and any multipath that is reflected or scattered up to the satellite. The satellite will view wide swaths of earth, such that any radiation source from earth would add to others for a cumulative interference effect in the satellite's antenna pattern which may be mitigated by the massive attenuation in the troposphere. To study the variation of received power with elevation angles in a realistic urban setting, eight ground-based TX (1.5 m above the ground) locations were chosen in the NYU Brooklyn courtyard (see Figure 5.2), having LOS elevation angles in 10° decrements ranging from 80° to 10°. Due to the space limitation of the measurement area, the farthest TX provided a 15° elevation angle boresight to the RX instead of 10°. The channel sounder requires a clear LOS link for calibration, but TX locations 1 through 8 were somewhat blocked by tree foliage. To overcome this issue, two additional TX locations - TX 9 and 10 were chosen, which had the same link lengths as TX 6 and 7, respectively, for free space calibration without any link obstructions [67].

While foliage would further attenuate energy from mobiles on earth received at a satellite or backhaul system, it could also serve as a source of scattering, so the experiments were designed to carefully try to detect any energy whatsoever in any possible boresight direction used on the ground

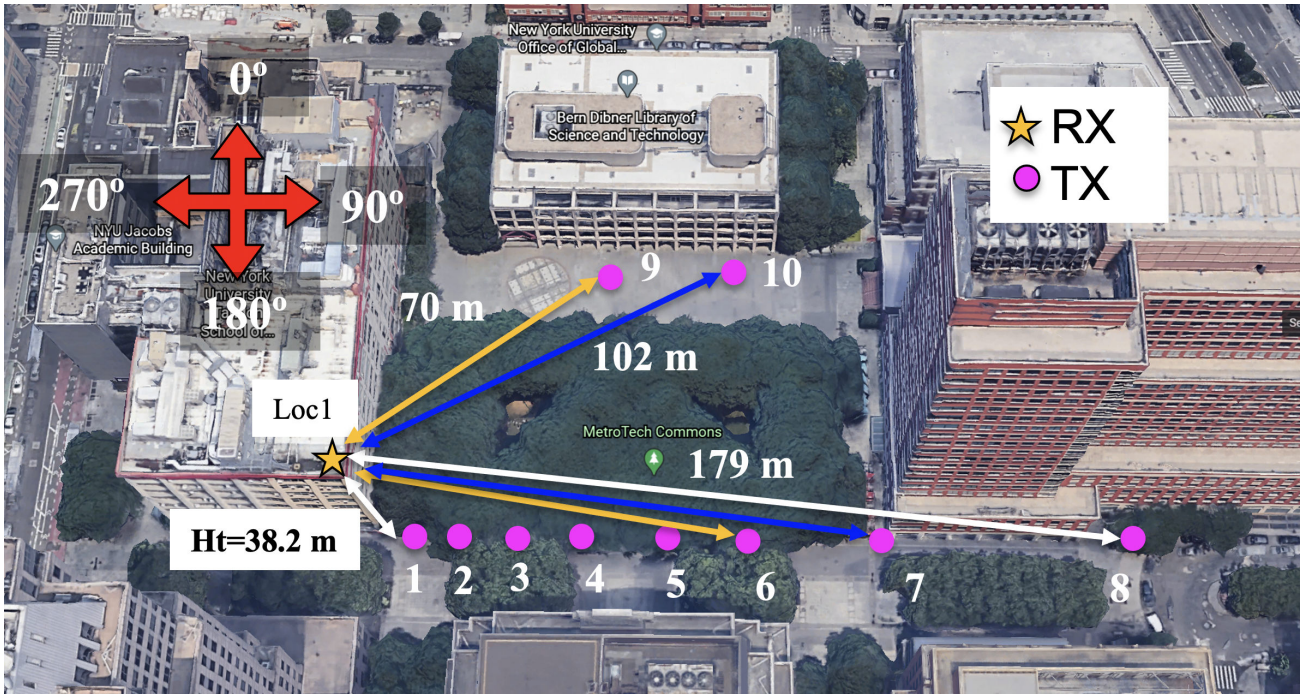

Figure 5.2: Rooftop surrogate satellite measurement campaign. The surrogate satellite (and backhaul) receiver RX location is at 38.2 m above the ground on the rooftop identified as a yellow star. Ten mobile TX locations on the ground are identified as purple circles. The LOS elevation pointing angles from TX1-8 to the RX location are 80° to 15°, respectively [67].

and roof-based RX.

A multipath power delay profile (PDP) for the (sometimes foliage-blocked) LOS boresight TX-RX pointing combination was first measured at each TX location, and then the TX was rotated 360° in the azimuth plane by steps of 8° (the HPBW of the antennas used at both the TX and RX), and this was repeated at elevation angles of 0°, 8°, 16°, 24°, and 32°. For each TX pointing angle, an exhaustive manual search was conducted at the roof-mounted RX to attempt to capture any signals (e.g., direct path, reflected, or scattered rays).

5.5 142 GHz Rooftop Measurement Results

Figure 5.4 presents the measured receiver power at the rooftop RX (38.2 m above the ground) from the ground-based TXs (1.5 m above the ground) at different elevation angles and distances from 40 to 180 m, corresponding to TX1-8 as shown in Figure 5.2. The 0° elevation angle signifies the horizontal plane and the positive values represent the TX elevation angles above the horizon. The yellow curve shows the best-fit measured power of the foliage-blocked LOS links between the ground TX and roof mounted RX, and reveals 7.1 dB foliage loss beyond free space at 142 GHz with a standard deviation of 3.7 dB about the best fit since the foliage loss is affected by the wind.

When the ground-based TX antenna is pointing at a 0° elevation angle on the horizon (the blue

Figure 5.3: The RX is at heights of 1.5 m above the roof corner, which prevents the RX from being shadowed by the railing boundary, emulating a passive receiver in a satellite. The TXs are at heights of 1.5 m above ground working as mobile terminals [67].

curve in Figure5.4), there is virtually no power captured by the rooftop RX even when the ground TX has antenna pattern energy leaking from its antenna pattern while pointing nearly directly to the roof (the boresight elevation angle is 15°). The worst case of interference was found when the TX is at Location 6 (70 m) and Figure5.4 shows how raising the elevation angle of the ground based transmitter dramatically increases energy detected by the roof-mounted RX, due to antenna pattern leakage and multipath from surrounding buildings.

5.5.1 Analysis of Interference between Satellite and Terrestrial Networks

Obviously, this measurement campaign and Figure 5.4 is cursory and does not consider the massive attenuation due to the troposphere slant path. As shown in Figs. 1.1 and 1.4, the slant paths close to the horizon (e.g., 0-15°) experience much more atmospheric absorption and path loss due to longer path length within the troposphere than with overhead paths (e.g., 90° elevation angle). Thus, if antenna patterns of earth transmitters are carefully designed (e.g., adaptive antenna patterns with very low sidelobes overhead), the passive receiver in the air (satellite) will not receive interference from the ground, enabling spectrum sharing between satellites and ground terminals. This approach would limit OOBE, as well.

Analysis of the interference from ground transmitters to the TEMPEST-D satellite receiver at 165 GHz, one of the major satellite systems working at sub-THz frequency bands [206] was further considered to determine preliminary satellite interference levels from a mobile system on earth. The required sensitivities of the TEMPEST-D satellite radiometric passive sensors are astounding, only $\Delta T_e = 0.1$ Kelvin, implying 7 dB SNR (permissible interference level at 20% of the required sensitivity

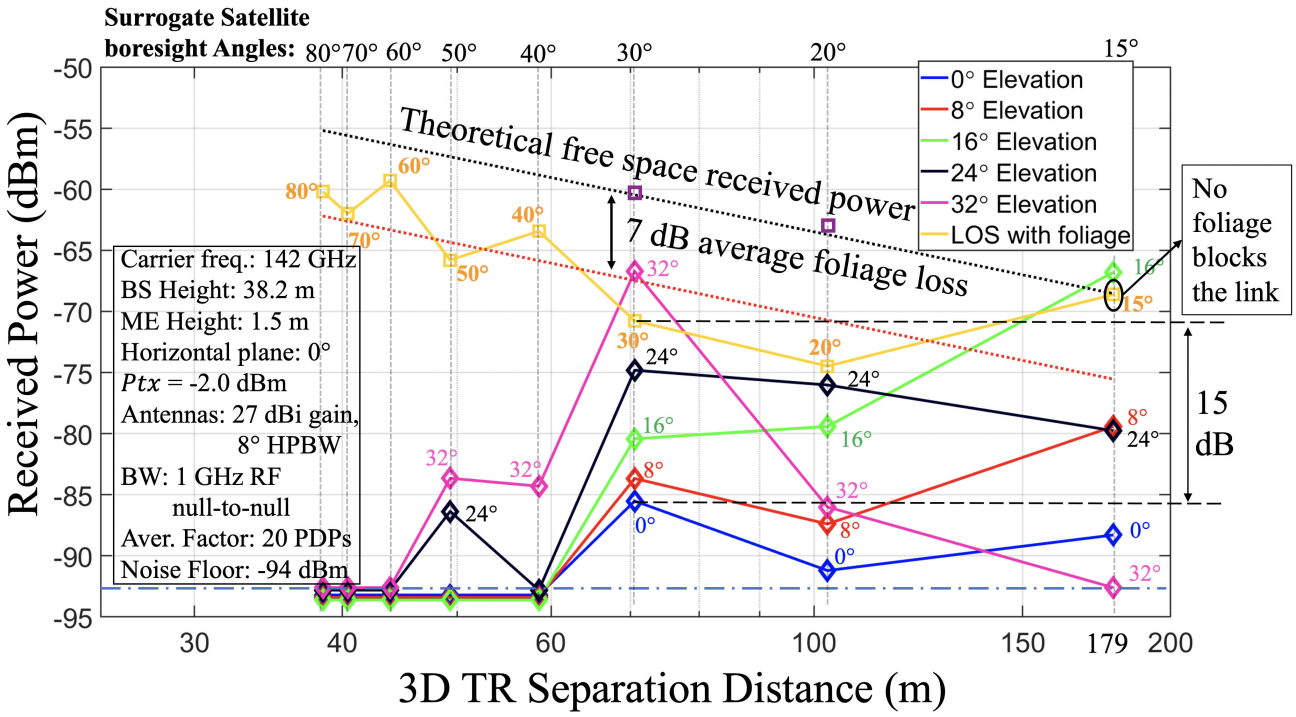

Figure 5.4: The rooftop base station (38.2 m above the ground) received power vs. different distances and different elevation angles form ground users (1.5 m above the ground) at 142 GHz [32].

$\Delta P[\text{W}] = k\Delta T_e B$ [219]) would occur for a interference level of -133.0 dBm over $B = 200$ MHz, $I[\text{dBm}] = 10\log_{10}(k\Delta T_e B \times 10^3) - \text{SNR} = -133.0$ dBm, where k is the Boltzmann's constant $= 1.38 \times 10^{-23}$J/K, and I is the noise/interference level (see Table II in [219]).

The signal between a ground TX and a satellite undergoes several stages of propagation and attenuation [211]:

$$PL = PL_b + PL_g + PL_s, \tag{5.1}$$

where PL is the total path loss in dB, PL_b is the basic propagation path loss in dB, PL_g is the atmospheric gasses attenuation in dB, and PL_s is the attenuation due to either ionospheric or tropospheric scintillation in dB. The basic propagation path loss is modeled as:

$$PL_b = \text{FSPL}(h/\sin(\alpha), f_c) + SF + CL(\alpha, f_c), \tag{5.2}$$

where $\text{FSPL}(h/\sin(\alpha), f_c)$ is the free space path loss in dB, SF is a log-normal distributed shadow fading in dB, $CL(\alpha, f_c)$ is the cluster loss in dB (e.g., foliage loss, building penetration loss), $h/\sin(\alpha)$ is approximately the link distance in meters, α is the elevation pointing angle in degrees from the ground terminals to the satellite, and f_c is the carrier frequency in Hz [211]. When the TX is in LOS of the satellite, the cluster loss is negligible in (5.2).

Assuming the ground-based TX is in LOS of the satellite and transmits its main beam at an elevation angle of $\alpha = 10°$, the basic propagation loss PL_b in (5.1) at $f_c = 165$ GHz with $h = 400$ km altitude is 204.0 dB. The atmospheric gasses attenuation P_g in (5.1) is ~ 35.2 dB [31]. Assuming reasonable parameters for a mobile ground station transmitting a 200 mW signal at 165 GHz [220]

using a 15 dBi gain antenna [221], the theoretical received power at the TEMPEST-D radiometer would be -201.2 dBm which is more than 60 dB (a factor of 1,000,000) below the minimum signal detection level at the satellite (-133 dBm over 200 MHz). This implies that if N mobile devices were operating on the ground, each with similar transmitter power levels and all N devices were within the passband and the main beam of the satellite receiver, the total contribution of the entire terrestrial network interference power I (NOTE: variable capital I for interference power, assuming each interference adds power non-coherently) is $I[\text{dBm}] = -201.2\text{dBm} + 10\log_{10}(N)$ = -133.0 dBm. Solving for N yields N = 6.6 million mobile ground devices would sum up to be equal to the noise floor seen by the satellite receiver, therefore not causing deleterious effects. If the satellite was overhead or not near the horizon, properly designed mobile antennas could provide tens of dB additional attenuation that could offset the smaller tropospheric loss on overhead paths.

Improved antenna patterns (e.g., spatial filtering) at both the ground and the satellite need to be considered, and foliage and building blockage (for indoor systems) would provide greater protection than this simple example shows. Note that we did not consider any rain/fog/cloud attenuation, foliage/building penetration loss, the impact of in-building use, or any antenna pointing offset issue which would further attenuate the ground-based transmissions. The analysis indicates that with proper transmit power limits and antenna designs, active terrestrial mobile communications could possibly not interfere with the passive satellite applications at frequencies above 100 GHz, although much more study is needed to ensure the protection of the expensive and ultra-sensitive satellites after they are launched.

Note that the interference analysis in this letter is focused on frequencies above 100 GHz between the active terrestrial networks and satellite passive receivers in space, and the downlink of satellite networks which is generally below 40 GHz is not considered. This analysis gives some insights into the key issues for spectrum sharing and suggests that current regulations that prohibit any ground-based transmitters in bands above 100 GHz may be too restrictive in light of the intense attenuation of sub-THz and THz frequencies through the troposphere over long slant-paths. The spectrum mask (out-of-band emission limits for ground-based transmitters) can be properly designed as a function of the elevation angle, based on this analysis for the passive satellite frequency bands above 100 GHz [46].

5.6 Foliage Loss at 142 GHz

The rooftop surrogate satellite measurements could also be used to measure and estimate the foliage loss at 142 GHz as presented in Table 5.1 and Figure 5.5. The heights of birch trees in the NYU courtyard, were 8-10 m as shown in Figure 5.5. The foliage of the birch trees was between 5-10 m in height above the ground and began falling from the trees during the measurements in November 2020. Slant link length (L) through foliage at different TX-RX separation distances and elevation angles (θ ranges between 80°-20°) is approximately $L = 5\text{ m}/sin(\theta)$ = 5-15 m with an average slant

Table 5.1: Foliage-blocked LOS links (TX1-7 to RX) and clear LOS links (TX8-10 to RX) from the ground-mounted TXs (1.5 m ht) to the roof-mounted RX (38.2 m above the ground) at 142 GHz, with TX transmit power of -2 dBm and identical 27 dBi gain horn antennas at both of the TX and RX. The predicted received power (assuming free space propagation) Pr_{FS} in dBm, measured received power through foliage-blocked links Pr in dBm, and corresponding foliage loss ($Pr_{FS} - Pr$) in dBm at different TX-RX separation distances and elevation angles are presented. The negligible difference of the predicted and measured received power of the clear LOS links at TX8, TX9, and TX10 validated the accuracy of the 142 GHz channel sounder system used in this report .

	Foliage-blocked LOS Links							**Clear LOS links**		
Ground TXs	TX1	TX2	TX3	TX4	TX5	TX6	TX7	TX8	TX9	TX10
Distance [m]	38.5	40.4	43.9	49.3	58.6	70.6	102.7	178.9	70.6	102.7
θ	80°	70°	60°	50°	40°	30°	20°	15°	30°	20°
Pr_{FS} **[dBm]**	-55.2	-55.6	-56.3	-57.3	-58.8	-60.5	-63.7	-68.5	-60.5	-63.7
Pr **[dBm]**	-60.2	-62.0	-59.3	-65.8	-63.4	-70.8	-74.5	-68.6	-60.9	-64.3
$(Pr_{FS} - Pr)$ **[dB]**	5.0	6.4	3.0	8.5	4.6	10.3	10.8	0.1	0.4	0.6
μ, σ **[dB]**	6.9 dB, 3.0 dB							Free Space Calibrations		

link length of 7.9 m (3.4 m standard deviation) through the foliage.

The predicted received power (assuming free space propagation) Pr_{FS} in dBm, measured received power through foliage-blocked links Pr in dBm (with the TX transmit power of -2 dBm and identical 27 dBi gain horn antennas at both of the TX and RX), and corresponding foliage loss ($Pr_{FS} - Pr$) in dBm at different TX-RX separation distances and elevation angles are presented in Table 5.1. The negligible difference of the predicted and measured received power of the clear LOS links at TX8, TX9, and TX10 validated the accuracy of the 142 GHz channel sounder system used in this report . The foliage loss at 142 GHz ranges from 3-11 dB with a 6.9 dB average loss beyond free space and a standard deviation of 3.0 dB, revealing an average foliage attenuation rate of 0.9 dB/m which is higher than the 0.4 dB/m foliage attenuation rate at 73 GHz [109], indicating foliage loss (signal attenuation through foliage) increase with carrier frequencies.

The surrogate satellite measurements and preliminary analysis suggest that propagation on the horizon (e.g., elevation angles $\leq 15°$) may not cause interference (same or adjacent bands) between passive satellite sensors and terrestrial transmitters at frequencies above 100 GHz if the antenna patterns of the transmitters are carefully designed to avoid radiation in space (e.g., adaptive antenna patterns with very low sidelobes). This work offers a critical first step in addressing the spectrum co-existence challenges across the entire mmWave and THz RF ecosystem to spur technology development in future terrestrial networks in the sub-THz and THz bands.

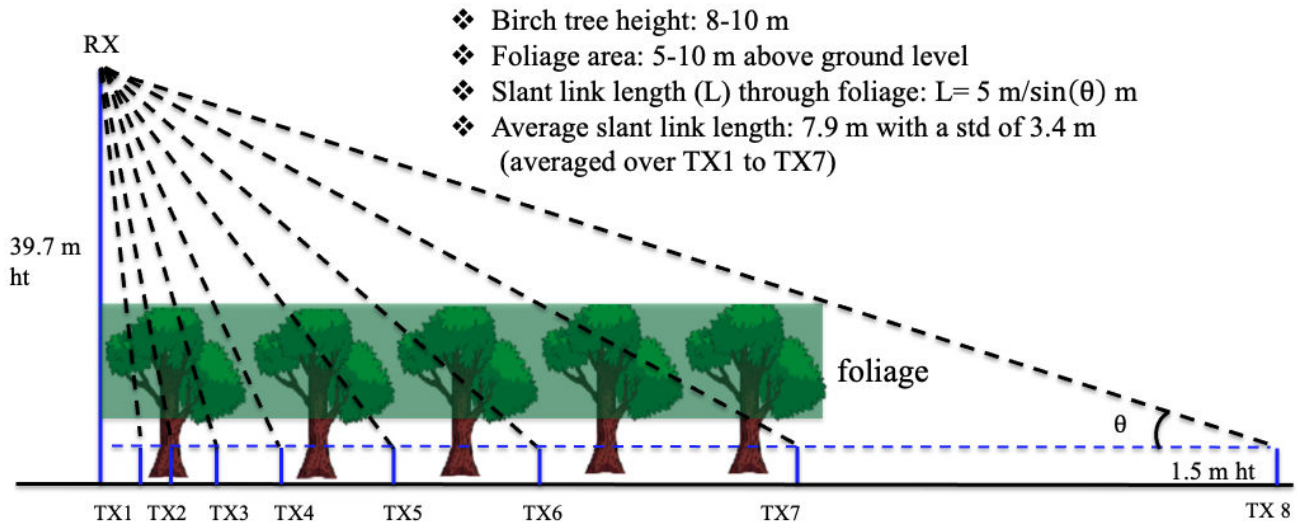

Figure 5.5: Foliage loss analysis at 142 GHz.

5.7 High Altitude Platform Stations (HAPS)

High altitude platform station (HAPS) is a communication platform deployed in the stratosphere (e.g., 18-24 km above the ground), which can utilize solar power to operate for several months without disturbances and to provide connectivity for a large area (e.g., with a diameter of 200 km) [222]. HAPS experiences a low propagation delay (e.g., 1-2 ms) and negligible Doppler shift compared to low earth orbit (LEO) satellites, and it is much easier and cheaper to launch and maintain [223]. HAPS can support various applications including mobile broadband in rural areas, Internet of Things (IoT), public safety, autonomous factory, and disaster relief [1, 209, 224]. There are many ongoing HAPS projects and innovations such as Google Loon, HAPSMobile, and Airbus Zephyr to provide 4G LTE and 5G services to the sparsely populated areas in the global wireless connectivity [191].

The global cellular industry standardization organization, 3GPP, is working on specifying 5G new radio (NR) standard for non-terrestrial networks (NTN), including geostationary earth orbit (GEO) satellites, LEO satellites, HAPSs, and unmanned aerial vehicles (UAVs), and the initial specification is expected to be delivered in 3GPP NR Release 17 [211]. Two extensive literature surveys of air-to-ground communication channel modeling in the frequency range of 1-5 GHz with an altitude up to 11 km are provided in [210, 212, 225] including various scenarios of urban, suburban, rural, hilly, forest, and ocean. Air-to-ground and air-to-air communications utilizing millimeter wave at 60 GHz with propagation measurements, channel models, and beam alignment algorithms are presented in [226, 227].

In this Section, we propose two types of architectures of HAPS, where the HAPS is working as a base station (i.e., regenerative architecture) and as a repeater (i.e., bent-pipe architecture) respectively, and present their corresponding system performance.

Table 5.2: Specific solutions of two architectures of HAPS.

Solution	Payload	Beam control	L1/MAC Latency	FL/AL single and bandwidth	Notes
Simple repeater	Light	NO		Common	
Advanced repeater			Longer (FL + AL)	Depending on solutions	Beam control solution is needed
Relay station (IAB)		Yes			
BS (RU only)				Independent (Possible separate optimizations)	Heavy data in FL due to low layer split
BS (DU + RU)			Shoter (AL only)		
BS (full BBU)	Heavy				

5.7.1 Two Types of Architectures of HAPS

HAPS stations are envisioned to support various use cases utilizing different carrier frequencies and bandwidth (e.g., LTE, cmWave NR, and mmWave NR), such as wide-coverage backhaul for non-terrestrial group mobility at $\sim$ 10 Gbps data rate, high-speed wireless backhaul for temporary industrial networks with around 1 Gbps data rate, and mobile broadband services and IoT for wide-area coverage (e.g., rural area connectivity or disaster relief) at tens of Mbps data rate [223].

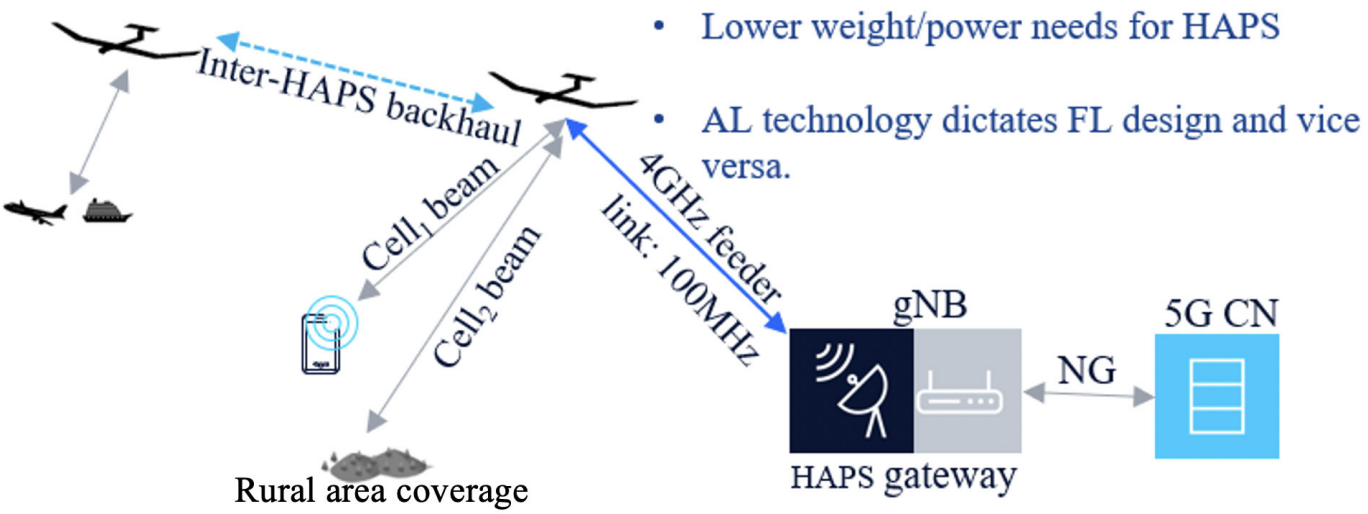

Figure 5.6: Bent-pipe HAPS architecture: HAPS as a repeater.

There are two types of architectures of HAPS that can be considered as a desired unified solution to satisfy the wide range of requirements for the various HAPS use cases. The first type is transparent or bent-pipe (BP) architecture where the HAPS station is working as a RF repeater or a relay station, as shown in Figure 5.6. The repeaters can be a simple RF repeater, an advanced repeater with beam control, or a relay station (integrated access and backhaul, IAB), each with different payload and power consumption requirements. The BP architecture requires low weight and power consumption on HAPS. However, the access link (AL) air interface and the feeder link (FL) design need to be considered together.

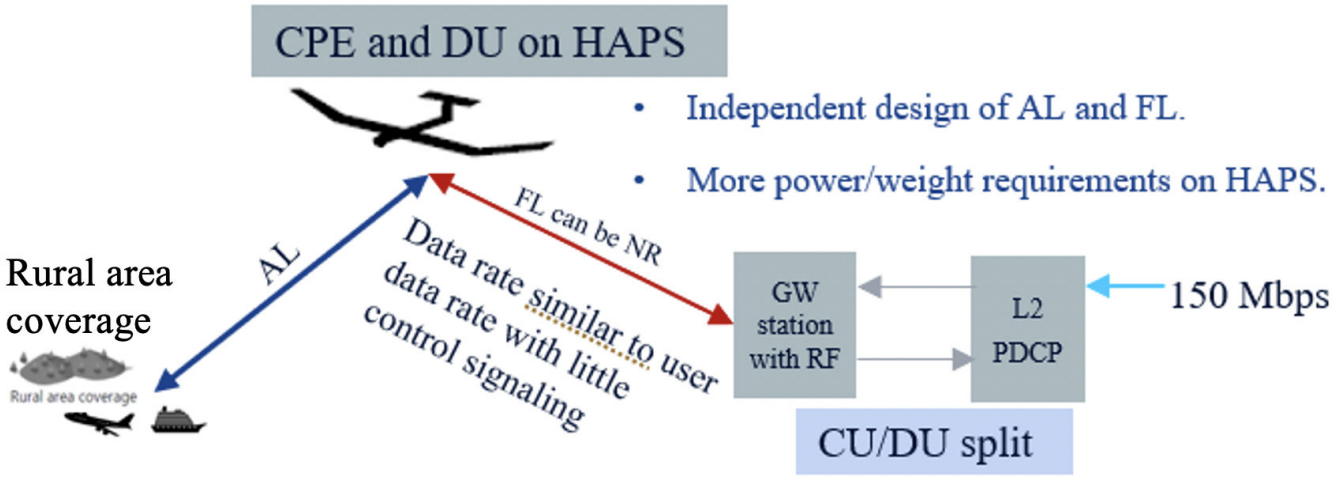

Figure 5.7: Re-generative HAPS architecture: HAPS as a base station.

The second type is regenerative (RG) architecture where the HAPS is working as a base station (e.g., radio unit (RU), distributed unit (DU) + RU, or full baseband unit (BBU)) as shown in Figure 5.7. The RG architecture HAPS can utilize independently optimized designs for AL and FL but it has higher power and weight requirements on HAPS.

The specific solutions of the two architectures, including the payload and technologies requirements, are presented in Table 5.2. The hardware complexity, payload requirements, and power consumption of different solutions increase from a simple repeater to a full BBU based solution. Note that the MAC layer latency (e.g., 1-2 ms) of the BP based and the RU-only based solutions (with delay path FL+AL) is higher since the base station MAC entity is located on the ground. In general, the BP architecture HAPS will be cheaper than the RG architecture HAPS system.

5.7.2 System Model

A typical HAPS scenario where the HAPS is flying at an altitude of 20 km with a speed of 75-120 km/hr in a circular route of 6 km diameter to maintain a station-keeping flight pattern and provide consistent coverage on the ground [223]. HAPS provides data services to UEs via AL over the 4G LTE or 5G NR air interface, where lower frequency bands are preferred to provide a large coverage area. The aggregated traffic of the AL is transported by the FL, connecting the HAPS to one or more ground gateway stations (backhaul) [223]. In our simulations, the origin is at the cell center and a gateway station is placed 45 km away from the origin on the x-axis.

Both single-cell and multi-cell cases (7 cells in particular) are considered corresponding to different HAPS use cases in the simulations. A single antenna with 8 dBi antenna gain, 65° half power beam width (HPBW) in both vertical and horizontal gain patterns, and a 30 dB front-to-back ratio is used to serve the single cell. A single-cell HAPS requires less hardware and power consumption, while a multi-cell HAPS utilizes a more complex antenna array to provide a larger coverage [223].

A hexagonal antenna array structure composed of six side panels and an underneath panel facing downward to the ground as illustrated in Figure 5.8 is used to provide the largest possible terrestrial

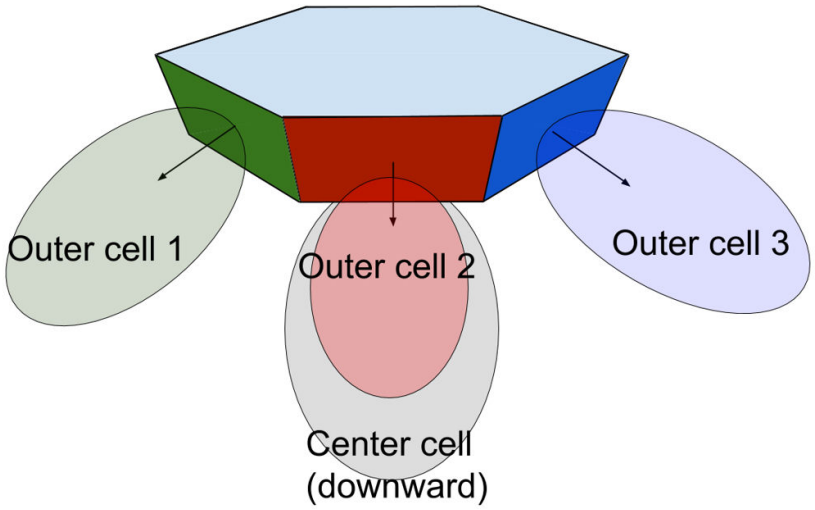

Figure 5.8: A hexagonal antenna array with a downward facing panel serving the center cell and six outward facing panels serving six outer cells [223].

coverage in seven cells. The bottom panel is a 2 rows $\times$ 2 columns $\times$ 2 polarizations antenna array with boresight pointing downward, and the side panel is a 4 rows $\times$ 2 columns $\times$ 2 polarizations antenna array with $1/2\lambda$ spacing between adjacent elements, boresight pointing down 23° from horizon. The maximum gain of each antenna element is 5 dBi and the HPBW is 90° in both vertical and horizontal gain patterns, with a 30 dB front-to-back ratio. This design effectively sectorizes the large service area to seven cells, one center cell surrounded by six outer cells.

LTE band 1 (DL at 2.1 GHz, UL at 1.8 GHz) with 20 MHz bandwidth and full frequency reuse in all seven cells, as well as in the single-cell case, is used for the access link (service link) in the simulation settings, and the system parameters are listed in Table 5.3. There are 20 uniformly distributed UEs for the single-cell case and 210 uniformly distributed UEs for the 7-cell case. All UEs are assumed to be outdoor in a rural area, and the large-scale propagation channel is modeled according to the 3GPP NTN channel model [211], where the LOS/NLOS status, path loss, shadow fading, and clutter loss are dependent on the elevation angle from the UE to HAPS, as has been shown in [209].

The center frequency of the feeder link (the link between the HAPS and gateway station) is 3.65 GHz. The HAPS is assumed to be in an unobstructed LOS link to the ground gateway station, so the propagation path loss of the feeder link is assumed to be free space path loss. The detailed system parameters of the feeder link are shown in Table 5.4.

5.7.3 Repeater Model for Bent-Pipe (BP) HAPS

In the design of a BP architecture system, a repeater is equipped on the HAPS to provide consistent connectivity and data service from the ground gateway station to a large area. The repeater on the BP HAPS is working as a bi-directional amplifier of RF signals in both downlink (2.1 GHz) and uplink (1.8 GHz). The repeater model specified in 3GPP TR 25.956 [228] is used for the BP architecture HAPS system, with 105 dB repeater gain, 7 dB repeater noise figure, and the

Table 5.3: System parameters for Access Link.

Environment	Outdoor Rural Marocell (RMa) area
HAPS altitude	20 Km
Carrier Frequency	DL: 2.1 GHz, UL: 1.8 GHz
Channel bandwidth	DL: 20 MHz, UL: 1 MHz
Pathloss model	NTN Path Loss model [209, 211]
BS Tx power	20 W per panel (43 dBm)
BS antenna array	As per Section 5.7.2
BS noise figure	5 dB
UE Tx power	23 dBm
UE Antenna Gain	0 dBi, omni-pattern
UE noise figure	7 dB
UL resource allocation	1 MHz per UE
User distribution	20 UEs uniformly distributed for single cell cases; 210 UEs uniformly distributed for 7-cell cases;
Traffic model	Full buffer

maximum average output power of 30 dBm.

Compared to the regenerative architecture, the additional path loss of the BP architecture (∼137.7 dB, the exact value depends on the instantaneous HAPS location in its flight pattern) introduced by the feeder link will be compensated by the gateway antenna gain (32.3 dBi) and the HAPS repeater gain (105 dB). Thus, using a 105 dB gain repeater in a bent-pipe HAPS system will result in approximately the same transmit power as in a regenerative HAPS system.

The noise will be amplified by the repeater by $105 + 7 = 112$ dB (the repeater gain plus the repeater noise figure), and then attenuated by the path loss in the access link, which will be around 121 dB to 200 dB [209], resulting in a noise power level much lower than the thermal noise at the UE receivers and hence can be safely ignored.

Utilizing a higher gain repeater ($\geq$ 105 dB) at HAPS will result in a higher transmit power for BP architecture than the RG architecture HAPS system, but it leads to higher power consumption and lower energy efficiency.

Table 5.4: System parameters for Feeder Link.

Carrier frequency	3.65 GHz
Pathloss Model	FSPL
Gateway Transmit Power	43 dBm (20 W)
Gateway Antenna	parabolic antenna, 32.3 dBi
Gateway Noise Figure	3 dB
Gateway Location	X-axis (45 km, 0, 0)
Feeder Link length	∼50 km
Feeder link FSPL	∼137.7 dB
HAPS repeater Gain	105 dB
Repeater Noise Figure	7 dB

5.7.4 Consumption Factor and Power-Efficiency Factor of HAPSs

Consumption factor theory, as introduced in [189, 229], is used to provide quantitative analysis and comparison of energy efficient design choices for wireless communication networks, in terms of the minimum energy consumption per bit required to achieve error-free communication [189]. The required energy consumption per bit can be used to evaluate the system design choices of multi-hop (repeater based bent-pipe HAPS) versus single-hop (base station based regenerative HAPS) communications.

Figure 5.9 illustrates the situation when the source and sink communicating through a relay is preferred, for the case of free-space channels, and can be expressed as (see Eq. (94) in [189]):

$$1 > \frac{\left(\frac{d_1}{d_3}\right)^2}{\left(\frac{G_{RX,relay}}{G_{RX,sink}}\right)} + \frac{\left(\frac{d_2}{d_3}\right)^2}{\left(\frac{H_{relay}}{H_{source}}\right)}, \tag{5.3}$$

where d_1, d_2, and d_3 are the distances in meters between the source to relay, relay to sink, and source to sink, respectively, as shown in Figure5.9. $G_{RX,relay}$ and $G_{RX,sink}$ are the gain of the repeater at HAPS and gain of mobile devices in this report (including antenna gains). H_{relay} and H_{source} are the power-efficiency factors of the repeater and base station at HAPS, respectively. The detailed derivations of (5.3) are provided in [189]. The power-efficiency factor H of a N-stage cascaded system can be defined as:

$$H = \left\{ 1 + \sum_{k=1}^{N} \frac{1}{\prod_{i=k+1}^{N} G_i \left(\frac{1}{\eta_k} - 1\right)} \right\}^{-1}, \tag{5.4}$$

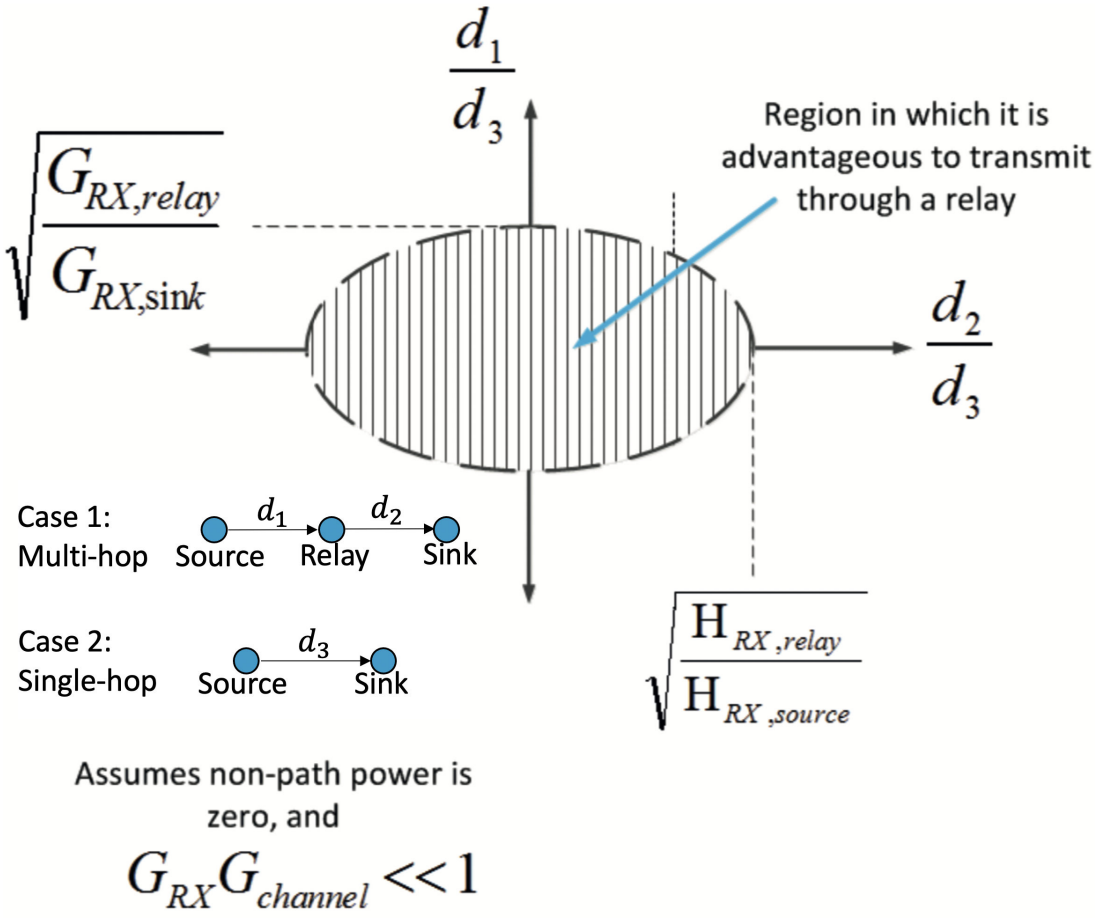

Figure 5.9: It is advantageous to use a relay (repeater) provided the relay link distances are contained within the ellipse defined by (5.3) according to consumption factor theory [189]. This assumes free space propagation.

where H ranges between 0 and 1, G_i is the gain of the i^{th} stage, η_i is the efficiency of the i^{th} signal path component. An H of 1 denotes a perfectly power efficient system that transfers all consumed energy into a radiated signal [189, 229].

For the bent-pipe HAPS architecture, the source is the gateway station, the relay is the repeater at HAPS, and for the regenerative HAPS architecture, the source is the base station at HAPS, with $d_1 \approx 50$ km and $d_2 = d_3 > 20$ km. In this report , since $G_{RX,relay} \gg G_{RX,sink}$ and $\left(\frac{d_1}{d_3}\right)^2 < \frac{25}{4}$, (5.3) depends on the ratio of the power efficiency factors of the relay (repeater) and source (base station). Assume a simple scenario that the repeater is a cascade of an omni-antenna $G_{R,Ant1} = 1$ to receive and transmit signals between the HAPS and gateway station, followed by a mixer with gain $G_{R,M}$ and power efficiency $\eta_{R,M}$, followed by an RF amplifier with gain $G_{R,Amp}$ and power efficiency $\eta_{R,Amp}$, and followed by an antenna to receive and transmit signals between the HAPS and UEs with gain $G_{R,Ant2}$ (assuming antennas have power efficiency of 1). The power-efficiency factor of the repeater at HAPS H_{relay} is:

$$H_{relay} = \left\{1 + (\frac{1}{\eta_{R,M}} - 1) + \frac{1}{G_{R,M}}(\frac{1}{\eta_{R,Amp}} - 1)\right\}^{-1}. \tag{5.5}$$

For the regenerative architecture, assume the base station on the HAPS is a cascade of a baseband

amplifier with gain $G_{B,Amp1}$ and power efficiency $\eta_{B,Amp1}$, followed by an RF mixer with gain $G_{B,M}$ and power efficiency $\eta_{B,M}$, followed by an RF amplifier with gain $G_{B,Amp2}$ and power efficiency $\eta_{B,Amp2}$, and followed by the antenna to receive and transmit between the HAPS and UEs $G_{B,Ant}$ (assuming antennas have power efficiency of 1). The power-efficiency factor of the repeater at HAPS H_{source} is:

$$H_{source} = \{1 + (\frac{1}{\eta_{B,Amp1}} - 1) + \frac{1}{G_{B,Amp1}}(\frac{1}{\eta_{B,M}} - 1) + \frac{1}{G_{B,Amp1}G_{B,M}}(\frac{1}{\eta_{B,Amp2}} - 1)\}^{-1}. \quad (5.6)$$

If the power-efficiency factor of the repeater at HAPS H_{relay} is larger than the power-efficiency factor of the base station at HAPS H_{source}, using a repeater at HAPS (the bent-pipe architecture) is more energy-efficient than using a base station at HAPS (the regenerative architecture).

5.7.5 System Simulation Setup

There were 12 simulation runs to compare the system performances of the two architectures of HAPSs, with 20 uniformly distributed UEs (17 LOS, and 3 NLOS) over an area with a radius of 60 km on the ground for the single-cell case and with 210 uniformly distributed UEs (175 LOS, and 35 NLOS) over an area with a 100 km radius on the ground for the multi-cell case (7-cell). In each simulation run, the HAPS was placed in a different location on the 6km circular flight pattern centered at the origin in 30° azimuth angle increment from the x-axis (0° azimuth angle). The UE locations and the LOS/NLOS condition of each UE were kept the same for the 12 simulation runs with different HAPS locations.

Note that the Doppler frequency shift induced by the HAPS velocity is minor relative to the subcarrier spacing of the OFDM waveform and can be corrected by the receiver [223]. Detailed simulation settings can be found in [223].

5.7.6 Simulation results of Single cell and Multicell HAPS

The spectral efficiency (SE) of data transmission is an important indicator of the HAPS system performance, which usually varies across the service area depending on the UE location as well as channel conditions [223]. The SE of a user is the amount of data transferred to (DL) or from (UL) the user normalized by the time-frequency resources used by the system for data transfer. Suppose M_u packets have been transmitted for user u, the SE η_u is calculated as:

$$\eta_u = \left(\sum_{i=1}^{M_u} N_{u,i}\right) / \left(\sum_{i=1}^{M_u} T_{u,i}B_{u,i}\right), \quad (5.7)$$

where $N_{u,i}, T_{u,i}, B_{u,i}$ are respectively the number of information bits, transmission time, and allocated bandwidth for the i-th packet of user u.

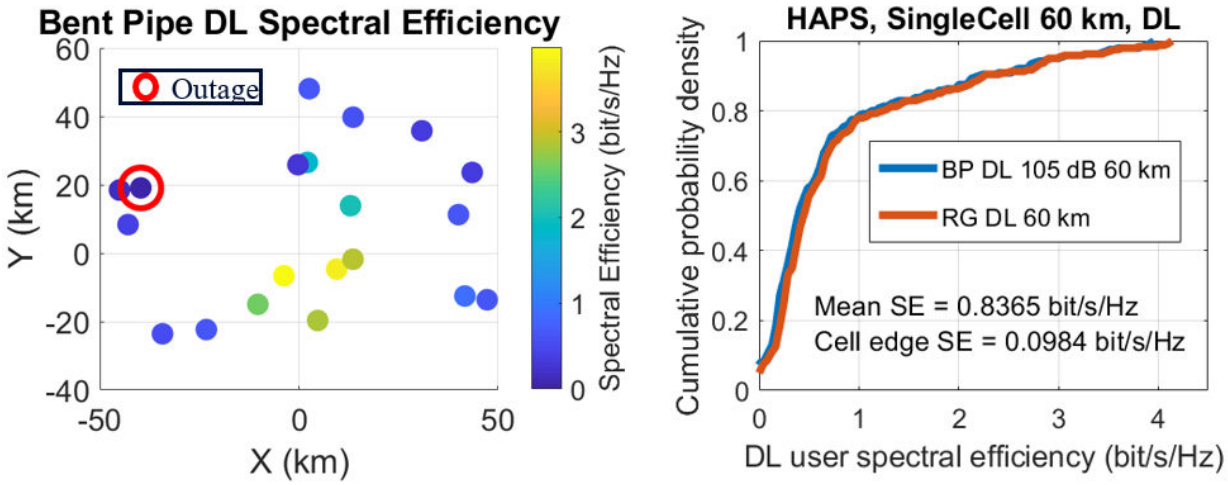

(a) HAPS DL single-cell user distribution and spectral efficiency (SE).

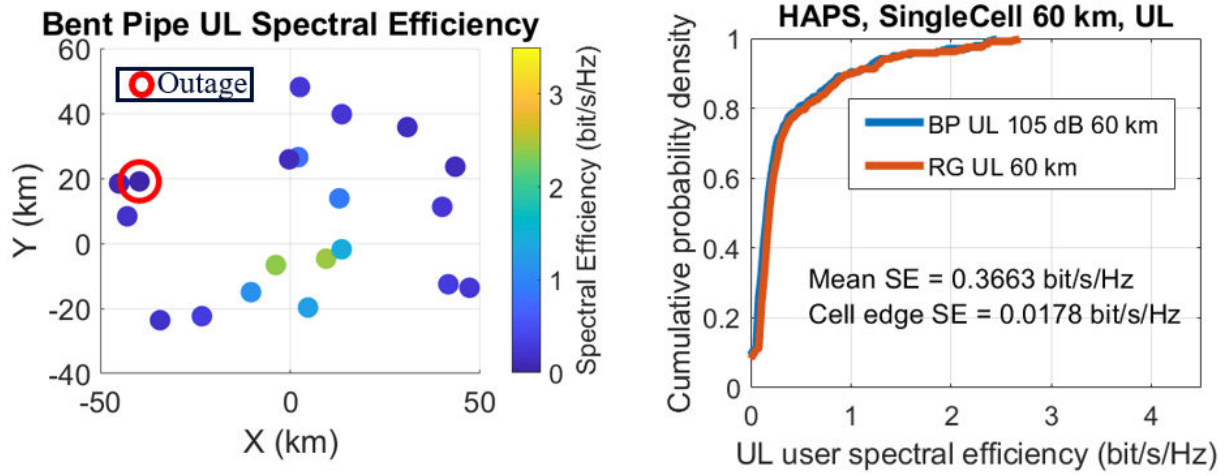

(b) HAPS uplink single-cell user distribution and spectral efficiency (SE).

Figure 5.10: Single cell (60 km radius) user density distributions from system simulations with omni-directional antennas at UEs.

Figure 5.10 shows the user SE distribution in a single cell with a radius of 60 km for both downlink and uplink with all the UEs using omni-directional antennas. There is one user in outage, which is NLOS of the HAPS, out of 20 UEs, and as expected the users having a low SE tend to be located at the cell boundaries or in a NLOS shadow fade. The RG architecture and BP architecture have similar system performance as expected. A mean SE of ∼0.84 bit/s/Hz for DL and 0.37 bit/s/Hz for UL is observed for both architectures. The cell edge SE is defined as the average SE of the lowest 5% users, and the cell edge SE is about 0.10 bit/s/Hz for DL and 0.02 bit/s/Hz for UL. The uplink coverage is limited by the low EIRP at UEs (23 dBm).

Table 5.5 characterizes the system performance of the two HAPS architectures in terms of mean system SE and cell edge SE. In general, both BP HAPS with a 105 dB gain repeater and RG HAPS can provide ∼60 km radius coverage for one cell with DL total throughput of 17 Mbps using a 20 MHz channel bandwidth. UL mean and cell edge throughput are 366 Kbps and 18 Kbps, respectively, with a 1 MHz channel bandwidth.

Table 5.5: Spectral Efficiency for a 60 km radius single cell.

	Spectral Efficiency (bit/s/Hz/cell)			
	DL (20 MHz)		UL (1 MHz)	
	BP	RG	BP	RG
Mean SE	0.837	0.841	0.366	0.370
Cell edge SE	0.098	0.105	0.018	0.019

Multi-cell cases with a proper design of antennas on HAPS will provide a larger coverage than the single-cell HAPS system. Multi-cell performance is studied for two implementation options: i) HAPS steers the sector beam while in its flight pattern to serve a fixed cell coverage area (beam steering, applicable to both LTE and NR) [223]; ii) HAPS does not steer beams, but the UE dynamically switches beam via NR beam management (beam selection) [230].

Figure 5.11 shows the user SE distribution in a 7-cell area with a radius of 100 km for both downlink and uplink with all the UEs using omni-directional antennas, where beam steering techniques are used on the HAPS. The user SE is averaged over the 12 simulation runs with the HAPS in different locations in the flight pattern. The BP and RG architectures have similar performance in the multi-cell case, with just minor fluctuations due to feeder link path loss changes due to the HAPS movement. The downlink mean SE is 1.22 bit/s/Hz/cell and the downlink cell edge SE is about 0.15 bit/s/Hz/cell. In the uplink, the mean SE is 0.64 bit/s/Hz/cell and the cell edge SE is 0.03 bit/s/Hz/cell. Compared to the single case as shown in Figure 5.10, using a hexagon antenna design for HAPS factorization can provide a larger coverage area and better system performance. However, the uplink coverage is still challenging in the multi-cell case. Directional high gain antennas at the UE would improve the UL SE.

Another implementation option is to rely on the beam selection mechanism in NR based on UE's

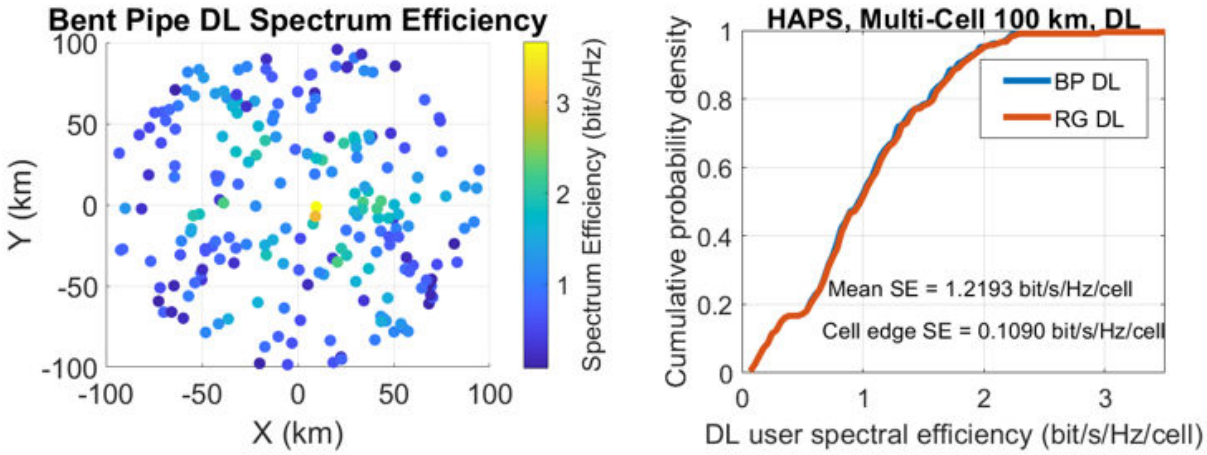

(a) Downlink multi-cell user distribution and spectral efficiency for omni-antenna UEs with beam steering.

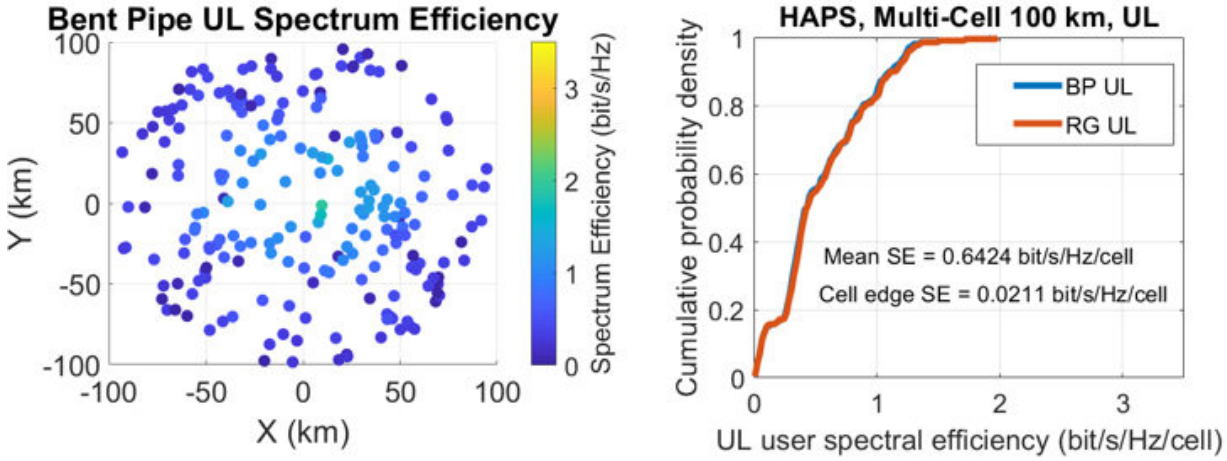

(b) Uplink multi-cell user distribution and spectral efficiency for omni-antenna UEs with beam steering.

Figure 5.11: Multi-cell (100 km radius) user density distributions from system simulations with omni-directional antennas at UEs with beam steering on the HAPS.

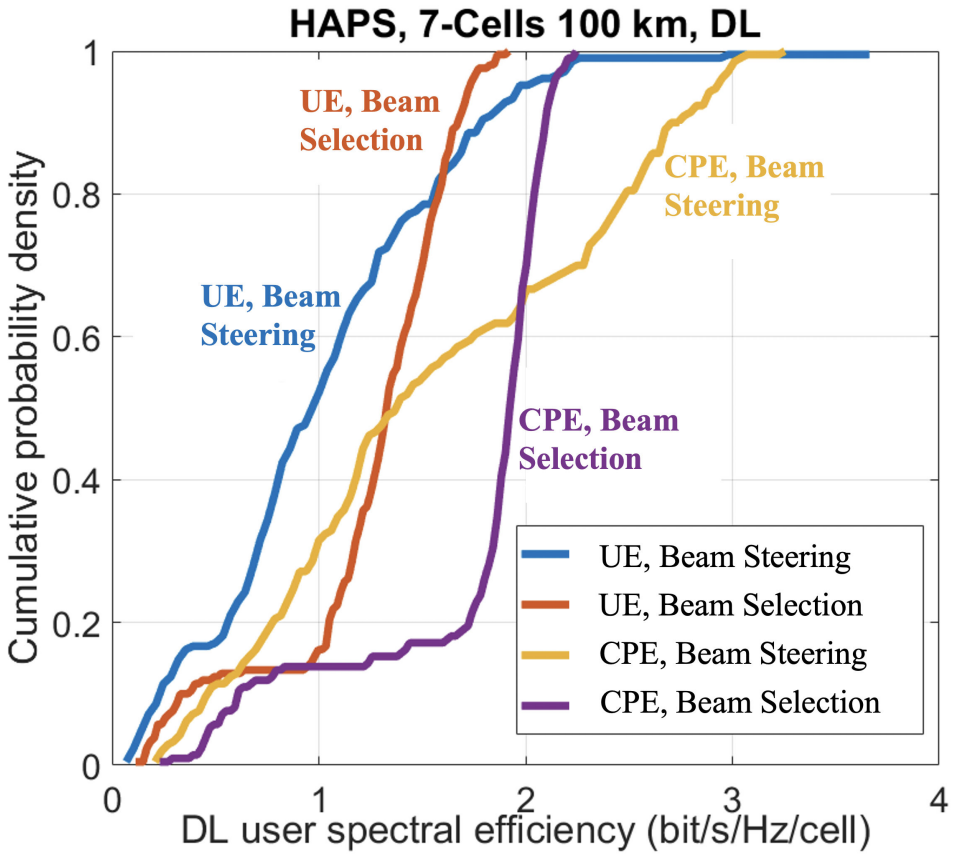

Figure 5.12: User DL spectral efficiency with beam steering and beam selection for UE (omni-antenna) and CPE (directional antenna) options.

beam measurement [230] instead of HAPS actively steering the beam to serve a fixed cell. The system performance with the same settings and UE distributions is shown in Figs. 5.12, 5.13 and Table 5.6. The downlink mean SE is 1.32 bit/s/Hz/cell and the cell edge SE is about 0.22 bit/s/Hz/cell. In the uplink, the mean SE is 0.70 bit/s/Hz/cell and the cell edge SE is 0.05 bit/s/Hz/cell. Comparison of the user SE with beam steering and beam selection are presented in Figs. 5.12 and 5.13, indicating NR beam selection may provide a tangible improvement over beam steering. This is because the UE can experience a higher beamforming gain when the beam is not steered. However, the signaling overhead associated with beam measurement, reporting, and indication is not modeled in the simulations.

We also consider the Customer Premises Equipment (CPE) with a directional antenna, assuming 12 dBi maximum antenna gain and 60° HPBW in both vertical and horizontal gain patterns. The omni-antenna UEs are replaced with these CPE devices with the same location and fading condition in the simulations. The directional antenna of a CPE is always pointing to HAPS in azimuth (assume optimum orientation in azimuth), but the antenna boresight elevation angle is assumed to be 0° (in the horizon). When beam steering is applied to CPE devices, the downlink mean SE increases to 1.69 bit/s/Hz/cell and the cell edge SE increases to 0.34 bit/s/Hz/cell. The uplink mean SE increases to 0.83 bit/s/Hz/cell and the cell edge SE increases to 0.06 bit/s/Hz/cell.

When NR beam selection is applied to CPE devices, the downlink mean SE increases to 1.80 bit/s/Hz/cell and the cell edge SE increases to 0.47 bit/s/Hz/cell. The uplink mean SE increases to

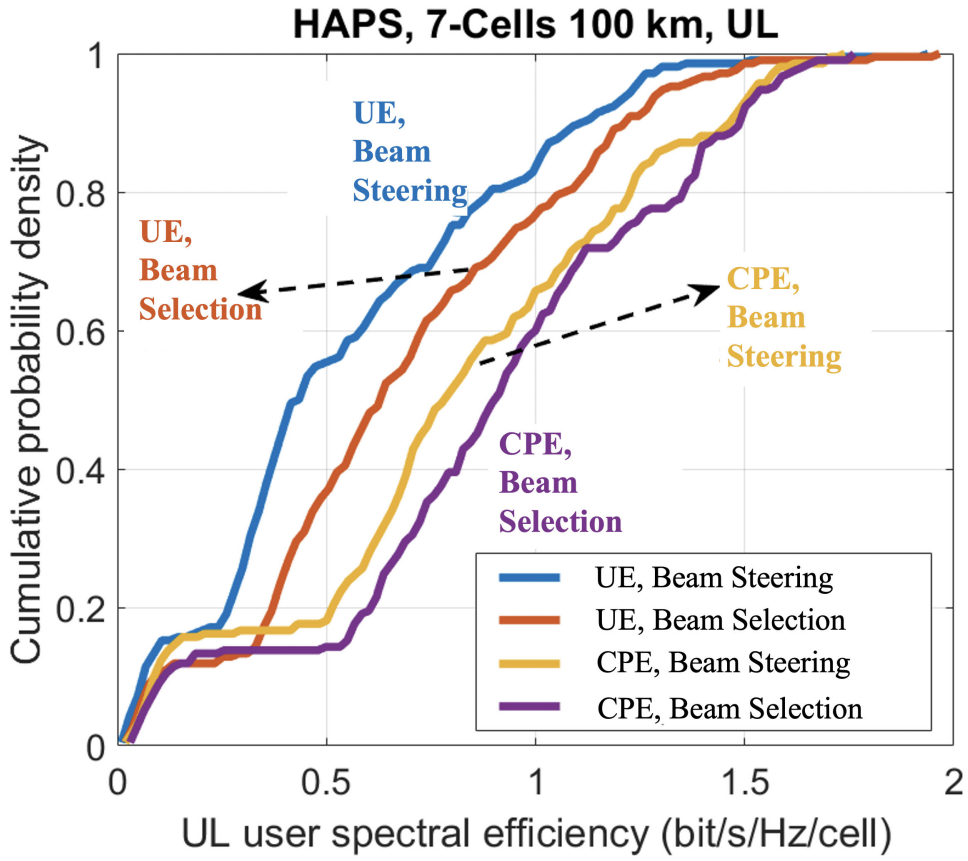

Figure 5.13: User UL spectral efficiency with beam steering and beam selection for UE (omni-antenna) and CPE (directional antenna) options.

0.89 bit/s/Hz/cell and the cell edge SE increases to 0.06 bit/s/Hz/cell. Figs. 5.12 and 5.13 show that directional antenna at the UE side can greatly improve the throughput for both the mean and cell edge user SE, and the BP architecture and RG architecture perform similarly as expected. For better coverage and capacity, using the NR beam selection for devices equipped with directional antennas is the preferred option.

5.8 Conclusion

This chapter analyzes Non-Terrestrial Networks (air-to-ground and ground-to-air propagation), spectrum sharing techniques between satellite and terrestrial networks, and presents rooftop surrogate satellite measurements at 142 GHz conducted in Downtown Brooklyn, NY. Elevation angles and antenna sidelobes play an important role in the received power in air-to-ground channels. Reflected rays by neighboring buildings from the ground to the air are about 20 dB lower than the direct LOS path, showing that if the propagation of ground terminals is kept on the horizon (e.g., $\leq 15°$), with reduced sidelobes there may not be any interference in the same or adjacent bands between surrogate satellites and terrestrial terminals, or between terrestrial backhaul links and mobile links at frequencies above 100 GHz. The average foliage loss in urban microcell environments is 6.9 dB

Table 5.6: Spectral Efficiency for a 100 km radius multi-cell area.

7-Cell Spectral Efficiency (bit/s/Hz/cell)			
Cases		DL (20 MHz)	UL (1 MHz)
		BP& RG	BP& RG
Beam Steering for omni-UE	Mean SE	1.219	0.642
	Cell edge SE	0.146	0.035
Beam Selection for omni-UE	Mean SE	1.323	0.699
	Cell edge SE	0.216	0.051
Beam Steering for CPE	Mean SE	1.694	0.827
	Cell edge SE	0.339	0.060
Beam Selection for CPE	Mean SE	1.797	0.889
	Cell edge SE	0.470	0.063

(a 7-8 m slant link length through foliage) with the foliage attenuation rate of 0.9 dB/m at 142 GHz. Measurements and models presented here contribute to the understanding that THz will be useful for urban wireless communication, even in NLOS, as well as non-terrestrial (e.g., satellite and UAV communications) wireless channels, and may help with spectrum sharing techniques between the satellites and the ground terminals.

In this chapter, we have also presented two practical architecture designs of HAPS systems, which are capable of providing a single cell coverage of 60 km and multi-cell coverage of a 100 km radius. Both the repeater based solution and the CU/DU split based solutions are viable technical options. However, HAPS weight and power limitations and feeder link capacity dictate the practical design. Consumption factor theory is used to provide quantitative analysis and comparison of energy efficiency of the two architectures. The situation when using the repeater based architecture is more power efficient based on consumption factor theory is presented. While the HAPS is executing a repetitive flight pattern, fixed cell areas can be continually served by either beam steering from the HAPS or by NR beam management based on UE measurement. In the 100 km radius multi-cell case, with a 20 MHz bandwidth, DL sector throughput is 26 Mbps and DL cell edge throughput is 4 Mbps. While in the UL with a 1 MHz bandwidth, the UL mean and cell edge throughput is 0.7 Mbps and 50 Kbps, respectively. The uplink coverage is limited by UE transmit power and UE antenna gain. Directional antennas at the UE may significantly help improve the throughput for both DL and UL. A repeater based solution is preferred over the full BBU at HAPS concerning the hardware complexity and cost. Utilizing a high gain repeater in a bent-pipe HAPS system can result in approximately the same or even stronger transmit power as in a regenerative HAPS system, which leads to a similar or even better performance in terms of spectral efficiency even with relatively low complexity. Consumption factory theory allows quantitative comparisons of power efficiency with

different architectures or designs of communication systems, providing insights for power budget analysis of future communication systems operating at data rates of hundreds of Gbps. Terrestrial networks co-existence with HAPS systems is an essential research topic for future work.

Chapter 6

Conclusions

Sub-THz and THz channel sounding techniques that are used to measure the channel impulse responses are critical to measure, learn, and model the wireless channels at frequencies above 100 GHz. This report presented the current spectrum regulations above 100 GHz around the world, introduced the main channel sounding techniques including the frequency-domain VNA-based channel sounders, and time-domain correlation-based and THz pulse-based channel sounders. The novel design of sliding-correlation based channel sounder at NYU WIRELESS was detailed presented.

Using the channel sounder at NYU WIRELESS, we first analyzed the fundamental propagation issues including antenna cross-polarization, reflection, penetration, and scattering at 142 GHz and compared the proprieties to lower frequencies at 28 and 73 GHz. It showed that reflection is a little stronger (1-2 dB stronger) at 142 GHz than at 28 GHz and 73 GHz for common materials like drywall and clear glasses. However, the partition loss is observed to be larger at higher frequencies for most materials. Scattering effects were observed at 142 GHz frequencies but the scattered power is 20 dB below the specular reflection power which means for most indoor and outdoor obstructions, the surfaces were considered smooth at 142 GHz and the scattered power was negligible compared to the specular reflection.

With the same channel sounder system, extensive radio propagation measurements in indoor hotspot office (TR separation distance of 4-46 m) and outdoor urban microcell environments (TR separation distance of 20-117 m) were conducted for both LOS and NLOS scenarios. The path loss components of both CI and CIF models in both LOS and NLOS scenarios are notably similar over different frequency bands from mmWave to sub-THz frequencies (e.g., 28, 38, 73, and 142 GHz), when referenced to the free space path loss in the first meter (near field) [39, 43, 44, 91, 141], implying the wireless channels at THz frequencies are not that different from today's mmWave channels with the exception of the first meter path loss. Measurements showed that there was not much difference between the channels below and above 100 GHz. The statistical distribution at higher frequencies (e.g., 140 GHz) for important channel parameters like the number of clusters, delay spread, the number of subpaths per cluster is the same as frequencies below 100 GHz (e.g., 28 and 73 GHz), which means with some modification to the distribution parameters, the channel models developed

for frequencies below 100 GHz can still be used at higher frequencies [67, 92].

This report also analyzed both the single-cell and multi-cell base station coverage of sub-THz systems at 142 GHz in outdoor UMi scenarios based on the realistic channel models derived from field measurements we conducted. The single-cell base station can provide coverage of a 200 m radius, and the 7-cell base stations can provide total coverage of a 400 m radius. The 7-cell architecture can greatly improve the coverage and system performance in terms of the average and median SE compared to the single-cell case but has a worse performance to the cell-edge users. In the 7-cell case, with a 1 GHz bandwidth, DL sector throughput is 4.5 Gbps and DL cell-edge throughput is 40 Mbps. The uplink coverage is limited by UE transmit power and UE antenna gain.

Other important application components for future generation communications (6G and beyond) such as non-terrestrial networks (e.g., satellites, HAPS, and UAVs) and intelligent reflecting surfaces were also studied in this report. Key propagation-related characteristics and optimal phase shift solutions of IRSs for different incident and reflection angles were presented in Chapter VI. Raytracing-based simulations of IRSs were performed at 28 GHz in both indoor and outdoor scenarios, and the results show that IRS can greatly extend coverage and improve capacity at low cost.

In general, this report provides the fundamental knowledge and a comprehensive understanding of the wireless channels at sub-THz frequencies, and it also demonstrates how the engineering efforts to create mmWave 5G networks will carry forward to frequencies as high as 800-900 GHz, meaning that the engineering developments of adaptive beamforming, wideband channel allocation, and site-specific installation used to create today's 5G networks will hold for the coming several decades as mobile communications move up into the THz range.

Bibliography

[1] T. S. Rappaport *et al.*, "Wireless Communications and Applications Above 100 GHz: Opportunities and Challenges for 6G and Beyond (Invited)," *IEEE Access*, vol. 7, pp. 78 729–78 757, Feb. 2019.

[2] A. Ghosh, A. Maeder, M. Baker, and D. Chandramouli, "5G Evolution: A View on 5G Cellular Technology Beyond 3GPP Release 15," *IEEE Access*, vol. 7, pp. 127 639–127 651, Sept. 2019.

[3] T. S. Rappaport, "5g's killer app will be 6g: Massive mimo millimeter waves, and small cell infrastructure will pay off for future tech generations," *IEEE Spectrum OP-ED*, Aug. 2021.

[4] H. Viswanathan and P. E. Mogensen, "Communications in the 6G Era," *IEEE Access*, vol. 8, pp. 57 063–57 074, 2020.

[5] M. J. Marcus, J. M. Jornet, and X. C. Roman, "Opening Spectrum > 95 GHz for Practical Use: Recent Actions on Sharing and Regulatory Issues," in *submission to 2021 IEEE International Microwave Symposium (IMS)*, Feb 2021, pp. 1–4.

[6] H. Elayan, O. Amin, B. Shihada, R. M. Shubair, and M.-S. Alouini, "Terahertz band: The last piece of rf spectrum puzzle for communication systems," *IEEE Open Journal of the Communications Society*, vol. 1, pp. 1–32, 2020.

[7] M. J. Marcus, "Progress in opening access to spectrum above 100 ghz," *IEEE Wireless Communications*, vol. 26, no. 2, pp. 2–3, 2019.

[8] Ministry of Internal Affairs and Communications, "Frequency Assignment Plan (as of March 2019)," March 2019. [Online]. Available: https://www.tele.soumu.go.jp/e/adm/freq/search/share/plan.htm

[9] Conference of European Postal and Telecommunications, "ERC Recommendation 70-03: Relating to the use of Short Range Devices (SRD)," Oct. 2018.

[10] Federal Communications Commission, "Notice of Proposed Rulemaking: ET Docket No. 18-21," Feb. 2018.

[11] FCC, "Spectrum horizons," *First Report and Order – ET Docket 18-21*, Washington D. C., 2019.

[12] The office of communications (Ofcom), "Statement:Support innovation in the 100-200 GHz range," *UK*, October 1, 2020.

[13] mmWave Coalition, "mmWave Coalition's NTIA comments," Jan. 2019. [Online]. Available: http://mmwavecoalition.org/mmwave-coalition-millimeter-waves/mmwave-coalitions-ntia-comments/

[14] "Ieee standard for high data rate wireless multi-media networks–amendment 2: 100 gb/s wireless switched point-to-point physical layer," *IEEE Std 802.15.3d-2017 (Amendment to IEEE Std 802.15.3-2016 as amended by IEEE Std 802.15.3e-2017)*, pp. 1–55, Oct. 2017.

[15] V. Petrov, D. Moltchanov, and Y. Koucheryavy, "Applicability assessment of terahertz information showers for next-generation wireless networks," in *2016 IEEE International Conference on Communications (ICC)*, May 2016, pp. 1–7.

[16] V. Petrov, A. Pyattaev, D. Moltchanov, and Y. Koucheryavy, "Terahertz band communications: Applications, research challenges, and standardization activities," in *2016 8th International Congress on Ultra Modern Telecommunications and Control Systems and Workshops (ICUMT)*, Oct. 2016, pp. 183–190.

[17] K. Sengupta, T. Nagatsuma, and D. M. Mittleman, "Terahertz integrated electronic and hybrid electronic–photonic systems," *Nature Electronics*, vol. 1, no. 12, p. 622, 2018.

[18] Federal Comm. Commission, "Use of Spectrum Bands Above 24 GHz For Mobile Radio Services: GN Docket No. 14-177," Dec 2018.

[19] A. Maltsev *et al.*, "Channel models for IEEE 802.11ay," doc.: IEEE 802.11-15/1150r9, Mar. 2017.

[20] A.-A. A. Boulogeorgos *et al.*, "Terahertz Technologies to Deliver Optical Network Quality of Experience in Wireless Systems Beyond 5G," *IEEE Communications Magazine*, vol. 56, no. 6, pp. 144–151, 2018.

[21] I. F. Akyildiz, J. M. Jornet, and C. Han, "Terahertz band: Next frontier for wireless communications," *Physical Communication*, vol. 12, pp. 16–32, 2014.

[22] T. Kürner and S. Priebe, "Towards THz communications-status in research, standardization and regulation," *Journal of Infrared, Millimeter, and Terahertz Waves*, vol. 35, no. 1, pp. 53–62, 2014.

[23] M. J. W. Rodwell, Y. Fang, J. Rode, J. Wu, B. Markman, S. T. Šuran Brunelli, J. Klamkin, and M. Urteaga, "100-340ghz systems: Transistors and applications," in *2018 IEEE International Electron Devices Meeting (IEDM)*, Dec. 2018, pp. 14.3.1–14.3.4.

[24] H. Aggrawal, P. Chen, M. M. Assefzadeh, B. Jamali, and A. Babakhani, "Gone in a picosecond: Techniques for the generation and detection of picosecond pulses and their applications," *IEEE Microwave Magazine*, vol. 17, no. 12, pp. 24–38, Dec. 2016.

[25] D. M. Mittleman, "Twenty years of terahertz imaging," *Opt. Express*, vol. 26, no. 8, pp. 9417–9431, Apr. 2018.

[26] M. Tonouchi, "Cutting-edge terahertz technology," *Nature photonics*, vol. 1, no. 2, pp. 97–105, 2007.

[27] J. Harvey *et al.*, "Exploiting High Millimeter Wave Bands for Military Communications,Applications, and Design," *IEEE ACCESS*, 2019.

[28] J. N. Murdock and T. S. Rappaport, "Consumption factor: A figure of merit for power consumption and energy efficiency in broadband wireless communications," in *2011 IEEE GLOBECOM Workshops (GC Wkshps)*, Dec. 2011, pp. 1393–1398.

[29] ——, "Consumption factor and power-efficiency factor: A theory for evaluating the energy efficiency of cascaded communication systems," *IEEE Journal on Selected Areas in Communications*, vol. 32, no. 2, pp. 221–236, Feb. 2014.

[30] H. T. Friis, "A note on a simple transmission formula," *Proceedings of the IRE*, vol. 34, no. 5, pp. 254–256, May 1946.

[31] ITU-R, "Attenuation by Atmospheric Gases," Tech. Rep. P.676-11, Sept. 2016.

[32] Y. Xing and T. S. Rappaport, "Terahertz Wireless Communications: Co-sharing for Terrestrial and Satellite Systems above 100 GHz (Invited)," *in IEEE Communications Letters*, pp. 1–5, June 2021.

[33] H. J. Liebe, T. Manabe, and G. A. Hufford, "Millimeter-wave attenuation and delay rates due to fog/cloud conditions," *IEEE transactions on antennas and propagation*, vol. 37, no. 12, pp. 1617–1612, 1989.

[34] T. S. Rappaport, J. N. Murdock, and F. Gutierrez, "State of the art in 60-GHz integrated circuits and systems for wireless communications," *Proceedings of the IEEE*, vol. 99, no. 8, pp. 1390–1436, Aug. 2011.

[35] Y. Yang, M. Mandehgar, and D. Grischkowsky, "Determination of the water vapor continuum absorption by THz-TDS and Molecular Response Theory," *Opt. Express*, vol. 22, no. 4, pp. 4388–4403, Feb. 2014.

[36] J. Ma, J. Adelberg, R. Shrestha, L. Moeller, and D. M. Mittleman, "The Effect of Snow on a Terahertz Wireless Data Link," vol. 39, Mar. 2018.

[37] J. Ma, R. Shrestha, L. Moeller, and D. M. Mittleman, "Channel performance for indoor and outdoor terahertz wireless links," *APL Photonics*, vol. 3, no. 5, pp. 1–13, Feb. 2018.

[38] T. S. Rappaport, R. W. Heath, Jr., R. C. Daniels, and J. N. Murdock, *Millimeter Wave Wireless Communications*. Pearson/Prentice Hall, 2015.

[39] T. S. Rappaport *et al.*, "Millimeter Wave Mobile Communications for 5G Cellular: It Will Work!" *IEEE Access*, vol. 1, pp. 335–349, May 2013.

[40] T. S. Rappaport, Y. Xing, G. R. MacCartney, A. F. Molisch, E. Mellios, and J. Zhang, "Overview of Millimeter Wave Communications for Fifth-Generation (5G) Wireless Networks-With a Focus on Propagation Models," *IEEE Transactions on Antennas and Propagation*, vol. 65, no. 12, pp. 6213–6230, Dec. 2017.

[41] S. Sun, G. R. MacCartney, Jr., and T. S. Rappaport, "A Novel Millimeter-Wave channel simulator and applications for 5G wireless communications," in *IEEE International Conference on Communication (ICC)*, May 2017, pp. 1–7.

[42] G. R. MacCartney, Jr. and T. S. Rappaport, "Rural macrocell path loss models for millimeter wave wireless communications," *IEEE Journal on Selected Areas in Communications*, vol. 35, no. 7, pp. 1663–1677, July 2017.

[43] Y. Xing, T. S. Rappaport, and A. Ghosh, "Millimeter Wave and sub-THz Indoor Radio Propagation Channel Measurements, Models, and Comparisons in an Office Environment (Invited)," *in IEEE Communications Letters*, pp. 1–5, June 2021.

[44] S. Sun *et al.*, "Investigation of Prediction Accuracy, Sensitivity, and Parameter Stability of Large-Scale Propagation Path Loss Models for 5G Wireless Communications," *IEEE Transactions on Vehicular Technology*, vol. 65, no. 5, pp. 2843–2860, May 2016.

[45] M. K. Samimi, T. S. Rappaport, and G. R. MacCartney, Jr., "Probabilistic omnidirectional path loss models for millimeter-wave outdoor communications," *IEEE Wireless Communications Letters*, vol. 4, no. 4, pp. 357–360, Aug. 2015.

[46] mmWave Coalition, "US246 Petition For Rulemaking," Aug. 2019. [Online]. Available: https://mmwavecoalition.org/mmwc-filing/us246-petition-for-rulemaking/

[47] Z. Qingling and J. Li, "Rain attenuation in millimeter wave ranges," in *2006 7th International Symposium on Antennas, Propagation EM Theory*, Oct. 2006, pp. 1–4.

[48] ITU-R, "Specific attenuation model for rain for use in prediction methods, propagation in non-ionized media," Tech. Rep. P.838-3, 2005.

[49] R. Crane, *Electromagnetic Wave Propagation through Rain.* New York: John Wiley and Sons, 1996.

[50] A. Hirata *et al.*, "Effect of Rain Attenuation for a 10-Gb/s 120-GHz-Band Millimeter-Wave Wireless Link," *IEEE Transactions on Microwave Theory and Techniques*, vol. 57, no. 12, pp. 3099–3105, Nov. 2009.

[51] H. Xu *et al.*, "Measurements and models for 38-GHz point-to-multipoint radiowave propagation," *IEEE Journal on Selected Areas in Communications*, vol. 18, no. 3, pp. 310–321, Mar. 2000.

[52] Z. Qingling and J. Li, "Rain attenuation in millimeter wave ranges," in *2006 7th International Symposium on Antennas, Propagation & EM Theory.* IEEE, 2006, pp. 1–4.

[53] K. Su, L. Moeller, R. B. Barat, and J. F. Federici, "Experimental comparison of performance degradation from terahertz and infrared wireless links in fog," *J. Opt. Soc. Am. A*, vol. 29, no. 2, pp. 179–184, Feb. 2012.

[54] ——, "Experimental comparison of terahertz and infrared data signal attenuation in dust clouds," *J. Opt. Soc. Am. A*, vol. 29, no. 11, pp. 2360–2366, Nov. 2012.

[55] M. L. F. J. F. Ma, Jianjun, "Experimental comparison of terahertz and infrared signaling in controlled atmospheric turbulence," *Journal of Infrared, Millimeter, and Terahertz Waves*, vol. 36, no. 2, pp. 130–143, Feb. 2015.

[56] J. Ma, F. Vorrius, L. Lamb, L. Moeller, and J. F. Federici, "Comparison of experimental and theoretical determined terahertz attenuation in controlled rain," *Journal of Infrared, Millimeter, and Terahertz Waves*, vol. 36, no. 12, pp. 1195–1202, 2015.

[57] E. Moon, T. Jeon, and D. R. Grischkowsky, "Long-Path THz-TDS Atmospheric Measurements Between Buildings," *IEEE Transactions on Terahertz Science and Technology*, vol. 5, no. 5, pp. 742–750, Sept. 2015.

[58] M. Aladsani, A. Alkhateeb, and G. C. Trichopoulos, "Leveraging mmWave Imaging and Communications for Simultaneous Localization and Mapping," in *International Conference on Acoustics, Speech, and Signal Processing (ICASSP)*, May 2019, pp. 1–4.

[59] O. Kanhere and T. S. Rappaport, "Position locationing for millimeter wave systems," in *IEEE 2018 Global Communications Conference*, Dec. 2018, pp. 1–6.

[60] D. M. Mittleman, R. H. Jacobsen, R. Neelamani, R. G. Baraniuk, and M. C. Nuss, "Gas sensing using terahertz time-domain spectroscopy," *Applied Physics B: Lasers and Optics*, vol. 67, no. 3, pp. 379–390, Sept. 1998.

[61] X.-F. Teng, Y.-T. Zhang, C. C. Poon, and P. Bonato, "Wearable medical systems for p-health," *IEEE reviews in Biomedical engineering*, vol. 1, pp. 62–74, Dec. 2008.

[62] D. M. Mittleman, "Perspective: Terahertz science and technology," *Journal of Applied Physics*, vol. 122, no. 23, p. 230901, 2017.

[63] S. Chinchali *et al.*, "Network offloading policies for cloud robotics: a learning-based approach," *arXiv preprint arXiv:1902.05703*, Feb. 2019.

[64] S. Garg *et al.*, "Enabling the Next Generation of Mobile Robotics using 5G Wireless," *Proceedings of IEEE, submitted*, .

[65] M. Chen *et al.*, "Cognitive internet of vehicles," *Computer Communications*, vol. 120, pp. 58–70, May 2018.

[66] Y. Xing and T. S. Rappaport, "Indoor Wireless Channel Properties at Millimeter Wave and Sub-Terahertz Frequencies," in *submitted to IEEE 2019 Global Communications Conference*, Dec. 2019, pp. 1–6.

[67] ——, "Propagation Measurements and Path Loss models for sub-THz in Urban Microcells," in *Proc. IEEE International Conference on Communications*, June 2021, pp. 1–6.

[68] N. A. Abbasi *et al.*, "Double directional channel measurements for thz communications in an urban environment," in *ICC 2020 - 2020 IEEE International Conference on Communications (ICC)*, June 2020, pp. 1–6.

[69] S. L. H. Nguyen *et al.*, "Comparing Radio Propagation Channels Between 28 and 140 GHz Bands in a Shopping Mall," *European Conference on Antennas and Propagation*, pp. 1–5, Apr. 2018.

[70] A. Al-Saman, M. Cheffena, O. Elijah, Y. A. Al-Gumaei, S. K. Abdul Rahim, and T. Al-Hadhrami, "Survey of millimeter-wave propagation measurements and models in indoor environments," *Electronics*, vol. 10, no. 14, 2021.

[71] Y. L. Y. C. N. A. T. K. A. F. M. Chong Han, Yiqin Wang, "Terahertz Wireless Channels: A Holistic Survey on Measurement, Modeling, and Analysis," October 2021.

[72] W. L. Chan, J. Deibel, and D. M. Mittleman, "Imaging with terahertz radiation," *Reports on progress in physics*, vol. 70, no. 8, p. 1325, 2007.

[73] S. Rey, J. M. Eckhardt, B. Peng, K. Guan, and T. Kürner, "Channel sounding techniques for applications in THz communications: A first correlation based channel sounder for ultra-wideband dynamic channel measurements at 300 GHz," in *2017 9th International Congress on Ultra Modern Telecommunications and Control Systems and Workshops (ICUMT)*, Nov. 2017, pp. 449–453.

[74] G. R. MacCartney and T. S. Rappaport, "A flexible millimeter-wave channel sounder with absolute timing," *IEEE Journal on Selected Areas in Communications*, vol. 35, no. 6, pp. 1402–1418, June 2017.

[75] Y. Xing and T. S. Rappaport, "Propagation Measurement System and Approach at 140 GHz–Moving to 6G and Above 100 GHz," in *IEEE 2018 Global Communications Conference*, Dec. 2018, pp. 1–6.

[76] R. Piesiewicz, C. Jansen, D. Mittleman, T. Kleine-stmann, M. Koch, and T. Kurner, "Scattering analysis for the modeling of thz communication systems," *IEEE Transactions on Antennas and Propagation*, vol. 55, no. 11, pp. 3002–3009, 2007.

[77] Z. Hossain, C. N. Mollica, J. F. Federici, and J. M. Jornet, "Stochastic interference modeling and experimental validation for pulse-based terahertz communication," *IEEE Transactions on Wireless Communications*, vol. 18, no. 8, pp. 4103–4115, Aug. 2019.

[78] T. S. Rappaport, *Wireless Communications: Principles and Practice*, 2nd ed. Upper Saddle River, NJ: Prentice Hall, 2002.

[79] S. L. H. Nguyen *et al.*, "Comparing Radio Propagation Channels Between 28 and 140 GHz Bands in a Shopping Mall," *European Conference on Antennas and Propagation*, pp. 1–5, Apr. 2018.

[80] S. L. Nguyen, K. Haneda, and J. Putkonen, "Dual-band multipath cluster analysis of small-cell backhaul channels in an urban street environment," in *Globecom Workshops (GC Wkshps), 2016 IEEE*, Dec. 2016, pp. 1–6.

[81] S. Kim, W. T. Khan, A. Zajić, and J. Papapolymerou, "D-band channel measurements and characterization for indoor applications," *IEEE Transactions on Antennas and Propagation*, vol. 63, no. 7, pp. 3198–3207, July 2015.

[82] C. L. Cheng, S. Kim, and A. Zajić, "Comparison of path loss models for indoor 30 GHz, 140 GHz, and 300 GHz channels," in *2017 11th European Conference on Antennas and Propagation*, Mar. 2017, pp. 716–720.

[83] G. R. MacCartney, Jr., T. S. Rappaport, M. K. Samimi, and S. Sun, "Millimeter-wave omnidirectional path loss data for small cell 5G channel modeling," *IEEE Access*, vol. 3, pp. 1573–1580, Aug. 2015.

[84] 3GPP, "Study on channel model for frequencies from 0.5 to 100 GHz," 3rd Generation Partnership Project (3GPP), TR 38.901 V14.0.0, May 2017.

[85] E. R. P. Laura, "Charaterization of sub-THz and mmWave Propagation Channel for Indoor Scenarios," *Eucap*, pp. 1–4, July 2018.

[86] S. Bhardwaj, N. K. Nahar, and J. L. Volakis, "All electronic propagation loss measurement and link budget analysis for 350 ghz communication link," *Microwave and Optical Technology Letters*, vol. 59, no. 2, pp. 415–423, July 2016.

[87] S. Priebe, C. Jastrow, M. Jacob, T. Kleine-Ostmann, T. Schrader, and T. Kurner, "Channel and Propagation Measurements at 300 GHz," *IEEE Transactions on Antennas and Propagation*, vol. 59, no. 5, pp. 1688–1698, May 2011.

[88] T. Kleine-Ostmann, C. Jastrow, S. Priebe, M. Jacob, T. Kürner, and T. Schrader, "Measurement of channel and propagation properties at 300 ghz," in *2012 Conference on Precision electromagnetic Measurements*, July 2012, pp. 258–259.

[89] N. Khalid and O. B. Akan, "Wideband THz communication channel measurements for 5G indoor wireless networks," in *2016 IEEE International Conference on Communications (ICC)*, May 2016, pp. 1–6.

[90] G. R. MacCartney, Jr. *et al.*, "A flexible wideband millimeter-wave channel sounder with local area and NLOS to LOS transition measurements," in *2017 IEEE International Conference on Communications (ICC)*, May 2017, pp. 1–7.

[91] Y. Xing and T. S. Rappaport, "Millimeter Wave and Terahertz Urban Microcell Propagation Measurements and Models (Invited Paper)," *in IEEE Communications Letters*, pp. 1–5, Sept. 2021.

[92] S. Ju *et al.*, "Millimeter Wave and Sub-Terahertz Spatial Statistical Channel Model for an Indoor Office Building," *IEEE Journal on Selected Areas in Communications, Special Issue on TeraHertz Communications and Networking*, vol. 39, no. 6, pp. 1561–1575, June 2021.

[93] D. Dupleich *et al.*, "Characterization of the propagation channel in conference room scenario at 190 ghz," in *2020 14th European Conference on Antennas and Propagation (EuCAP)*, March 2020, pp. 1–5.

[94] F. Undi *et al.*, "Angle-resolved thz channel measurements at 300 ghz in an outdoor environment," in *2021 IEEE International Conference on Communications Workshops (ICC Workshops)*, June 2021, pp. 1–7.

[95] J. M. Jornet and I. F. Akyildiz, "Channel modeling and capacity analysis for electromagnetic wireless nanonetworks in the terahertz band," *IEEE Transactions on Wireless Communications*, vol. 10, no. 10, pp. 3211–3221, Oct. 2011.

[96] C. Wang, C. Lin, Q. Chen, B. Lu, X. Deng, and J. Zhang, "A 10-gbit/s wireless communication link using 16-qam modulation in 140-ghz band," *IEEE Transactions on Microwave Theory and Techniques*, vol. 61, no. 7, pp. 2737–2746, July 2013.

[97] T.Wu, T. S. Rappaport, M. Knox, and D. Shahrjerdi, "A Wideband Sliding Correlator-Based Channel Sounder with Synchronization in 65 nm CMOS," in *IEEE 2019 International Symposium on Circuits and Systems (ISCAS)*, May 2019, pp. 1–5.

[98] G. R. MacCartney, Jr. and T. S. Rappaport, "A flexible millimeter-wave channel sounder with absolute timing," *IEEE Journal on Selected Areas in Communications*, vol. 35, no. 6, pp. 1402–1418, June 2017.

[99] L. J. Ippolito and J. Feil, "Propagation effects handbook for satellite systems design," 2002.

[100] T. S. Rappaport and D. A. Hawbaker, "Wide-band microwave propagation parameters using circular and linear polarized antennas for indoor wireless channels," *IEEE Transactions on Communications*, vol. 40, no. 2, pp. 240–245, Feb 1992.

[101] M. Shafi, M. Zhang, A. L. Moustakas, P. J. Smith, A. F. Molisch, F. Tufvesson, and S. H. Simon, "Polarized mimo channels in 3-d: models, measurements and mutual information," *IEEE Journal on Selected Areas in Communications*, vol. 24, no. 3, pp. 514–527, March 2006.

[102] N. Iqbal, J. Luo, C. Schneider, D. Dupleich, R. Müller, S. Haefner, and R. S. Thomä, "Stochastic/deterministic behavior of cross polarization discrimination in mmwave channels," in *2017 IEEE International Conference on Communications (ICC)*, May 2017, pp. 1–5.

[103] T. S. Rappaport and S. Deng, "73 GHz wideband millimeter-wave foliage and ground reflection measurements and models," in *2015 IEEE International Conference on Communication Workshop (ICCW)*, June 2015, pp. 1238–1243.

[104] W. G. Newhall, T. S. Rappaport, and D. G. Sweeney, "A spread spectrum sliding correlator system for propagation measurements," in *RF Design*, Apr. 1996, pp. 40–54.

[105] W. G. Newhall, K. Saldanha, and T. S. Rappaport, "Using RF channel sounding measurements to determine delay spread and path loss," in *RF Design*, Jan. 1996, pp. 82–88.

[106] W. G. Newhall and T. S. Rappaport, "An antenna pattern measurement technique using wideband channel profiles to resolve multipath signal components," in *Antenna Measurement Techniques Association 19th Annual Meeting & Symposium*, Nov. 1997, pp. 17–21.

[107] R. G. Vaughan, "Polarization diversity in mobile communications," *IEEE Transactions on Vehicular Technology*, vol. 39, no. 3, pp. 177–186, Aug. 1990.

[108] Y. Xing *et al.*, "Verification and calibration of antenna cross-polarization discrimination and penetration loss for millimeter wave communications," in *2018 IEEE 88th Vehicular Technology Conference*, Aug. 2018, pp. 1–6.

[109] T. S. Rappaport and S. Deng, "73 GHz wideband millimeter-wave foliage and ground reflection measurements and models," in *IEEE International Conference on Communications Workshops (ICCW)*, June 2015, pp. 1238–1243.

[110] C. R. Anderson and T. S. Rappaport, "In-building wideband partition loss measurements at 2.5 and 60 GHz," *IEEE Transactions on Wireless Communications*, vol. 3, no. 3, pp. 922–928, May 2004.

[111] G. D. Durgin, T. S. Rappaport, and H. Xu, "Partition-based path loss analysis for in-home and residential areas at 5.85 GHz," in *1998 IEEE Global Communications Conference (GLOBECOM)*, vol. 2, Nov. 1998, pp. 904–909.

[112] R. Davies, M. Bensebti, M. A. Beach, and J. P. McGeehan, "Wireless propagation measurements in indoor multipath environments at 1.7 GHz and 60 GHz for small cell systems," in *[1991 Proceedings] 41st IEEE Vehicular Technology Conference*, May 1991, pp. 589–593.

[113] C. Thajudeen, A. Hoorfar, F. Ahmad, and T. Dogaru, "Measured complex permittivity of walls with different hydration levels and the effect on power estimation of twri target returns," *Progress in Electromagnetics Research*, vol. 30, pp. 177–199, 2011.

[114] H. Zhao *et al.*, "28 GHz millimeter wave cellular communication measurements for reflection and penetration loss in and around buildings in New York city," in *2013 IEEE International Conference on Communications (ICC)*, June 2013, pp. 5163–5167.

[115] G. D. Durgin, T. S. Rappaport, and H. Xu, "Measurements and models for radio path loss and penetration loss in and around homes and trees at 5.85 GHz," *IEEE Transactions on Communications*, vol. 46, no. 11, pp. 1484–1496, Nov. 1998.

[116] J. Ryan, G. R. MacCartney, Jr., and T. S. Rappaport, "Indoor Office Wideband Penetration Loss Measurements at 73 GHz," in *IEEE International Conference on Communications Workshop*, May 2017, pp. 1–6.

[117] J. Kokkoniemi, J. Lehtomäki, and M. Juntti, "Measurements on penetration loss in terahertz band," in *2016 10th European Conference on Antennas and Propagation (EuCAP)*, Apr. 2016, pp. 1–5.

[118] Y. P. Zhang and Y. Hwang, "Measurements of the characteristics of indoor penetration loss," in *1994 IEEE 44th Vehicular Technology Conference (VTC)*, vol. 3, June 1994, pp. 1741–1744.

[119] L. M. Frazier, "Radar surveillance through solid materials," in *Command, Control, Communications, and Intelligence Systems for Law Enforcement*, vol. 2938. International Society for Optics and Photonics, Feb. 1997, pp. 139–147.

[120] A. K. M. Isa, A. Nix, and G. Hilton, "Impact of diffraction and attenuation for material characterisation in millimetre wave bands," in *2015 Loughborough Antennas and Propagation Conference (LAPC)*, Nov. 2015, pp. 1–4.

[121] B. Kapilevich, M. Einat, A. Yahalom, M. Kanter, B. Litvak, and A. Gover, "Millimeter Waves Sensing Behind Walls-Feasibility Study With FEL Radiation," *Proceedings of FEL 2007, Novosibirsk, Russia*, 2007.

[122] R. R. Skidmore, T. S. Rappaport, and A. L. Abbott, "Interactive coverage region and system design simulation for wireless communication systems in multifloored indoor environments: SMT PLUS," in *Proceedings of the 5th IEEE International Conference on Universal Personal Communications*, vol. 2, Sept. 1996, pp. 646–650.

[123] S. Y. Seidel and T. S. Rappaport, "900 MHz path loss measurements and prediction techniques for in-building communication system design," in *1991 Proceedings of the 41st IEEE Vehicular Technology Conference*, May 1991, pp. 613–618.

[124] A. A. Goulianos, A. L. Freire, T. Barratt, E. Mellios, P. Cain, M. Rumney, A. Nix, and M. Beach, "Measurements and characterisation of surface scattering at 60 ghz," in *2017 IEEE 86th Vehicular Technology Conference (VTC-Fall)*, Sept 2017, pp. 1–5.

[125] J. Ma, R. Shrestha, W. Zhang, L. Moeller, and D. M. Mittleman, "Terahertz wireless links using diffuse scattering from rough surfaces," *IEEE Transactions on Terahertz Science and Technology*, vol. 9, no. 5, pp. 463–470, Sep. 2019.

[126] A. Navarro, D. Guevara, and D. A. Parada, "Diffuse Scattering Implementation and Verification in Ray Launching Based Tool at 5.4 GHz," *32nd URSI GASS, Montreal*, Aug. 2017.

[127] V. Degli-Esposti, F. Fuschini, E. M. Vitucci, and G. Falciasecca, "Measurement and modelling of scattering from buildings," *IEEE Transactions on Antennas and Propagation*, vol. 55, no. 1, pp. 143–153, Jan. 2007.

[128] J. Järveläinen, K. Haneda, M. Kyrö, V. Kolmonen, J. Takada, and H. Hagiwara, "60 GHz radio wave propagation prediction in a hospital environment using an accurate room structural model," in *2012 Loughborough Antennas Propagation Conference (LAPC)*, Nov. 2012, pp. 1–4.

[129] V. Degli-Esposti, "A diffuse scattering model for urban propagation prediction," *IEEE Transactions on Antennas and Propagation*, vol. 49, no. 7, pp. 1111–1113, July 2001.

[130] S. Ju *et al.*, "Scattering Mechanisms and Modeling for Terahertz Wireless Communications," in *Proc. IEEE International Conference on Communications*, May. 2019, pp. 1–7.

[131] V. Degli-Esposti, F. Fuschini, E. M. Vitucci, and G. Falciasecca, "Measurement and modelling of scattering from buildings," *IEEE Transactions on Antennas and Propagation*, vol. 55, no. 1, pp. 143–153, Jan 2007.

[132] O. Kanhere and T. S. Rappaport, "Position Location for Futuristic Wireless Communications: 5G and Beyond," *IEEE Communications Magazine*, pp. 70–75, Feb. 2021.

[133] K. Haneda *et al.*, "5G 3GPP-like channel models for outdoor urban microcellular and macrocellular environments," in *2016 IEEE 83rd Vehicular Technology Conference (VTC2016-Spring)*, May 2016, pp. 1–7.

[134] S. Sun *et al.*, "MIMO for millimeter-wave wireless communications: beamforming, spatial multiplexing, or both?" *IEEE Communications Magazine*, vol. 52, no. 12, pp. 110–121, Dec. 2014.

[135] 3GPP, "Study on channel model for frequencies from 0.5 to 100 GHz," 3rd Generation Partnership Project (3GPP), TR 38.901 V16.1.0, Dec. 2019.

[136] Q. Wu and R. Zhang, "Towards Smart and Reconfigurable Environment: Intelligent Reflecting Surface Aided Wireless Network," *IEEE Communications Magazine*, vol. 58, no. 1, pp. 106–112, Jan. 2020.

[137] L. Pometcu and R. D'Errico, "Characterization of sub-thz and mmwave propagation channel for indoor scenarios," in *12th European Conference on Antennas and Propagation (EuCAP 2018)*, April 2018, pp. 1–4.

[138] M. Jacob and T. Kurner, "Radio channel characteristics for broadband WLAN/WPAN applications between 67 and 110 GHz," in *2009 3rd European Conference on Antennas and Propagation*, March 2009, pp. 2663–2667.

[139] K. Guan, B. Peng, D. He, J. M. Eckhardt, S. Rey, B. Ai, Z. Zhong, and T. Kürner, "Channel Characterization for Intra-Wagon Communication at 60 and 300 GHz Bands," *IEEE Transactions on Vehicular Technology*, vol. 68, no. 6, pp. 5193–5207, June 2019.

[140] Y. Xing *et al.*, "Sub-THz Indoor Propagation Measurements Documentation: A Guide to Understand the Measurements and Data," NYU WIRELESS Technical Report, TR 2021-002, Dec. 2021.

[141] G. R. MacCartney, Jr. *et al.*, "Indoor office wideband millimeter-wave propagation measurements and models at 28 GHz and 73 GHz for ultra-dense 5G wireless networks (Invited Paper)," *IEEE Access*, vol. 3, pp. 2388–2424, Oct. 2015.

[142] S. Nie *et al.*, "72 GHz millimeter wave indoor measurements for wireless and backhaul communications," in *2013 IEEE 24th International Symposium on Personal Indoor and Mobile Radio Communications (PIMRC)*, Sept. 2013, pp. 2429–2433.

[143] K. Haneda *et al.*, "Indoor 5G 3GPP-like channel models for office and shopping mall environments," in *2016 IEEE International Conference on Communications Workshops (ICC)*, May 2016, pp. 694–699.

[144] S. Sun, G. R. MacCartney, Jr., and T. S. Rappaport, "Millimeter-wave distance-dependent large-scale propagation measurements and path loss models for outdoor and indoor 5G systems," in *2016 IEEE 10th European Conference on Antennas and Propagation (EuCAP)*, Apr. 2016, pp. 1–5.

[145] T. S. Rappaport *et al.*, "Wideband millimeter-wave propagation measurements and channel models for future wireless communication system design," *IEEE Transactions on Communications*, vol. 63, no. 9, pp. 3029–3056, Sept. 2015.

[146] S. Sun *et al.*, "Propagation Path Loss Models for 5G Urban Micro- and Macro-Cellular Scenarios," in *2016 IEEE 83rd Vehicular Technology Conference (VTC 2016-Spring)*, May 2016, pp. 1–6.

[147] ——, "Path loss, shadow fading, and line-of-sight probability models for 5G urban macrocellular scenarios," in *2015 IEEE Globecom Workshops (GC Wkshps)*, Dec. 2015, pp. 1–7.

[148] K. Haneda *et al.*, "Frequency-agile pathloss models for urban street canyons," *IEEE Transactions on Antennas and Propagation*, vol. 64, no. 5, pp. 1941–1951, May 2016.

[149] G. R. MacCartney, Jr. *et al.*, "Millimeter wave wireless communications: New results for rural connectivity," in *Proceedings of the 5th Workshop on All Things Cellular: Operations, Applications and Challenges: in conjunction with MobiCom 2016*, ser. ATC '16. New York, NY, USA: ACM, Oct. 2016, pp. 31–36.

[150] M. Hata, "Empirical formula for propagation loss in land mobile radio services," *IEEE Transactions on Vehicular Technology*, vol. 29, no. 3, pp. 317–325, Aug. 1980.

[151] S. Piersanti, L. A. Annoni, and D. Cassioli, "Millimeter waves channel measurements and path loss models," in *2012 IEEE International Conference on Communications (ICC)*, June 2012, pp. 4552–4556.

[152] G. R. MacCartney, Jr. *et al.*, "Path loss models for 5G millimeter wave propagation channels in urban microcells," in *2013 IEEE Global Communications Conference (GLOBECOM)*, Dec. 2013, pp. 3948–3953.

[153] 5GCM, "5G Channel Model for bands up to 100 GHz," Tech. Rep., Oct. 2016.

[154] T. A. Thomas *et al.*, "A prediction study of path loss models from 2-73.5 GHz in an urban-macro environment," in *2016 IEEE 83rd Vehicular Technology Conference (VTC 2016-Spring)*, May 2016, pp. 1–5.

[155] G. R. MacCartney, Jr., S. Deng, and T. S. Rappaport, "Indoor Office Plan Environment and Layout-Based mmWave Path Loss Models for 28 GHz and 73 GHz," in *2016 IEEE 83rd Vehicular Technology Conference (VTC Spring)*, May 2016, pp. 1–6.

[156] S. Deng, M. K. Samimi, and T. S. Rappaport, "28 GHz and 73 GHz millimeter-wave indoor propagation measurements and path loss models," in *IEEE International Conference on Communications Workshops (ICCW)*, June 2015, pp. 1244–1250.

[157] 3GPP, "Technical Specification Group Radio Access Network; Study on channel model for frequencies from 0.5 to 100 GHz (Release 15)," TR 38.901 V15.0.0, June 2018. [Online]. Available: http://www.3gpp.org/DynaReport/38901.htm

[158] T. S. Rappaport *et al.*, "Overview of millimeter wave communications for fifth-generation (5G) wireless networks - with a focus on propagation models," *IEEE Transactions on Antennas and Propagation*, vol. 65, no. 12, pp. 6213–6230, Dec. 2017.

[159] S. Sun *et al.*, "Millimeter wave multi-beam antenna combining for 5G cellular link improvement in New York City," in *2014 IEEE International Conference on Communications (ICC)*, June 2014, pp. 5468–5473.

[160] ——, "Synthesizing Omnidirectional antenna patterns, received power and path loss from directional antennas for 5G millimeter-wave communications," in *IEEE Global Communications Conference (GLOBECOM)*, Dec. 2015, pp. 3948–3953.

[161] M. K. Samimi and T. S. Rappaport, "3-D millimeter-wave statistical channel model for 5G wireless system design," *IEEE Transactions on Microwave Theory and Techniques*, vol. 64, no. 7, pp. 2207–2225, July 2016.

[162] H. Wang *et al.*, "Power amplifiers performance survey 2000-present," [Online]. Available: https://gems.ece.gatech.edu/PA_survey.html, 2019.

[163] 3GPP, "Technical Specification Group Radio Access Network; Study on new radio access technology: Radio Freqyency (RF) and co-existence aspects (Release 14)," 3rd Generation Partnership Project (3GPP), TR 38.803 V14.2.0, Sept. 2017.

[164] *IEEE 802.15-06-0477-00-003C, RF Impairment MODELS FOR 60 GHz-band SYS/PHY Simulation*, IEEE Std., Tech. Rep., Nov. 2006.

[165] Y. Qi, M. Hunukumbure, H. Nam, H. Yoo, and S. Amuru, "On the phase tracking reference signal (pt-rs) design for 5g new radio (nr)," in *2018 IEEE 88th Vehicular Technology Conference (VTC-Fall)*, Aug 2018, pp. 1–5.

[166] M. Cudak, T. Kovarik, T. A. Thomas, A. Ghosh, Y. Kishiyama, and T. Nakamura, "Experimental mm wave 5g cellular system," in *2014 IEEE Globecom Workshops (GC Wkshps)*, Dec 2014, pp. 377–381.

[167] T. A. Thomas, M. Cudak, and T. Kovarik, "Blind phase noise mitigation for a 72 ghz millimeter wave system," in *2015 IEEE International Conference on Communications (ICC)*, June 2015, pp. 1352–1357.

[168] F. Rice, B. Cowley, B. Moran, and M. Rice, "Cramer-rao lower bounds for qam phase and frequency estimation," *IEEE Transactions on Communications*, vol. 49, no. 9, pp. 1582–1591, Sep. 2001.

[169] M. Moeneclaey and G. de Jonghe, "Ml-oriented nda carrier synchronization for general rotationally symmetric signal constellations," *IEEE Transactions on Communications*, vol. 42, no. 8, pp. 2531–2533, Aug 1994.

[170] Aalto University, AT&T, BUPT, CMCC, Ericsson, Huawei, Intel, KT Corporation, Nokia, NTT DOCOMO, New York University, Qualcomm, Samsung, University of Bristol, and University of Southern California, "5G Channel Model for bands up to 100 GHz," Tech. Rep., Oct. 2016. [Online]. Available: http://www.5gworkshops.com/5GCM.html

[171] METIS, "METIS Channel Model," METIS2020, Deliverable D1.4 v3, July 2015.

[172] mmMAGIC, "Measurement results and final mmmagic channel models," H2020-ICT-671650-mmMAGIC/D2.2 v2.0, Dec. 2017. [Online]. Available: https://5g-ppp.eu/mmmagic/

[173] S. Sun *et al.*, "Propagation models and performance evaluation for 5G millimeter-wave bands," *IEEE Transactions on Vehilcular Technology*, July 2018.

[174] Y. Xing *et al.*, "Sub-THz Outdoor Urban Microcell Measurements Documentation: A Guide to Understand the Measurements and Data," NYU WIRELESS Technical Report, TR 2021-003, Dec. 2021.

[175] S. Ju and T. S. Rappaport, "140 GHz Urban Microcell Propagation Measurements for Spatial Consistency Modeling," in *Proc. IEEE International Conference on Communications*, June 2021, pp. 1–6.

[176] S. Sun *et al.*, "Synthesizing omnidirectional antenna patterns, received power and path loss from directional antennas for 5G millimeter-wave communications," in *2015 IEEE Global Communications Conference (GLOBECOM)*, Dec. 2015, pp. 3948–3953.

[177] T. S. Rappaport *et al.*, "Broadband millimeter-wave propagation measurements and models using adaptive-beam antennas for outdoor urban cellular communications," *IEEE Transactions on Antennas and Propagation*, vol. 61, no. 4, pp. 1850–1859, Apr. 2013.

[178] G. R. MacCartney, Jr. and T. S. Rappaport, "Millimeter-Wave Base Station Diversity for 5G Coordinated Multipoint (CoMP) Applications," *IEEE Transactions on Wireless Communications*, May 2019.

[179] M. K. Samimi and T. S. Rappaport, "3-D millimeter-wave statistical channel model for 5G wireless system design," *IEEE Transactions on Microwave Theory and Techniques*, vol. 64, no. 7, pp. 2207–2225, July 2016.

[180] S. Ju and T. S. Rappaport, "Sub-Terahertz Spatial Statistical MIMO Channel Model for Urban Microcells at 142 GHz," in *2021 IEEE Global Communications Conference (GLOBECOM)*, Dec. 2021, pp. 1–6.

[181] O. Kanhere, S. Ju, Y. Xing, and T. S. Rappaport, "Map Assisted Millimeter Wave Localization for Accurate Position Location," in *IEEE Globecom*, Dec. 2019, pp. 1–6.

[182] J. Zhang, P. Tang, L. Yu, T. Jiang, and L. Tian, "Channel measurements and models for 6g: current status and future outlook," *Frontiers of Information Technology and Electronic Engineering*, vol. 21, pp. 39–61, Jan. 2020.

[183] A. Ali, N. Gonzalez-Prelcic, R. W. Heath, and A. Ghosh, "Leveraging sensing at the infrastructure for mmwave communication," *IEEE Communications Magazine*, vol. 58, no. 7, pp. 84–89, Aug. 2020.

[184] S. H. Dokhanchi *et al.*, "A mmwave automotive joint radar-communications system," *IEEE Transactions on Aerospace and Electronic Systems*, vol. 55, no. 3, pp. 1241–1260, Feb. 2019.

[185] Y. Chen, C. Han, Z. Yu, and G. Wang, "140 ghz channel measurement and characterization in an office room," in *ICC 2021 - IEEE International Conference on Communications*, June 2021, pp. 1–6.

[186] S. Kim *et al.*, "D-band channel measurements and characterization for indoor applications," *IEEE Transactions on Antennas and Propagation*, vol. 63, no. 7, pp. 3198–3207, July 2015.

[187] D. Serghiou *et al.*, "Ultra-wideband terahertz channel propagation measurements from 500 to 750 ghz," in *2020 International Conference on UK-China Emerging Technologies (UCET)*, Sept. 2020, pp. 1–4.

[188] H.-J. Song, "Los channel response measurement at 300 ghz for short-range wireless communication," in *2020 IEEE Wireless Communications and Networking Conference Workshops (WCNCW)*, June 2020, pp. 1–3.

[189] J. N. Murdock and T. S. Rappaport, "Consumption factor and power-efficiency factor: A theory for evaluating the energy efficiency of cascaded communication systems," *IEEE Journal on Selected Areas in Communications*, vol. 32, no. 2, pp. 221–236, Feb. 2014.

[190] New York University, *NYUSIM*, 2016. [Online]. Available: http://wireless.engineering.nyu.edu/nyusim/

[191] Y. Xing, F. Hsieh, A. Ghosh, and T. S. Rappaport, "High altitude platform stations (haps): Architecture and system performance," in *2021 IEEE 93rd Vehicular Technology Conference (VTC2021-Spring)*, June 2021, pp. 1–6.

[192] F. Liu *et al.*, "Joint Radar and Communication Design: Applications, State-of-the-Art, and the Road Ahead," *IEEE Transactions on Communications*, vol. 68, no. 6, pp. 3834–3862, Feb. 2020.

[193] A. Ali, N. Gonzalez-Prelcic, and A. Ghosh, "Automotive radar radiations as signals of opportunity for millimeter wave v2i links," in *2019 53rd Asilomar Conference on Signals, Systems, and Computers*, Nov. 2019.

[194] L. Zhang, M. Xiao, G. Wu, M. Alam, Y. Liang, and S. Li, "A survey of advanced techniques for spectrum sharing in 5g networks," *IEEE Wireless Communications*, vol. 24, no. 5, pp. 44–51, 2017.

[195] World Radiocommunication Conference 2019 (WRC-19), "Final Acts," Nov. 2019. [Online]. Available: https://www.itu.int/pub/R-ACT-WRC.14-2019/en

[196] 3GPP TR 38.821, "Technical Specification Group Radio Access Network; Solutions for NR to support non-terrestrial networks (NTN)," 3rd Generation Partnership Project (3GPP), TR 38.821 V16.0.0, Dec. 2019.

[197] J. C. Liljegren, S. . Boukabara, K. Cady-Pereira, and S. A. Clough, "The effect of the half-width of the 22-ghz water vapor line on retrievals of temperature and water vapor profiles with a 12-channel microwave radiometer," *IEEE Transactions on Geoscience and Remote Sensing*, vol. 43, no. 5, pp. 1102–1108, 2005.

[198] T. S. Rappaport, S. DiPierro, and R. Akturan, "Analysis and simulation of interference to vehicle-equipped digital receivers from cellular mobile terminals operating in adjacent frequencies," *IEEE Transactions on Vehicular Technology*, vol. 60, no. 4, pp. 1664–1676, May 2011.

[199] Federal Communications Commission, "Commission Staff Requests That Interested Parties Supplement the Record on Draft Interference Rules for Wireless Communications Service and Satellite Digital Audio Radio Service: WT Docket No. 07-293. ," April 2010.

[200] M. M. Sohul, M. Yao, T. Yang, and J. H. Reed, "Spectrum access system for the citizen broadband radio service," *IEEE Communications Magazine*, vol. 53, no. 7, pp. 18–25, 2015.

[201] 3GPP, "Technical specification group radio access network; study on licensed-assisted access to unlicensed spectrum (release 13)," 3rd Generation Partnership Project (3GPP), TR 36.889 V13.0.0, June 2015.

[202] B. Chen, J. Chen, Y. Gao, and J. Zhang, "Coexistence of LTE-LAA and Wi-Fi on 5 GHz With Corresponding Deployment Scenarios: A Survey," *IEEE Communications Surveys Tutorials*, vol. 19, no. 1, pp. 7–32, 2017.

[203] G. Hattab, E. Visotsky, M. C. Cudak, and A. Ghosh, "Uplink interference mitigation techniques for coexistence of 5g millimeter wave users with incumbents at 70 and 80 ghz," *IEEE Transactions on Wireless Communications*, vol. 18, no. 1, pp. 324–339, 2019.

[204] National Aeronautics and Space Administration (NASA), "U.S. Standard Atmosphere," 1976.

[205] S. Karapantazis and F. Pavlidou, "Broadband communications via high-altitude platforms: A survey," *IEEE Communications Surveys Tutorials*, vol. 7, no. 1, pp. 2–31, 2005.

[206] S. C. Reising *et al.*, "Temporal Experiment for Storms and Tropical Systems Technology Demonstration (TEMPEST-D) Mission: Enabling Time-Resolved Cloud and Precipitation Observations from 6U-Class Satellite Constellations," *Proceedings of the 31st Annual AIAA/USU Conference on Small Satellites, Logan UT, USA*, p. 7, Aug. 2017.

[207] A. C. Clarke, "Extra-Terrestrial Relays: Can Rocket Stations Give World-wide Radio Coverage?" *Wireless World*, pp. 305–308, October 1945.

[208] A. Mohammed, A. Mehmood, F. Pavlidou, and M. Mohorcic, "The Role of High-Altitude Platforms (HAPs) in the Global Wireless Connectivity," *Proceedings of the IEEE*, vol. 99, no. 11, pp. 1939–1953, 2011.

[209] F. Hsieh and M. Rybakowski, "Propagation Model for High Altitude Platform Systems Based on Ray Tracing Simulation," in *2019 13th European Conference on Antennas and Propagation (EuCAP)*, April 2019, pp. 1–5.

[210] W. Khawaja, I. Guvenc, D. W. Matolak, U. Fiebig, and N. Schneckenburger, "A survey of air-to-ground propagation channel modeling for unmanned aerial vehicles," *IEEE Communications Surveys Tutorials*, vol. 21, no. 3, pp. 2361–2391, May 2019.

[211] 3GPP TR 38.811, "Study on New Radio (NR) to Support Non-Terrestrial Networks," 3rd Generation Partnership Project (3GPP), TR 38.811 V1.0.0, June 2018.

[212] A. A. Khuwaja, Y. Chen, N. Zhao, M. Alouini, and P. Dobbins, "A survey of channel modeling for uav communications," *IEEE Communications Surveys Tutorials*, vol. 20, no. 4, pp. 2804–2821, July 2018.

[213] W. Khawaja, O. Ozdemir, and I. Guvenc, "Uav air-to-ground channel characterization for mmwave systems," in *2017 IEEE 86th Vehicular Technology Conference (VTC-Fall)*, 2017, pp. 1–5.

[214] ITU, "the international telecommunication union's first world telecommunication policy forum on mobile satellite systems." [Online]. Available: https://www.itu.int/newsarchive/wtpf96/fact.html

[215] TEMPEST-D, "Temporal experiment for storms and tropical systems technology-demonstration (tempest-d)." [Online]. Available: https://directory.eoportal.org/web/eoportal/satellite-missions/t/tempest-d

[216] TROPICS, "Time-resolved observations of precipitation structure and storm intensity with a constellation of smallsats (tropics)." [Online]. Available: https://tropics.ll.mit.edu/CMS/tropics/

[217] ATMS, "Advanced technology microwave sounder (atms)/joint polar satellite system (jpss)." [Online]. Available: https://www.jpss.noaa.gov/atms.html

[218] Y. Xing, T. S. Rappaport, and A. Ghosh, "Millimeter Wave and Sub-Terahertz Indoor Office Building Propagation Measurements and Channel Models at 28, 73, and 142 GHz," *IEEE Journal on Selected Areas in Communications, Special Issue on TeraHertz Communications and Networking*, vol. 39, no. 6, pp. 1561–1575, June 2021.

[219] International Telecommunications Union, "Performance and interference criteria for satellite passive remote sensing," Geneva, Switzerland, RS Series ITU-R RS.2017-0, Aug. 2012.

[220] A. S. H. Ahmed *et al.*, "A 200mW D-band Power Amplifier with 17.8% PAE in 250-nm InP HBT Technology," in *2020 15th European Microwave Integrated Circuits Conference (EuMIC)*, Jan. 2021, pp. 1–4.

[221] A. Simsek *et al.*, "A 146.7 GHz Transceiver with 5 GBaud Data Transmission using a Low-Cost Series-Fed Patch Antenna Array through Wirebonding Integration," in *2020 IEEE Radio and Wireless Symposium (RWS)*, Jan. 2020.

[222] S. Karapantazis and F. Pavlidou, "Broadband communications via high-altitude platforms: A survey," *IEEE Communications Surveys Tutorials*, vol. 7, no. 1, pp. 2–31, May 2005.

[223] F. Hsieh *et al.*, "UAV-based Multi-cell HAPS Communications: System Design and Performance Evaluation," in *2020 Global Communications Conference (GLOBECOM)*, Dec. 2020, pp. 1–6.

[224] A. Mohammed, A. Mehmood, F. Pavlidou, and M. Mohorcic, "The role of high-altitude platforms (haps) in the global wireless connectivity," *Proceedings of the IEEE*, vol. 99, no. 11, pp. 1939–1953, Nov. 2011.

[225] R. Amorim, H. Nguyen, P. Mogensen, I. Z. Kovács, J. Wigard, and T. B. Sørensen, "Radio channel modeling for uav communication over cellular networks," *IEEE Wireless Communications Letters*, vol. 6, no. 4, pp. 514–517, 2017.

[226] M. Polese *et al.*, "An experimental mmwave channel model for uav-to-uav communications," Sept. 2020.

[227] S. Garcia Sanchez *et al.*, "Millimeter-wave base stations in the sky: An experimental study of uav-to-ground communications," *IEEE Transactions on Mobile Computing*, pp. 1–1, Aug. 2020.

[228] 3GPP, "Universal Terrestrial Radio Access (UTRA): repeater planning guidelines and system analysis," 3rd Generation Partnership Project (3GPP), TR 25.956 V16.0.0, June. 2020.

[229] T. S. Rappaport and J. N. Murdock, "Power efficiency and consumption factor analysis for broadband millimeter-wave cellular networks," in *2012 IEEE Global Communications Conference (GLOBECOM)*, Dec. 2012.

[230] 3GPP, "Technical Specification Group Radio Access Network; NR: Physical layer procedures for data (Release 16)," 3rd Generation Partnership Project (3GPP), TS 38.214 V16.2.0, June 2020.